FRAGMENTATION, GRANULAR TRANSITION & IMPACT PERFORMANCE OF CERAMICS

by

Amartya Bhattacharjee

A dissertation submitted to The Johns Hopkins University in conformity with the requirements for the degree of Doctor of Philosophy.

Baltimore, Maryland

May, 2021

Abstract

Brittle materials under impact loading exhibit a transition from a cracked solid to a granular medium. Appropriate representation of this transition to granular mechanics and the resulting initial fragment size and shape distribution in computational models is not well understood. The current work provides a numerical model to analyze competitive crack coalescence in the transition regime and provides insight into the onset of comminution and the initial conditions for subsequent granular flow. Crack statistics obtained from initial flaws using a wing crack growth based damage model have been used to discretely model elliptical cracks in three dimensions, with and without a minimal intersection constraint. These cracks are then allowed to coalesce with nearby cracks along favourable directions and the output fragment statistics are predicted. The evolving fragmentation offers insight into the onset of comminution as well as the final transition to granular mechanics and the resulting initial fragment statistics. A simple phenomenological model has been proposed that suggests a transition criterion resembling the one obtained from the numerical

model.

A micromechanical multi-physics model for ceramics has been recalibrated using the new granular transition criterion and new experimental data, and used to simulate impact experiments with boron carbide in ABAQUS. The dominant physical mechanisms in boron carbide have been identified and simulated in the framework of an integrated constitutive model that combines crack growth, amorphization and granular flow. The integrative model is able to accurately reproduce some of the key cracking patterns of Sphere Indentation experiments and Edge On Impact experiments.

Based on this integrative model, linear regression has been used to study the sensitivity of sphere indentation model predictions to the input parameters. The sensitivities are connected to physical mechanisms, and trends in model outputs have been intuitively explored. These results help suggest material modifications that might improve material performance, prioritize calibration experiments for materials-by-design iterations, and identify model parameters that require more in-depth understanding.

The dynamic performance of armor ceramics is related to their microstructure through various mechanisms that are either intrinsic to the material or the specific loading conditions. Although this relationship has previously been explored in the context of some mechanisms like crack growth and interaction, the microstructural dependence of the parameters of some other mechanisms

ABSTRACT

such as fragmentation and subsequent granular flow is not well understood. This thesis studies the influence of microstructural defects on the fragment size and shape distribution in comminuted armor ceramics, which has a significant effect on the associated granular mechanics of the material. The crack coalescence and fragmentation model has been modified to account for anisotropic crack growth and to predict fragment shape more accurately. Fragment statistics predicted via the model are used to infer fragment morphology for different initial microstructures. Existing geomechanics literature then helps to link the trends to bulk granular friction. The observations suggest that an optimal defect size and spacing in the initial intact ceramic will enhance impact performance as compared to fine dispersed defects in the ceramic matrix.

In some impact experiments, structural fragmentation of ceramics could precede microstructure driven granular transition and limit the strength of ceramics. In the last part of this thesis, the link between structural fragmentation, fragment sizes and analytical structural fragmentation criteria are explored and suggested as future directions.

Primary Reader and Advisor: Lori Graham-Brady

Secondary Reader: Ryan C. Hurley

Secondary Reader: Stavros Gaitanaros

Acknowledgments

First and foremost, I would like to thank my advisor, Dr. Lori Graham-Brady. Lori has been a true mentor throughout my doctoral education as well as in life. She has encouraged me to pursue independent research directions and actively guided me throughout the process. Despite both research and administrative commitments, her ability to make time for her students has been both inspiring and motivating. Lori's approachable persona is often reflected by the rest of the research group; inquisitiveness is met without judgment and criticism without hostility. From my early days in the research group, Lori has encouraged us to develop our leadership skills through participation in departmental organizations and provided us with opportunities to enhance our teaching abilities. On the whole, Lori has taught me about balance in research and in life, pursuing ideas while keeping a foot on the ground,and above all enjoying both research and life.

I would like to thank Dr. Ryan C. Hurley, who has essentially been my co-advisor throughout the last couple of years. Ryan's valuable feedback in

weekly meetings and his prompt, meticulous reviews have immensely helped me towards the completion of this thesis.

I am grateful to Dr. Stavros Gaitanaros for being a member of my Graduate Board Oral (GBO) committee at a short notice, as well as part of my thesis committee.

I am thankful to my other Department Qualifying Exam (DQE) and GBO committee members: Drs. Sauleh Siddiqui, Jafaar El-Awady, and Jaime Guest.

Over the course of my Ph.D., I had the opportunity to collaborate with some amazing researchers. The weekly ceramics modelling meeting provided me with a semi-formal avenue to present my work and have it reviewed, to be exposed to new ideas and to visualize a comprehensive picture. Drs. Andrew L. Tonge, K.T. Ramesh, Mark Robbins, Nilanjan Mitra, Ryan C. Hurley, past and present students and postdocs in the meetings, and everyone else involved in the larger ceramics research group have been useful collaborators directly or indirectly. In particular, the late Dr. Robbins' profound knowledge and sharp remarks will be missed. I have collaborated with Drs. Mehmet Cil, Qinglei Zeng, and Weixin Li for the implementation of the ceramics integrative model. Dr. Anindya Bhaduri, who is also my group-mate and friend, has been an indispensable collaborator for the sensitivity analysis study.

In the last year of my Ph.D., I have also been involved in a project to study the fragmentation of carbon varying boron carbide. As a part of this project I

have collaborated with Dr. Richard Haber's group at Rutgers University (Dr. Bruce Yang and Kent Christian) on the processing side and Dr. Arezoo Zare in Dr. K.T. Ramesh's group on the experimental side. I am particularly obliged to Arezoo for bearing with my constant emails and never-ending questions. Aside from her research contribution, Arezoo's role as an intermediary has been indispensable to the project.

Within my research group (Anindya, Ashwini, Audrey, David,Farah, Jamey, Mehmet,Nicolas, Noah), I have enjoyed our pre-COVID in-person and current virtual meetings. I will always remember the surprise feel of our furry groupmate, Jessie's cold nose!

When I first joined Hopkins, being involved in the Civil & Systems Engineering Graduate Association (CSEGA) helped foster a sense of community. The outdoor excursions, movie nights, coffee hours, happy hours, game nights, DQE practice sessions, and myriad other adventures provided much-needed recreational opportunities. I would also like to thank the Graduate Student Organization for the many inter-departmental socialization avenues.

I would also like to acknowledge all the administrative personnel and staff at the Civil & Systems Engineering and the Hopkins Extreme Material Institute.

Over the years I have made many friends in Charm City, including folks from my department, Hopkins, my neighborhood, the dog park, and the Poke-

mon Go community in Hampden. Their support, perspective, and affection have made my time in Baltimore fulfilling.

My journey at Hopkins coincides with my journey alongside my partner and best friend, Jaime. His constant encouragement and support through challenges has helped me focus and achieve my goals. Our dog, W the Apricot, has been the biggest stress buster of all, and I cherish our daily evening walks.Above all I express my sincerest gratitude to my family in India (Ma, Baba, Didi, Tanumoy, and Mithi) for their constant love and support.

My research was sponsored by the Army Research Laboratory and was accomplished under Cooperative Agreement Number W911NF-12-2-0022. The views and conclusions contained in this document are my own and should not be interpreted as representing the official policies, either expressed or implied, of the Army Research Laboratory or the U.S. Government. The U.S. Government is authorized to reproduce and distribute reprints for Government purposes notwithstanding any copyright notation herein.

Dedication

Dedicated to the people and doggies I love.

Contents

Abstract **ii**

Acknowledgments **v**

List of Tables **xvi**

List of Figures **xviii**

1 Introduction **1**

1.1 Ceramics as armor material 1

1.2 Boron Carbide - a model armor ceramic 3

1.2.1 Mechanisms & Modelling 4

1.2.1.1 Fracture 4

1.2.1.2 Amorphization 7

1.2.1.3 Granular Flow 8

1.3 Gaps in modelling & outline of the thesis 11

CONTENTS

2 Fragmentation & granular transition **15**

2.1 Introduction 15

2.2 Methodology 22

2.2.1 Initial defects and the crack growth model 24

2.2.2 Simulation of three-dimensional cracks 27

2.2.3 Crack coalescence due to crack growth 29

2.2.3.1 Calculation of stress intensity factor for crack coalescence 31

2.2.3.2 Coalescence surface approach 38

2.2.3.3 Coalescence zone approach 40

2.2.3.4 Threshold distance for crack coalescence 42

2.2.3.5 Comparison of the two approaches 45

2.2.4 Dilation and extracting fragment statistics 47

2.3 Results -

Transition to granular medium 49

2.3.1 Effective fragmentation ratio 49

2.3.2 Granular Phase Transition 57

2.3.3 Phenomenological model for transition 59

2.4 Results - Fragment statistics 61

2.4.1 Comparison with experiments 68

2.5 Discussion 73

2.6 Conclusion 79

3 Implementation in integrated ceramics model 81

3.1 Introduction 81

3.2 Overview - Integrative Model 84

3.2.1 Kinematics and EOS 84

3.2.2 Amorphization 85

3.2.3 Fracture and Fragmentation 86

3.2.4 Transition to granular mechanics 88

3.2.5 Granular Plasticity 89

3.2.5.1 Two surface Drucker Prager model 89

3.2.5.2 Continuum breakage mechanics model (CBM) . . 91

3.3 Numerical Simulations - Integrative Model 93

3.3.1 Calibration of model parameters 93

3.3.1.1 Calibration of transition damage 95

3.3.1.2 Calibration of critical breakage energy density . . 96

3.3.1.3 Calibration of grading index 98

3.3.2 Simulation of Sphere Indentation Experiments 100

3.3.3 Simulation of Edge On Impact Experiments 101

3.4 Results - Integrative Model 102

3.4.1 Sphere Indentation Simulations 102

3.4.2 Edge On Impact Simulations 109

3.5 Summary 117

4 Sensitivity analysis 119

4.1 Introduction 119

4.2 Problem setup - Sensitivity Analysis 122

4.3 Results - Sensitivity Analysis 126

4.3.1 Original parameter set: Correlation study 126

4.3.2 Derived parameter set: Correlation study 127

4.3.3 Granular material percentage 129

4.3.3.1 Analysis with original parameter set 130

4.3.3.2 Analysis with derived parameter set 133

4.3.4 Depth of Penetration 135

4.3.4.1 Analysis with original parameter set 136

4.3.4.2 Analysis with derived parameter set 138

4.4 Discussion 140

4.4.1 Physical Mechanisms and Trends 140

4.4.2 Implications towards designing materials 142

4.4.3 Implications towards modelling and calibration 145

4.5 Summary 146

5 Microstructure & fragment morphology 148

5.1 Introduction 148

5.2 Microstructural Fragmentation - Fragment statistics 152
5.2.1 Input Crack Statistics 152
5.2.2 Crack Coalescence 155
5.2.3 Extracting Fragment Statistics 157
5.2.4 Morphology and Granular Friction 161
5.2.4.1 Critical state friction angle - Alshibli & Cil 163
5.2.4.2 Critical state friction angle - Extreme Vertices Model Roundedness 165
5.3 Results & Discussion 168
5.3.1 Resolution dependence of morphological indices 168
5.3.2 Constant volume fraction of defects 169
5.3.2.1 General morphological trends 172
5.3.2.2 Average particle friction 175
5.3.3 Design implications 178
5.4 Conclusion 180

6 Summary & Future Directions 182

6.1 Summary 182
6.2 Future Directions 186
6.2.1 Carbon varying fragmentation of boron carbide 186
6.2.2 Sensitivity Analysis 187
6.2.3 Structural Fragmentation 188

CONTENTS

A Structural Fragmentation - ABAQUS simulations **190**

A.1 ABAQUS simulations of Kolsky bar experiments 190

A.2 Resolution dependence of fragment statistics 195

B Structural Fragmentation - Phenomenological Model **198**

B.1 Fragmentation Criterion - micostructure driven transition 208

B.2 Fragmentation Criterion - failed area fraction driven transition . 209

B.3 Comparison of prediction with fragmentation models 211

B.4 Extension to three dimensions 215

Bibliography **220**

Vita **255**

List of Tables

2.1 Default material and model parameters (Defect density values correspond to random orientation of cracks). 23

3.1 List of boron carbide material parameters for the integrative model. 94
3.2 Calculation of critical breakage energy density (E_C). 97
3.3 Material parameters of tungsten carbide spherical indenter. . . . 100
3.4 Material parameters of steel projectile. 101

4.1 List of model parameters selected for sensitivity analysis. 125
4.2 Derived parameters selected for sensitivity analysis. 126
4.3 Variation inflation factor (VIF) with original parameters. 127
4.4 Derived parameter list. 128
4.5 Variation inflation factor (VIF) with derived parameters. 128
4.6 Correlation coefficients (sensitivity analysis for GMP with original parameters). 131
4.7 Regression results (sensitivity analysis for GMP with original parameters). 132
4.8 Correlation coefficients (sensitivity analysis for GMP with derived parameters). 134
4.9 Regression results (sensitivity analysis for GMP with derived parameters). 134
4.10 Correlation coefficients (sensitivity analysis for MDR with original parameters). 137
4.11 Regression results (sensitivity analysis for MDR with original parameters). 137
4.12 Regression results (sensitivity analysis for MDR with derived parameters). 139
4.13 Summary of expected correlation of model parameters with granular material % 142

4.14 Suspected of expected correlation of model parameters with instantaneous depth of penetration. 143
4.15 Summary of sensitivity analysis: top 10 model parameters in decreasing order. The colour code represents the mechanisms corresponding to the parameters. Olive, purple and teal correspond to wave speed, crack growth and granular mechanics, respectively. GMP is more strongly influenced by fracture related parameters, while MDR is more strongly influenced by granular mechanics parameters. 144

5.1 Summary of the changes made to the fragmentation model. . . . 152
5.2 Cases of constant values of initial carbon and initial damage content studied. 172

List of Figures

2.1 Outline of steps Involved in the fragmentation model. 25
2.2 Outline of wing crack growth based damage model [55]. 26
2.3 Simplification of defect wing crack assemblies to slanted cracks. . 27
2.4 3-D elliptical crack generation. 29
2.5 2-D crack problem geometry. 33
2.6 2-D crack problem geometry. 35
2.7 Estimating 2-D geometry from 3-D problem. 40
2.8 Steps involved in coalescence surface approach (l_{thresh} denotes the threshold distance). 41
2.9 Representative image of two parallel elliptical cracks with coalescence zones and common 2D coalescence patterns. 43
2.10 EFR evolution with damage with change in coalescence time. . . 45
2.11 Representative images of simulated cracks in a solid: (a) Crack network (red), (b) Crack network (red) embedded in solid matrix (gray). 48
2.12 Representative image of connected regions (a) before and (b) after the dilation procedure. 50
2.13 Comparison of the coalescence zone approach for 1mm and 2mm simulation box size and the coalescence surface approach for 1mm simulation box. 51
2.14 Variation of mean fragment size with damage and EFR at $\eta = 22e12cracks/m^3$ and $\dot{\epsilon} = 10^6 s^{-1}$ for different initial defect sizes. . . 52
2.15 Effective fragmentation ratio, $EFR = 1 - V_{Lf}/V_{Sample}$. 54
2.16 Fragmentation with increasing EFR. 55
2.17 Variation of stress and EFR with damage. The solid and dotted lines in the EFR v/s damage plot correspond to Richard's 5-parameter fit for coalescence zone and coalescence surface approaches respectively. The 0.25, 0.5 and 0.75 EFR states have been highlighted in the stress-damage and EFR-damage curves for both the coalescence zone and coalescence surface approaches. 55

2.18 Volume CDF or fraction passing with fragment size, excluding the largest fragment, for different EFR values. 56
2.19 Schematic representation of phenomenological granular transition model. 62
2.20 Fragment size distribution at $\eta = 20e12cracks/m^3$ and $\dot{\epsilon} = 10^6 s^{-1}$ for varying EFR. 64
2.21 Variation of scaled mean fragment size with damage and EFR at initial defect size of 10μ and $\dot{\epsilon} = 10^6 s^{-1}$, for different crack densities (η). 65
2.22 Variation of mean roundedness index with damage and EFR at $\eta = 22e12cracks/m^3$ and $\dot{\epsilon} = 10^6 s^{-1}$ for different initial defect sizes. 65
2.23 Variation of mean solidity with damage and EFR at $\eta = 22e12cracks/m^3$ and $\dot{\epsilon} = 10^6 s^{-1}$ for different initial defect sizes. 66
2.24 Variation of mean roundedness index with damage and EFR at initial defect size of 10μ and $\dot{\epsilon} = 10^6 s^{-1}$ for different crack densities (η). 66
2.25 Variation of mean solidity with damage and EFR at initial defect size of 10μ and $\dot{\epsilon} = 10^6 s^{-1}$ for different crack densities (η). 67
2.26 Enlarged representative image of fragments showing directionality. 67
2.27 Fragment size distribution obtained from Kolsky bar dynamic fragmentation of Boron Carbide [105]. 69
2.28 Power law distribution exponent of fragment sizes from numerical model. 70
2.29 Mean volume averaged fragment size with change in EFR for fragments less than 100μ. 71
2.30 Comparison of simulating cracks with and without minimal intersection. 76

3.1 Geometry of Sphere Indentation Simulations. 99
3.2 Geometry of Edge On Impact Simulations. 101
3.3 Damage and density contours of Sphere Indentation simulation at 500 m/s impact velocity, $15\mu s$ after impact (CBM Model). 103
3.4 Damage and density contours of Sphere Indentation simulation for the cylinder section at 600 m/s impact velocity, $15\mu s$ after impact (CBM Model). 103
3.5 Comparison of damage contour of Sphere Indentation simulations for the cylinder section for CBM and TSDP models at 500 m/s impact velocity, $15\mu s$ after impact. 105
3.6 Comparison of density contour of Sphere Indentation simulations for the cylinder section for CBM and TSDP models at 500 m/s impact velocity, $15\mu s$ after impact. 105

3.7 Damage contour of Sphere Indentation simulations showing radial cracking with impact velocity, 15μs after impact (CBM Model).106
3.8 Density contour of Sphere Indentation simulations showing radial cracking with impact velocity, 15μs after impact (CBM Model).107
3.9 Damage and density contour of Sphere Indentation simulation showing radial cracking at 500 m/s impact velocity, 15μs after impact (TSDP Model). 107
3.10 Granular material percentage and amorphized material percentage for Sphere Indentation simulations with impact velocity, 15 μs after impact (CBM Model). 108
3.11 Maximum depth of penetration of the indenter for Sphere Indentation simulations with impact velocity (CBM Model). 109
3.12 Damage contour of Edge On Impact simulation at an impact velocity of 1010 m/s (CBM Model). 110
3.13 Comparison of damage pattern from [137] with Edge On Impact simulation (CBM Model) for 469 m/s impact velocity. (a) experimental damage pattern at 6.1 μs (b) numerical damage pattern at 6 μs (c) numerical density pattern at 6 μs (d) numerical out of plane strain pattern at 6 μs. 110
3.14 Comparison of damage pattern from [135] with Edge On Impact simulation (CBM Model) for 1010 m/s impact velocity. (a) experimental damage pattern at 6.1 μs (b) numerical damage pattern at 6 μs (c) numerical density pattern at 6 μs (d) numerical out of plane strain pattern at 6 μs. 111
3.15 Comparison of damage pattern from [135] (top row) with Edge On Impact simulation (bottom row) for 823 m/s impact velocity (CBM Model). The experimental damage front, numerical damage front and numerical granular front are highlighted in yellow (dashed), red (dotted) and blue (dashed-dotted) respectively. . . . 111
3.16 Variation of damage contour of Edge On Impact simulation (CBM Model), 4.5μs after impact at (a) Surface , (b) Section, (c) Mid-plate.113
3.17 Comparison of experimental damage front velocity with Edge On Impact simulation (CBM Model) damage and granular front velocity at different impact velocities. Inset image shows the granular and damage front from ABAQUS simulation for 469 m/s impact velocity, 6μs after impact. 114
3.18 Surface contour of Edge On Impact simulations (CBM Model) showing amorphized region with different impact velocities. . . . 114
3.19 Granular material percentage and amorphized material percentage for Edge On Impact simulation (CBM Model) with impact velocity, 7.5μs after impact. 115

3.20 Comparison of damage contour of Edge On Impact simulation for (a) CBM and (b) TSDP models at 742 m/s impact velocity, 7.5μs after impact. 117

4.1 Correlation plot with original parameters shown in Tab. 4.1. . . . 127
4.2 Correlation plot with derived parameters shown in Tab. 4.4. . . . 129
4.3 Histogram of granular material percentage at 15 μs after impact based on 500 samples in the input parameter space. 130
4.4 t-statistic plot (sensitivity analysis for GMP with original parameters). 133
4.5 t-statistic plot (sensitivity analysis for GMP with derived parameters). 135
4.6 Histogram of maximum depth of penetration (rebound case) based on 342 samples in the input parameter space. 136
4.7 t-statistic plot (sensitivity analysis for MDR with original parameters). 138
4.8 t-statistic plot (sensitivity analysis for MDR with derived parameters). 139

5.1 Illustration of flaw orientation, fully defined in three dimensions by angles α_{flaw} and θ_{flaw}. 153
5.2 Generation of 3D crack assembly: (a) Effective crack in chapter 2, (b) Defect with wing crack model. 154
5.3 Representative image showing different views of a crack (in red) with a coalescence zone (in cyan). 157
5.4 Fragment Statistics for $\eta_{flaw} = 22e12 cracks/m^3$, $s_{flaw} = 10\mu$ and $C = 0.2$: (a)Form Factor ($Form$); (b) Aspect Ratio (AR); (c) Roundedness Index (R_H); (d) True Sphericity Index (TSI). Red dotted lines represent the mean values of indices. 162
5.5 Representative image of voxellized fragments with extreme vertices indicated as red dots. 166
5.6 Representative image of the largest ellipsoid inscribed in the orthogonal bounding box containing the fragment aligned along the principal directions. 167
5.7 Resolution dependence of morphological indices: (a) $d_{sphere} = 2\nabla_{res}$, (b) $d_{sphere} = 4\nabla_{res}$, (c) $d_{sphere} = 10\nabla_{res}$. 170
5.8 Box plots showing the spread of morphological indices for a sphere with varying resolution: (a) $Form$, (b) I_r, (c) R_{EV}. 171
5.9 Average values of morphological indices and total number of fragments at a given d_{frag} for varying s_{flaw} and constant initial damage, $\Omega_i = 0.022$: (a) $Form$, (b) I_r, (c) R_{EV}, (c) N_{frag}. 176

5.10 Global average values of morphological indices and corresponding contribution to critical state friction angle for fragments larger than 6 times the resolution size: (a) $Form$, (b) I_r, (c) R_{EV}, (c) $\Delta\phi_{CS}$. 179

A.1 Damage and Porosity contours for ABAQUS simulations of unconfined Kolsky bar experiments at strain rate of 465 s^{-1}: (a) Damage contour for $\Omega_f = 0.125$, 20 μs after impact; (b) Porosity contour for $\Omega_f = 0.125$, 20 μs after impact; (c) Damage contour for $\Omega_f = 3.5$, 33.6 μs after impact; (b) Porosity contour for $\Omega_f = 3.5$, 33.6 μs after impact. 191
A.2 Stress time curve of ABAQUS simulation of unconfined dynamic Kolsky Bar experiment at strain rate of 465 s^{-1}. 192
A.3 Fragment Statistics obtained from ABAQUS simulations of unconfined Kolsky bar experiments at strain rate of 465 s^{-1} and $\Omega_f = 0.125$: (a) Roundedness Index (R_H); (b) True Sphericity Index (TSI). 193
A.4 Fragment statistics using fragmentation model (Chapter 5) for $trace(\Omega) = 2$ and resolution corrected statistics from ABAQUS simulations of unconfined Kolsky bar experiments at strain rate of 465 s^{-1} and $\Omega_f = 0.125$: (a) Roundedness Index (R_H); b) True Sphericity Index (TSI). 197

B.1 Representative image of weak zones in a cracked microstructure. (a) Crack wing crack assemblies, (b) Simplified cracks, (c) Cracked microstructure with weak zones represnted by buckled or failed columns, (d) Enlarged view of a buckled or failed micro-column. 200
B.2 Representative image of fragment sizes contained between weak zones. (a) Mean fragment size measure transverse to the direction of maximum principal compressive stress, (b) Mean fragment size measure along the direction of maximum principal compressive stress. 208
B.3 Evolution of ℓ_{R2} with time for PAD B4C at a strain rate of $360ms^{-1}$, calculated using TR code. (a) Comparison with Stress, (b) Comparison with FAF. 212
B.4 Comparison of average normalized structural fragment size ($\bar{\ell}$) computed using a microstructure fragmentation criterion and a FAF criterion with normalized strain rate ($\bar{\dot{\epsilon}}$) for structure driven fragmentation with the models of Grady, Glen & Chudnovsky, Zhou et al., Levy & Molinari, Modified Grady as well as the model developed in this work. 216

Chapter 1

Introduction

1.1 Ceramics as armor material

Ceramics are brittle or quasi-brittle materials used in a vast range of applications from body and vehicle armors, semi-conductors, scratch-resistant shields, kitchenware, and everyday appliances. While the properties of ceramics can be as varied as their chemical composition and structure, armor ceramics in particular are characterized by high energy absorption, high hardness, high compressive strength and preferably low density. All these properties make them suitable for impact and blast resistance during combat [1].

The earliest development of a ceramic armor consisted of an alumina front plate with a woven metallic back plate [2]. Pioneering studies [3–6] of ballistic performance of an alumina plate with an aluminium back face impacted by

steel projectile observed projectile erosion, ceramic cracking and conoid formation, and backplate yielding with ceramic rubble collection. Depending on the thickness of the ceramic plate and the impact velocity, projectile penetration through the plate or projectile dwell [7] with radial flow was observed. The latter further motivated research in advanced armor ceramics.

Rod-impact and particle impact experiments on ceramics by [8] provided a comprehensive picture of the failure patterns. Upon impact, shallow ring cracks form which extend as Hertzian cone cracks [9,10] below the surface, followed by radial cracking as the impactor further penetrates. This is followed by extensive comminution right under the indenter, lateral cracking, and flow of the comminuted material laterally and in the direction opposite to that of the impactor. The tendency of the comminuted material to dilate and flow is the consequence of a phenomenon often termed as 'granular flow', extensively studied in geomechanics [11–13], astrophysics [14,15], and manufacturing [16]. For low porosity advanced ceramics, the inability of the material to flow generates significant penetration resistance and often results in penetrator rebound. [8] hypothesized that the frictional resistance of the pulverized ceramic under the indenter could be the most significant property towards penetration resistance and this property could be dependent upon the fragment morphology, incipient pressure and strain rate.

Other researchers also made similar observations [17–20] about the ex-

istence and the importance of the behavior of the material in the comminuted zone under the impactor. Other mechanisms often at play in impact experiments on advanced ceramics are plasticity (dislocation slip [21, 22], twinning [21, 23]), amorphization [24], phase-transformation [25–27]. [28] studied the link between structure, material properties and penetration resistance of various armor ceramics, and suggested simplified relationships.

1.2 Boron Carbide - a model armor ceramic

Boron carbide, with its relatively low density, high Hugoniot Elastic Limit (HEL) and high hardness [29], is of special interest for research in the field of armor ceramics [30]. The primary mechanisms active in impact experiments of boron carbide have been identified as crack growth from defects in the material, amorphization, and granular flow after comminution. The following subsections will briefly describe these mechanisms and give a high-level overview of the modelling approaches.

1.2.1 Mechanisms & Modelling

1.2.1.1 Fracture

When a projectile impacts a ceramic, it generates an elastic wave that travels into the material as well as the projectile. The region in front of the projectile is in a state of uniaxial strain. When the impact velocity is substantial, it can lead to the formation of a shock front. As the wave travels through the material its spreads out until it reaches an interface and reflects back. This interface can be air or some other material, depending on the backing material. If the impedance of the ceramic is lower than that of the material at the interface, the reflected wave is compressive. If the impedance is higher than the material at the interface, then the reflected wave is tensile. Despite their high compressive strength, ceramics are weak in tension. This can lead to spall failure due to tensile stresses from the reflected wave. One way to avoid this is to have a sufficiently thick ceramic plate that distributes the stresses. As the elastic wave travels through the material it activates crack growth from pre-existing defects in the material. Microcracking in ceramics leads to elastic plastic transition above the Hugoniot elastic limit (HEL). The state of stress in the material varies from being compressive near the indenter to more complicated states further away, depending on wave interactions. For split-Hopkinson pressure bar (Kolsky bar) experiments, where the sample size is small, the re-

sulting equilibrated stress state is compressive after a steady state is reached. Hence, dynamic compression crack growth is of particular importance in ceramics, especially in the region under the penetrator. However, for certain specimen geometries and boundary conditions, tensile cracking can also lead to material failure in ceramics, such as spall failure.

The microstructure of ceramics is characterized by the grain size and defects or secondary phases in the material. These defects can either be grain boundary defects [31], pores or inclusions [32]. In general for brittle materials, under static unconfined compressive stresses, wing cracks emanate from the most favorably oriented defects leading to structural failure of the material via large axial splitting macrocracks [33]. As the level of confinement in the material increases, many cracks activate simultaneously and interact with one another leading to a more ductile behavior. Dynamic crack initiation and growth in ceramics, is however a more complicated phenomenon. Typically, high defect densities and high strain rate in ceramics lead to simultaneous growth and interaction of various crack populations. In the absence of substantial confinement, crack growth is still, however, dominated by wing crack mechanism.

Overall, the dynamic fracture and fragmentation of brittle materials is of interest in several disciplines: geomechanics, mining, astrophysics, armor systems. The process is incredibly complicated, dependent on the loading condi-

tions and the specific material of interest. A set of experimental studies by Ravi-Chandar & Knauss [34–37] investigated the quasi-brittle dynamic fracture process in thin sheets of Homalite-100 and found that the fracture process is governed by a complex interplay of microstructure dependent crack initiation, crack growth, crack arrest, crack branching, and crack tip wave interactions. In addition to this, dynamic crack coalescence [38, 39] and the post-fragmentation behaviour can also be of interest depending on the field and the application.

Crack growth in ceramics can occur between grains or through a grain. The resulting fracture surfaces are referred to as intergranular and transgranular respectively [40]. Depending on this nature of crack growth, fracture toughness values can vary significantly which affects the rate of crack growth. The kind of crack growth is often not only a function of the material, but also of the grain size and loading rate [41]. For dynamic fracture of Boron Carbide, the crack growth is predominantly transgranular [42].

Modelling dynamic crack growth either involves tracking the growth of discrete cracks through cohesive zone models [43], crack bands [44, 45], extended finite element method [46–49], discontinuous galerkin method [50], phase field models [51–54], or continuum damage models that track the growth of crack populations with homogenization schemes to account for the evolving damaged material properties [55, 56]. Phase field models can be used to accurately

predict the three dimensional micro-cracking patterns in quasi-static brittle failure [57] and can be extended to account for the various failure modes and mechanisms in dynamic brittle fragmentation.

1.2.1.2 Amorphization

The crystal structure of boron carbide is complicated, consisting of an icosahedron located in a rhombohedral lattice and connected by linear three atom bonds [58, 59]. Under high pressure and shear, loss of crystal structure leads to a significant loss of shear strength [60]. Several alternate viewpoints such as bending of the three atom chains [61], breaking of the icosahedra [62] and dislocation nucleation [63] have been suggested as reasons behind such lattice destabilization. Destabilization causes quasi-plastic sliding along narrow bands and is referred to as amorphization. Amorphization in boron carbide could also lead to crack nucleation, suggested by a substantial increase in the number of fine fragments beyond an impact velocity that corresponds to the onset of amorphization [24]. Amorphization mitigation in boron carbide is thus an active area of research [64–67].

Modelling efforts for amorphization include calibration of the JHB model [68] for Boron Carbide [69], anisotropic non-linear elastic continuum models [70–72], and micromechanical continuum models [73].

1.2.1.3 Granular Flow

Under high rate loading the region right under the indenter is extremely fragmented, and the level of fragmentation reduces further away from the indenter. The properties of this region heavily influence the impact performance of a ceramic. It should be noted that during impact, the granular material in this region is initially extremely compacted, before it starts bulking and exerting pressure on the surrounding material. As the indenter penetrates through the comminuted material, the fragments become mobile, grinding past themselves as well as the penetrator, and often eroding the latter in the process. The fragments rearrange themselves, close existing pores, and undergo further re-fragmentation. This entire process is incredibly complex and hard to simulate. Existing approaches of modelling granular flow in ceramics can be grouped as particle based and continuum models.

1. Particle based models: Particle based models, such as discrete element methods [74, 75] and material point method [76] model the basic interaction between individual particles. These particles can be as small as molecules or atoms, or as large as collection of molecules. The size of the particles and the number of particles chosen depend upon the scale of the system and the physics that one intends to model. For example, for granular flow problems in ceramics, if one intends to capture fragmentation during granular flow, the particles should be simulated at the scale of the

defects, such as microcracks in ceramics or the the grain size of the material. On the other hand if the focus is on accurately simulating abrasion or frictional behavior, one should model particles at the scale of the asperities on fragments. The scale of the system is either limited by the experimental dimensions one intend to simulate, or the number of particles one needs to obtain an statistically significant average global behavior. The models are able to simulate versatile deformation behavior, but are often computationally infeasible to model large systems accurately.

2. Continuum models: Unlike particle based models, continuum models are restricted by their mesh; their performance and accuracy is limited by the size of a discretized volume or an element. While system accuracy increases with refinement of element size, the element size in itself is limited by the size of a representative volume element (RVE) used to approximate mesoscale properties. Nevertheless, since these models assume homogenized properties at the mesoscale, they are generally more computationally efficient than particle based models and can be used to simulate larger systems. Continuum models of granular flow can be further grouped as classical plasticity models and micromechanics based models.

   Various classical plasticity yield criteria and flow rules have been used in the past to model the comminuted zone. The Johnson-Holmquist models (JH-I [77], JH-II [78],JHB [68]) use pressure-dependent Mises yield cri-

teria for the damaged material. [79] used a Mohr-Coulumb model with a density-dependent consolidation surface and non-associative flow rule. Granular flow in cavity expansion problems has been modelled using Mohr-Coulumb [80] and Tresca yield criterion [81]. Two surface viscoplastic granular flow models were developed and employed by [79, 82]. [82] used a pressure-dependent Drucker Prager model, a hydrostatic compression cap, and an associative flow rule to model granular plasticity. [83] used a non-associative viscoplastic Drucker-Prager model for the completely comminuted state. A teardrop shape has also been used to model the yield surface of granular materials [84].

Micromechanical models, albeit more complicated, are more physically representative of a system and are capable of reproducing complex deformation states while retaining the efficiency of continuum models. In armor ceramic literature, the most commonly used micromechanical models are the FRAGBED models [85–87] and the breakage mechanics models [88–90]. The former is a mesoscale analogue of dislocation mechanics; the latter is grounded on the breakage mechanics theory developed in [91–93] and models particle refragmentation, porosity evolution, particle rearrangement, and associated granular kinematics using internal state variables.

1.3 Gaps in modelling & outline of the thesis

Despite substantial progress over the last decades in deciphering the physics associated with the impact response of boron carbide and armor ceramics in general, there are still questions left to be examined. Some of these stem from a lack of physical understanding, others are drawbacks associated with modelling approaches. As an example, the physics of phase transition of boron carbide, melting of projectile, the evolution of Poisson's ratio with damage in the material, and crack nucleation due to amorphization is still not completely understood. On the other hand, models rooted in the assumption of a continuum are limited by their ability to handle states where the continuum assumption does not necessarily. Nevertheless, their ability to efficiently model large systems and predict overall material behavior with reliable accuracy has made these models vital tools in understanding the impact behavior of armor ceramics.

One such challenge with continuum modelling approaches is with simulating the competitive crack coalescence and inferring when granular physics is activated in a highly cracked system. One way to do so is by calibrating models against experiments. This, however, ignores the true microstructural dependence on such transition. Hence it is necessary to

have a general physically based granular transition criteria that can be implemented in ceramic codes.

The objective of the Materials in Extreme Dynamic Environments (MEDE) program at Johns Hopkins is to iteratively develop new and improved boron carbide via a materials-by-design loop approach. In this approach, each iteration of a material is circulated through a nexus of processing, experiments and modelling efforts. It is essential to understand the most significant material properties and their influence on material performance.

The microstructure of a material influences its impact performance through various associated mechanisms. Some of these connections are well explored, such as the link between defect populations and crack growth. But some connections are more indirect, albeit as important as the others. These include the dependence of initial material microstructure on granular flow.

This thesis attempts to bridge these gaps in modelling. Chapter 2 discusses the development of a new fragmentation model that addresses competitive crack coalescence and provides a tool which helps determine the onset of granular mechanics in a solid as well as helps calibrate the properties of the resulting granular media for different initial microstructures. Chapter 3 recalibrates an integrated ceramics model based on some

new experimental data and the granular transition criterion developed in Chapter 2. The recalibrated ceramics model is employed to simulate sphere indentation and edge on impact experiments of boron carbide for varying initial impact velocities. The results from these simulations are compared against existing experimental literature. Chapter 4 explores the sensitivities of sphere indentation model predictions on parameters of the integrated ceramics model. The results of the sensitivity study assists the materials-by-design approach in the MEDE program by providing valuable feedback towards material processing modifications as well as prioritizing calibration experiments. This is a collaborative effort with Dr. Anindya Bhaduri who performed the sensitivity study on ABAQUS simulations I performed. I analyzed Dr. Bhaduri's results, and explored connections with physical mechanisms and the corresponding implications on material design modifications. Chapter 5 of the thesis uses a modified version of the fragmentation model developed in chapter 2 to study the influence of the ceramic microstructure on initial fragment morphology, probe the implications on granular friction, and thereby the impact performance. Finally, chapter 6 summarizes the results and discusses new directions for previously unanswered questions. These include: experimental validation of the results from chapter 5; analysis of the difference between structural fragmentation and microstructure driven fragmenta-

tion and granular transition (discussed in chapter 2); identification of the strength implications of structural fragmentation on Kolsky bar experiments; and future directions for the development of a phenomenological structural fragmentation criterion.

Chapter 2

Fragmentation & granular transition

2.1 Introduction

Applicability of constitutive models of brittle materials depend upon the class of problems, the microstructure, the loading conditions and the state of the material. Depending upon the class of problems, certain physics which are more important than others can be prioritized. The kind of defects (e.g. pores, microcracks and inclusions) in the microstructure, their size and shape influence the growth of mesoscale cracks. The loading conditions affect the crack path and ultimately the failure pattern. The state of the material, e.g. solid or comminuted, signifies the applicability of certain idealizations. Often

the same constitutive model cannot be used to represent the behaviour of the same material in different states. This requires different approaches of modelling such states along with inexpensive methods of handling the transition between those states.

For uncomminuted brittle materials, mesocale crack growth from microstructural defects is dominated by the loading conditions. While mode I crack growth from the largest and most favourably oriented microcracks dominate the fracture process in tension, compression crack loading leads to different modes of crack growth depending on the degree of confinement. Under moderate to low confinement, wing crack growth from microcracks is recorded in the literature [33, 94, 95].

In ceramic armour systems subjected to penetration, rock blasting or asteroid impacts, typical strain rates are much higher than in classical static wing crack growth models [33]. In such applications, inertial effects dominate the crack growth, and the dynamic stress intensity factor [96] is used as a measure to determine the rate of crack growth. While for static cases in uniaxial compression, only the most favourable cracks grow into macro-cracks and cause failure [33], dynamic crack growth causes simultaneous growth of a population of cracks. This renders weakest link failure models [97] based on macro-crack initiation unsuitable for dynamic compressive loading.

Armor ceramics have very high initial defect densities, in the form of pores

and inclusions, which serve as initiation sites for cracks. At low rates cracks tend to initiate only from the largest pores and inclusions, but at high rates, even the very small defects present in the material lead to cracks. In other words millions of cracks initiate and propagate simultaneously. Model representations that explicitly account for every crack are therefore infeasible. This is when continuum damage models [55, 56] are particularly useful over discrete modeling of cracks [43], crack bands [44,45] or phase field models [51–54]. However, the applicability of such continuum-based models before the onset of comminution, in which the cracks approach the element size, is questionable.

This state of the material when the cracks start connecting to eventually form an initial fragmented media is referred to as the granular transition regime. After such transition, granular physics dominates the material behavior. This is often the case in the Mescall zone in impact experiments [17, 86]. Continuum modelling of such behavior is accomplished through plasticity based models [82] or breakage mechanics models [89]. Handling the granular transition is an area of active research.

One viewpoint on the growth of cracks in the granular transition regime assumes that, as these cracks grow, they interact with one another, influencing their growth, which manifests not only through changes in effective properties of the surrounding matrix [96, 98] but also in changes to the local stress field and the direction of crack growth. When such changes occur, one is deal-

ing with simultaneous growth and coalescence of multiple cracks. These coalesced cracks now behave as larger individual cracks. Eventually many of these cracks connect with one another to form a network of connected cracks that fragment the domain into smaller particles. This process involves a competition not only between isolated wing crack growth and crack coalescence but also between the different modes of crack coalescence [99, 100] and the growth of secondary cracks [101].

An alternate viewpoint of crack growth in the granular transition regime is that fragmentation is driven by crack branching [102, 103]. Crack branching requires higher crack velocities ($0.43 - 0.46C_R$ [104]). For high crack densities, crack coalescence might occur before such crack velocity is reached and any significant crack branching might have occurred. Under such situations, crack branching alone might not influence the fragmentation process. Right before the onset of fragmentation, the length scale of cracks can be expected to be comparable to the spacing, making homogenization of damaged matrix properties based on dilute approximation questionable.

The fragment size distribution resulting from the fragmentation process has been observed over two different length scales [105, 106]: a) the length scale of the defects (Regime I), b) the macroscopic scale (Regime II). Scanning electron microscope images of the fracture surface, for Regime I fragments, showed defects located on the fracture surface and not inside the material.

This suggests transgranular fracture with the microstructural defects serving as crack initiation sites. On the contrary, Regime II fragments are a consequence of transverse and axial splitting macro-cracks, which are influenced by the specimen geometry, boundary conditions and the loading rate. For a projectile impacting a ceramic plate, the Mescall zone at the tip of the penetrator [17] or the slip zone in earthquake faults [107] is composed of heavily comminuted material that undergoes granular flow. This is analogous to the Regime I fragmentation observed in [105, 106].

[108, 109] show that the strength as well as the failure mechanism of thermally shocked boron carbide with more initial defects is different from that of the pristine material. This hints towards an obvious dependence of the failure criterion with microstructural defects. This might also mean that calibration of initial conditions for granular flow in the comminuted zone, from initial fragment statistics obtained from thermally shocked samples might not be accurate.

Understanding fracture and fragmentation in the post peak strength region of ceramics as they transition on the granular mechanics yield surface from a high strength to low strength regime is a non-trivial task. The instabilities associated with crack growth in a competitive environment and the multiple possible modes of crack coalescence are not well understood and are difficult to address. In most cases, the transition to granular phase has been mod-

elled either through metrics specific to a model or non-physical threshold of physical quantities [82, 83]. In [83], the transition from lattice plasticity to granular physics is modelled as a gradual transition described by a damage parameter. When this parameter reaches unity, the material is fully granular. Typical transitional damage values in models, estimated from crack statistics, might be set at a lower value than what might actually lead to failure or granular transition. Often these are based on calibration experiments and/or signify the limit of applicability of continuum assumption [82]. Quantifying crack lengths for a network of intersecting cracks is often impossible, and a more accurate damage quantification might be in terms cracked surface area per unit volume [109]. [110, 111] has tried to model the granular phase transition using a Continuum Damage Breakage Mechanics (CDBM) model using a critical damage threshold (α) expressed as function of the strain invariant ratio ($\xi = I_1/\sqrt{I_2}$). The study concludes that depending on the loading conditions, a damaged solid can transition to a pseudo-liquid granular flow phase or a pseudo-gas fragmentation phase. The damage threshold (α) in the model is a parameter that represents the state of the material. It varies between $\alpha = 0$ for a material without any damage to $\alpha = 1$ for a fully damaged material and affects the elastic constants in the model. The model predicts a rapid transition from a fragmented stage to granular flow. [112] predicts a sharp transition of colliding solids to fragmentation based on the critical threshold of the impact

energy to “binding energy” ratio for colliding solids.

It should be noted, however, that fragmentation can occur well before granular transition, and may be influenced by the specimen geometry. In such cases the peak strength is limited by fragmentation and not due to the competition between softening of the modulus and increase in stress due to increase in strain. This can be expected in unconfined Kolsky bar experiments, where structural fragmentation (Regime II) can limit stress buildup. This kind of fragmentation has not been studied in this work.

An in-depth understanding of the fragmentation process and the resulting initial fragment statistics is necessary. This information can be used to adequately calibrate granular flow models after comminution. While there is an abundance of literature on fragmentation modelling of brittle materials in tension [113–117], the understanding of fragmentation in compression is limited. Most of the work is focused on characterizing macro-scale structural fragments [105], which possibly do not play a role in the granular physics. [75] developed particle based discrete model brittle fragmentation and studied the evolution of fragment statistics. While such models provide a sophisticated treatment of crack growth, coalescence and granular flow, they are expensive with a number of tunable parameters. The objective of the current work is to provide a physics based granular transition criterion, that can be easily implemented in continuum damage based model codes as well as provide an

understanding of initial conditions of post fragmentation granular flow.

In this work, the transition to granular mechanics for ceramics under high rate loading conditions has been addressed. Crack distributions are first obtained from a wing crack growth-based continuum model for uniaxial loading conditions. Two different algorithms for three dimensional crack coalescence are then used. The outputs of the algorithms have been used to predict the transition to granular phase as well as the resulting fragment size distribution at the onset of granular flow. The transition criterion has been expressed in terms of an equivalent crack length or a damage-stress combination. A phenomenological transition model has also been proposed, which suggests a similar form for the granular phase transition criterion, and can be used in continuum brittle fragmentation codes, to capture the change from comminuted ceramic to a granular medium, and provide input parameters for subsequent granular flow. Although the algorithms and transition model rely on uniaxial loading conditions, with a proper crack growth criterion and 3D-anisotropic damage model [118, 119], they can be extended to multi-axial loading.

2.2 Methodology

This section details the various steps involved in the fragmentation model, summarized in Fig. 2.1. The model involves the simulation of the cracked mi-

Table 2.1. Default material and model parameters (Defect density values correspond to random orientation of cracks).

Parameter	**Variable**	**Units**	**Value**
Defect Density (random orientation)	η	m^{-3}	$22\text{x}10^{12}$
Defect size	l_i	μ	10
Fracture Toughness	K_{IC}	$MPa\sqrt{m}$	2.5
Strain Rate	$\dot{\epsilon}$	s^{-1}	10^6
Elastic Modulus	E	GPa	461
Density	ρ	kg/m^3	2520
Poisson's Ratio	ν		0.177
Coefficient of friction	μ_{flaw}		0.8

crostructure at a given instant using a three dimensional voxelized space called the simulation box. Each crack is represented by a collection of connected voxels. The simulation box contains many such cracks. As the microstructure becomes progressively more cracked, neighboring cracks start coalescing with one another. Gradually the microstructure is transformed into a network of three dimensional connected voxels representing cracked material. A connected region of voxels representing uncracked material, completely enclosed by voxels representing cracked material is a fragment. Section 2.2.1 discusses evaluating the initial instantaneous statistics of crack populations from initial defects using a wing crack growth based damage model. Three dimensional cracks are then simulated from these crack statistics as explained in Sec. 2.2.2. Section 2.2.3.1 discusses a 2D crack coalescence problem using stress intensity factor based calculations. Section 2.2.3 attempts to model crack coalescence due to

further crack growth using two different approaches: (a) Coalescence surface approach (Sec. 2.2.3.2), (b) Coalescence zone approach (Sec. 2.2.3.3). Section 2.2.3.4 explains the choice of a threshold distance for crack coalescence. The two approaches have been compared in Sec. 2.2.3.5. Finally, Sec. 2.2.4 discusses a connected region algorithm to extract fragments followed by a dilation procedure on the connected regions to compensate for any loss of material mass due to resolution size.

2.2.1 Initial defects and the crack growth model

The analysis begins with randomly spaced initial defects, with a given size and orientation distribution. Two different defect size distributions are considered: (a) a delta distribution (i.e. a single fixed defect size) and (b) a lognormal distribution. The initial orientation distribution is taken to be a uniform distribution in the range $[0, 2\pi]$ radians. Crack growth is modelled by a modified version of the [55] model that accounts for orientation distribution of defects. The initial defect population is binned into a set of representative defect sizes and defect orientations. [55] calculate the growth of wing cracks associated with each crack population bin at a particular time instant (Fig. 2.2). This model uses a discretized measure of a 2-dimensional scalar damage value, Ω, to estimate the degradation of elastic properties and the resulting stress state

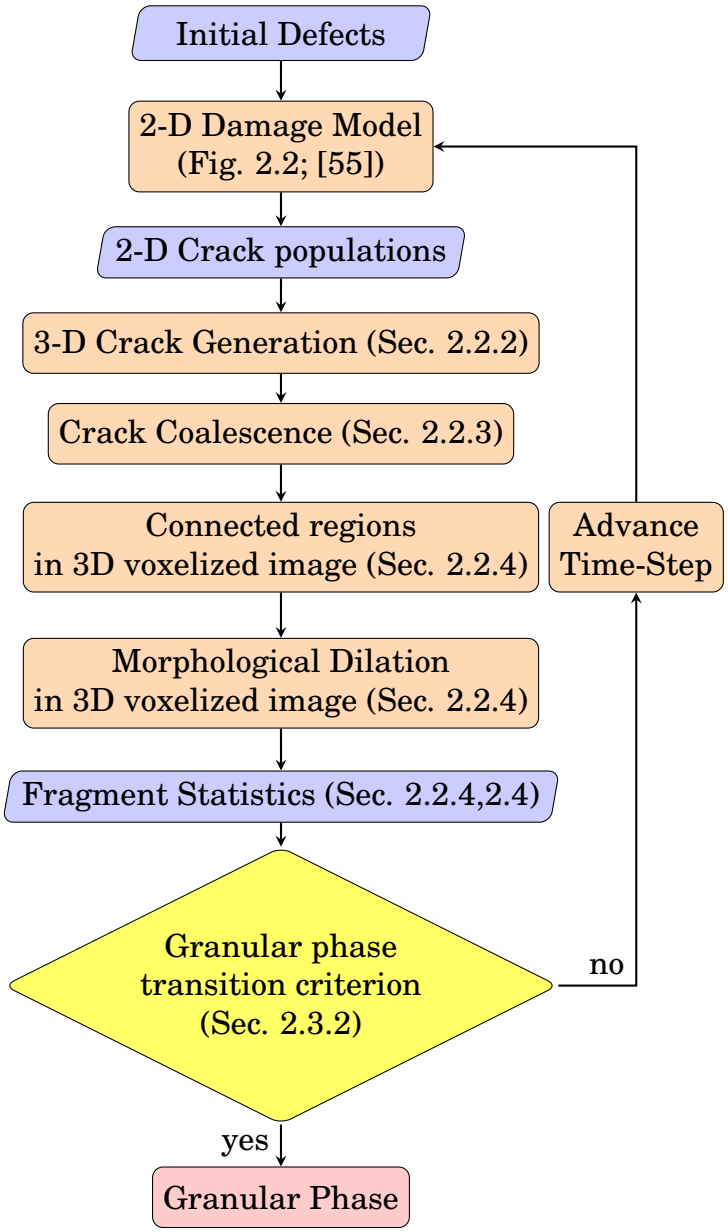

Fig. 2.1. Outline of steps Involved in the fragmentation model.

using an effective medium approach. The scalar damage is defined as:

$$\Omega = \int_0^{L_w} \eta_{2D}(l_w) l_w^2 f_{l_w}(l_w) dl_w, \tag{2.1}$$

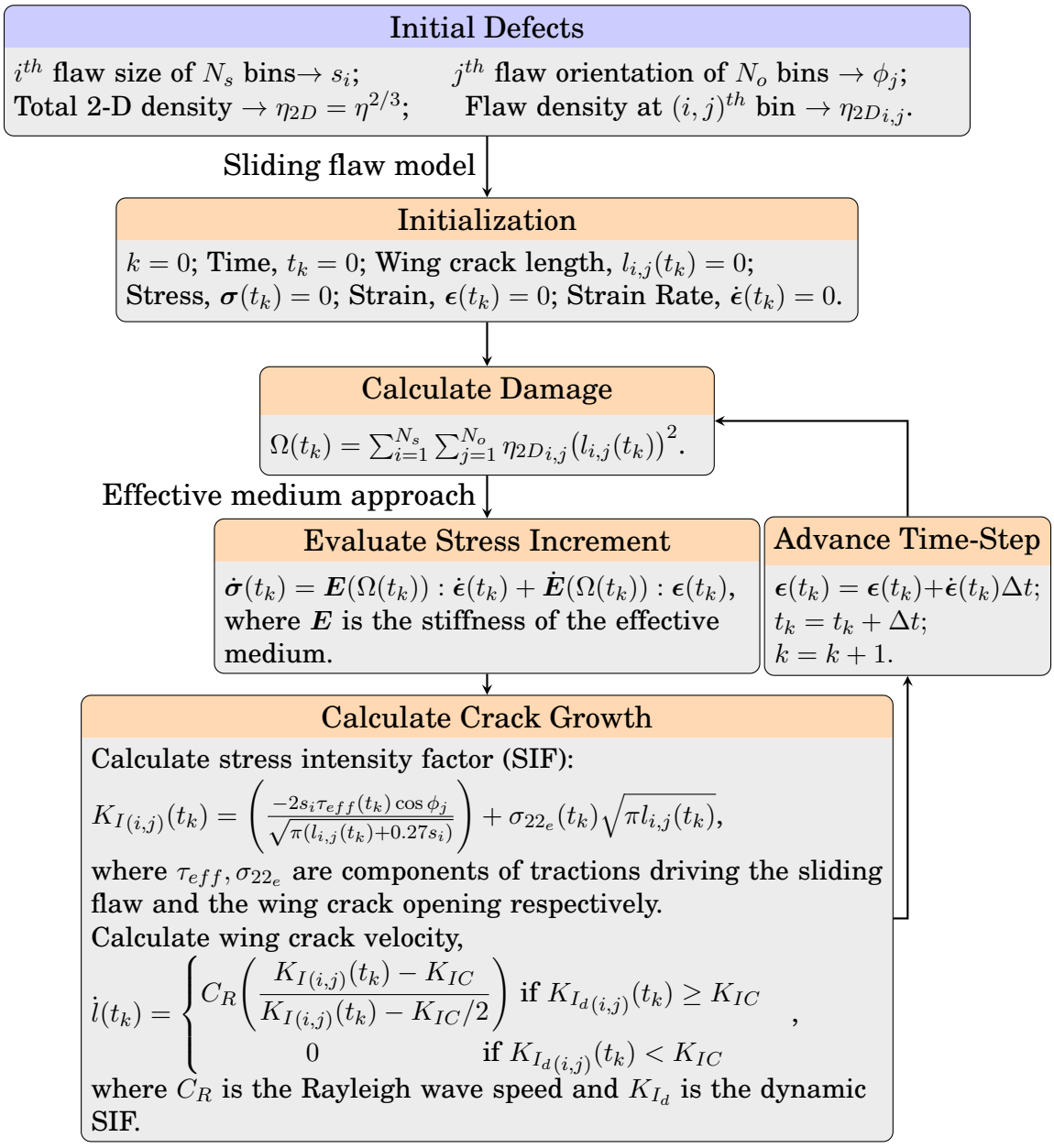

Fig. 2.2. Outline of wing crack growth based damage model [55].

where l_w is the half wing-crack length, $\eta_{2D}(l_w)$ is the 2D crack density (number of cracks per unit area) at a given l_w, f_{l_w} is the probability density function of the wing crack length distribution, L_w is the length of the largest wing crack.

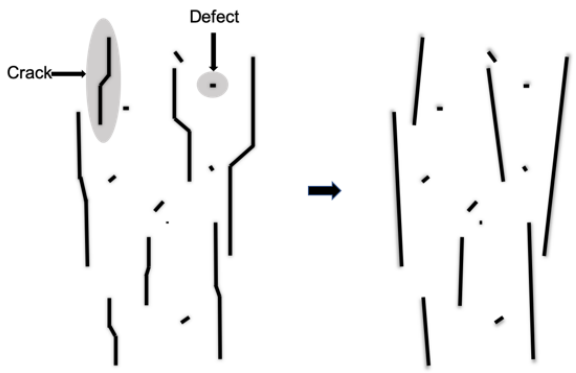

Fig. 2.3. Simplification of defect wing crack assemblies to slanted cracks.

Incremental crack growth is estimated from a dynamic crack growth criterion. Crack growth occurs when the dynamic stress intensity factor equates or exceeds the fracture toughness. In the fragmentation model, the crack lengths and orientations at a given stage are estimated from the wing crack lengths obtained using the [55] model, by joining the tips of the wing cracks (Fig. 2.3). It should be noted that this simplification is only used for the crack coalescence calculation in the fragmentation model, and not for estimating incremental crack growth between successive time steps. Unless otherwise specified, the material properties and model parameters in Tab. 2.1 have been used.

2.2.2 Simulation of three-dimensional cracks

Because the [55] model is framed in two dimensions, the line cracks predicted by the model are translated to elliptical cracks in the three dimensional fragmentation model. The cracks are simulated in a three dimensional box

with periodic geometry. This simulation box is a collection of cuboid voxels, and the size of each voxel is referred to as the resolution size. A voxel either belongs to a crack, or it is part of the intact material. The major axis of an elliptical crack is the crack length and its inclination with respect to the y-axis is the effective crack orientation from the [55] model. The ratio of the lengths of the major and minor axes of the ellipse has been chosen to be 1:1, but it can be set to any value. The size of the simulated sample should be large enough to accurately capture a representative range of crack sizes, including the largest cracks. The resolution size should be small enough to capture the smallest crack sizes and the corresponding small fragments. Of course, larger simulation boxes and finer resolution lead to increased computational effort.

For the 3D problem, let the y-axis refer to the direction of maximum principal compression. The angle of inclination of the major axis of an ellipse with the y-axis is the same as the complement of the corresponding 2D crack orientation (θ_{2D}). In addition, the projection of the major axis on the plane perpendicular to direction of maximum principal compression (or the xz plane) is random. Now given a certain fixed major axis orientation, the minor axis can lie on any plane containing the major axis. This ensures that the only constraint we apply on the ellipses is the inclination of its major axis with respect to the direction of maximum principal compression (y-axis). This has been accomplished by generating an ellipse in the xy plane with its major axis aligned along the x-axis,

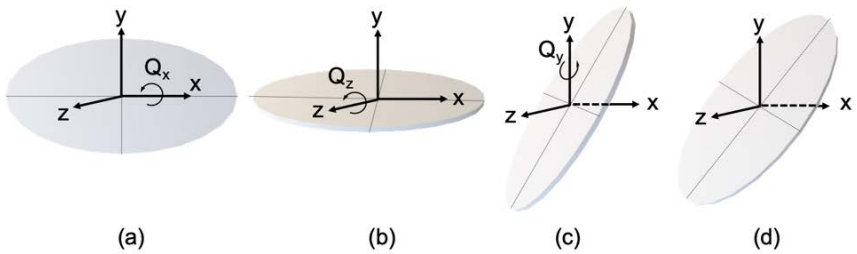

Fig. 2.4. 3-D elliptical crack generation.

and then rotating it first by a random angle about the x-axis (θ_x), followed by the corresponding 2D crack orientation angle about the z-axis ($\theta_z = \theta_{2D}$), and then a random angle about the y-axis (θ_y). The steps have been shown in Fig. 2.4. The corresponding rotation matrices are Q_x, Q_z, Q_y in the order of rotation. It can be shown that these set of rotations are equivalent to generating an ellipse with a major axis inclined at $\pi/2 - \theta_{2D}$ with the y-axis and its projection having a random angle in the xz plane, followed by rotating that ellipse about its major axis by a random angle.

2.2.3 Crack coalescence due to crack growth

As cracks grow under increased loading, they are more likely to coalesce with neighboring cracks. [120] has developed a probabilistic two dimensional crack coalescence model for fixed flaw orientation. Coalescence of three-dimensional cracks, however, is a complicated phenomenon. Different modes of coalescence have been recorded in the literature [99], and the competition between cracks growing in a competitive environment means that they would prefer one crack

over the other to coalesce with [121]. Multiple factors like the length and orientation of individual cracks and the crack bridges affect the order and mode of crack coalescence. The [55] model calculates the instantaneous growth of individual crack populations growing in isolation in an effective matrix, but it does not address coalescence. Instead, this coalescence is addressed in the 3D fragmentation model presented here, which considers size, proximity and orientation of cracks to determine if coalescence occurs. While there is some crack coalescence that occurs throughout loading, crack coalescence accelerates dramatically when the cracks are significantly large and comminution is about to begin. Since the objective of this work is focused on the onset of comminution, when rapid coalescence leads to fragmentation, crack coalescence is assumed to be instantaneous and the number density of individual crack populations due to coalescence is assumed to remain constant. A uniform global stress and strain state is assumed throughout the simulation box. This is the instantaneous state calculated using the effective properties of the matrix via the self-consistent model. The global stresses, in addition to the local influence from nearby cracks, drive crack coalescence. The following section describes an analytical model for 2-D crack coalescence followed by two numerical approaches of implementing it in three dimensions and identifying the onset of fragmentation.

2.2.3.1 Calculation of stress intensity factor for crack coalescence

Calculating the stress intensity factor for crack growth in a three- dimensional problem involves a complete 3D stress analysis [122–124]. Given the multiple possible elliptical crack orientations in the current problem, this might be quite challenging as well as expensive. For simplification, the problem is approached by a two dimensional model (Fig. 2.5). Even in this simplified representation, there are two cracks which are associated with orientation and length. The crack bridge that joins the two cracks also has an orientation and length. This six-parameter problem has to be solved numerically for all possible position and orientation scenarios, which is still largely infeasible. In order to avoid such expensive numerical calculations, the problem is simplified by assuming that the stress field acting on a crack is a combination of the global stresses that act on the crack face as well as the stresses acting on it due to the stress field of the nearby crack. The model adopts something similar to the mean-field approach typically adopted in homogenization theory. [125] adopted the mean-field approach for crack problems and found good agreement with results for homogenized properties of cracked solids. This agreement, and general agreement of mean-field homogenization [126], despite the possibility of some inclusions or cracks interacting significantly, is typically argued to occur because of the cancellation of shielding and amplifying interactions. A similar

argument can be made here. Exact modelling of the local stresses, given the parameter space and the sheer number of cracks, is not feasible. The current approach provides an approximation of the interaction of nearby cracks.

It is worth mentioning that compressive stresses acting on the crack face do not contribute significantly to crack growth and/or coalescence, so this analysis focuses on shear stresses. Therefore, the stresses acting on a crack are as follows:

1. Shear stresses acting along crack 1:

   (a) Global stresses,

   $$\tau_{crack1}^{global} = \frac{\sigma_1}{2}(1-\alpha)\sin(2\theta_1); \tag{2.2}$$

   (b) Stresses from crack 2, τ_{crack1}^{c2}.

2. Shear stresses acting along crack 2:

   (a) Global stresses,

   $$\tau_{crack2}^{global} = \frac{\sigma_1}{2}(1-\alpha)\sin(2\theta_2); \tag{2.3}$$

   (b) Stresses from crack 1, τ_{crack2}^{c1} .

The stress on crack 1 is related to the stresses on crack 2, which in turn relates to the stresses on crack 1 (from 2(b) above), creating a feedback loop in the analysis. Assuming that the stresses on crack 2 due to crack 1 (2(b) above) are smaller than those due to the global stress (2(a) above), we can ignore the

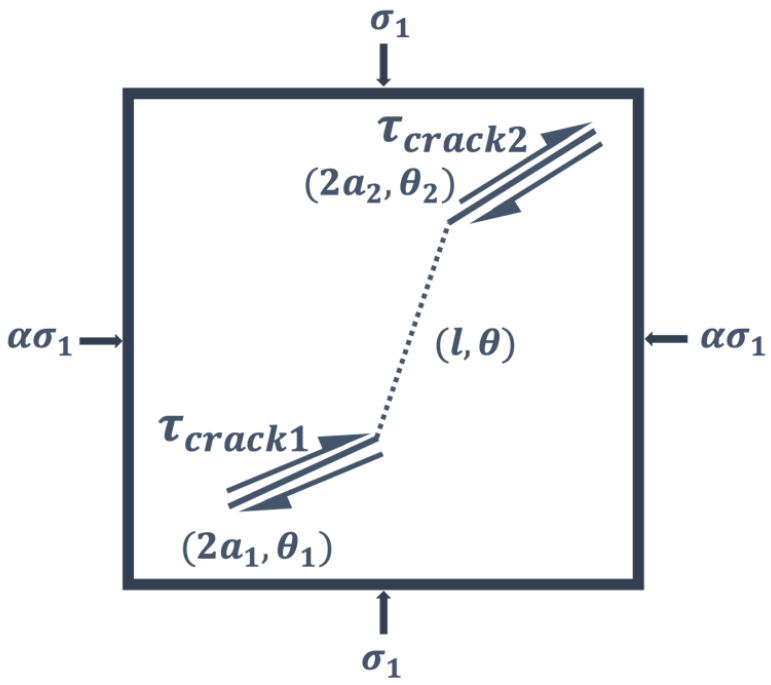

Fig. 2.5. 2-D crack problem geometry.

effects of crack 1 on crack 2, when calculating the effects of crack 2 on crack 1 (1(b) above). From [127], for a pure mode II isolated crack of length $2a$ with an infinite boundary defined in a complex plane with the origin at the crack center by complex number z and polar coordinates at the crack tip (r, θ),

$$\sigma_{ij}^2(r,\theta) = \begin{cases} \sigma_{12}^{\infty} \sum_{n=0}^{\infty} \left[\psi_n^{'}(a) g_n^{2,ij}(\theta) r^{n-1/2} \right] \quad for \ \ |z-a| < 2a \\ \sigma_{12}^{\infty} \sum_{n=0}^{\infty} \left[\tilde{\psi}_n^{'}(a) \tilde{g}_n^{2,ij}(\theta) r^{-n} \right] \quad for \ \ |z-a| > 2a \end{cases}, \tag{2.4}$$

where,

$$\psi_n^{'}(a) = \frac{(-1)^{n+1}(2n+1)!}{2^{3n+1/2}(2n-1)(n!)^2 a^{n-1/2}}, \tag{2.5a}$$

$$g_n^{2,11}(\theta) = 1/2\Big[(n+7/2)\sin\left((n-1/2)\theta\right) - (n-1/2)\sin\left((n-5/2)\theta\right)\Big], \tag{2.5b}$$

$$g_n^{2,22}(\theta) = 1/2\Big[(-n+1/2)\sin\left((n-1/2)\theta\right) + (n-1/2)\sin\left((n-5/2)\theta\right)\Big], \tag{2.5c}$$

$$g_n^{2,12}(\theta) = 1/2\Big[(n+3/2)\cos\left((n-1/2)\theta\right) - (n-1/2)\cos\left((n-5/2)\theta\right)\Big], \tag{2.5d}$$

$$\tilde{\psi}_n^{'}(a) = \frac{(-1)^n(n-1)(2n)!a^n}{2^n(2n-1)(n!)^2}, \tag{2.5e}$$

$$\tilde{g}_n^{2,11}(\theta) = \Big[(n/2-2)\sin\left(n\theta\right) + (-n/2)\sin\left((n+2)\theta\right)\Big], \tag{2.5f}$$

$$\tilde{g}_n^{2,22}(\theta) = \Big[(-n/2)\sin\left(n\theta\right) + (n/2)\sin\left((n+2)\theta\right)\Big], \tag{2.5g}$$

$$\tilde{g}_n^{2,12}(\theta) = \Big[(-n/2+1)\cos\left(n\theta\right) + (n/2)\cos\left((n+2)\theta\right)\Big]. \tag{2.5h}$$

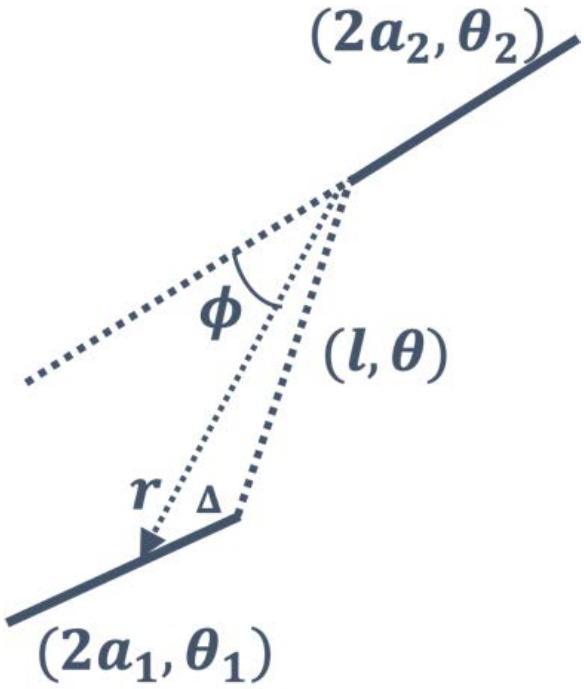

Fig. 2.6. 2-D crack problem geometry.

The complete asymptotic stress field from [127] has been used to determine the shear stress contribution from crack 2 on crack 1.

From the geometry of the problem (Fig. 2.6),

$$\phi = \arctan\left[\frac{l\sin(\theta-\theta_2) - \Delta\sin(\theta_2-\theta_1)}{l\cos(\theta-\theta_2) + \Delta\cos(\theta_2-\theta_1)}\right], \tag{2.6a}$$

$$r = \Delta\cos(\theta_2-\theta_1+\phi) + l\cos(\theta-\theta_2-\phi). \tag{2.6b}$$

Using Eqn. 2.4 and transforming the stresses to obtain the shear stresses along crack 1 orientation, the shear component along crack 1 due to crack 2

stresses is given as:

$$\tau^{c2}_{crack1} = \frac{\tau^{global}_{crack2}}{2a_1}\int_0^{2a_1} \kappa(a_2, r, \phi, \zeta) d\Delta, \tag{2.7}$$

where,

$$\kappa(a_2, r, \phi, \zeta) = \begin{cases} \sum_{n=0}^{\infty} \psi_n^{'}(a_2) r^{n-1/2}\Big[(n+3/2)\cos\left((n-1/2)\phi + 2\zeta\right) \\ -(n-1/2)\cos\left((n-5/2)\phi + 2\zeta\right)\Big] & \text{when } r \leq 2a_2 \\ \sum_{n=0}^{\infty} \tilde{\psi}_n^{'}(a_2) r^{-n}\Big[(1-n/2)\cos\left(n\phi - 2\zeta\right) \\ +\, n/2\cos\left((n+2)\phi - 2\zeta\right)\Big] & \text{when } r > 2a_2 \end{cases}, \tag{2.8}$$

and, $\zeta = -(\theta_2 - \theta_1 + \phi)$.

The total shear stress acting on crack 1 is $\tau_{crack1} = \tau^{global}_{crack1} + \tau^{c2}_{crack1}$.

Therefore,

$$\tau_{crack1} = \frac{\sigma_1}{2}(1-\alpha)\Big[\sin(2\theta_1) + \sin(2\theta_2)\frac{1}{2a_1}\int_0^{2a_1} \kappa(a_2, r, \phi, \zeta) d\Delta\Big]. \tag{2.9}$$

Crack growth will occur when the mode I stress intensity factor (SIF), K_I along the crack bridge exceeds the critical stress intensity factor (K_{IC}) for the material.

$$K_I \geq K_{IC} \implies \tau_{crack1}\sqrt{\pi a_1} f_I(\theta - \theta_1) \geq K_{IC}, \tag{2.10}$$

where, $f_I(\lambda) = -\frac{3}{4}\sin\left(\frac{3\lambda}{2}\right) - \frac{3}{4}\sin\left(\frac{\lambda}{2}\right)$.

In this work the series was truncated after 10 terms. This leads to a small relative error, as shown in [127]. In almost all cases the practical values of r were well below the crack size. It should be noted that the series expansion does not include explicit representation of friction at the crack surfaces.

We can also similarly use a mixed mode crack growth criterion based on energy release rate. For the current work however, Eqn. 2.10 has been used for crack coalescence.

Extending the crack coalescence approach to three dimensions involves dealing with complicated geometries and locations of multiple elliptical cracks as well as accounting for three dimensional stresses. There are no known analytical solutions for such problems. In this paper two approaches to tackle three dimensional crack coalescence are highlighted. In one of the approaches, pairs of individual cracks are connected by coalescence surfaces running along the crack edges (Sec. 2.2.3.2), while in the other approach each crack edge is surrounded by a probable zone along which coalescence is likely to occur (Sec. 2.2.3.3). In either case, the three dimensional problem has been simplified to a two dimensional problem similar to the one discussed above, where the 2-D orientation of cracks and crack bridge are equal to the inclination of the corresponding 3-D feature with the y-axis (direction of maximum principal compression). The lengths in the 2-D problem are simply the lengths of the corresponding features in the 3-D problem. All simulations in the paper represent

dynamic unconfined uniaxial loading scenarios, and the value of α is therefore set to zero.

2.2.3.2 Coalescence surface approach

Figure 2.7 illustrates the first approach for 3D crack coalescence. Consider a crack (C_1) and one of the voxels (P_1) along the edge of that particular crack, as well as the nearest voxel (P_2) lying along the edge of another crack (C_2). The approach in Sec. 2.2.3.1 is used to determine whether crack growth is feasible along the direction P_1P_2 that does not exceed a threshold distance. If crack growth is not feasible, then the nearest voxel on another crack within the region is assessed. The feasibility of crack growth is again determined by using the 2-dimensional crack coalescence model in Sec. 2.2.3.1. The length and the complement of the inclination, relative to the direction of maximum principal compression (y-axis), of the line joining the center of the crack, C_1, and the crack edge point, P_1, are calculated as a_1 and θ_1 respectively. Similarly, the corresponding values for the line joining the center of C_2 and P_2 are calculated as a_2 and θ_2. The length and complement of the inclination, relative to the y-axis, of the crack bridge joining the points P_1 and P_2 are calculated as l and θ (See Fig. 2.7). If the mode I stress intensity factor (K_I) for the growth of crack C_1 along the bridge direction P_1P_2, exceeds the critical stress intensity factor (Eqn. 2.10), then the crack will grow in that direction and coalescence would

occur.

After K_I is assessed for P_1P_2, the next step is to move to an adjacent voxel on the edge of crack C_1 and then identify the closest point along the edge of crack C_2, and repeat the analysis to determine if there is crack bridging. The direction on C_2 along which the distance to the adjoining point, P_3, on crack C_1 reduces is chosen. All voxels along the triangle $P_1P_2P_3$ are assigned to be cracked. After fixing the direction, we keep pairing points along C_2 with P_1 and assigning voxels containing incremental triangles to cracked regions, till we reach a point P_4 beyond which all points exceed a certain threshold distance. This threshold distance explained in Sec. 2.2.3.4 is the measure of potential crack growth over a given future time period. Now from P_3 again a similar search is done for points to pair on C_2 which are less than the threshold distance, along the aforementioned direction. This process of mapping points has been illustrated in Fig. 2.8a. This process is repeated until we reach a point P_m on C_1 and P_n on C_2 beyond which no points can be found on C_2 that are less than the threshold distance. This is when we search for other cracks to pair with and repeat the same procedure with crack C_3 starting with P_o the point closest to P_m on C_3. After pairing these points, additional coalescence surfaces are created as shown on Fig. 2.8b using the approach of incremental triangles. We also check whether the P_o and P_n are less than the threshold distance. If so, we end up creating a new surface enclosed in the triangle $P_mP_nP_o$ by assigning

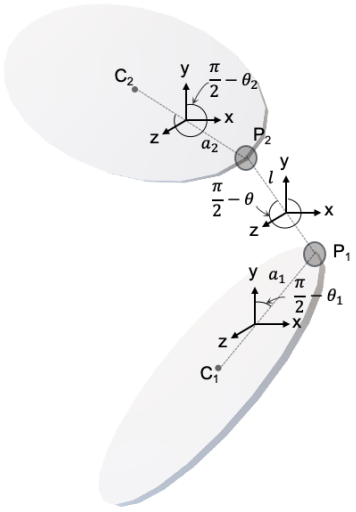

Fig. 2.7. Estimating 2-D geometry from 3-D problem.

all voxels along the surface to cracked regions.

2.2.3.3 Coalescence zone approach

A more efficient approach is to specify a coalescence zone surrounding the edge of a crack, across which coalescence can take place. The coalescence zone is a volume measure as opposed to a coalescence surface. In this case, for each crack edge point the average bridge length in a particular direction, for which crack coalescence is feasible, is determined by solving a 2-D crack coalescence problem similar to Sec. 2.2.3.1. For the 2-D problem in Fig. 2.5, the bridge length, l, is determined for a given value of θ_1, $2a_1$, θ for all possible combinations of θ_2 and $2a_2$. $2a_1$ is the major axis length of the crack C_1 and θ_1 is the

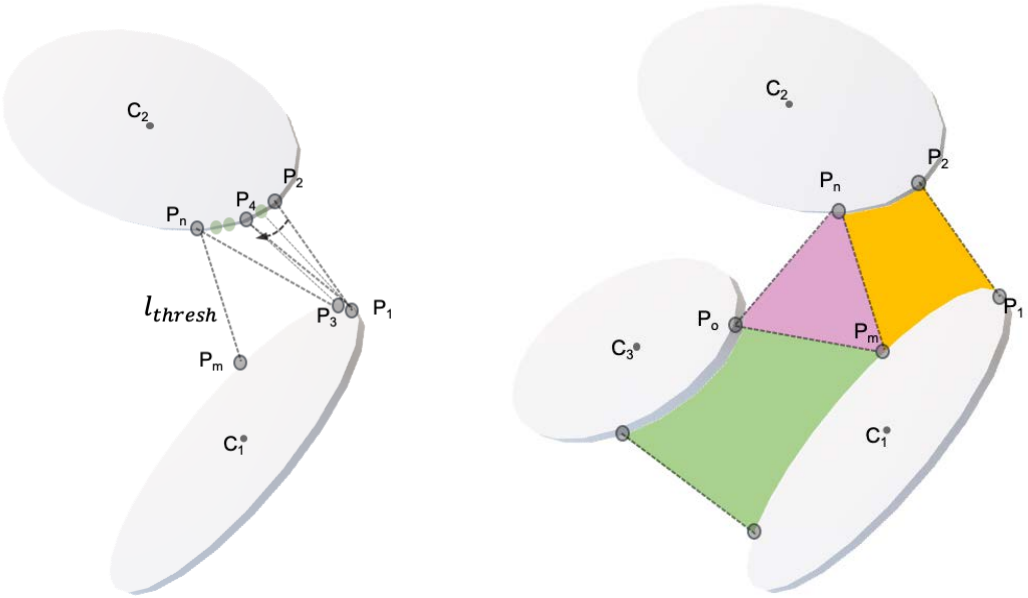

(a) **(b)**

Fig. 2.8. Steps involved in coalescence surface approach (l_{thresh} denotes the threshold distance).

complement of the angle this segment makes with respect to the y-axis (Fig. 2.7). Similarly the values for $2a_2$, θ_2, l and θ are found. In the end, for each crack edge point we have a set of l values corresponding to different θ values for multiple combinations of θ_2 and $2a_2$. After repeating the process for all points along the edge of a crack, we can specify a domain around the entire crack edge, where coalescence is feasible. The maximum length of crack coalescence is set as the threshold distance mentioned in Sec. 2.2.3.4. Figure 2.9 shows three different scenarios of crack coalescence. The left column shows the representative image of two parallel elliptical cracks staggered in different ways. The middle column shows the coalescence zone around the cracks and the right column shows the 2D coalescence pattern represented. The thick and dotted lines correspond to crack assemblies and coalescence cracks respectively. These patterns only show a few possible coalescence modes. In reality the simulated cracks are not necessarily parallel to each other.

2.2.3.4 Threshold distance for crack coalescence

The threshold distance is defined here as the maximum projected distance a crack can grow within a specific period of time. In the application to later stage crack coalescence, coalescence is allowed to occur across a given distance along favourable crack directions. In the wing crack growth problem, this distance is obtained by projecting the current crack velocity and acceleration into

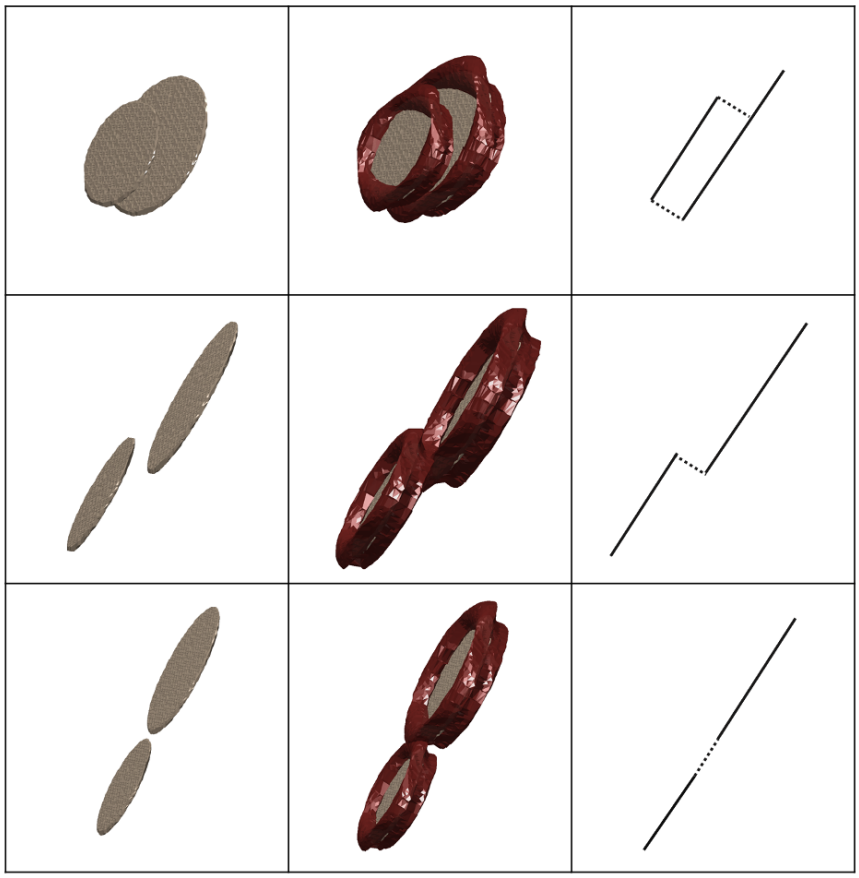

Fig. 2.9. Representative image of two parallel elliptical cracks with coalescence zones and common 2D coalescence patterns.

future timesteps and making sure that the crack velocity never exceeds the Rayleigh wave speed (C_R) of the material. For very high damage values, prior to fragmentation, it is difficult to determine the stress decay with increase in damage. At this stage the solid is heavily cracked and still not in its granular phase. This state of intensive cracking violates the dilute approximations used in the formulation of continuum-based damage models. To overcome this issue, it has been assumed that in the post peak strength phase of rapid damage growth, beyond a threshold damage value which determines the limit of applicability of continuum damage models, stress drops at a constant rate. The average stress, during the post-peak stress drop period, averaged over a given number of timesteps, is the stress that is used in the crack coalescence model, and the crack growth over these timesteps is the threshold or link distance in our model. If we use more timesteps, the stress drops but the allowable threshold distance increases, balancing each effect. This has been demonstrated in Fig. 2.10. In the figure t_{coa} is the time over which crack coalescence occurs, C_R is the Rayleigh wave speed and $\eta^{-1/3}$ represents an average measure of crack center spacing. The change in effective fragmentation ratio (a measure of the degree of fragmentation in a given material and will be defined later in Sec. 2.3.1) with damage does not appear to be very sensitive to change in the number of time-steps used to calculate the threshold distance for crack coalescence. In our model we have chosen 5 timesteps for calculating the threshold distance.

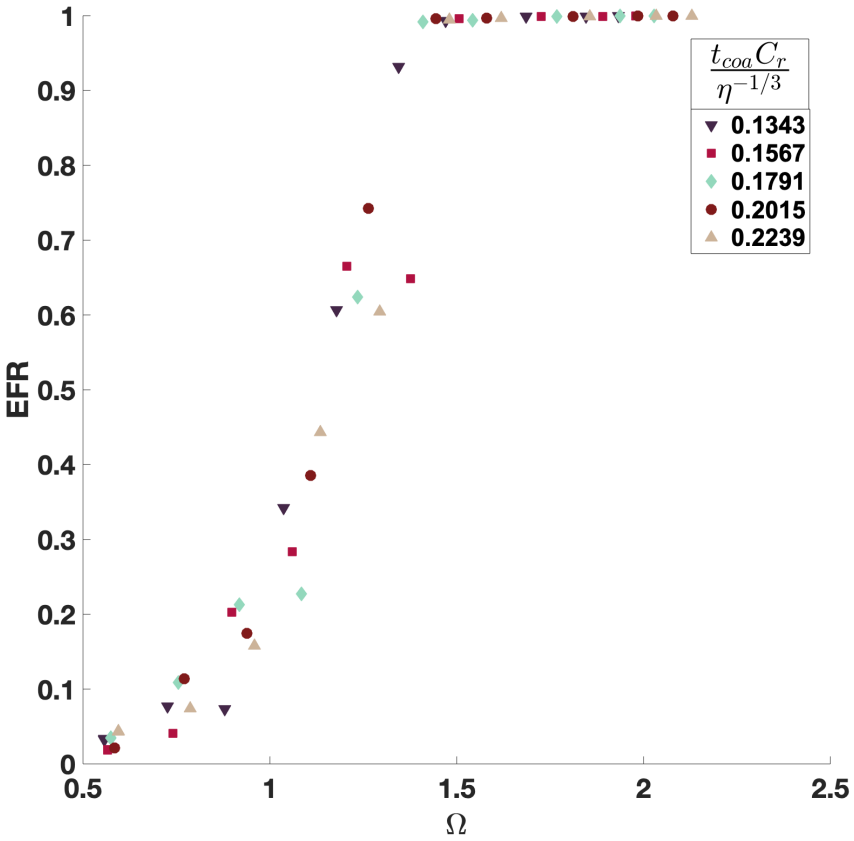

Fig. 2.10. EFR evolution with damage with change in coalescence time.

The damage values reported correspond to the total wing crack growth-based damage at the end of 5 timesteps.

2.2.3.5 Comparison of the two approaches

The coalescence surface approach involves a search along the edge of each crack for nearby cracks, pairing points to connect with a new crack if they satisfy the growth criterion. The coalescence zone approach, on the other hand, creates a coalescence zone which is independent of the presence of nearby

cracks and is based on an average measure of crack size and orientation. This makes the coalescence surface approach significantly more expensive than the coalescence zone approach. The coalescence surface approach connects only along crack edges, whereas the coalescence zone, although initiating new connections from a crack edge, can form connections anywhere on a crack. The coalescence surface approach connects with one crack edge at a time, while the zone approach can connect with multiple points on the edges of different cracks, starting from the same crack edge point. The coalescence zone approach is unable to resolve fragments smaller than the size of the coalescence zone. This is not a limitation of the coalescence surface approach, which can track longer crack bridge distances. The main limitation, however, lies in the computational expense of the coalescence surface approach. If multiple cracks are close to one another and along favorable directions of crack growth, one can expect all of them to eventually be interconnected, even though there might be a preferential order of crack connections.

It is worth noting that the reduction from three dimensions to two dimensions will lead to out-of-plane shear stresses. However, for a 2D crack, out-of-plane global stresses only lead to a shear stress field near the crack tip. Since it is assumed that crack growth is primarily tensile in nature, even under a global shear stress, then ignoring the out-of-plane stresses does not have a significant effect on the growth of coalescence cracks.

Figure 2.13 shows how the degree of fragmentation defined as the effective fragmentation ratio or EFR (further detail in 2.3.1) evolves with Damage for the two approaches and a smaller (1 mm) simulation box, along with a comparison of the coalescence zone approach for a larger simulation size (2 mm). As expected, the coalescence zone approach predicts a significantly higher degree of fragmentation than the coalescence surface approach. In view of this and given the significant computational expense of the coalescence surface approach, the coalescence zone approach has been used to model fragmentation for all simulations henceforth. We note that the coalescence zone approach often exhibits a sudden drop in EFR values (around a damage value of 1.2 in Fig. 2.17) that is a consequence of the numerical approach will be discussed in Sec. 2.5.

2.2.4 Dilation and extracting fragment statistics

Figure 2.11a shows the representative image of the network of cracks with coalescence zones in a solid. Figure 2.11b shows the corresponding image of the cracked solid. The embedded crack network is shown in red while the solid matrix is shown in gray. The blobs at the ends of the crack lines on the surface of the cracked solid (Fig. 2.11b) are the coalescence zones.

After simulating crack coalescence, the connected regions are obtained using MATLAB's bwconncomp, assuming periodic boundaries. After finding the

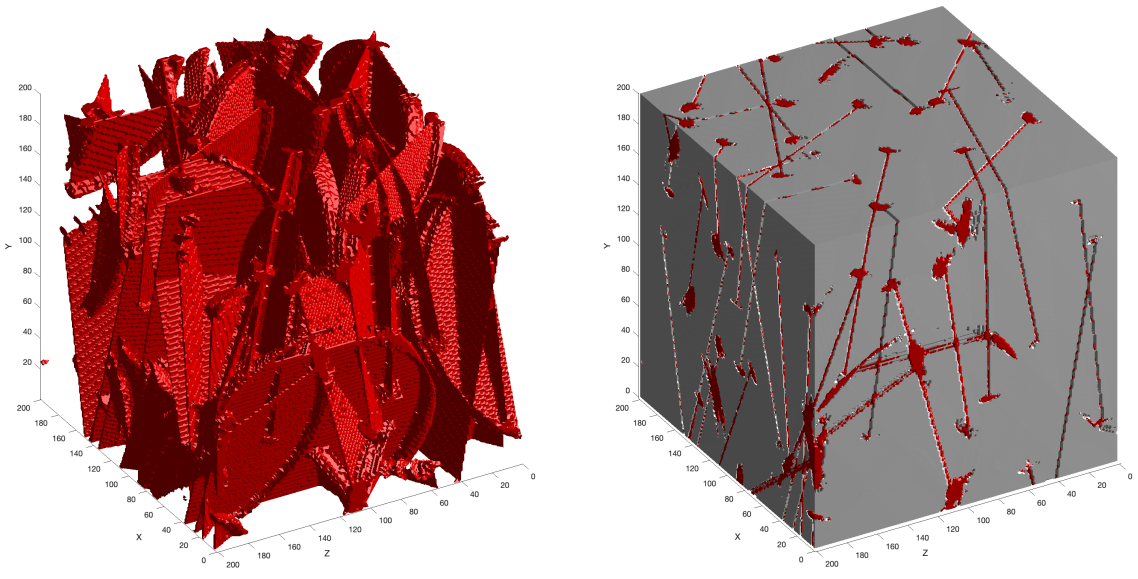

Fig. 2.11. Representative images of simulated cracks in a solid: (a) Crack network (red), (b) Crack network (red) embedded in solid matrix (gray).

connected regions, a dilation procedure has been adopted to reallocate the voxels corresponding to coalescence zones and cracked regions to nearby connected regions (Fig. 2.12). This eliminates any loss in material volume that would arise as an artifact of our numerical approach. Finally, the fragment size statistics have been extracted from the dilated regions using the regionprops3 function. The fragment statistics that have been obtained include the fragment sizes, roundedness and solidity of fragments. The roundedness Index developed by [128] is defined as $R = \frac{\mathcal{V}}{\mathcal{S}\sqrt[3]{abc}}$, where $\mathcal{V}$ and $\mathcal{S}$ are the volume and surface area of the object; parameters a,b,c are the principal axes of an equivalent ellipsoid. Solidity is defined as the volume fraction of voxels in the convex hull that are a part of the fragment. Roundedness Index value close to

0.33 would imply a perfectly round fragment, while solidity values lower than 1 signify increased angularity of fragments.

Figure 2.13 shows convergence for different sample sizes using the coalescence zone approach. For all further analysis, we have used a 2 mm simulation box that ensures convergence. After fixing the size of the simulation box, the size of each voxel (also referred to as the resolution) is chosen depending on computational constraints and the ability to accurately model cracks. A coarser resolution means that we will not be able to resolve cracks and fragments smaller than the resolution size. The resolution size has been chosen such that it can model the smallest cracks in the system. For most of these simulations the average initial half flaw size is around 10 μ. We have therefore chosen a cell size of 5 μ for all subsequent simulations.

2.3 Results - Transition to granular medium

2.3.1 Effective fragmentation ratio

The mean fragment size (d_{frag}) at a given initial defect size is non-unique with damage (Fig. 2.14a). This suggests that there is some other characteristic quantity that has a more unique relationship with fragment statistics than

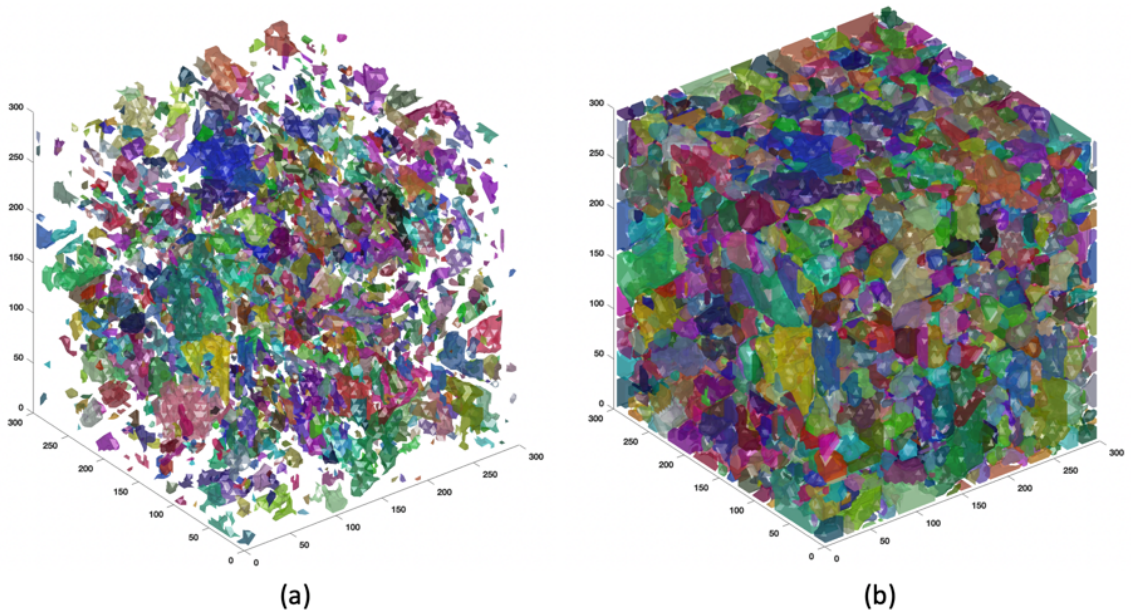

Fig. 2.12. Representative image of connected regions (a) before and (b) after the dilation procedure.

damage. One such possible measure is the degree of fragmentation, captured here by the effective fragmentation ratio (EFR). The EFR is defined as the ratio of the volume occupied by all but the largest fragment to the simulation box volume (Fig. 2.15). The largest fragment, appearing in gray in Fig. 2.15, provides insight into the onset of fragmentation. When very little fragmentation has occurred, the largest fragment occupies a large part of the volume, encloses other fragments and is connected to the boundary of the simulation box (Fig. 2.16 a,b). When significant fragmentation has occurred, the largest fragment is not necessarily connected to the boundary (Fig. 2.16 c). However, it is worth noting that a smaller simulation box might also lead to lower EFR values, as it may not be large enough to capture the tail end of the fragment

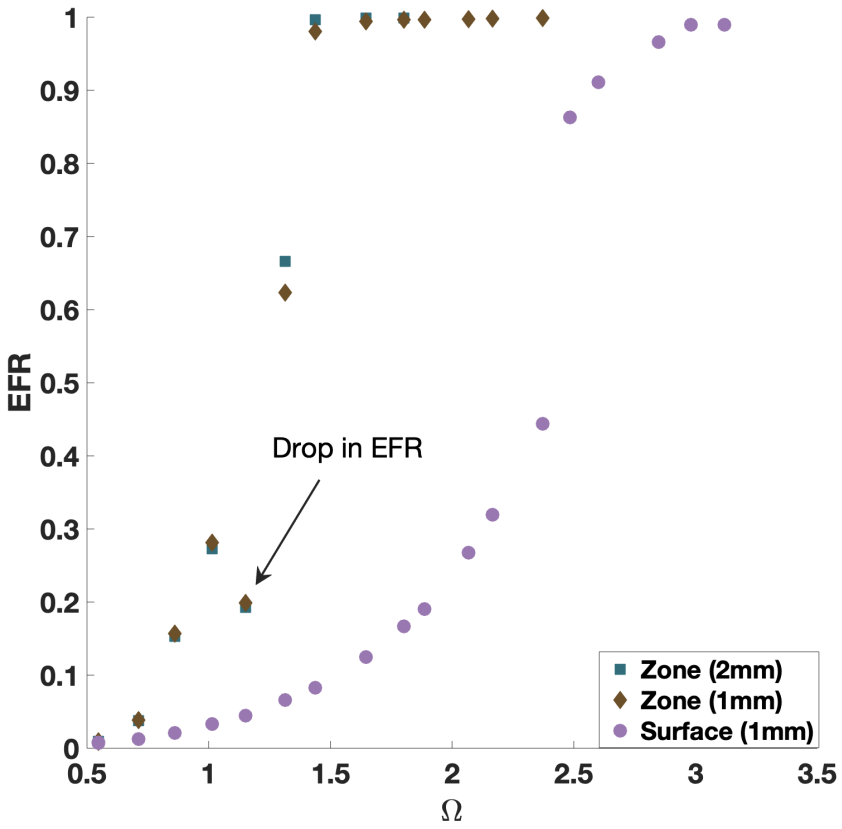

Fig. 2.13. Comparison of the coalescence zone approach for 1mm and 2mm simulation box size and the coalescence surface approach for 1mm simulation box.

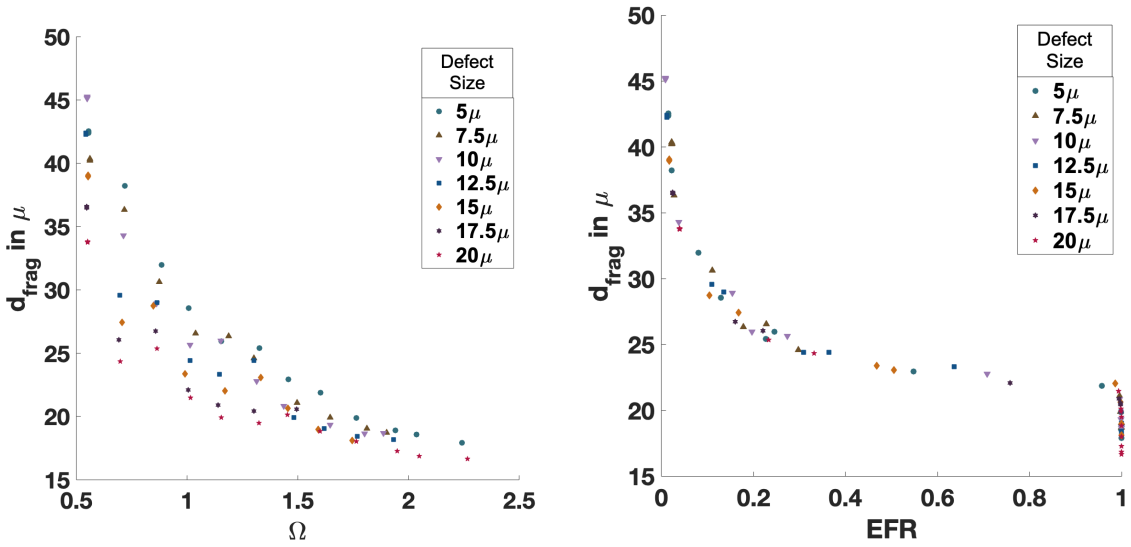

(a) Variation with Ω **(b)** Variation with EFR

Fig. 2.14. Variation of mean fragment size with damage and EFR at $\eta = 22e12cracks/m^3$ and $\dot{\epsilon} = 10^6 s^{-1}$ for different initial defect sizes.

size distribution. In these simulations, the simulation box is at least 10 times the length of the largest wing crack (not the average). Figure 2.17 shows the evolution of stress with damage as well as the corresponding EFR values for both the coalescence zone approach and the coalescence surface approach. As expected, EFR increases with damage. The 5-parameter Richard's asymmetric growth curve [129] has been used to fit the EFR values (solid and dotted EFR lines in Fig. 2.17):

$$EFR = \Xi_0 + \frac{\Xi_\infty}{\left(1 + \Omega_\phi e^{k_g(\Omega - \Omega_m)}\right)^{1/\Omega_\phi}}, \tag{2.11}$$

where Ξ_0 is the lower asymptote, Ξ_∞ is the upper asymptote, Ω is the damage, Ω_m is the damage at maximum growth, k_g is the growth rate and Ω_ϕ is a variable which fixes the point of inflection.

For the current problem $\Xi_0 = 0$, $\Xi_\infty = 1$, so there are only three parameters that require fitting. The fitted EFR-damage curve has been used to interpolate and obtain damage thresholds corresponding to any given EFR value. The 0.25, 0.5 and 0.75 EFR values have been highlighted along the EFR-damage curves as well as the stress-damage curve. It is observed that any significant fragmentation will mostly occur on the post peak strength part of the stress-strain curve. Figure 2.14b shows that the mean fragment size at a given initial defect size bears a unique relationship with EFR, for a constant defect density. In most cases, for the coalescence zone approach, the jump from around EFR=0.7 to EFR=0.9 happens almost instantaneously as seen in Fig. 2.17, suggesting a threshold EFR of 0.75 could be used to mark a sharp transition to granular phase. Figure 2.18 shows a plot of the fraction passing by weight with fragment size (d) for different EFR values at a 3D crack density, $\eta = 20e12cracks/m^3$ and strain rate of $10^6 s^{-1}$. The curves are obtained from the discrete CDF of fragment volumes excluding the largest fragment. When the curves are smooth and do not have an outlier fragment, causing them to terminate far below one, it can be argued that all the fragments follow a smooth distribution and the material is completely fragmented. Otherwise it will suggest that there are

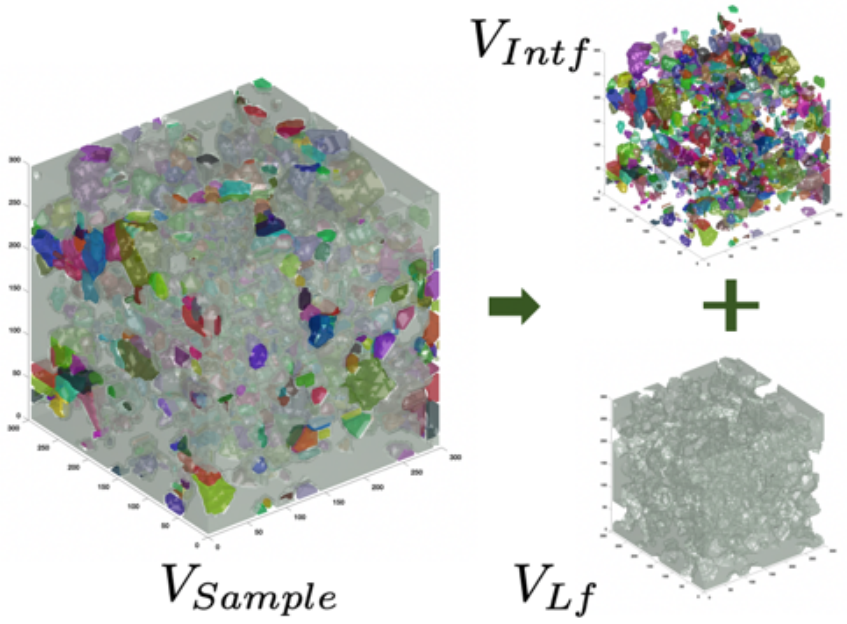

Fig. 2.15. Effective fragmentation ratio, $EFR = 1 - V_{Lf}/V_{Sample}$.

only some small fragments contained within a mostly intact material. It is obvious from the figure that at EFR<0.75 the material hasn't completely fragmented, whereas at EFR>0.9 it can be argued that the material has completely fragmented. EFR=0.75 is close to the highest EFR value at which an outlier fragment in the CDF of fragment volumes is clearly discernible. Any further fragmentation will be a consequence of particle breakage during granular flow where granular mechanics dominate. This further supports the idea of granular transition at an EFR of 0.75.

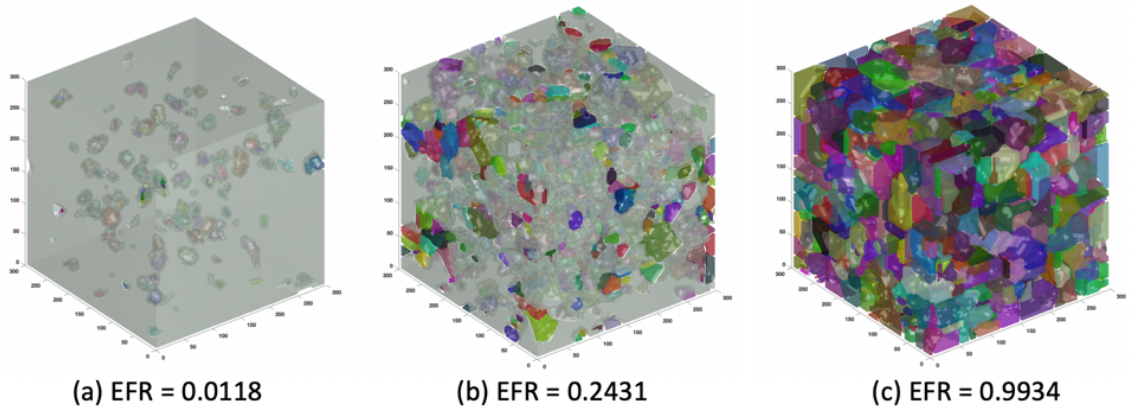

Fig. 2.16. Fragmentation with increasing EFR.

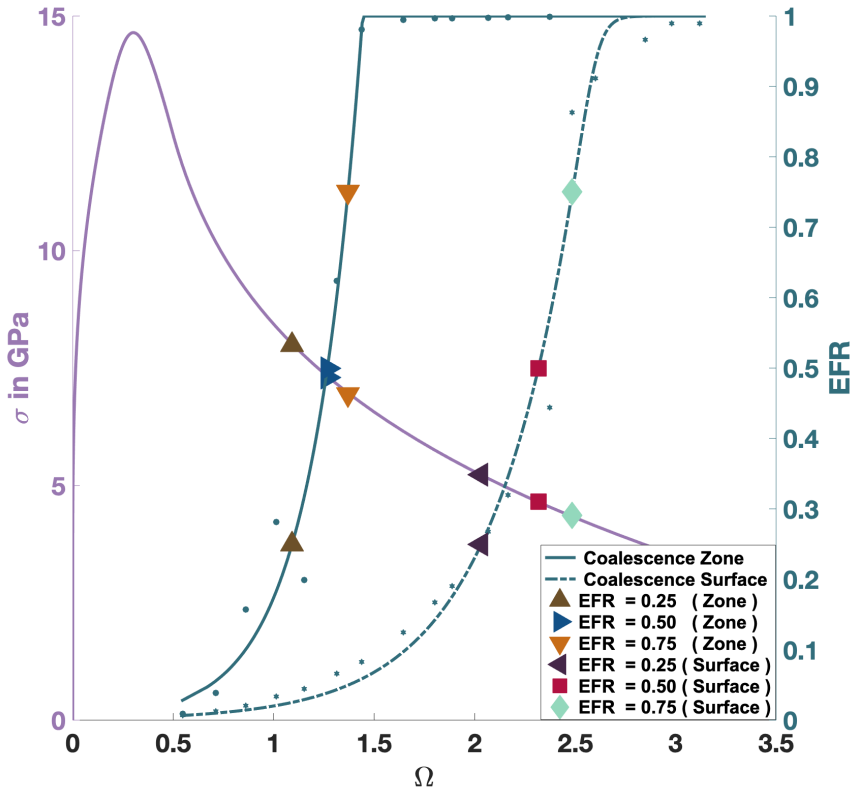

Fig. 2.17. Variation of stress and EFR with damage. The solid and dotted lines in the EFR v/s damage plot correspond to Richard's 5-parameter fit for coalescence zone and coalescence surface approaches respectively. The 0.25, 0.5 and 0.75 EFR states have been highlighted in the stress-damage and EFR-damage curves for both the coalescence zone and coalescence surface approaches.

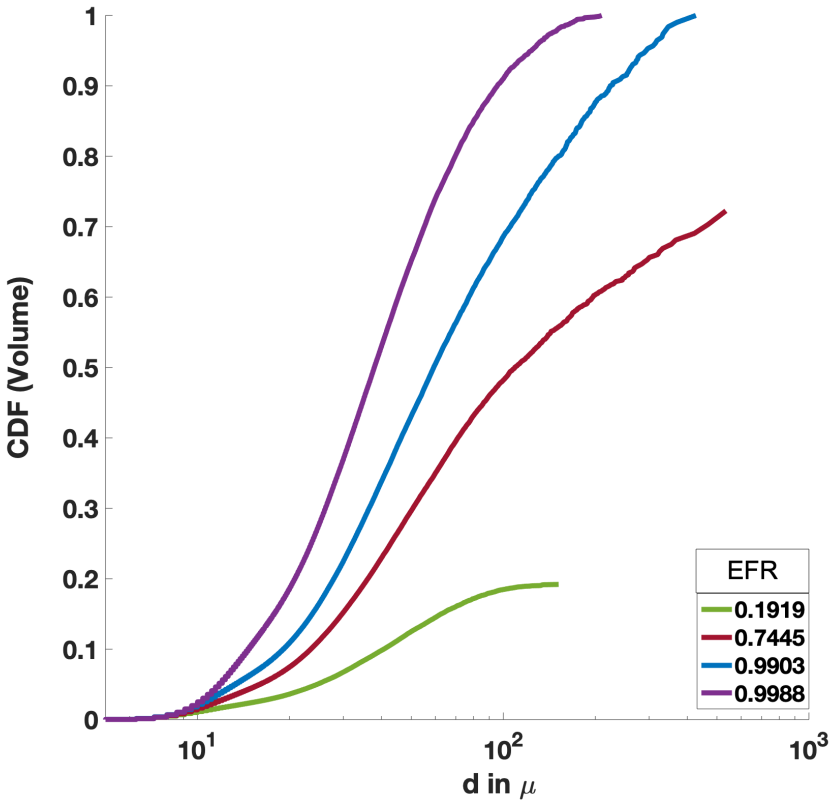

Fig. 2.18. Volume CDF or fraction passing with fragment size, excluding the largest fragment, for different EFR values.

2.3.2 Granular Phase Transition

The fragmentation model contains a number of microstructural parameters, such as initial defect size ($2l_{initial}^{defect}$), initial three-dimensional crack density (η), polycrystalline fracture toughness (K_{IC}), strain rate ($\dot{\epsilon}$) and elastic modulus (E). Significant changes in the dependence of EFR on damage were only observed when changing $l_{initial}^{defect}$ and η. Two-dimensional damage is calculated as,

$$\Omega = \sum_{j} \sum_{k} \eta(k, \theta_j)^{2/3} l_w(k, \theta_j)^2, \tag{2.12}$$

where $\eta(k, \theta_j)$ and $l_w(k, \theta_j)$ are the 3-dimesnional crack density and the wing crack length corresponding to the k_{th} initial defect size and j_{th} initial defect orientation. $\eta^{2/3}$ represents the two-dimensional crack density analogue. Initial damage has been defined as

$$\Omega_i = \sum_{j} \sum_{k} \eta(k, \theta_j)^{2/3} l_{initial}^{defect}(k, \theta_j)^2. \tag{2.13}$$

The representative initial crack length is defined as,

$$l_i = \sqrt{\frac{\Omega_i}{\eta^{2/3}}}. \tag{2.14}$$

The representative final crack length is defined as,

$$l_f = \sqrt{\frac{\Omega_f}{\eta^{2/3}}}, \tag{2.15}$$

where Ω_f is the Ω at transition.

l_i and l_f are the root mean square values of the initial and final crack lengths respectively. Using these expressions, for random orientation of initial defects, after performing an exhaustive set of fragmentation simulations for various strain rates, initial defect populations, elastic moduli and fracture toughness, the following fit was found for granular transition at EFR=0.75:

$$\Omega_i = 293.6{\Omega_{f_{0.75}}}^{-1.049\frac{\sigma_{f_{0.75}}\eta^{-1/6}}{K_{IC}}^{-2.784}}, \tag{2.16}$$

where $\Omega_{f_{0.75}}$ and $\sigma_{f_{0.75}}$ represent the state variables for transition damage and transition stress at EFR=0.75.

The adjusted R-squared value for this expression is 0.96. However this definition is difficult to apply in practice, since it requires knowledge of both the damage and stress at an EFR of 0.75. Alternatively, a simpler function in terms of the representative crack length and the initial defect distribution was used to provide an R-squared value of 0.92:

$$l_f = 1.354\eta^{-1/3} - 0.6977 l_i. \tag{2.17}$$

The results have been compared against the case of fixed flaw orientation along the most favorable direction in [55] using a similar parametric study of the fragmentation model. This leads to the transition fit with an adjusted R-squared value of 0.98:

$$l_f = 1.576\eta^{-1/3} - 1.095l_i. \tag{2.18}$$

Although, the trend appears to be similar to the random orientation case, the coefficients are slightly different. A more general form of the transition equation will be discussed in Sec. 2.5.

In the following section, a phenomenological fragmentation model will be discussed. It predicts a similar form of the transition criterion as Eqn. 2.17.

2.3.3 Phenomenological model for transition

We propose a simple phenomenological model for granular transition. The initial defect size is taken to be $2l_i$, the final crack length to be $2l_f$ and the three-dimensional crack density to be η. It is assumed that a given percentage of the defect centers need to be connected for fragmentation to occur. This assumption is arbitrary and can be set to any given value to meet a certain degree of fragmentation. For random orientation, θ, and initial defect size, l_i,

the mean vertical projection of a defect is

$$\frac{2}{\pi}\int_0^{\pi/2} l_i \cos\theta d\theta = 0.637 l_i. \tag{2.19}$$

Assuming defect locations are uncorrelated and follow a Poisson process, the defect spacing is an exponentially distributed random variable with mean spacing $\frac{1}{\lambda} = \eta^{-1/3}$,

$$f_x(x) = \lambda e^{-\lambda x}. \tag{2.20}$$

Therefore the cumulative density function is

$$F_x(x) = 1 - e^{-\lambda x}. \tag{2.21}$$

The spacing that corresponds to 90% crack coalescence is $x = -\frac{ln(0.1)}{\lambda} = 2.3026\eta^{-1/3}$.

In other words, for fragmentation to occur, 90% of all defect center spacings have to be connected to each other. In order for that to happen, the final crack length plus the mean vertical projection of the initial defect size should therefore become equal to $2.3026\eta^{-1/3}$. Hence,

$2l_f + 2 * 0.637 l_i = 2.3026\eta^{-1/3}$.

So, the material transitions when

$$l_f = 1.151\eta^{-1/3} - 0.637 l_i. \tag{2.22}$$

If we assume that the criterion for fragmentation involves 75% of the the defect centers to be connected to each other, the transition criterion can be rewritten as

$$l_f = 0.693\eta^{-1/3} - 0.637 l_i. \tag{2.23}$$

These expressions have a similar form to Eqns. 2.17 and 2.18 , though the coefficients are underestimated.

In general, the fragmentation criterion can be expressed as $2(l_f + C_2 l_i) = C_1 \eta^{-1/3}$. Figure 2.19 shows a schematic representation of the problem. The constants C_1 and C_2 are determined by the percentage of cracks that need to be connected in order to achieve a certain degree of fragmentation and the percentage of initial defects that actually get activated. The latter would depend on the flaw friction, confining stresses and also to some extent on the strain rate. The constant C_2 will depend on the orientation of initial defects. It is close to 0.637 for random defect orientation and $\cos(\theta_{fixed})$ for a fixed defect orientation, θ_{fixed}.

2.4 Results - Fragment statistics

In the numerical fragmentation model, the connected regions correspond to individual fragments. The total number of voxels in a bounded region times the volume of each voxel is a measure of fragment volume. Fragment size has

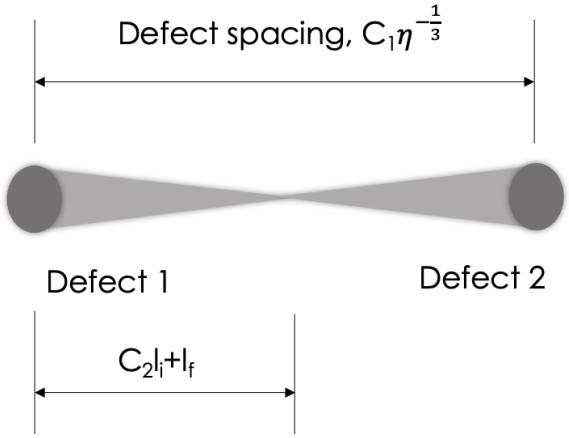

Fig. 2.19. Schematic representation of phenomenological granular transition model.

been computed as the cube root of fragment volume. Fragment size distribution, obtained for different values of initial defect sizes and strain rates, always followed a power law distribution, except for the smallest fragment sizes, which likely reflects the limitation of the selected resolution size. Figure 2.20 shows the fragment size distribution at different EFR values for 3D crack density, $\eta = 20e12 cracks/m^3$ at a strain rate of $10^6 s^{-1}$. The largest fragment has been omitted for these plots. [75] also observed an evolving power law distribution for high-rate brittle fragmentation. However it is not clear what extent of fragmentation from their particle based models is analogous to the onset of granular physics in continuum damage models.

As mentioned before, the mean fragment size (d_{frag}) at a given EFR and flaw density does not seem to depend significantly on the initial defect size (Fig. 2.14). This should not be confused with the final fragment size distribution

obtained from experiments with different initial defect sizes. This is because post granular phase energy dissipation due to refragmentation might still be different, due to different residual energies in either case. However, there is a dependence of the mean fragment size (d_{frag}) v/s EFR with crack density values (η). This is not unexpected; for a similarly scaled system one might expect the mean fragment size (d_{frag}) to scale with $\eta^{-1/3}$. In reality a proportionate scaling of the system does not necessarily scale the local stress states similarly, and thus affects the coalescence zone.

Figure 2.21 shows the variation of scaled mean fragment size ($d_{frag}\eta^{1/3}$) with damage and EFR for different crack densities. It is worth noting that the initial defect size was not scaled proportionately, and the same value was used. Other fragment properties like solidity, mean roundedness index can also be extracted. These properties have a more complicated relationship with EFR for different initial defect sizes and defect densities. Figures 2.22, 2.23 show the variation of mean roundedness index and solidity with EFR and damage for different initial defect sizes (or half flaw size) respectively. Figures 2.24, 2.25 show the same for crack density. The general trend appears to suggest that roundedness and solidity decrease with increase in damage (or EFR) for given value of crack density and initial defect size except for some minor aberrations mostly observed at lower EFR values. This suggests that particles tend to be more angular at a higher level of fragmentation. Based on a transition EFR

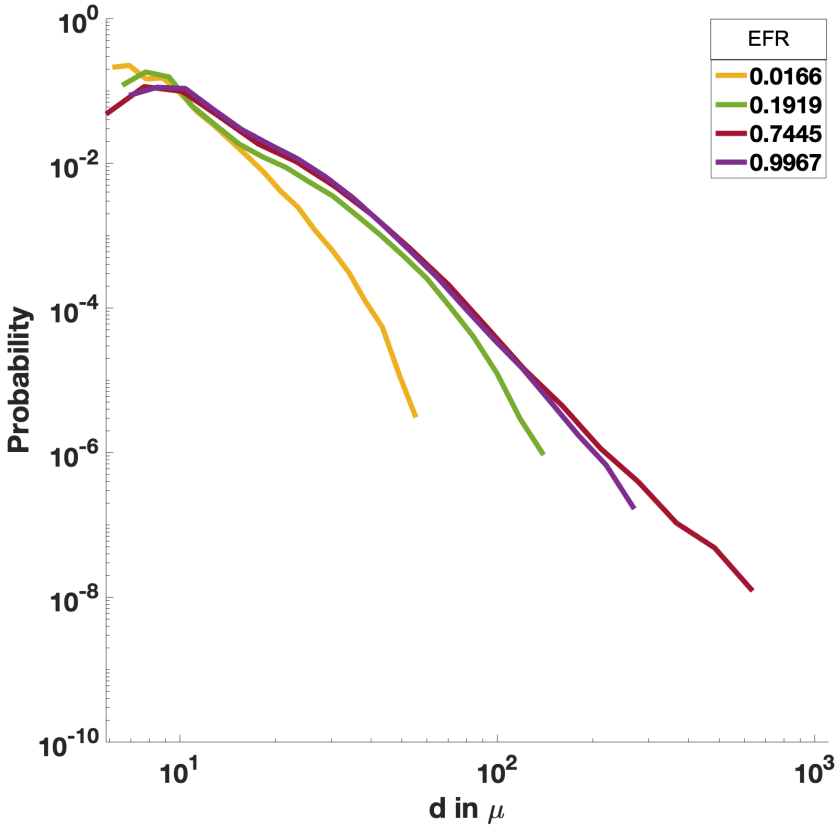

Fig. 2.20. Fragment size distribution at $\eta = 20e12cracks/m^3$ and $\dot{\epsilon} = 10^6 s^{-1}$ for varying EFR.

= 0.75 to 0.9, a mean solidity value of 0.91 and a mean roundedness index of 0.26-0.27 is suggested.

Figure 2.26 shows the enlarged image of a few large fragments. It appears that there is some directionality in the orientation of the large fragments, with their longer direction being oriented along the direction of maximum principal compression.

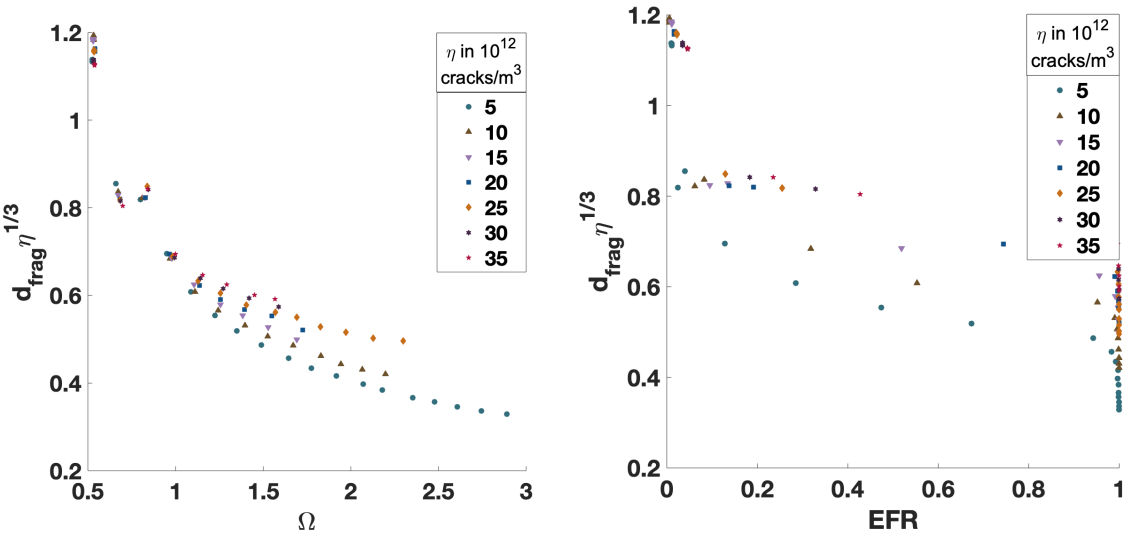

(a) Variation with Ω **(b)** Variation with EFR

Fig. 2.21. Variation of scaled mean fragment size with damage and EFR at initial defect size of 10μ and $\dot{\epsilon} = 10^6 s^{-1}$, for different crack densities (η).

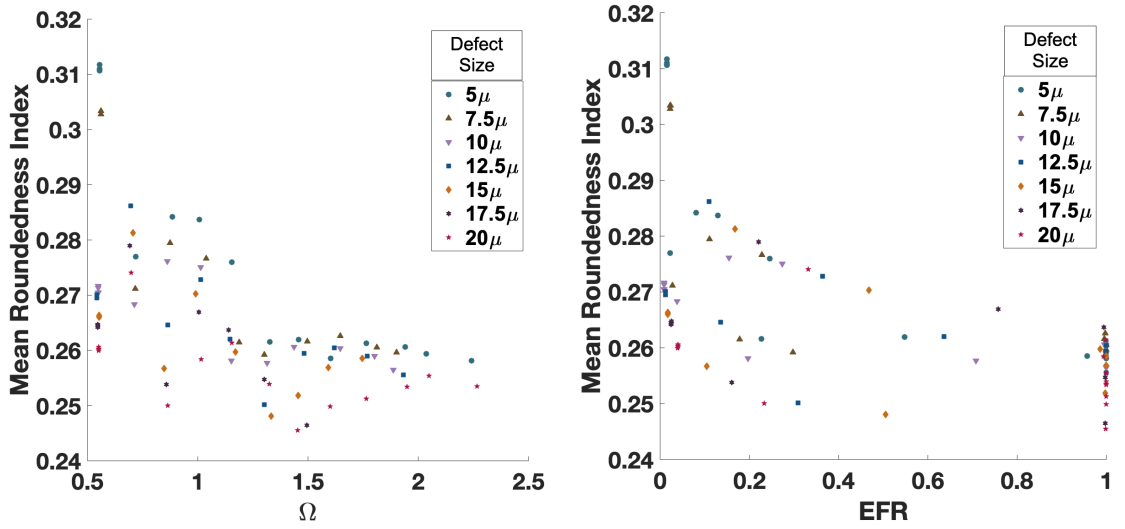

(a) Variation with Ω **(b)** Variation with EFR

Fig. 2.22. Variation of mean roundedness index with damage and EFR at $\eta = 22e12 cracks/m^3$ and $\dot{\epsilon} = 10^6 s^{-1}$ for different initial defect sizes.

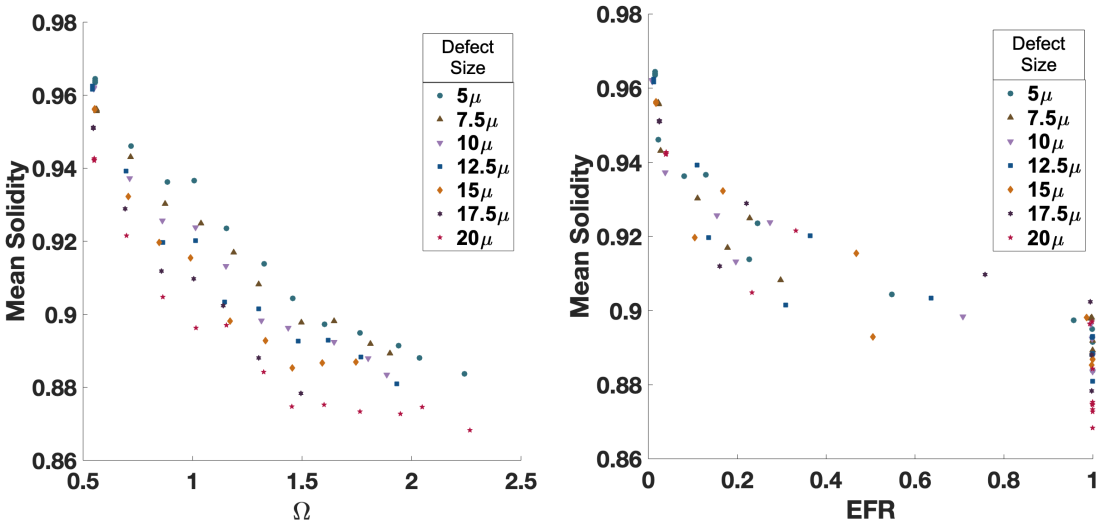

(a) Variation with Ω **(b)** Variation with EFR

Fig. 2.23. Variation of mean solidity with damage and EFR at $\eta = 22e12 cracks/m^3$ and $\dot{\epsilon} = 10^6 s^{-1}$ for different initial defect sizes.

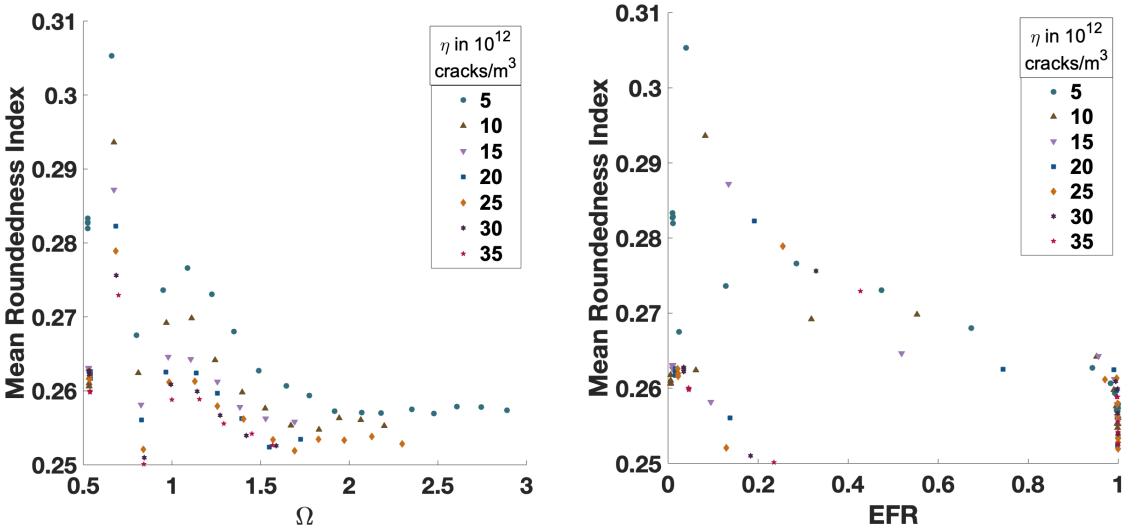

(a) Variation with Ω **(b)** Variation with EFR

Fig. 2.24. Variation of mean roundedness index with damage and EFR at initial defect size of 10μ and $\dot{\epsilon} = 10^6 s^{-1}$ for different crack densities (η).

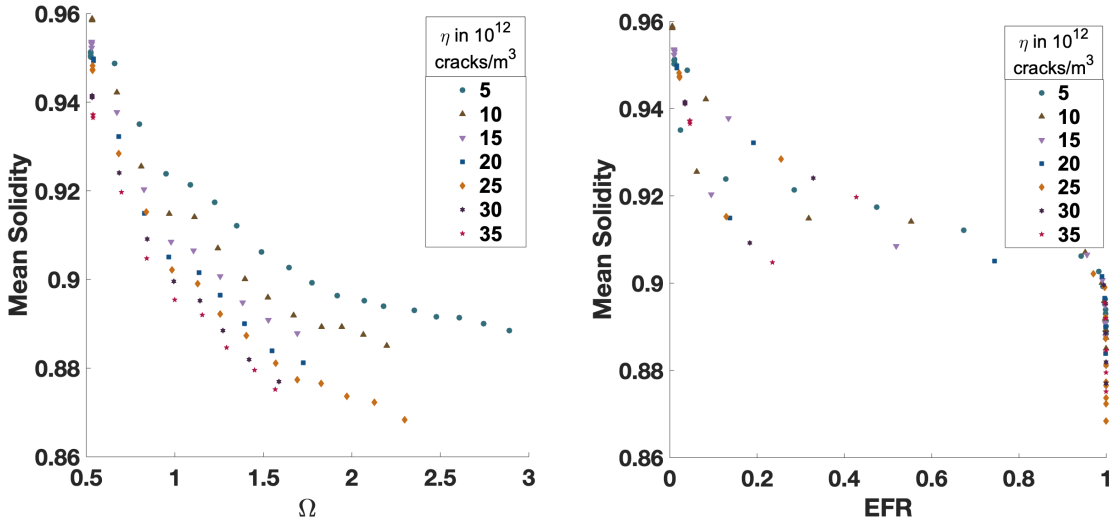

(a) Variation with Ω **(b)** Variation with EFR

Fig. 2.25. Variation of mean solidity with damage and EFR at initial defect size of 10μ and $\dot{\epsilon} = 10^6 s^{-1}$ for different crack densities (η).

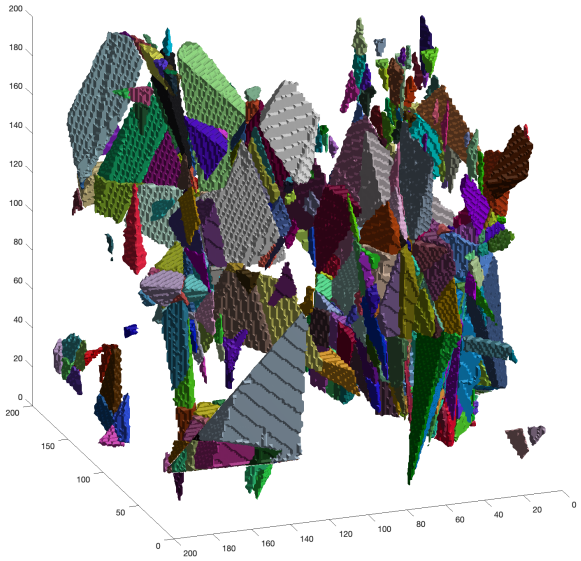

Fig. 2.26. Enlarged representative image of fragments showing directionality.

2.4.1 Comparison with experiments

[105] looks at the rate dependent fragmentation of boron carbide using a Split-Hopkinson pressure bar setup for confined and uniaxial compressive loading. The fragment size distribution for dynamic uniaxial compression best simulates the loading conditions in the current work. There are two distinct fragmentation regimes - a regime dominated by the processing induced microstructural flaws (Regime I) and another one that is dominated by boundary conditions and macroscopic structural failure (Regime II). The current work assumes periodic boundary conditions and is unable to account for problem specific macroscopic structural failure. The fragment size distribution generated from the current work is induced by the microstructural defect population modelled as micro-cracks and it is best compared with the Regime I fragments obtained from experiments. It has been assumed that the stress state in the experiments is homogeneous and simulates more or less a uniaxial loading condition. Also, any further fragmentation due to granular flow has been neglected or at least assumed to not significantly alter the nature of the initial distribution of fragment sizes.

Figure 2.27 shows the normalized histogram of fragment size distribution for dynamic uniaxial loading [105]. The two distinct fragmentation zones can be easily demarcated. Fragments less than 100μ (Regime I) appear to exhibit a power law relationship similar to our observations. The power law exponent for

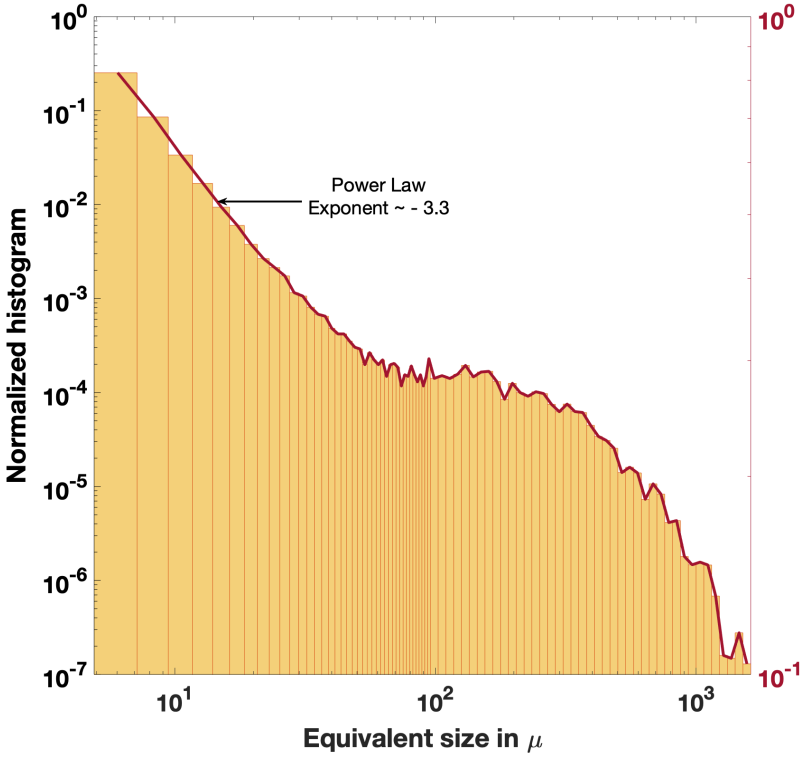

Fig. 2.27. Fragment size distribution obtained from Kolsky bar dynamic fragmentation of Boron Carbide [105].

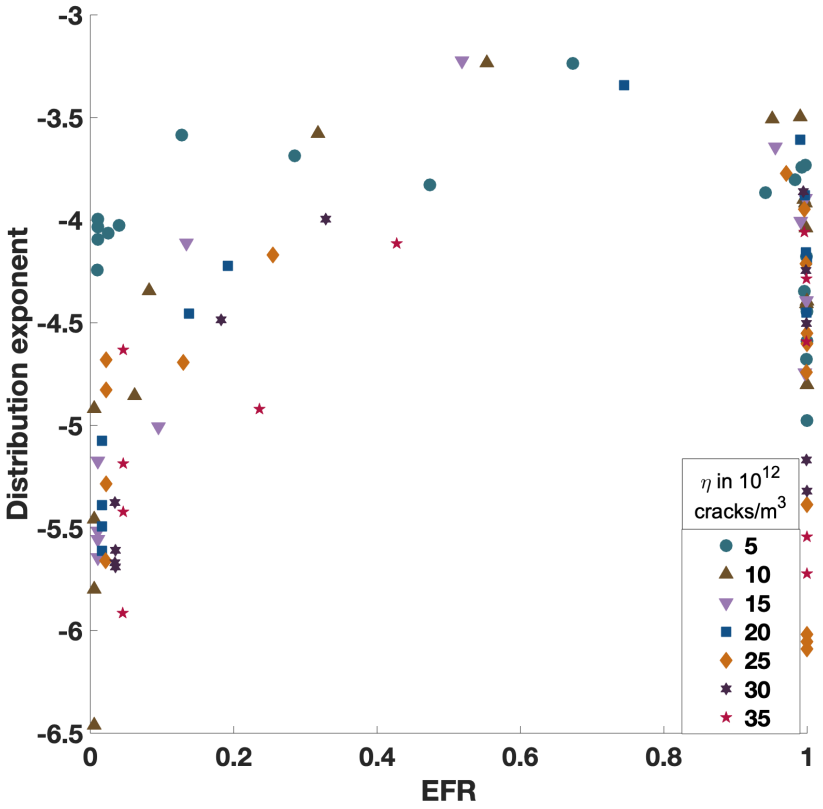

Fig. 2.28. Power law distribution exponent of fragment sizes from numerical model.

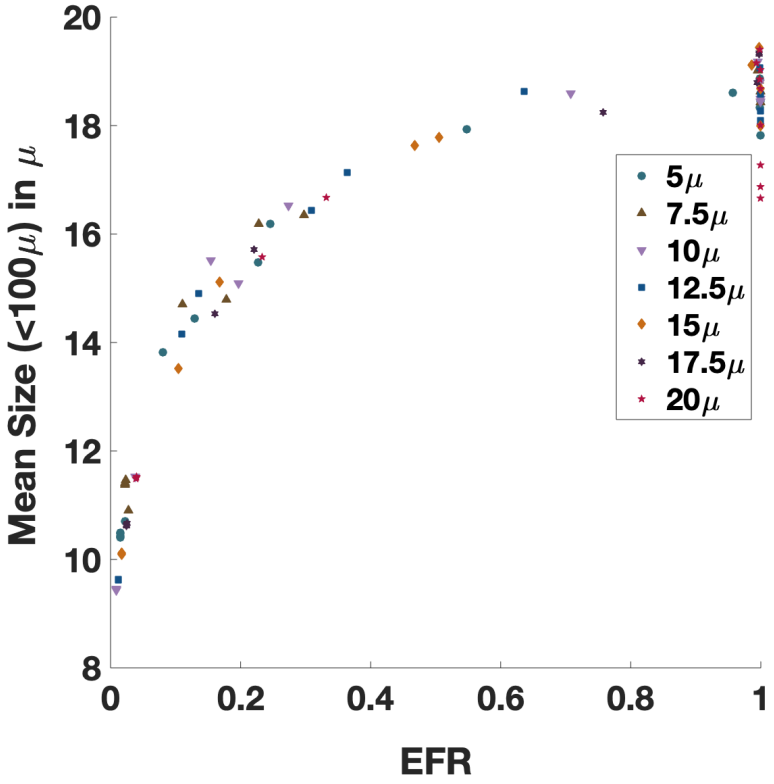

Fig. 2.29. Mean volume averaged fragment size with change in EFR for fragments less than 100μ.

Regime I is around 3.3, whereas in the numerical model the exponent for EFR = 0.75 is around 3.5 (Fig. 2.28). The volume-averaged mean size of fragments less than 100 μ, computed from Hogan's data is around 17.8 μ. This agrees well with the corresponding mean size at around EFR=0.75 from the numerical model (Fig. 2.29). In Fig. 2.29 the fragment size seems to initially increase with EFR, unlike in Fig. 2.14, because the fragments greater than 100μ have not been included. As EFR increases, more of the larger fragments re-fragment to create smaller fragments. It is worth noting that the size reported for Hogan's data corresponds to an equivalent diameter, while the size calculated from the numerical model is simply the cube root of the fragment volume. The numerical model is three dimensional while the fragment sizes calculated from Hogan's experiments are obtained by calculating the major and minor axis lengths from two-dimensional projection of three-dimensional particles.

The new transition criterion was used to recalibrate an integrated ceramics model for simulations of sphere indentation and edge on impact experiments of boron carbide in Chapter 3. It led to more accurate representation of key failure patterns.

2.5 Discussion

The current approach treats granular transition as a near instantaneous mechanism. While it is not unreasonable to think that the mobilization of a few fragments accelerates fragmentation and subsequent granular behaviour, the process of crack coalescence might initiate much earlier. The model used to simulate dynamic crack growth ignores the modification of the number density of crack populations and their crack lengths. It remains unclear how sensitive the transition is to early stage coalescence. Early stage crack coalescence increases crack length but reduces crack density; these competing effects on damage might balance one another. However the competing effects might change the mode of crack propagation to one in which a wing crack growth-based damage model might be unable to account for. These are general limitations of wing-crack growth-based models.

The presented approach is generic and can also be exercised with other damage models by modifying the input crack statistics. In the numerical model, cracks have been generated randomly without any restriction on crack intersection. Simulating minimally intersecting cracks involves ensuring that most of the ellipses do not intersect with one another. This can be computationally challenging, especially at high crack density and for large crack lengths. This has been attempted in the current work by trying to generate cracks of a given size in the simulation box volume iteratively until there is no intersection with

previously generated cracks. At every iteration the location is reset and at every ten iterations the Q_x and Q_y matrices are reset, essentially changing the crack orientation. If we fail to generate any such cracks in 500 iterations, the crack corresponding to the minimum number of intersecting voxels has been accepted. It is observed that generating minimally intersecting cracks does not affect the evolution of EFR with damage (Fig. 2.30). Given the computational challenge and the insensitivity of EFR to the constraint of minimal crack intersection, it makes sense to ignore the effect for parametric evaluation of fragmentation.

It has been observed that for the coalescence zone approach there are some outlier points in the EFR v/s damage curves (Fig. 2.13), where the EFR seems to drop before increasing again and following the general trend. EFR is not strictly monotonic with damage and the lack of monotonicity is not due to randomness in the model as this drop often happens around the same damage value for two independent set of simulations (Coalescence zone approach for different simulation box sizes in Fig. 2.13 , different crack generation techniques in Fig. 2.30). A closer look at the coalescence zone approach suggests that this drop might be an artifact of the coalescence zones. While the coalescence zone approach is a much more efficient way of numerically accounting for crack coalescence, it treats the coalescence cracks as larger volumes. This is not a significant problem in general, but often the voxels associated with coa-

lescence zones erode some of the smaller fragments. There are certain damage values around which the contribution of these zones towards creating new connections is overshadowed by them eroding the smaller fragments and later on reassigning those voxels to part of the largest fragment. It has been checked that when a sudden drop in EFR occurs, the number of fragments generated also decrease, which supports the above reasoning. Since the overall trend still remains monotonic, and the drop occurs at lower EFR values than those associated with fragmentation, the computational advantage of the coalescence zone approach outweighs the lack of monotonicity.

Given the range of strain rates studied (10^4 to $10^6 s^{-1}$), significant strain rate dependency on the fragmentation criterion or fragment sizes at the onset of granular flow was not observed. This does not imply that strain rate does not affect fragmentation. Strain rate affects the stress-strain response, as well the residual stresses immediately after the onset of granular mechanics. This will influence further granular behaviour and/or further fragment breakage. However, strain rate does not seem to affect the transition damage values under high rate conditions. The ranges of strain rate studied (10^4 to $10^6 s^{-1}$) were such that multiple cracks were activated simultaneously and not a single or few large cracks, as one might observe under low rate conditions. Lower strain rate would increase the size of the largest cracks and the current simulation box will not be able to account for it. The inability to activate multiple de-

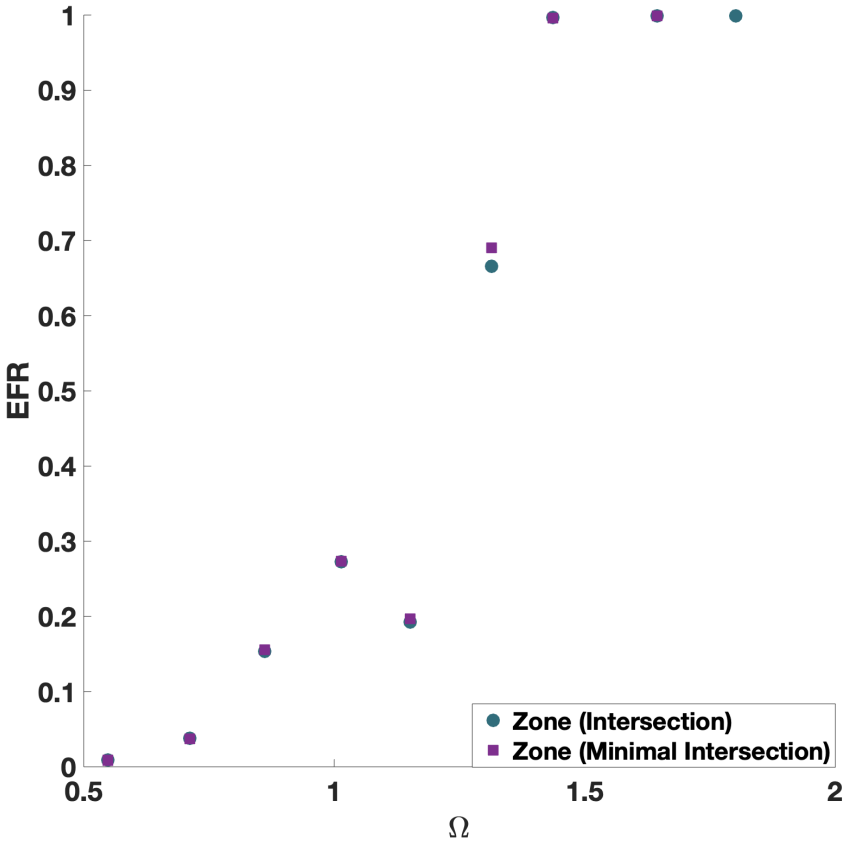

Fig. 2.30. Comparison of simulating cracks with and without minimal intersection.

fects might lead to larger fragments at low rates, in which case the size of the fragments might be larger than the continuum scale and the macroscopic conditions might dominate the problem. Low rate fragmentation is also not the focus of the current work.

The transition wing crack length appears to be more sensitive to defect spacing than it is to defect size (Eqns. 2.17 & 2.22). This might suggest material modification in favour of controlling the defect spacing rather than defect size to obtain desirable behaviour. Future work should focus on microstructural dependence of fragmentation, granular transition, flow and subsequent overall material behaviour under high rate conditions.

Most of the simulations in the study correspond to a randomly oriented defect distribution. However for the case of a fixed defect orientation along the most favourable direction, a transition equation has been similarly predicted (Eqn. 2.18), and it has a similar form to that of the random defect orientation case (Eqn. 2.17). A more general way of explaining granular transition is in terms of active defects. For sliding crack models, the activation of defects depends upon the defect orientation, defect size, the stress field, the strain rate, the crack face friction coefficient and the fracture toughness. While comparing between different initial defect orientations, the same number of defects which are able to overcome the crack face frictional constraint should have similar transitional response. In the absence of confinement, cracks with orientations

greater than the friction angle can be activated. It is worth noting that overcoming the crack face friction (μ_{flaw}) is not a sufficient condition for wing crack growth. However, we will denote these cracks as active cracks henceforth. So, the density of active defects is $\eta_{active} = \frac{tan^{-1}(\mu_{flaw})}{\pi/2}\eta$. From Eqns. 2.12 & 2.15 and for uniform crack size distribution,

$$l_f = \sqrt{E[l_w^2]} \implies l_f = \sqrt{E[{l_{w}}_{active}^2]\frac{\eta_{active}}{\eta}} \implies l_f = {l_f}_{active}\sqrt{\frac{tan^{-1}(\mu_{flaw})}{\pi/2}}, \quad (2.24)$$

where, ${l_w}_{active}$ and ${l_f}_{active}$ are the l_w and l_f equivalent for active defects. Also, it can be assumed that the initial defect size is independent of the orientation distribution. Using these relations, Eqn. 2.17 can be rewritten as:

$${l_f}_{active} = 1.354\left(\frac{\pi/2}{tan^{-1}(\mu_{flaw})}\right)^{1/6}\eta_{active}^{-1/3} - 0.6977\left(\frac{\pi/2}{tan^{-1}(\mu_{flaw})}\right)^{1/2}l_i \quad (2.25)$$

For $\mu_{flaw} = 0.8$, Eqn. 2.25 can be written as ${l_f}_{active} = 1.5588\eta_{active}^{-1/3} - 1.0645l_i$.

This is very similar to Eqn. 2.18 in which all the similar sized defects have the same orientation and are activated simultaneously. In reality, the exact nature of the transition equation will also depend on the correlation between micro-structural defect density, size and orientation.

While the computational time required for each simulation varied significantly, the analyses were not highly computationally intensive. For example, for the coalescence zone approach, each simulation took between 30 mins and

2 hours on a single core with a memory limit of around 4.9 GB per core.

2.6 Conclusion

A physically based granular transition criterion for continuum models of high rate impact of brittle ceramics has been proposed. The model assumes near-instantaneous granular transition and suggests that a certain combination of state variables need to meet a certain threshold for fragmentation and transition to a granular state. This transition criterion serves as a switch in continuum codes for brittle dynamic fragmentation that activates granular physics. The outputs of the model also help characterize the initial conditions for granular mechanics as a function of initial defect characteristics. A simple phenomenological transition model also proposes a similar form of transition equation without delving into the mechanics of crack growth. Power law distributed fragment sizes with an evolving distribution exponent is similar to particle dynamics based fragmentation models [75]. Comparison of initial fragmentation with high rate impact experiment of boron carbide [105] also demonstrate similar power law distributed fragments in the microstructure dependent regime with comparable sizes. The modified granular transition criterion implemented in an integrated ceramics model shows more accurate reproduction of failure patterns in sphere indentation and edge on impact ex-

periments (Chapter 3).

Chapter 3

Implementation in integrated ceramics model

3.1 Introduction

Ceramics are brittle or quasi-brittle materials used in a vast range of applications from body and vehicle armors, semi-conductors, scratch-resistant shields, kitchenware and everyday appliances. While the properties of ceramics can be as varied as their chemical composition and structure, armor ceramics in particular are characterized by high energy absorption, high hardness, high compressive strength and preferably low density. All these properties make them suitable for impact and blast resistance during combat. Boron carbide, with its relatively low density and high hardness, is of special interest for re-

search in the field of armor ceramics [30].

A ceramic constitutive model suitable for a given size and/or application might not be able to capture the relevant physics for another application. Particle based models [75] attempting to capture the very large number of microscale defects in ceramics are computationally intensive. Numerical models of discrete cracks [43, 46] or crack like features [44, 45, 51–54] are not suitable for modelling simultaneous propagation of millions of micro-cracks, as is often the case for high rate simulations of armor ceramics. Continuum damage models [78, 130–132] are applicable so long as the continuum assumption holds true. The applicability of such models in penetration or fragmentation problems are dependent on the numerical solver and the output property of interest. Ensemble averaging of atomistic properties of single crystal ceramics provides a more meaningful representation of micro-mechanical properties like fracture toughness, moduli and Poisson's ratio. However, these models also have some non-physical parameters that are difficult to calibrate experimentally. Often, calibration of these parameters based on macroscopic response might be appropriate for modelling the physics and mechanisms involved in the experiments they are used to calibrate against, but may not be suitable for other loading scenarios. Despite these limitations, many of these models can be used for extreme environment simulations, some of which are often infeasible or expensive to replicate in laboratories. They can also help us understand

key trends and guide material processing towards improving material performance.

Like most other materials, scale separation becomes quintessential in modelling armor ceramics. From the point of simulations this might not only mean differences in the physics at different scales, but also the calibration of parameters. As an example, fragmentation in ceramics is observed typically at two scales: a microstructure-dependent scale leading to smaller fragments and a geometry-dependent macroscale [105]. Depending on the problem, fragmentation can either lead to granular phase transition and granular flow as observed in the Mescall region [17, 86], or it can also lead to disintegration and limit the peak strength, as observed in unconfined Kolsky bar experiments [133]. From a modelling viewpoint, this can lead to a different calibration of the fragmentation or granular transition criterion for different experiments, depending on the dominant fragmentation mechanism. In addition to this, the resolution of the simulations limits the fragment size that can be captured in a continuum granular mechanics model. The fragment statistics are used to calibrate such granular mechanics models (Chapter 2) and thereby influence the calibration at a given resolution.

The key micro-mechanisms in boron carbide under impact are amorphization [24], crack growth, crack interaction and crack coalescence [120] leading to fragmentation followed by granular flow [8]. The current chapter exercises an

integrated ceramics model [82,90,134] that combines these key features with a modified granular transition criterion developed in chapter 2 and tries to simulate key failure mechanisms observed in Sphere Indentation experiments [20] and Edge On Impact experiments [135–137].

3.2 Overview - Integrative Model

The integrated model builds on [82] and combines multiple mechanisms that are deemed dominant in boron carbide. It incorporates amorphization induced damage from [73], fracture dominated by the growth and interaction of wing cracks from sliding flaws [55, 82], fragmentation and transition to granular mechanics (Chapter 2) and granular plasticity. A Continuum breakage mechanics model (CBM) [88,89] is used to simulate granular flow induced plasticity. The current implementation in the integrative model is an improvement over previous implementations by [82, 90, 134] as it combines all the mechanisms independently developed and/or improved by the aforementioned authors with a modified physics based granular transition criterion based on chapter 2 with recalibration of some model parameters.

3.2.1 Kinematics and EOS

Multiplicative split of the deformation gradient tensor ($\boldsymbol{F}$) [138] into deformation associated with micro-crack induced damage ($\boldsymbol{F}^{ed}$), amorphization ($\boldsymbol{F}^{a}$) and granular plasticity ($\boldsymbol{F}^{gp}$) is used to model the kinematics as,

$$\boldsymbol{F} = \boldsymbol{F}^{ed}\boldsymbol{F}^{gp}\boldsymbol{F}^{a}. \tag{3.1}$$

The temperature (θ), Hugoniot pressure (p_H), Grüneisen coefficient (Γ_0), reference density (ρ_0), the cold energy(e_c) and the specific heat at constant entropy (c_η) is used in the Mie Grüneisen EOS to compute the pressure of the intact solid (p_S) as

$$p_S\Big(J^{ed},\theta\Big) = p_H\Big(J^{ed}\Big)\Big[1-\frac{\Gamma_0}{2}\Big(1-J^{ed}\Big)\Big] + \rho_0\Gamma_0\Big[e_c\Big(J^{ed}\Big) + c_\eta\Big(\theta-\theta_0\Big)\Big]. \tag{3.2}$$

3.2.2 Amorphization

Amorphization is modelled as parallel bands along which sliding occurs [73]. There are three primary parts that describe the phenomenon. This includes a criterion for initiation of amorphization bands followed by sliding along these bands and damage induced due to these bands which in turn affects the transition to granular flow and the rate of crack growth due to degradation of the critical stress intensity factor. The damage induced due to amorphization

is calculated as,

$$D_a = k_a \gamma_s^{n_a} \left(\frac{d}{2}\right)^3, \tag{3.3}$$

where γ_s is the shear deformation, k_a and n_a are material parameters associated with the number density of failed bands, d is the band spacing.

It has been assumed that damage induced due to amorphization linearly degrades the fracture toughness (K_{IC}) of the material as shown in Eqn. (3.4).

$$K_{IC}{}^{eq} = K_{IC}\Big(1 - \frac{D_a}{D_c}\Big), \tag{3.4}$$

where $K_{IC}{}^{eq}$ is the equivalent effective fracture toughness and D_c is the critical failure damage.

3.2.3 Fracture and Fragmentation

The model, developed by [82], incorporates defect distribution in the material as micro-cracks and is based on classical wing-crack growth from sliding flaw models of [33, 139]. Macroscale material variability has been addressed in [82] by generating microstructural realizations of local flaw distribution. Crack interactions are modelled using an effective medium approach incorporating dynamic crack growth [55]. A non-dimensional damage parameter, D [55, 82] is used to calculate the properties of the effective medium. The damage parameter is a summation of the damage induced due to amorphization,

D_a and micro-cracking, D_m (Eqn. (3.5)).

$$D_m = \sum_{k=1}^{N_{bins}} \omega_k {s_k}^3, \tag{3.5}$$

where N_{bins} represent the number of flaw families with ω_k being the number of flaws in each flaw family having a representative flaw size s_k. The degradation of the elastic properties of the medium with growth of damage is calculated as:

$$K(D_m) = \left({K_0}^{-1} + D_m(Z_n + 4Z_c)\right)^{-1}, \tag{3.6a}$$

$$G(D_m) = \left({G_0}^{-1} + \frac{2D_m}{15}(3Z_r + 2Z_n - 4Z_c)\right)^{-1}, \tag{3.6b}$$

with $Z_r = \frac{16(1-{\nu_0}^2)}{3E_0\left(1-\frac{\nu_0}{2}\right)}$, $Z_n = \frac{16(1-{\nu_0}^2)}{3E_0}$, $Z_c = \frac{-Z_n}{8}$.
K_0, G_0, ν_0 are the bulk modulus, shear modulus and the poisson's ratio of the undamaged material.

The local compliance matrix is used to calculate the local stress state of the material. A dynamic crack growth criterion based on [140] is used to calculate the crack velocity ($\dot{l}$) as

$$\dot{l} = V_{max}\frac{K_I - K_{IC}}{K_I - 0.5K_{IC}}^{\gamma_c}, \tag{3.7}$$

where V_{max} is the maximum crack velocity, K_I is the stress intensity factor,

K_{IC} is the fracture toughness and γ_c is the crack growth exponent which is a fitting parameter. The crack velocity is then used to compute incremental crack growth and the rate of damage.

3.2.4 Transition to granular mechanics

The damage parameter serves as a switch between a damaged continuum to a granular continuum determined by the threshold damage (Ω_f). This threshold damage is computed using the transition equations proposed by chapter 2. Chapter 2 estimates the extent of fragmentation at a damage threshold using a numerical crack coalescence model. For the onset of granular mechanics, sufficient fragmentation has to occur. Based on a parametric study, empirical transition equations were proposed, that correspond to a threshold degree of fragmentation. The empirical equations suggest the transition to granular mechanics occurs when the effective wing crack length reaches a certain threshold (l_f) determined by the initial flaw size (l_i), effective initial flaw density (η) and initial flaw orientation distribution. For a fixed defect orientation, the transition wing crack length (l_{f_d}) criterion is expressed as,

$$l_{f_d} = 1.576\eta^{-1/3} - 1.095l_i. \tag{3.8}$$

Equation (3.8) can be reformulated in terms of a damage based transition criterion, where the critical damage (Ω_{f_d}) is a function of the initial damage (Ω_i) as,

$$\Omega_{f_d} = \left(1.576 - 1.095\Omega_i^{1/3}\right)^3. \tag{3.9}$$

Similarly, for a random flaw orientation distribution, the transitional criterion can be expressed in terms of a transition wing crack length (l_{f_r}) as Eqn. (3.10) or a transition damage (Ω_{f_r}) as Eqn. (3.11).

$$l_{f_r} = 1.345\eta^{-1/3} - 0.698l_i. \tag{3.10}$$

$$\Omega_{f_r} = \left(1.345 - 0.698\Omega_i^{1/3}\right)^3. \tag{3.11}$$

3.2.5 Granular Plasticity

Granular plasticity has been modelled using two approaches. A two surface Drucker Prager plasticity model which will be referred to as the TSDP model in the rest of the work, and a Continuum breakage mechanics based model which will be referred to as the CBM model henceforth.

3.2.5.1 Two surface Drucker Prager model

A pressure dependent Drucker Prager model with a hydrostatic compression cap, originally developed and implemented in an integrated ceramics model by [82] has been used to model granular plasticity. The yield surface of the Drucker Prager model (F_{TS}) is defined as,

$$F_{TS}(\boldsymbol{\tau}) = \sqrt{\boldsymbol{\tau_{dev}} : \boldsymbol{\tau_{dev}}} - Y_{TS} + A_{TS}\left(\frac{tr(\boldsymbol{\tau})}{\sqrt{3}} - B_{TS}\right), \tag{3.12}$$

where Y_{TS}, A_{TS} and B_{TS} are material parameters representing the deviatoric strength in the absence of hydrostatic pressure, the granular friction and cohesive strength respectively.

The rate of plastic deformation ($\boldsymbol{d}^{gp}$) is modelled based on assumptions of associativity,

$$\boldsymbol{d}^{gp} = \dot{\lambda}\frac{\partial f_{TS}}{\partial \boldsymbol{\tau}} = \dot{\lambda}\left(\frac{\boldsymbol{\tau}_{dev}}{\sqrt{\boldsymbol{\tau_{dev}} : \boldsymbol{\tau_{dev}}}} + \frac{A_{TS}}{\sqrt{3}}\boldsymbol{I}\right), \tag{3.13}$$

where $\dot{\lambda}$ is the flow rate.

The high pressure response is modelled using a pore crushing model. The

yield surface of the crushing curve is defined as,

$$f_{pc}(p, J^{gp}, J) = \begin{cases} \dfrac{p}{p_c - p_0} - \dfrac{p_0}{p_c - p_0} exp\left(- \dfrac{p_c - p_0}{2p_0({J_0}^{gp} - 1)}(J^{gp} - {J_0}^{gp}) \right), & p < p0 \\ (J^{gp} - 1) - ({J_0}^{gp} - 1)J^2 \left(\dfrac{p_c - p}{p_c - p_0} \right)^2, & p_0 \leq p \leq p_c \\ J^{gp} - 1, & p > p_c \end{cases} \tag{3.14}$$

where p_0 is the plastic compaction initiation pressure for a given initial distension, ${J_0}^{gp}$ and maximum densification pressure, p_c.

Rate dependence for granular flow is accomplished via a Duvaut-Lions formulation by setting a relaxation time (τ_{GP}) based on the time required for a stress wave to travel through a fragment.

3.2.5.2 Continuum breakage mechanics model (CBM)

A rate dependent constitutive model developed by [88, 89] based on breakage theory in geomechanics [91–93], and previously implemented in an integrated ceramics model in [90], is used to model the continuum deformation of granular media. Overstress theory of viscoplasticity has been used to introduce

rate dependency in the model. The yield surface is defined as,

$$f_{BM} = \left(\sqrt{\frac{E_B}{E_C}}(1-B) - \gamma_d \tau_{RP}\right)\sqrt{\frac{E_B}{E_C}}(1-B)^2 + \left(\frac{q}{(M_d + M_{BM})p}\right)^2, \tag{3.15}$$

where E_B is breakage energy and is physically related to the energy dissipation due to particle breakage, B is the breakage index which denotes how close the fragment distribution is to the ultimate distribution, τ_{RP} is the relative porosity, and p and q are the pressure and deviatoric stress, respectively. E_C, γ_d, M_d, M_{BM} are material and model parameters. E_C is the critical breakage energy density and is related to the strain energy density at the onset of comminution, γ_d is related to the behavior associated with dilation, M_d is a dilatancy parameter and M_{BM} is the friction parameter. Energy dissipation due to particle breakage, reorganization of particles and friction dissipation is accounted for in the model.

The model captures the refragmentation of the initial fragments during granular flow via the evolution of breakage (B) as

$$\dot{B} = 2\dot{\lambda}_{BM}\left\langle\sqrt{\frac{E_B}{E_C}}(1-B) - \gamma_B \tau_{RP}\right\rangle \frac{(1-B)\kappa_{BM}\tau_{RP}}{\sqrt{E_B E_C}}. \tag{3.16}$$

The evolution of porosity (ϕ) and plastic strain (ε^p)are given by

$$\dot{\phi} = 2\dot{\lambda}_{BM}\left(\sqrt{\frac{E_B}{E_C}}(1-B) - \gamma_d\tau_{RP}\right)\sqrt{\frac{E_B}{E_C}}\frac{(1-B)(1-\tau_{RP}H(F_{BM}))}{E_\phi}, \tag{3.17}$$

$$\dot{\boldsymbol{\varepsilon}}^p = \left(\frac{\dot{\phi}}{1-\phi}\frac{1}{3}\boldsymbol{I} + \dot{\lambda}_{BM}\frac{3\boldsymbol{\sigma} - tr(\boldsymbol{\sigma})\boldsymbol{I}}{\Big((M_d + M_{BM})p\Big)^2}\right), \tag{3.18}$$

where $\dot{\lambda}_{BM}$ is a non negative multiplier defined by Eqn. (3.19) where N_{BM} is the strain rate sensitivity coefficient and η_{BM} is the viscosity parameter. γ_B and κ_{BM} are material parameters that control the initiation and evolution of breakage. $H(F_{BM})$ is the Heaviside step function of F_{BM} defined in Eqn. (3.20). $H(F_{BM}) = 1$ if $F_{BM} \geq 0$, otherwise $H(F_{BM}) = 0$.

$$\dot{\lambda}_{BM} = \frac{\Big\langle f_{BM}\Big\rangle^{N_{BM}}}{\eta_{BM}}, \tag{3.19}$$

$$F_{BM} = \left(\sqrt{\frac{E_B}{E_C}}(1-B) - \gamma_d\tau_{RP}\right). \tag{3.20}$$

The constitutive relationship is defined by,

$$\dot{\boldsymbol{\sigma}} = (1-\vartheta_{BM}B)\boldsymbol{D} : (\dot{\boldsymbol{\varepsilon}} - \dot{\boldsymbol{\varepsilon}}^p) - \vartheta_{BM}\frac{\boldsymbol{\sigma}}{(1-\vartheta_{BM}B)}\dot{B}, \tag{3.21}$$

where $\boldsymbol{D}$ is the stiffness and ϑ_{BM} is the grading index. ϑ_{BM} denotes how far the

initial distribution ($\left\langle d \right\rangle_0$) is from the ultimate fragment size distribution($\left\langle d \right\rangle_u$). It is calculated from the ratio of the second moments of the initial and final fragment size distributions as,

$$\vartheta_{BM} = 1 - \frac{\left\langle d^2 \right\rangle_u}{\left\langle d^2 \right\rangle_0}. \tag{3.22}$$

3.3 Numerical Simulations - Integrative Model

3.3.1 Calibration of model parameters

Calibration of mechanical, equation of state, microstructural, micromechanical, amorphization and granular flow parameters follow [90, 134]. Critical transition damage for initiation of granular mechanics [82, 90, 134] is newly recalibrated in this chapter as per chapter 2. Critical breakage energy density (E_C) in [89] is recalibrated using [143]. Grading index (ϑ) is re-estimated and some of the arguments of fragment size evolution for granular media in [89] are revisited in the context of a low porosity fragmenting ceramic. These updated calibrations are discussed in the sections that follow. A summary of the calibrated integrative model parameters is presented in Tab. 3.1.

Table 3.1. List of boron carbide material parameters for the integrative model.

Mechanical properties	Density (ρ_0)	2520 kg/m^3	[141]
	Shear modulus (K_0)	197 GPa	[55]
	Bulk modulus (G_0)	232 GPa	[142]
EOS parameters	Bulk sound speed (C_0)	9.6 km/s	[134]
	Us-Up slope (S)	0.91	
	Specific heat capacity (C_V)	962 $J/(kgK)$	[142]
	Gruneisen parameter (Γ_0)	1.28	
Microstructural parameters	Flaw density (η)	22e12 $cracks/m^3$	Calculated at JHU
	Minimum half flaw size (s_{min})	1μ	
	Maximum half flaw size (s_{max})	25μ	
	Flaw distribution exponent (α_{flaw})	2.6	
	Flaw orientation (θ_{flaw})	60°	Most damaging flaws
Micromechanical parameters	Fracture toughness (K_{IC})	2.5 $MPa\sqrt{m}$	[55]
	Rayleigh wave speed (C_R)	7.99 km/s	Calculated at JHU
	Flaw friction coefficient (μ_{flaw})	0.8	[108]
Amorphization parameters	Initial threshold (P_{a0})	50 GPa	[134]
	Shear enhancement coefficient (α_a)	7.63	
	Density change (η_a)	0.05	
	Reference amorphization rate ($\dot{\xi}_c$)	1.0	
	Rate sensitivity coefficient (m)	200	
	Completion stress (F_{ac})	200 GPa	
	Amorphous phase viscosity (μ_{band})	1 $kPa.s$	
	Initial shear resistance (τ_0)	7 GPa	
	Critical failure strain (γ_f)	0.3	
	Failed-band density parameter 1 (k_a)	1e23 m^{-3}	
	Failed-band density parameter 2 (η_a)	1	
	Energy dissipation rate per band (G_c)	100 J/m^2	
Granular transition	Transition damage (Ω_f)	3.5 (Fixed orientation) 2.9 (Random orientation)	Calculated (Chapter 2)
Granular parameters (TSDP)	Frictional slope (A_{TS})	0.72	[82]
	Purely deviatioric strength (Y_{TS})	0	
	Cohesive strength (B_{TS})	3 MPa	
	Reference crush pressure (p_0)	100 MPa	
	Reference distension (${J_0}^{GP}$)	2	
	Consolidation pressure (p_c)	10 GPa	
	Relaxation time (τ^{GP})	7e-9 s	
Granular parameters (CBM)	Critical breakage energy density (E_C)	1.15 MPa	Calculated
	Grading index (ϑ_{BM})	0.95	
	Crushability parameter (κ_{BM})	0.055	
	Friction parameter (M_{BM})	1.522	
	Particle breakage initiation parameter (γ_B)	0.63	
	Dilative behavior parameter (γ_d)	0.865	
	Strain rate sensitivity coefficient (N_{BM})	7.5	[90]
	Viscosity (η_{BM})	2e-13 ($Pa^{-1}.s$)	
	Minimum porosity w/o breakage (ϕ_l)	0.01	
	Maximum porosity w/o breakage (ϕ_u)	0.442	
	Porosity control parameter 1 (u)	0.12	
	Porosity control parameter 2 (l)	0.16	

3.3.1.1 Calibration of transition damage

Damage parameter is a summation of damage due to wing crack growth (Eqn. (3.5)) and amorphization induced damage. When the damage exceeds

the threshold set in chapter 2, granular physics is activated in the model. The constant critical threshold damage used in [82, 90, 134] is able to capture some structural fragmentation (macroscale fragments), but does not capture microscale fragments sufficiently, at or smaller than the resolution of integrative model simulations. This does not properly represent the initiation of granular mechanics in the Mescall region as explained in chapter 2. The current model uses the threshold defined in chapter 2. Flaw sizes are assumed to follow a Pareto distribution with the minimum half flaw size (s_{min}), maximum half flaw size (s_{max}) and the distribution exponent (α_{flaw}) defining the distribution. The mean squared average of initial flaw size can be expressed as

$$l_i = s_{min}\sqrt{\left(\frac{\alpha_{flaw}}{\alpha_{flaw}-2}\right)\left(\frac{1-\left(\frac{s_{min}}{s_{max}}\right)^{\alpha_{flaw}-2}}{1-\left(\frac{s_{min}}{s_{max}}\right)^{\alpha_{flaw}}}\right)}. \tag{3.23}$$

From the transitional criteria (Eqn. (3.9) and (3.11)), the transitional wing crack damage for fixed defect orientation distribution (Ω_{f_d}) and random defect orientation distribution (Ω_{f_r}) is estimated. For the chosen material properties (Tab. 3.1), Ω_{f_d}=3.5 and Ω_{f_r}=2.9 .

3.3.1.2 Calibration of critical breakage energy density

[143] explores the particle size effect in the behavior of granular boron carbide under quasi-static compression. The evolution of porosity, bulk modulus

with changing hydrostatic pressure is used to compute the critical breakage energy density, E_C [89, 93]. Equation (5.7) in [93] is used to compute the critical brekage energy density. The grading index (ϑ_{BM}) is calculated from the initial and final fragment size distribution for granular boron carbide from [143]. The pressure beyond which the bulk modulus of granular boron carbide starts increasing can be thought of as the critical comminution pressure, p_{CR} (Eqn. (5.7) of [93]) at which the breakage of fragments initiates. The grading index, critical comminution pressure and the corresponding bulk modulus (K_g) is used to calculate the value of E_C. The results of the calculation are listed in Tab. 3.2. In general, it can be expected that the strength of an individual fragment might decrease with increase in fragment size due to higher statistical probability of defects. However, the critical breakage energy density in a granular media might have a more complicated response than what can be explained by simple Weibull size scaling. This might arise for two reasons. The coordination number of particles varies with the size and shape distribution of particles and the volume fraction of the granular media. This has an influence on the average stress a particle experiences. On the other hand, although larger particles are more prone to failure due to the presence of more defects, the interaction gets more complicated when the defects are comparable to the particle size. This, in addition to other uncertainties, might help account for the initial increase in E_C (from particle size 170μm to 190μm in Tab. 3.2) with

increase in particle size followed by a general decreasing trend with increasing particle size (from particle size 190μm to 470μm in Tab. 3.2). In this study, given the uncertainties, an average value of 1.15 MPa has been used for E_C. The sensitivity of the output to this parameter will be evaluated in chapter 4.

Table 3.2. Calculation of critical breakage energy density (E_C).

Size (in μm)	Sample#	Critical comminution pressure, p_{CR} (in MPa)	Bulk Modulus, K_g (in MPa)	Grading Index, ϑ_{BM}	Critical Breakage Energy Density, E_C in (MPa)	$E_{C_{avg}}$ in (MPa)
170	1	17.83	115.22	0.97	1.34	1.11
	2	15.24	90.05		1.25	
	3	11.89	93.48		0.73	
190	1	18.03	145.81	0.97	1.09	1.51
	2	20.07	170.29		1.15	
	3	31.58	212.84		2.28	
320	1	34.37	325.61	0.99	1.80	1.37
	2	35.16	305.44		2.01	
	3	13.42	289.02		0.31	
470	1	14.72	171.20	1.00	0.63	0.63
Average E_C (in MPa)						1.15

3.3.1.3 Calibration of grading index

Grading index is a metric related to the evolution of fragment size distribution that signifies the proximity of the initial fragment size distribution to the final or critical distribution [89, 91–93]. It is calculated using Eqn. (3.22). For most granular media it has been observed in simulations and experiments that the largest grains do not undergo fragmentation as they are surrounded by many smaller grains leading to a more hydrostatic state of stress often referred to a "cushioning effect" [144, 145]. Therefore, it is assumed in breakage mechanics models that while the smallest grains fragment, the largest ones

often remain intact. This is contrary to the expectation of larger fragments being weaker due to statistical size effect [146]. In reality the interplay between size effect due to the number of defects and coordination number, both of which can be expected to have opposite effects on the probability of fracture with size, control the evolution of grain fragmentation until a steady state is reached. In case of extremely low porosity systems like the comminuted zone in ceramics, all fragments (or grains) are expected to be sufficiently supported. Hence, the effect of coordination number, should not play a role initially, and statistical size effect should dominate the failure response. For such systems, the assumption of the largest fragments (grains) not re-fragmenting might not hold true. Most experiments for granular media are not meant for such low porosity high pressure systems. Under high pressure dynamic loading conditions, this can lead to a very high grading index if there is significant fragmentation of the largest grain. For this work a grading index value of 0.95 has been selected. This is close to the values calculated from [143] in Tab. 3.2. As with all the parameters, the sensitivity of model outputs to grading index will be evaluated in chapter 4.

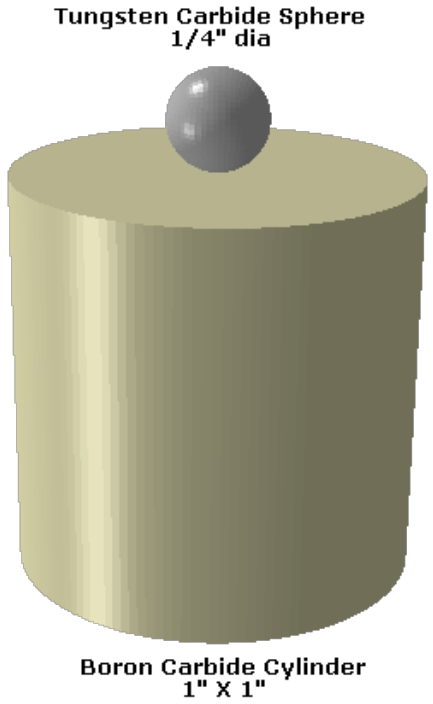

Fig. 3.1. Geometry of Sphere Indentation Simulations.

Table 3.3. Material parameters of tungsten carbide spherical indenter.

Physical properties				**EOS** [147]	
Elastic Modulus (GPa)	Density (kg/m^3)	Poisson's Ratio	C_0 (m/s)	S	Γ_0
255	14300	0.32	5180	1.309	1.2

Johnson-Cook Model [148]						
A (MPa)	B (MPa)	n	C	m	T_m (K)	T_{trans} (K)
3000	89000	0.65	0.000	1	1495	25

3.3.2 Simulation of Sphere Indentation Experiments

Sphere indentation experiments of boron carbide were simulated in ABAQUS. The details of the experimental technique can be found in [20]. The geometry

consists of a 1/4" diameter tungsten carbide sphere impacting a boron carbide cylinder, 1" diameter and 1" height (Fig. 3.1). Reduced integration 8-noded brick elements (C3D8R) were used to model both the tungsten carbide sphere and the boron carbide cylinder. Similar to [90], the cylinder was discretized using a mesh size of approximately 0.55 mm, with 99682 elements. A kinematic contact algorithm for frictionless surfaces was used. The integrated ceramics model was used for the boron carbide cylinder, with properties as listed in Tab. 3.1. The tungsten carbide sphere was modelled using the Johnson Cook material model parameters determined by [148]. The equation of state values from [147] were used (see Tab. 3.3). The simulations were conducted for ten different cases of 100 to 1000 m/s impact velocity with the CBM model. The results from the CBM model are compared against the TSDP for the 500 m/s impact velocity case.

3.3.3 Simulation of Edge On Impact Experiments

Table 3.4. Material parameters of steel projectile.

Physical properties						
Elastic Modulus (GPa)		Density (kg/m^3)		Poisson's Ratio		
202		7850		0.32		
Johnson-Cook Model [149]						
A (MPa)	B (MPa)	n	C	m	$T_m\ (K)$	$T_{trans}\ (K)$
2700	211	0.065	0.005	1.17	1800	293

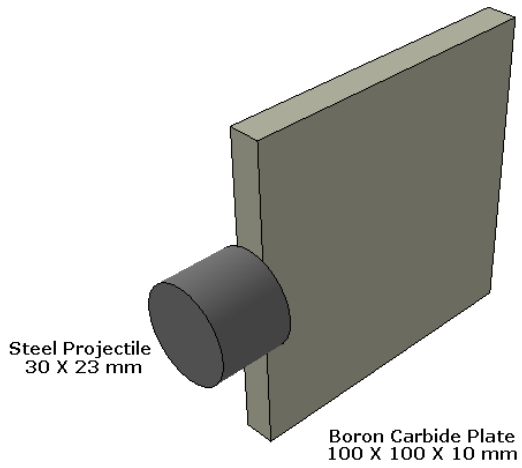

Fig. 3.2. Geometry of Edge On Impact Simulations.

Edge-On Impact experiments were performed by Strassburger on boron carbide and other ceramics. The experimental technique was developed in EMI, and the details of the experiments can be found in [135–137]. The simulation geometry consists of a steel projectile 30 mm in diameter and 23 mm in height impacting a 100 mm square and 10 mm thick boron carbide plate along the edge (Fig. 3.2). Reduced integration 8-noded brick elements were used in ABAQUS for both the plate and the projectile. A kinematic contact algorithm for frictionless surfaces was used. Johnson Cook model calibration for hardened steel [149] was used for the steel projectile (see Tab. 3.4). The integrated ceramics model was used for modelling the boron carbide plate. K_{IC} and ρ_0 were modified in this model to $2.9MPa\sqrt{m}$ and $2530kg/m^3$, respectively, to be consistent with the values reported in [137]. All the other parameters have been set to the same values as Tab. 3.1. The simulations were run until $7.5\mu s$

after impact for 8 different impact velocities from 50 to 1010 m/s using the CBM model and compared against the TSDP model for an impact velocity of 742 m/s.

3.4 Results - Integrative Model

3.4.1 Sphere Indentation Simulations

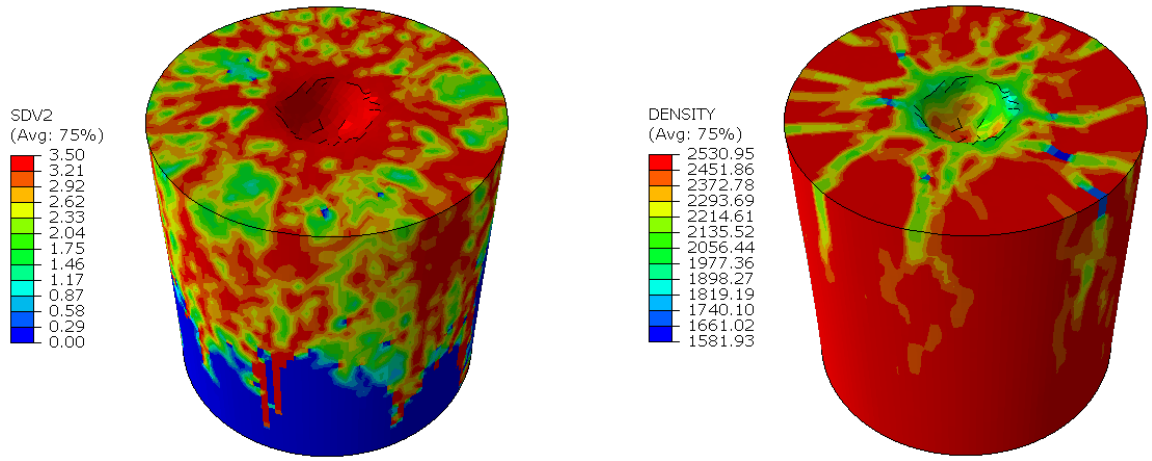

(a) Damage contour **(b)** Density contour

Fig. 3.3. Damage and density contours of Sphere Indentation simulation at 500 m/s impact velocity, 15μs after impact (CBM Model).

Typical features observed in Sphere Indentation experiments are a comminuted zone under the impactor with visible radial cracking on the surface. Immediately under the comminuted zone, cone cracks are also observed. In our simulations damage (Fig. 3.3a) and density (Fig. 3.3b) localizations are

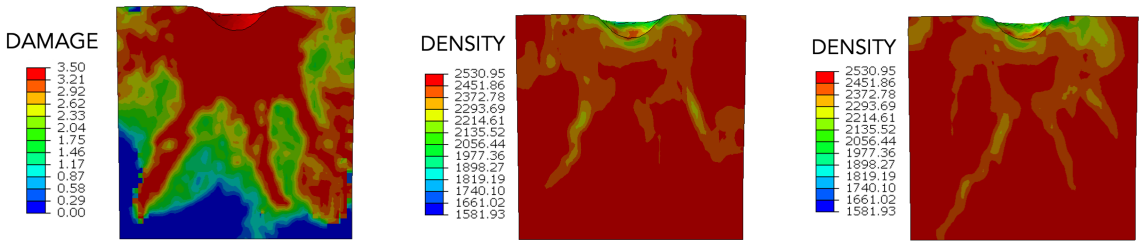

(a) Damage contour **(b)** Density contour (Plane 1) **(c)** Density contour (Plane 2)

Fig. 3.4. Damage and density contours of Sphere Indentation simulation for the cylinder section at 600 m/s impact velocity, 15μs after impact (CBM Model).

observed that are presumed to be related to larger scale radial cracks. Figure 3.4a shows the damage contour along a section of the ceramic cylinder $15\mu s$ after a spherical indenter impacts at 600 m/s. Figures 3.4b,3.4c shows the corresponding density contour along two orthogonal planes. High damage and low density regions under the indenter signify the presence of comminuted zone. In addition to that, we observe slanted damage and density localizations that have the appearance of cone cracks. Figures 3.4b,3.4c demonstrate that the slanted low density regions are repeatable across different orthogonal planes. This confirms that these low density regions are 3D cone crack like features, not simply an artifact of one particular cross-section. Some of the other features observed in experiments like crack branching and lateral cracking are observed at certain impact velocities but they are not repeated across all scenarios.

Figure 3.5 shows a comparison of the damage contour for the CBM model (Fig. 3.5a) and the TSDP model (Fig. 3.5b) for granular flow at 500 m/s impact

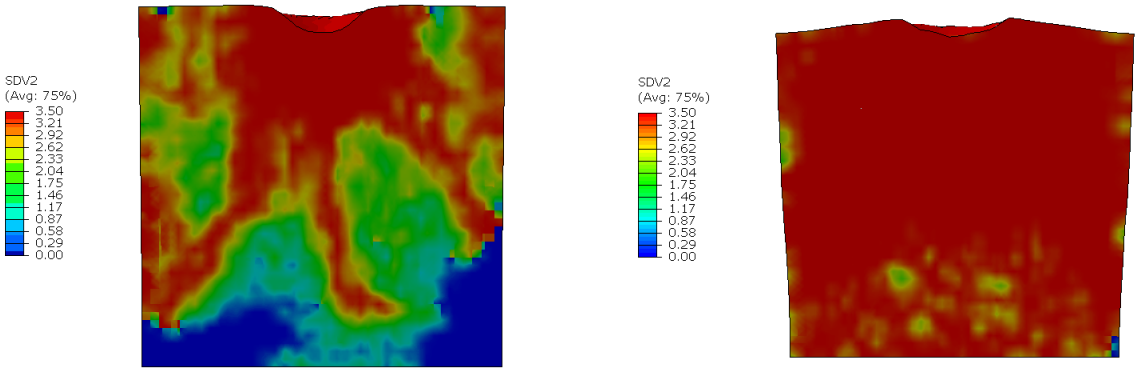

(a) CBM Model **(b)** TSDP Model

Fig. 3.5. Comparison of damage contour of Sphere Indentation simulations for the cylinder section for CBM and TSDP models at 500 m/s impact velocity, 15μs after impact.

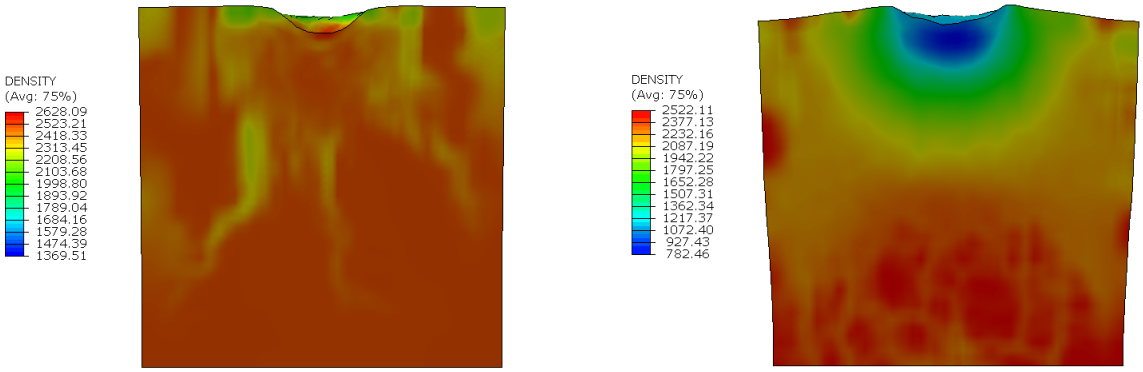

(a) CBM Model **(b)** TSDP Model

Fig. 3.6. Comparison of density contour of Sphere Indentation simulations for the cylinder section for CBM and TSDP models at 500 m/s impact velocity, 15μs after impact.

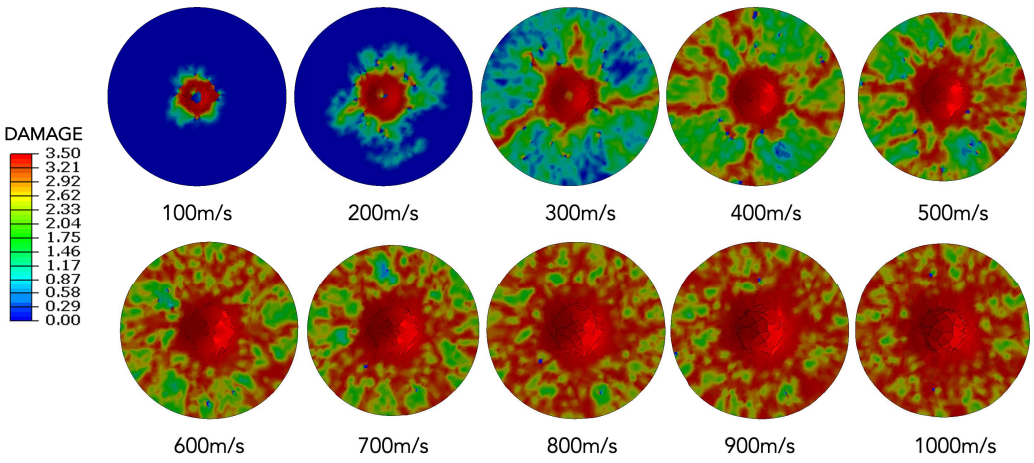

Fig. 3.7. Damage contour of Sphere Indentation simulations showing radial cracking with impact velocity, $15\mu s$ after impact (CBM Model).

velocity, $15\mu s$ after impact. Damage is more distributed for the TSDP model and distinguishable damage localized features don't exist. Figure3.6 shows a similar comparison for the density contour. Density localization into cone crack like features is more distinct in the CBM model (Fig. 3.6a). However the TSDP model (Fig. 3.6b) does exhibit some distributed low density bands along cone crack like planes. The TSDP model has a larger and better defined comminuted zone than the CBM model. Also, there is more dilation due to granular flow in the comminuted zone of the TSDP model.

Figure 3.7 shows the damage contour at the top of the cylinder, $15\mu s$ after impact at different velocities. Figure 3.8 shows the corresponding density contour. Density contour shows more radial crack-like localization than the corresponding damage contour. In either case, the number of radial crack like features increase with increase in impact velocity. However, determining the

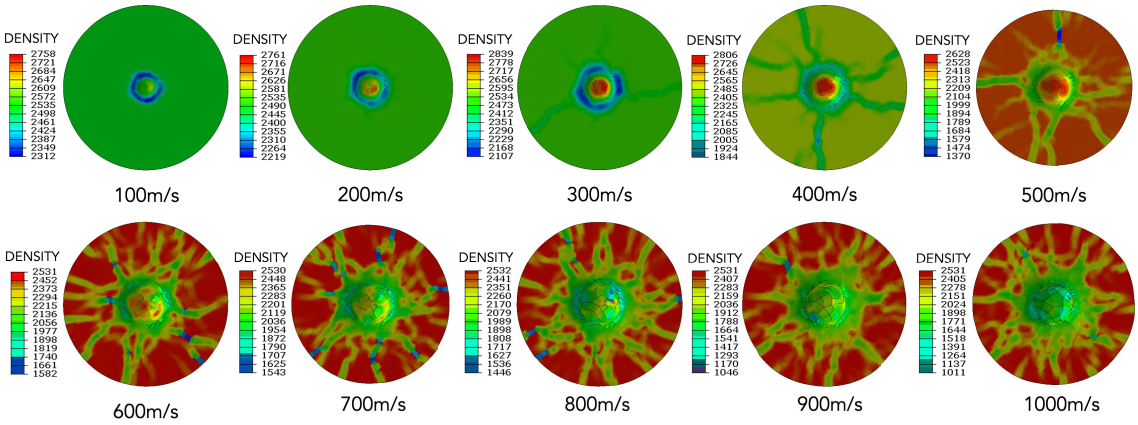

Fig. 3.8. Density contour of Sphere Indentation simulations showing radial cracking with impact velocity, $15\mu s$ after impact (CBM Model).

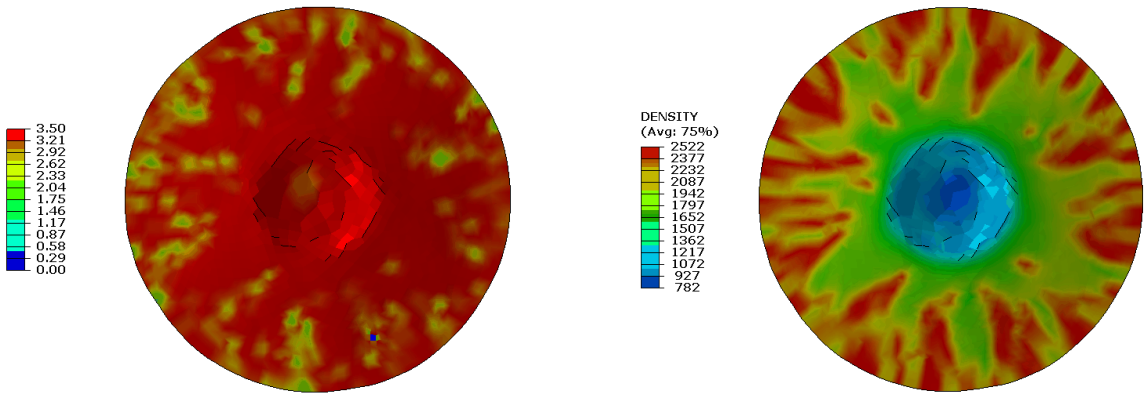

(a) Damage Contour **(b)** Density Contour

Fig. 3.9. Damage and density contour of Sphere Indentation simulation showing radial cracking at 500 m/s impact velocity, $15\mu s$ after impact (TSDP Model).

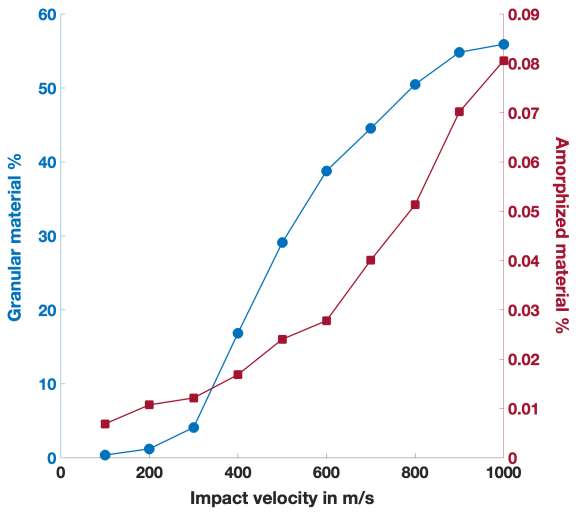

Fig. 3.10. Granular material percentage and amorphized material percentage for Sphere Indentation simulations with impact velocity, 15 μs after impact (CBM Model).

number of radial cracks is a subjective assessment. The number of observed radial cracks is however slightly less than the number of radial cracks observed in [20] for boron carbide. Radial cracks were not quantified in [19, 150]. Figure3.9 shows the damage and density contours at the top of the cylinder for the TSDP model. Once again, density is much better localized than damage in the TSDP model. Also, there is significantly more radial cracking than the CBM model.

Figure 3.10 shows that both the percentage of material that is granular and the percentage of material that is amorphized, $15\mu s$ after impact, increases with increase in impact velocity. The percentage of material that undergoes amorphization is, however, insignificant even at an impact velocity of 1000 m/s (less than 0.1%). Figure 3.11 shows that the maximum depth of penetra-

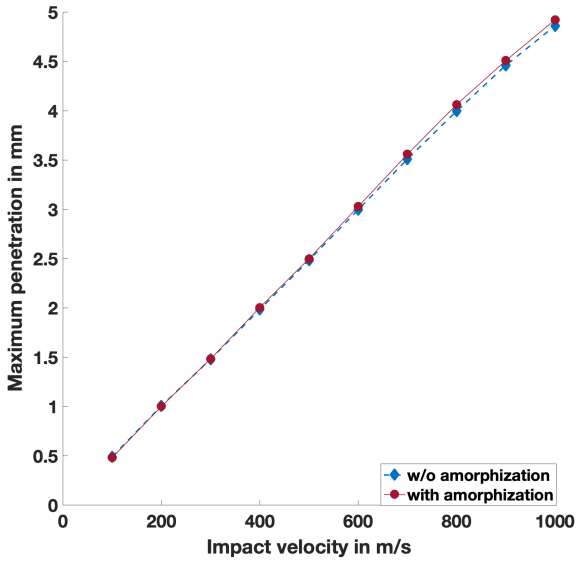

Fig. 3.11. Maximum depth of penetration of the indenter for Sphere Indentation simulations with impact velocity (CBM Model).

tion of the indenter almost linearly increases with increase in impact velocity. Amorphization does not seem to affect the depth of penetration of the indenter significantly for the impact velocity range studied here. [134] argues that significant amorphization is not observed in sphere indentation experiments until an impact velocity of around 2 km/s. We can expect the effect of amorphization to be more pronounced at higher impact velocities or for different shapes of indenter.

3.4.2 Edge On Impact Simulations

Figure 3.12 shows the evolution of the surface damage contour with time for 1010 m/s impact velocity in edge on impact simulation. The damaged re-

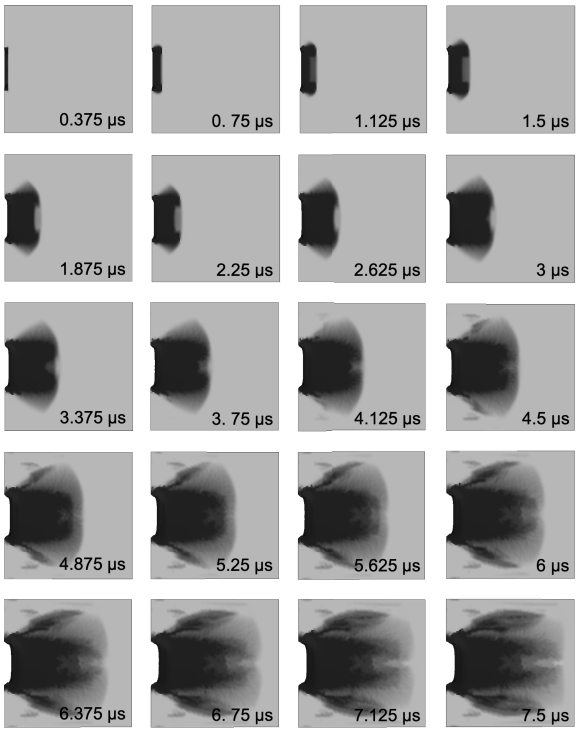

Fig. 3.12. Damage contour of Edge On Impact simulation at an impact velocity of 1010 m/s (CBM Model).

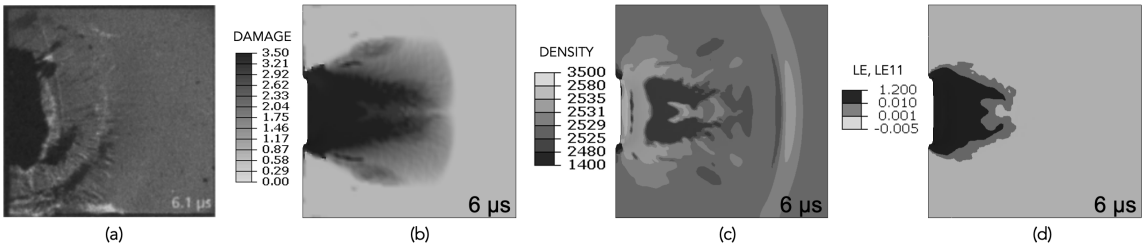

Fig. 3.13. Comparison of damage pattern from [137] with Edge On Impact simulation (CBM Model) for 469 m/s impact velocity. (a) experimental damage pattern at 6.1 μs (b) numerical damage pattern at 6 μs (c) numerical density pattern at 6 μs (d) numerical out of plane strain pattern at 6 μs.

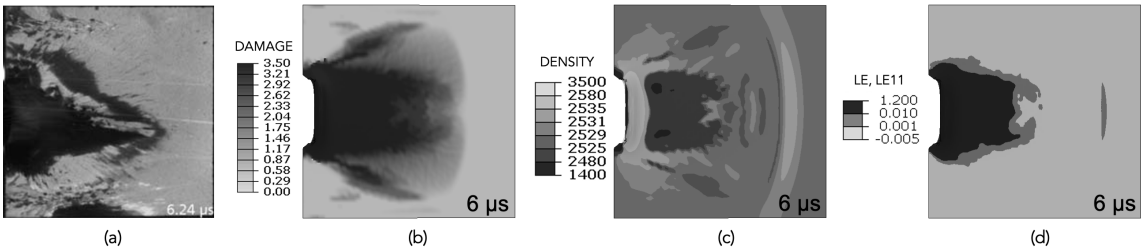

Fig. 3.14. Comparison of damage pattern from [135] with Edge On Impact simulation (CBM Model) for 1010 m/s impact velocity. (a) experimental damage pattern at 6.1 μs (b) numerical damage pattern at 6 μs (c) numerical density pattern at 6 μs (d) numerical out of plane strain pattern at 6 μs.

gion around the indenter grows with time. Around 2.625μs after impact, damage starts localizing into cone crack like features, which mostly become visible around 4μs. There is a distributed damaged region with a darker or more fragmented granular region inside.

Figures 3.13,3.14 show a comparison of the experiments performed by Strassburger [135–137] at two different impact velocities of 469 m/s and 1010 m/s. The experimental image (Fig. 3.13a, Fig. 3.14a) is based on the intensity of light reflected from the surface of the ceramic plate viewed via a high speed

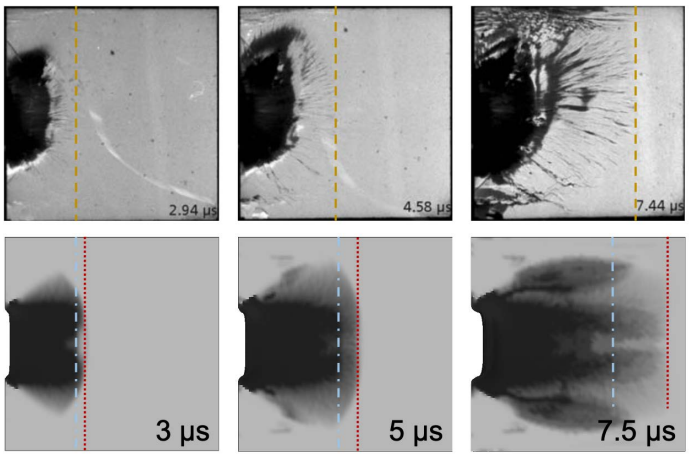

Fig. 3.15. Comparison of damage pattern from [135] (top row) with Edge On Impact simulation (bottom row) for 823 m/s impact velocity (CBM Model). The experimental damage front, numerical damage front and numerical granular front are highlighted in yellow (dashed), red (dotted) and blue (dashed-dotted) respectively.

camera. It is not clear exactly which model output would best represent the changes in intensity of reflected light. The intuitive options are damage, density and out of plane displacement at the surface. Figures 3.13b and 3.14b show the damage pattern for 469 m/s and 1010 m/s impact velocity, respectively. The predicted damage pattern differs slightly in the two cases, and there is a longer cone crack like damage localized feature observed for 1010 m/s impact, along with a wider fragmented or granular region. In this chapter the numerical damage front represents the boundary capturing $\Omega \geq 0$, and the numerical granular front or the edge of the granular region represents the boundary capturing $\Omega \geq \Omega_f$. The numerical granular front in Fig. 3.13b seems to be around the same location as the experimental damage front in Fig. 3.13a. However, in Fig. 3.14b, the numerical damage front seems to be in the same location

as the experimental damage front in Fig. 3.14a. In both Fig. 3.13c and Fig. 3.14c, the density pattern has been adjusted to show even the slightest amount of dilation. The density pattern in either figures mimic the corresponding numerical damage pattern. Predictions of out of plane strain (Fig. 3.13d and Fig. 3.14d) show a marked difference between the two impact velocities. The region experiencing higher out of plane strain grows with increasing impact velocity. However, it is still not clear if out of plane strain best correlates with the change in light intensity observed in experiments.

Figure 3.15 shows a comparison of the numerical damage contour (bottom row) with the experiemental image [135] (top row) at three different time instants. It appears as though the numerical damage front (red dotted line) always exceeds the experimental damage front (yellow dashed line), while the numerical granular front (blue dashed-dotted line) is at or behind the experimental damage front.

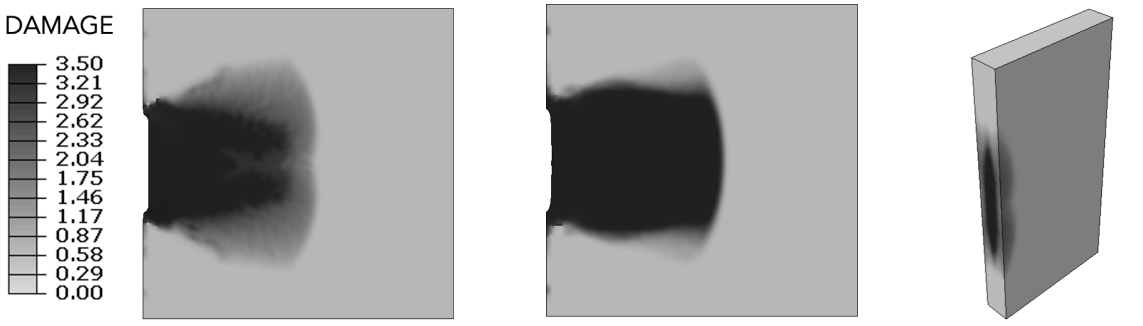

(a) Surface Damage **(b)** Sectional Damage **(c)** Mid-plate Damage

Fig. 3.16. Variation of damage contour of Edge On Impact simulation (CBM Model), 4.5μs after impact at (a) Surface , (b) Section, (c) Mid-plate.

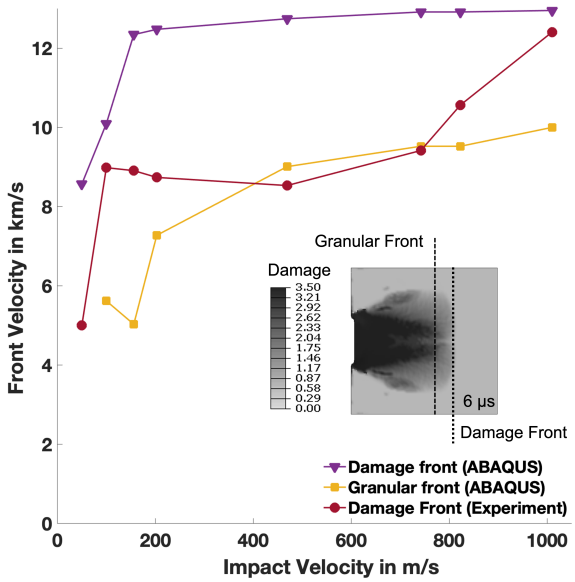

Fig. 3.17. Comparison of experimental damage front velocity with Edge On Impact simulation (CBM Model) damage and granular front velocity at different impact velocities. Inset image shows the granular and damage front from ABAQUS simulation for 469 m/s impact velocity, 6μs after impact.

Another interesting feature is that the velocity of the damage front in the middle of the plate always exceeds the velocity of the damage front at the surface of the plate (Fig. 3.16). For an impact velocity of 469 m/s, $4.5\mu s$ after impact, the distance to which granular and damage front at the middle section of the plate (Fig. 3.16b) has progressed exceeds the granular and damage front at the surface of the plate (Fig. 3.16a). Also mid-section damage, orthogonal to the plane of the plate, shows much higher damage at the middle than the surface (Fig. 3.16c).

The numerical damage front velocity and granular front velocity has been calculated and compared against the experimentally reported damage front velocity in Fig. 3.17. In the experiments, the damage front velocity initially rises

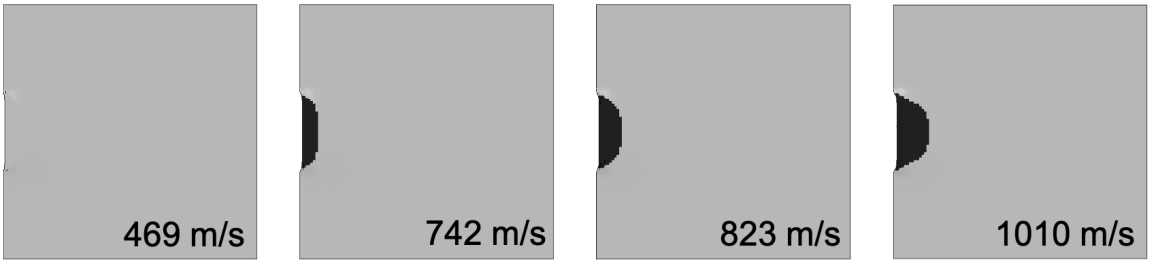

Fig. 3.18. Surface contour of Edge On Impact simulations (CBM Model) showing amorphized region with different impact velocities.

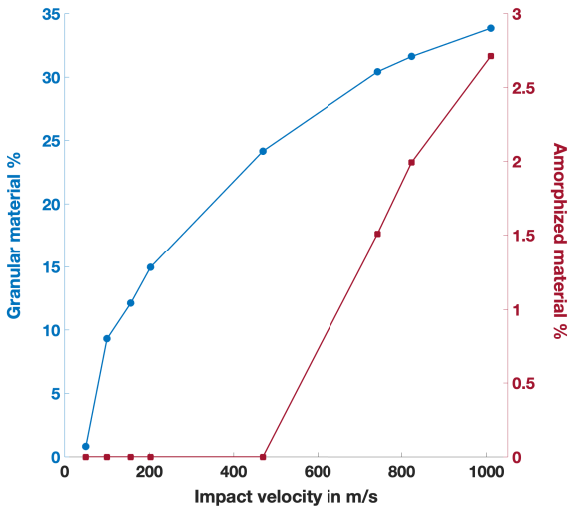

Fig. 3.19. Granular material percentage and amorphized material percentage for Edge On Impact simulation (CBM Model) with impact velocity, 7.5μs after impact.

sharply as a function of impact velocity and then plateaus until an impact velocity of around 469 m/s. Beyond this impact velocity, the damage front velocity gradually rises and reaches to around 12 km/s at an impact velocity of 1010 m/s. However, in the simulations, both the numerical damage front velocity and the granular front velocity sharply increase initially, followed by a more gradual increase with further increase in impact velocity. The experimental damage front velocity appears somewhat bounded between the granular and numerical damage front velocities, 6 μs after impact. This is not necessarily true at an early stage when the numerical damage front and granular front almost coincide. The inset image in Fig. 3.17 shows the numerical granular and damage fronts. Although the simulations do not capture the sudden rise in damage front velocity beyond 469 m/s impact velocity, they feature onset of amorphization around 742 m/s impact velocity, with the volume of amorphized region gradually increasing with further increase in impact velocity (see Fig. 3.18). Figure 3.19 shows a comparison of the growth in granular material percentage v/s amorphized material percentage, $7.5\mu s$ after impact with change in impact velocity. Despite the coincidence of the onset and increase in amorphization with the sudden rise in damage front velocity reported in experiments, it is not clear as to how amorphization can induce a sudden change in the damage front velocity. [73] does not account for new crack nucleation as a consequence of amorphization, but it is not obvious if that would lead to a rise

in front velocity. Another possible explanation of the experimentally observed rise in damage front velocity, beyond 469 m/s impact velocity, could be some sort of phase transformation that changes material properties. The current integrative model does not capture such phase transformation. To summarize, experimentally observed damage pattern in Edge On Impact experiments is correlated with the growth of cracks, change in density and out of plane displacements observed in simulations using the integrative model. Typical features like cone cracks, a distributed crack front and even secondary crack zones (for low impact velocity) observed in experiments [136] can be reproduced in the simulations. However, unlike the simulations, in the experiments for boron carbide, these patterns are not always symmetric and consistently discernible. The numerical damage front in most cases exceeds the experimental damage front, except 1010 m/s impact velocity. The change in experimental damage front velocity with impact velocity is not accurately captured by the numerical damage front.

Figure 3.20 shows a comparison of the damage contour observed at 742 m/s impact velocity, $7.5\mu s$ after impact, between the CBM model (Fig. 3.20a) with the TSDP model (Fig. 3.20b). In either cases the damage localization and the various features associated with it does not seem to significantly differ.

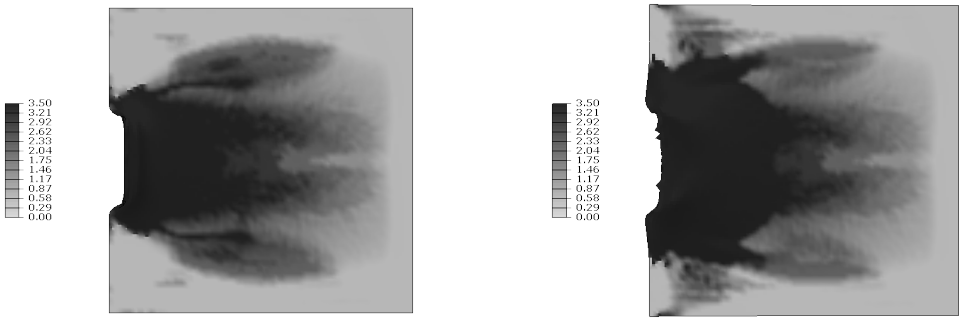

(a) CBM Model **(b)** TSDP Model

Fig. 3.20. Comparison of damage contour of Edge On Impact simulation for (a) CBM and (b) TSDP models at 742 m/s impact velocity, 7.5μs after impact.

3.5 Summary

A ceramics model that integrates multiple physical mechanisms has been recalibrated and used to simulate sphere indentation and edge on impact experiments in ABAQUS using boron carbide as a model material. The results from two different granular mechanics models have been compared. The simulations are able to replicate key cracking patterns observed in experiments through damage and density localizations.

Chapter 4

Sensitivity analysis

4.1 Introduction

Ballistic performance of boron carbide can be improved by modifying the mechanical properties via doping and grain boundary engineering. Reducing defect population by controlling the free carbon content and densification techniques [151] can help improve hardness. Significant research towards enhancing fracture toughness, strength and/or modulus through different sintering aids [152–159] has been conducted. Amorphization mitigation via silicon doping [64, 65] and boron enrichment [66, 67] has also been explored. However, performance enhancement via controlling granular flow through material modifications is not well understood, and the focus is driven on characterization of granular flow [160]. In addition to this plethora of research serving as a guide

for material modifications, ranking the properties with the most pronounced influence over ballistic performance is desirable.

The integrative model currently has a huge parameter space with significant uncertainty around most of the parameters. While many of these parameters are flags to control the onset or suppression of mechanisms, a significant number of these are model parameters which are directly or indirectly related to physical properties. As a result, there is a significant challenge in designing new materials due to several reasons. Firstly, the influence of model parameters and related material properties on model predictions is not well understood. Secondly, the design of new materials by modifying individual properties poses a fiscal challenge. Performing a set of experiments to calibrate multiple iterations of a material is expensive and laborious. A work-around that addresses both these issues is to understand the sensitivities of model predictions to model parameters. This will not only help us in understanding the trends that guide us towards improving material performance, but also in the selection of the most significant model parameters.

In this study, the integrated model has been used to assess the sensitivity of material behavior to selected model parameters for sphere indentation simulations. Broadly, there are two types of sensitivity analysis methods in the existing literature [161]: local and global. Some of the popular local methods include the one-at-a-time (OAT) method and the derivative-based methods.

OAT method [162–164] involves studying the effect of the output by locally perturbing one input variable at a time while keeping the other variables at their baseline values. Local derivative-based methods [165–167] involve estimating the partial derivative of the output with respect to an input variable by small perturbations of that variable around a fixed point in the input space. The partial derivatives act as natural sensitivity measures. Although fast and transparent, the main drawback of local methods is that they do not thoroughly explore the entire input space. The global sensitivity methods try to alleviate this problem and also try to study the effect of large changes in the input variables. Among the global sensitivity analysis method, variance based methods [162, 168, 169] and linear regression analysis [170, 171] have been most extensively used. Variance based methods are based on a decomposition of the variance of the output into terms corresponding to the different input variables as well as their interactions. The sensitivity measure of the output for a particular input variable is the amount of variance in the output attributable to that input variable. Since variance-based methods allow examination of sensitivites across the whole input space, they often make use of emulators/surrogates [172–175] to reduce the computational expense of too many model runs. Linear regression involves fitting of the input-output data assuming that the output is linearly related to the data. The standardized regression coefficients obtained from the regression fit can then be used as measures of

parameter sensitivity.

In this work, sensitivity analysis is performed based on linear regression fit to the ceramics model data to study the importance of parameters with respect to the selected quantities of interest. The most sensitive parameters have been identified, and their trends have been introspectively speculated and compared against simulation results. Finally, suggestions have been made towards material processing modifications and prioritization of calibration experiments and/or more in-depth modelling to support specific parameters. The following subsections will describe the setup, results and conclusions from a sensitivity analysis study of sphere indentation simulations in boron carbide. This is a collaborative work with Dr. Anindya Bhaduri conducted the sensitivity analysis on ABAQUS simulations run by me. I explored the connections to physical mechanisms and the corresponding design implications.

4.2 Problem setup - Sensitivity Analysis

[176] performed sensitivity analysis on ballistic impact of silicon carbide (SiC) ceramic plate with poly-ether-ether-ketone (PEEK) layer and selected peak normal contact force, plastic dissipation in ceramic and PEEK, transmitted impulse to the ceramic back face as output quantities of interest (QoIs).

Penetration state function defined using the residual bullet velocity and the depth of penetration is used as a QoI in ballistic impact of SiC/ultra high molecular weight polyethylene composite plate in [177]. Similarly crater size, number of radial cracks, ejecta velocity are useful QoIs for further studies of ballistic performance of ceramics.

In this chapter, sensitivity analysis of sphere indentation simulations has been performed using the same geometry and setup as highlighted in Sec. 3.3.2. The depth of penetration of the spherical indenter and the granular material percentage, 15 μs after impact, are selected as the two output QoIs.

As seen before in Fig. 3.10, amorphization does not play a significant role for the range of impact velocities studied. To simplify our problem, amorphization is deactivated and the CBM model for granular mechanics is employed. We have selected 20 parameters which we suspect play an important role. These include 4 mechanical, 6 microstructural and 10 granular flow parameters, shown in Tab. 4.1. The range of these parameters are chosen in order to bound commonly observed micro-mechanical values for different ceramics and granular solids as much as possible. In some cases when the parameter is not well understood, the range was selected based on engineering intuition. Scrambled Sobol sequences [178,179] are used to generate 500 space-filled samples in the 20-dimensional parameter space bounded by the ranges given in Tab. 4.1. The integrative model was then run for each of the 500 parameter combina-

tions. From each simulation, the percentage granular material as well as the evolution of the depth of penetration are obtained.

In this study, a linear regression model is fit to the selected QoIs, and statistical inference is performed to understand the relative importance between each of the parameters and the QoIs. If $\tilde{x} = [x_1, x_2, \ldots, x_n]$ denotes the set of n input parameters and y denotes the QoI, then the linear regression model assumes a linear relationship between $\tilde{x}$ and y given by:

$$y \approx b_0 + b_1 x_1 + b_2 x_2 + \cdots + b_n x_n \tag{4.1}$$

where $\tilde{b} = [b_0, b_1, b_2, \ldots, b_n]$ is the vector of unknown $n + 1$ coefficients which needs to be determined. After an initial analysis with the original dataset, leave-one-out-cross-validation (LOOCV) is performed and the individual cross-validated errors are used to detect potential outliers based on the residual interquartile range (IQR) given by:

$$IQR^{res} = Q_3^{res} - Q_1^{res} \tag{4.2}$$

where Q_3^{res} is the third quartile and Q_1^{res} is the first quartile of the residual values of each data point from the LOOCV analysis. After removing the outliers, linear regression is again performed on the remaining dataset. A parameter reduction is then performed by eliminating a group of parameters which does

not reduce the coefficient of determination (R^2) significantly compared to the one obtained with all the parameters. Linear regression is then performed on the remaining dataset with the reduced parameters.

In addition, some of the 20 integrative model parameters are combined to obtain a set of derived parameters which are either non-dimensional or more physically representative. These parameters are summarised in Tab. 4.2. After replacing some of the independent parameters they are associated with, a separate study is also performed with a new set of parameters (derived and original).

Table 4.1. List of model parameters selected for sensitivity analysis.

Type	Name	Symbol	Lower bound	Upper bound	Unit
Mechanical parameters	Poisson's ratio	ν_0	0.1	0.2	–
	Shear modulus	G_0	100	200	GPa
	Density	ρ_0	2000	3500	kg/m^3
	Fracture toughness	K_{IC}	2	5	$MPa\sqrt{m}$
Microstructural parameters	Flaw density	η	1e13	3e13	m^{-3}
	Minimum half flaw size	s_{min}	1	5	μ
	Maximum half flaw size	s_{max}	20	40	μ
	Flaw distribution exponent	α_{flaw}	2	3.5	–
	Flaw friction coefficient	μ_{flaw}	0.4	0.9	–
	Flaw orientation	θ_{flaw}	0.698	1.397	–
Granular parameters (CBM)	Critical breakage energy density	E_C	1	10	MPa
	Grading index	ϑ_{BM}	0.5	0.95	–
	Crushability parameter	κ_{BM}	0.03	0.08	–
	Friction parameter	M_{BM}	0.5	2	–
	Particle breakage initiation parameter	γ_B	0.5	0.96	–
	Dilative behavior parameter	γ_d	0.8	0.99	–
	Strain rate sensitivity coefficient	N_{BM}	1	8	–
	Maximum porosity w/o breakage	ϕ_u	0.2	0.6	–
	Porosity control parameter 1	u	0.075	0.2	–
	Porosity control parameter 2	l	0.075	0.2	–

Table 4.2. Derived parameters selected for sensitivity analysis.

Mean half flaw size	$s_{mean} = \left(\frac{{s_{min}}^{\alpha_{flaw}}}{1-\left(\frac{s_{min}}{s_{max}}\right)^{\alpha_{flaw}}}\right)\left(\frac{\alpha_{flaw}}{\alpha_{flaw}-1}\right)\left(\frac{1}{{s_{min}}^{\alpha_{flaw}-1}} - \frac{1}{{s_{min}}^{\alpha_{flaw}-1}}\right)$
Flaw spacing	$s_{spacing} = \eta^{-\frac{1}{3}}$
Range half flaw size	$s_{range} = s_{max} - s_{min}$
Initial damage	$\Omega_i = \eta\left[\left(\frac{{s_{min}}^{\alpha_{flaw}}}{1-\left(\frac{s_{min}}{s_{max}}\right)^{\alpha_{flaw}}}\right)\left(\frac{\alpha_{flaw}}{\alpha_{flaw}-3}\right)\left(\frac{1}{{s_{min}}^{\alpha_{flaw}-3}} - \frac{1}{{s_{min}}^{\alpha_{flaw}-3}}\right)\right]$
Longitudinal wave velocity	$V_L = \sqrt{\frac{2G_0(1-\nu_0)}{\rho_0(1-2\nu_0)}}$

4.3 Results - Sensitivity Analysis

4.3.1 Original parameter set: Correlation study

For an accurate interpretation of the linear regression coefficients, multicollinearity [180] of parameters should be avoided. The linear correlation coefficient heat map is shown in Fig. 4.1. It shows negligible correlation among the input parameters, which suggests the desired lack of multicollinearity. This is supported by the variance inflation factor (VIF) [180] values of each parameters shown in Tab. 4.3. VIF for a parameter is obtained by regressing that parameter with respect to the other remaining parameters, and has a lower bound of 1. The closer the VIF value for a parameter is to 1, the less the dependence of that parameter on the others. VIFs between 1 and 5 [181] suggest there is moderate correlation but represent an acceptable level of multicollinearity.

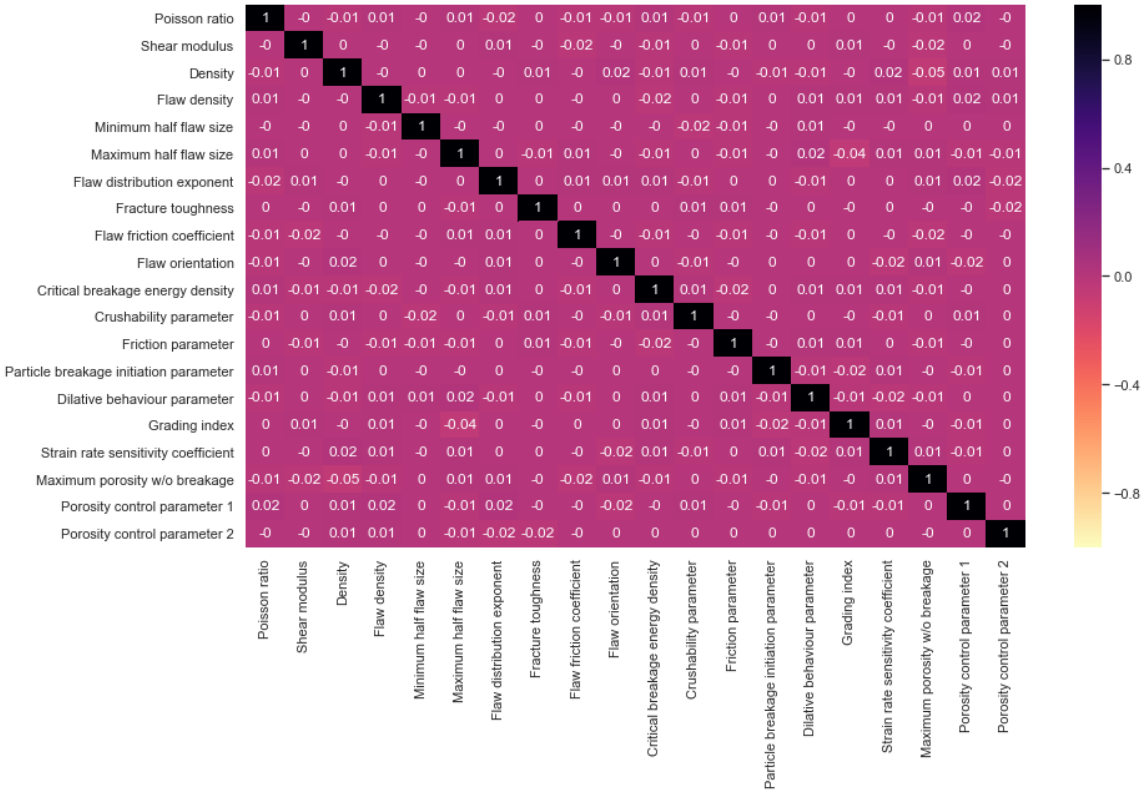

Fig. 4.1. Correlation plot with original parameters shown in Tab. 4.1.

Table 4.3. Variation inflation factor (VIF) with original parameters.

Parameters	ν_0	G_0	ρ_0	η	s_{min}	s_{max}	α_{flaw}	K_{IC}	μ_{flaw}	θ_{flaw}
VIF	1.002	1.001	1.004	1.002	1.001	1.003	1.002	1.001	1.001	1.001

Parameters	E_C	κ_{BM}	M_{BM}	γ_B	γ_d	ϑ_{BM}	N_{BM}	ϕ_u	u	l
VIF	1.002	1.001	1.001	1.001	1.002	1.003	1.002	1.004	1.002	1.001

4.3.2 Derived parameter set: Correlation study

The list of 19 derived parameters is shown in Tab. 4.4. Minimum half flaw size (s_{min}), maximum half flaw size (s_{max}), flaw distribution exponent (α_{flaw}),

flaw density (η), density (ρ_0) and Poisson's ratio (ν_0) are removed and replaced by mean half size (s_{mean}), flaw spacing ($s_{spacing}$), range half flaw size (s_{range}), initial damage (Ω_i) and longitudinal wave speed (V_L).

A correlation study, similar to the one with the original parameter set, is performed here. The correlation coefficient heat map is shown in Fig. 4.2 and the VIF values for each parameter are shown in Tab. 4.5. All the VIF values are within the acceptable range of 1-5. This suggests that the parameter combinations have an acceptable level of multicollinearity and linear regression analysis can be reliably performed.

Table 4.4. Derived parameter list.

G_0	K_{IC}	μ_{flaw}	θ_{flaw}	E_C	κ_{BM}	M_{BM}	γ_B	γ_d	ϑ_{BM}
N_{BM}	ϕ_u	u	l	s_{mean}	$s_{spacing}$	s_{range}	Ω_i	V_L	

Table 4.5. Variation inflation factor (VIF) with derived parameters.

Parameters	Ω_i	s_{mean}	V_L	G_0	$s_{spacing}$	s_{range}	γ_d	N_{BM}	ϑ_{BM}	ϕ_u
VIF	5.07	4.78	2.31	2.31	1.45	1.14	1.01	1.004	1.003	1.003

Parameters	θ_{flaw}	κ_{BM}	E_C	u	M_{BM}	μ_{flaw}	γ_B	K_{IC}	l
VIF	1.002	1.002	1.002	1.001	1.001	1.001	1.001	1.001	1.001

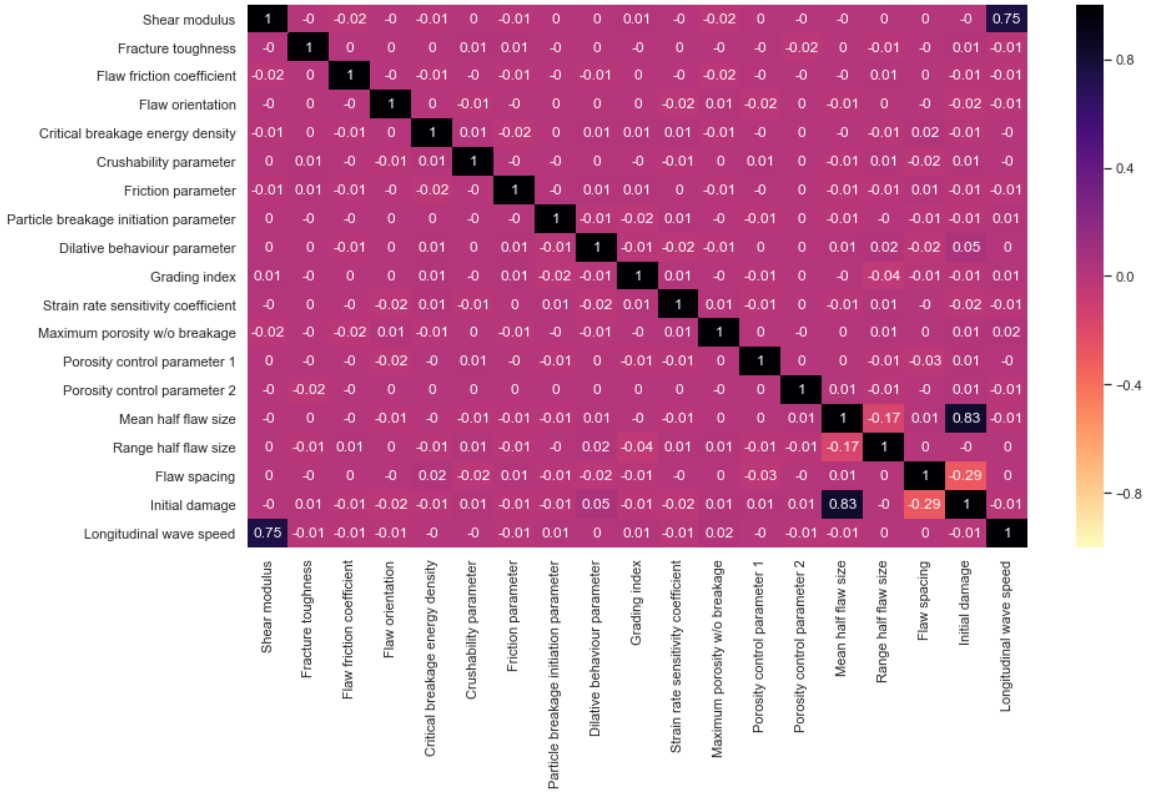

Fig. 4.2. Correlation plot with derived parameters shown in Tab. 4.4.

4.3.3 Granular material percentage

In this section, we study how the different mechanical, microstructural and granular parameters influence the granular material percentage (GMP) at 15 μs after impact. The histogram plot for GMP is shown in Fig. 4.3. The results show that this QoI varies considerably in the sampled parameter space from $\sim$ 5%-70%.

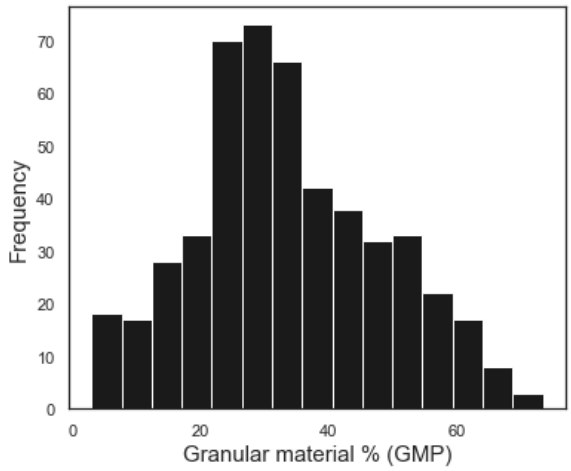

Fig. 4.3. Histogram of granular material percentage at 15 μs after impact based on 500 samples in the input parameter space.

4.3.3.1 Analysis with original parameter set

The linear correlation coefficients between GMP and each of the input parameters are calculated and shown in Tab. 4.6. Fracture toughness (K_{IC}) has the strongest correlation with GMP and the correlation is negative, which means the GMP decreases with increase in K_{IC}. Minimum half flaw size and friction parameter are also strongly correlated with GMP. On the other hand, Poisson's ratio and the flaw distribution coefficient have the weakest correlation. These correlation coefficients, however, only provide a preliminary crude idea about the sensitivities of the parameters. For a more detailed sensitivity analysis, we resort to linear regression analysis.

3 iterations of linear regression analysis are performed and the corresponding prediction results are shown in Tab. 4.7. As part of the prediction results,

Table 4.6. Correlation coefficients (sensitivity analysis for GMP with original parameters).

	K_{IC}	s_{min}	M_{BM}	G_0	ϑ_{BM}	θ_{flaw}	s_{max}	E_C	μ_{flaw}	ρ_0
Granular material %	-0.66	0.48	0.25	0.18	-0.14	-0.11	0.11	0.07	0.06	0.06

	ϕ_u	γ_d	N_{BM}	η	κ_{BM}	γ_B	u	l	α_{flaw}	ν_0
Granular material %	0.04	0.03	-0.03	0.02	-0.01	0.01	0.01	0.01	0.003	-0.001

the coefficient of determination (R^2), the adjusted coefficient of determination (adj. R^2) and the root mean squared error (RMSE) are reported. In the first iteration, analysis is done using the original dataset with sample size 500 and all 20 parameters. For the full data analysis, the R^2 value is 0.827, adj. R^2 value is 0.820 and the RMSE values is 0.4159. For the LOOCV analysis, the R^2, adj. R^2 and RMSE values are 0.811, 0.803 and 0.435 respectively. In the second iteration, the cross-validated errors for each individual data was obtained from the LOOCV analysis results in the first iteration and used to detect potential outliers based on the residual IQR (Eqn. (4.2)). 8 outliers are detected and then linear regression was performed with a dataset of sample size 492 and the same set of 20 parameters. The elimination of outliers helps improve all the 3 metrics (R^2, adj. R^2, RMSE) for both the full data and LOOCV analysis as shown in Tab. 4.7. For example, the R^2 improved from 0.827 to 0.841 for the full data analysis and from 0.811 to 0.826 for the LOOCV analysis. In the third iteration, a group of 8 parameters (ν_0, η, α_{flaw}, κ_{BM}, γ_B, γ_d, u, l) are removed such that

Table 4.7. Regression results (sensitivity analysis for GMP with original parameters).

	All data (500) with 20 parameters		Data w/o outliers (492) with 20 parameters		Data w/o outliers (492) with 12 reduced parameters	
	Full data	LOOCV	Full data	LOOCV	Full data	LOOCV
R^2	0.827	0.811	0.841	0.826	0.839	0.829
adj. R^2	0.820	0.803	0.834	0.819	0.835	0.825
RMSE	0.4159	0.435	0.392	0.410	0.395	0.406

the full data R^2 without these parameters is not significantly reduced. Linear regression analysis is then performed with the dataset of sample size 492 and a set of 12 reduced parameters. It is found from the results in Tab. 4.7 that for the full data analysis, the R^2 value reduces from 0.841 to 0.839 and the RMSE value increases from 0.392 to 0.395 but the adj. R^2 increases slightly from 0.834 to 0.835 which is desirable. For the LOOCV analysis, however, there is improvement in all the 3 metrics compared to those in the second iteration.

The standardized t-test statistic of each parameter obtained from the regression analysis in the third iteration is shown in Fig. 4.4. From the p-values (not shown), it is found that all 12 parameters are statistically significant for a significance level of 0.05. The t-test statistic bar plot in Fig. 4.4 gives an idea of the sign of correlation between each of the parameters and the output GMP. In the figure, the parameters are arranged such that the importance of parameters increases from top to bottom. It is thus seen that fracture toughness (K_{IC})

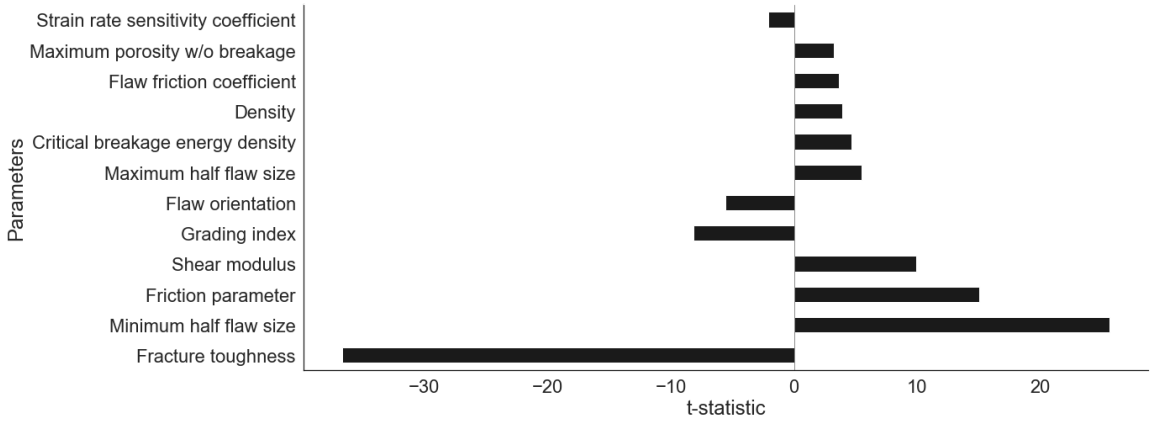

Fig. 4.4. t-statistic plot (sensitivity analysis for GMP with original parameters).

is the most sensitive parameter followed by minimum half flaw size (s_{min}) and friction parameter (M_{BM}). On the other hand, the strain rate sensitivity coefficient (N_{BM}) and maximum porosity without damage (ϕ_u) are among the least sensitive parameters, but still significant.

4.3.3.2 Analysis with derived parameter set

The linear correlation coefficients between GMP and each of the 19 derived input parameters shown in Tab. 4.4 are calculated and reported in Tab. 4.8. Fracture toughness (K_{IC}) has the strongest correlation with GMP (similar to the case in Sec. 4.3.3.1) while crushability parameter (κ_{BM}) and range half flaw size (s_{range}) have the weakest correlation.

Next, linear regression analysis is performed and the corresponding pre-

Table 4.8. Correlation coefficients (sensitivity analysis for GMP with derived parameters).

	K_{IC}	s_{mean}	Ω_i	M_{BM}	G_0	ϑ_{BM}	θ_{flaw}	V_L	E_C	μ_{flaw}
Granular material %	-0.66	0.47	0.32	0.25	0.18	-0.14	-0.11	0.09	0.07	0.06

	ϕ_u	γ_d	N_{BM}	$s_{spacing}$	γ_B	u	l	κ_{BM}	s_{range}
Granular material %	0.04	0.03	-0.03	-0.02	0.01	0.01	0.01	-0.01	0.01

Table 4.9. Regression results (sensitivity analysis for GMP with derived parameters).

	All data (500) with 19 parameters		Data w/o outliers (487) with 19 parameters		Data w/o outliers (487) with 14 reduced parameters	
	Full data	LOOCV	Full data	LOOCV	Full data	LOOCV
R^2	0.853	0.8395	0.875	0.8641	0.874	0.8655
adj. R^2	0.847	0.8331	0.870	0.857	0.870	0.8615
RMSE	0.3831	0.4006	0.3477	0.3632	0.3496	0.3613

diction results are shown in Tab. 4.9. It is noted that in the third and final iteration of the analysis, a group of 5 parameters (κ_{BM}, γ_B, N_{BM}, u, l) are removed such that the full data R^2 without these parameters is not significantly reduced. All these 5 parameters happen to be the granular parameters of the CBM model.

The standardized t-test statistic of each parameter obtained from the regression analysis in the third iteration are shown in Fig. 4.5. From the p-values, it is found that all the reduced 14 parameters are statistically significant for a significance level of 0.05. Fracture toughness (K_{IC}) is the most sen-

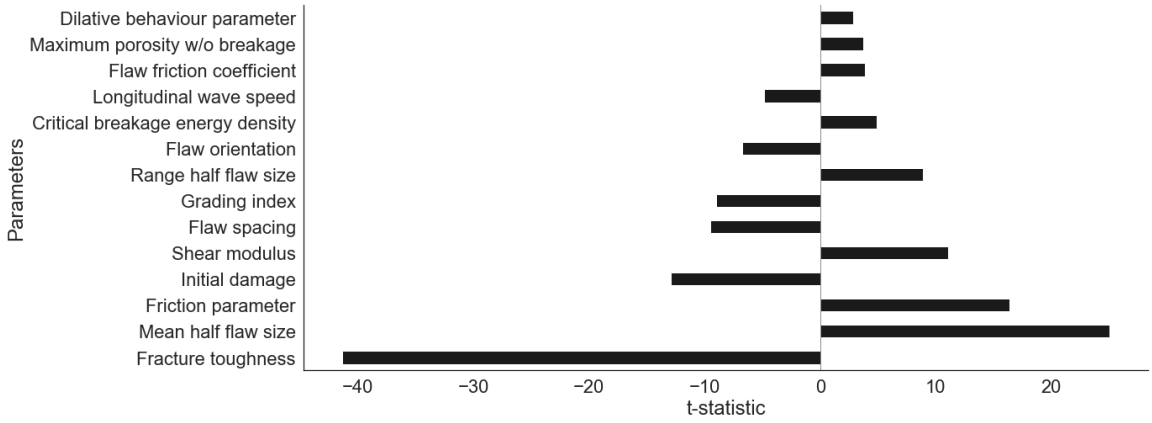

Fig. 4.5. t-statistic plot (sensitivity analysis for GMP with derived parameters).

sitive parameter followed by mean half flaw size (s_{mean}) and friction parameter (M_{BM}). On the other hand, dilative behaviour parameter (γ_d) and maximum porosity without damage (ϕ_u) are among the least sensitive parameters, but still significant. To sum up the sensitivity analysis of the granular material percentage, similar trends are found in the original and the derived parameter cases with respect to the order of importance of the parameters. For example, in both cases, the three most sensitive parameters and their importance order is very similar, the only difference being the original parameter s_{min} replaced by the derived parameter s_{mean}.

4.3.4 Depth of Penetration

One of the outputs of the integrative model is the evolution of the depth of penetration values with time. Two distinct cases are observed in the 500 simu-

lation outcomes. In one case, the sphere rebounds after impacting the cylinder, and in the other case, the sphere continues to penetrate into the cylinder. The maximum depth of penetration for the rebound case (MDR) is selected as the output QoI for sensitivity analysis. To be exact, 342 simulations lead to rebound of the sphere while the rest lead to sphere penetration. Thus, 342 samples are used for the sensitivity analysis of MDR. The histogram for the MDR output is shown in Fig. 4.6.

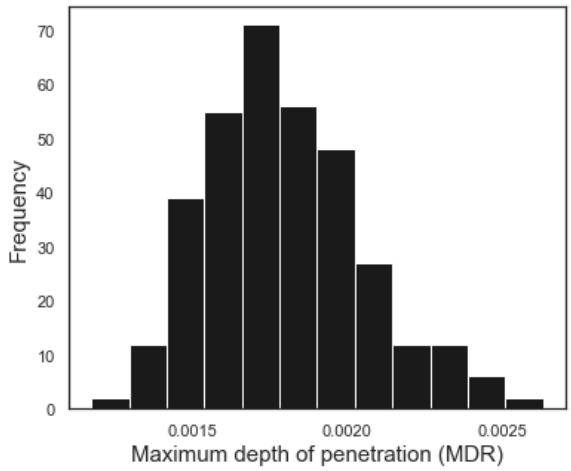

Fig. 4.6. Histogram of maximum depth of penetration (rebound case) based on 342 samples in the input parameter space.

4.3.4.1 Analysis with original parameter set

The linear correlation coefficients between MDR and each of the input parameters are shown in Tab. 4.10 which suggests friction parameter (M_{BM}) has the strongest correlation with MDR while maximum half flaw size has the weakest correlation with MDR.

Table 4.10. Correlation coefficients (sensitivity analysis for MDR with original parameters).

	M_{BM}	ϑ_{BM}	G_0	K_{IC}	N_{BM}	E_C	s_{min}	γ_d	ρ_0	ϕ_u
Maximum depth of penetration	-0.48	0.47	-0.35	-0.28	0.25	-0.25	-0.19	-0.07	-0.07	0.07

	α_{flaw}	κ_{BM}	θ_{flaw}	γ_B	u	l	μ_{flaw}	η	ν_0	s_{max}
Maximum depth of penetration	0.06	-0.06	-0.02	-0.02	-0.02	0.02	0.01	0.01	0.01	-0.003

Table 4.11. Regression results (sensitivity analysis for MDR with original parameters).

	All data (342) with 20 parameters		Data w/o outliers (329) with 20 parameters		Data w/o outliers (329) with 11 reduced parameters	
	Full data	LOOCV	Full data	LOOCV	Full data	LOOCV
R^2	0.911	0.8985	0.927	0.916	0.924	0.918
adj. R^2	0.905	0.892	0.922	0.911	0.922	0.915
RMSE	0.2984	0.3185	0.2554	0.273	0.260	0.270

Next, linear regression analysis is performed and the corresponding prediction results are shown in Tab. 4.11. After removing the outliers and reducing the number of parameters, the R^2, adj. R^2 and RMSE values are reported to be 0.918, 0.915 and 0.270 respectively for the LOOCV analysis.

The standardized t-test statistic of the 11 significant parameters obtained from the regression analysis in the third iteration are shown in Fig. 4.7. Friction parameter (M_{BM}) is the most sensitive parameter followed by grading in-

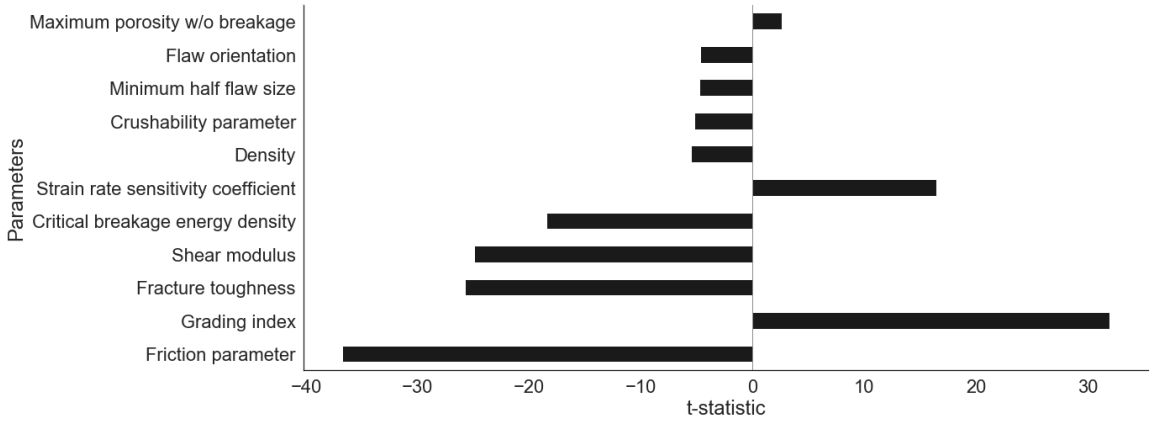

Fig. 4.7. t-statistic plot (sensitivity analysis for MDR with original parameters).

dex (ϑ_{BM}) and fracture toughness (K_{IC}). On the other hand, flaw orientation (θ_{flaw}) and maximum porosity without damage (ϕ_u) are among the least sensitive parameters, but still significant.

4.3.4.2 Analysis with derived parameter set

The linear correlation coefficient values between MDR and each of the derived input parameters (not reported here) are very similar to that shown in Sec. 4.3.4.1. The prediction results from the linear regression analysis shown in Tab. 4.12 indicates slight improvement in all the three metrics compared to that reported in Sec. 4.3.4.1. Figure 4.8 shows the standardized t-test statistic of the 11 significant parameters obtained from the regression analysis in the third iteration. Friction parameter (M_{BM}) is the most sensitive parameter followed by grading index (ϑ_{BM}) and fracture toughness (K_{IC}). On the other hand,

crushability parameter (κ_{BM}) and maximum porosity without damage (ϕ_u) are among the least sensitive parameters, but still significant.

Table 4.12. Regression results (sensitivity analysis for MDR with derived parameters).

	All data (342) with 19 parameters		Data w/o outliers (331) with 19 parameters		Data w/o outliers (331) with 11 reduced parameters	
	Full data	LOOCV	Full data	LOOCV	Full data	LOOCV
R^2	0.914	0.9023	0.929	0.919	0.926	0.920
adj. R^2	0.909	0.8965	0.924	0.914	0.924	0.917
RMSE	0.2933	0.3126	0.254	0.2713	0.258	0.269

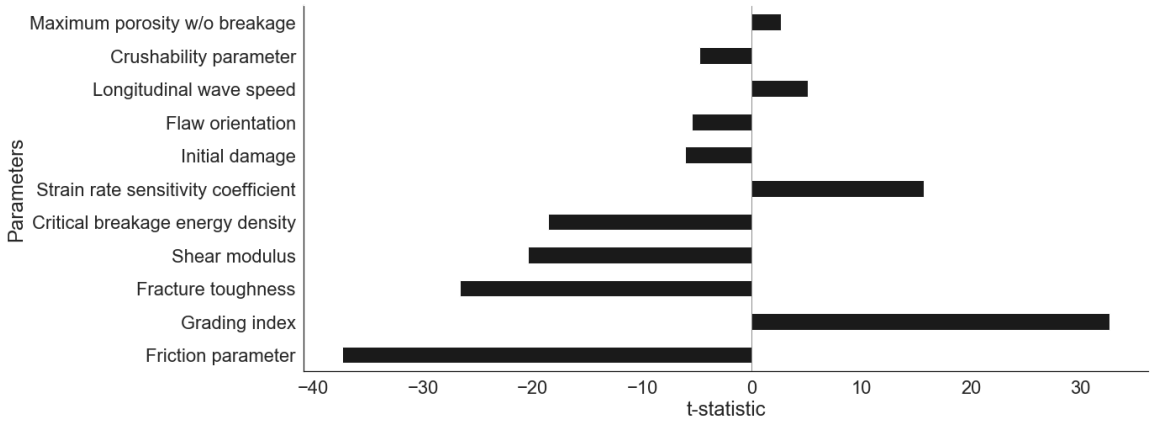

Fig. 4.8. t-statistic plot (sensitivity analysis for MDR with derived parameters).

4.4 Discussion

4.4.1 Physical Mechanisms and Trends

The influence of model parameters on a given model output is a complex interplay of the various mechanisms with which they are associated. Although there are multiple physical mechanisms active at any instant, only a few of them can be intuitively expected to play a crucial role in influencing the output. For example, as discussed before, amorphization may not play a critical role in these particular experiments because of the small amorphization volume observed in the present simulations, but wave propagation, crack growth and energy dissipation due to granular flow might. We have tried to isolate the parameters by the mechanism they might be responsible for, and determine the possible correlations with model output. Some parameters might be responsible for multiple mechanisms. The suspected influence of model parameters on physical mechanisms and the corresponding correlation with percentage granular region has been highlighted in Tab. 4.13. Most of the correlations reported in Tab. 4.6 and Tab. 4.8 match the physical intuition in Tab. 4.13. However, the suspected correlations from ρ_0, ν_0, α_{flaw}, μ_{flaw}, γ_d do not match the observed correlations. This might be due to complicated parameter interactions. At any rate, the magnitude of correlation corresponding to each of these parameters is very small, and they are not parameters that have a significant influence on

model QoIs.

As mentioned in Sec. 4.3.4, only 342 out of the 500 simulation led to rebound within 15 μs after impact. The simulations in which rebound did not occur within that duration may feature rebound at a later time, or may not feature rebound because of cylinder fragmentation. Hence, the 342 rebound cases were used to conduct the sensitivity study for depth of penetration. The depth of penetration is a more localised measure, intricately related to deformation mechanisms in the Mescall zone. This region is highly comminuted and almost certainly under granular flow. Unsurprisingly, the model parameters associated with granular mechanics seem to play a more significant role. In addition, the percentage of the region under granular flow is expected to have a weak influence as well. When more of the region is granular, the region right under the indenter might exhibit less granular flow. Thus, parameters associated with crack growth might have competing influences. The influence of the modulus, fracture toughness, critical breakage energy density is physically related to overall stiffness, and can be expected to be negatively correlated with the depth of penetration. For other granular mechanics model parameters, there is an indirect influence via porosity change and volumetric deformation. Table 4.14 highlights the suspected correlation of model parameters with the instantaneous depth of penetration. The influence of crack growth parameters on the maximum depth of penetration is complicated and unclear. Once again

physical intuition can be successfully used to justify correlations corresponding to wave speed and granular flow parameters except ρ_0, ν_0 and κ_{BM}.

Table 4.13. Summary of expected correlation of model parameters with granular material % .

Dominant Mechanism	Parameter	Physical argument for effect with increase	Expected correlation	Model correlation
Wave speed	ρ_0 V_L	Wave speed decreases Wave speed increases	Negative Positive	Positive
Wave speed & Crack growth	ν_0 G_0	Wave speed increases; Crack velocity increases	Positive	Negative Positive
Crack growth	η s_{min} s_{max} s_{mean} Ω_i	More crack growth	Positive	Positive
	α_{flaw} K_{IC} μ_{flaw}	Fewer cracks grow; lower crack velocity	Negative	Positive Negative Positive
	θ_{flaw} $s_{spacing}$ s_{range}	Complicated & Unclear	Unclear	Negative Positive
Granular flow (More energy dissipation $\Longrightarrow$ less region becomes granular)	E_C M_{BM} γ_B	Higher threshold strain energy density for particle breakage Lower rate of breakage $\Longrightarrow$ less energy dissipation	Positive	Positive
	κ_{BM} γ_d ϑ_{BM}	Higher rate of breakage Yield surface reached sooner Higher potential fragmentation $\Longrightarrow$ more energy dissipation	Negative	Negative Positive Negative
	u	ϕ_{max} decreases, less potential energy dissipation due to change in porosity	Positive (unclear)	Positive
	N_{BM}	Higher rate of breakage $\Longrightarrow$ more energy dissipation (Unclear)	Negative (unclear)	Negative
	ϕ_u l	ϕ_{max} increases ϕ_{min} decreases $\Longrightarrow$ more potential energy dissipation due to change in porosity		Positive

4.4.2 Implications towards designing materials

Table 4.15 lists the top ten most sensitive parameters from regression studies for percent granular material and depth of penetration using original and derived model parameters. In either case, fracture toughness (K_{IC}), granular friction (M_{BM}), shear modulus (G_0), grading index (ϑ_{BM}), minimum flaw size (s_{min}) seem to be important. The strain rate sensitivity coefficient of granu-

Table 4.14. Suspected of expected correlation of model parameters with instantaneous depth of penetration.

Dominant Mechanism	Parameter	Physical argument for effect with increase	Expected correlation	Model correlation
Wave speed	ρ_0	Less granular region	Positive	Negative
	V_L	Wave speed increases		Positive
Wave speed & Crack growth	ν_0	More granular region	Negative	Positive
	G_0	More granular region; Higher stiffness		Negative
Crack growth	η	More granular region; Rapid granular transition; More inelastic deformation	Unclear	Positive
	s_{min}			Negative
	s_{max}			
	s_{mean}			
	Ω_i			
	α_{flaw}	Less granular region; Less inelastic deformation		Positive
	K_{IC}			Negative
	μ_{flaw}			Positive
	θ_{flaw}	Complicated & Unclear		Negative
	$s_{spacing}$			
	s_{range}			Positive
Granular flow	ϑ_{BM}	Higher potential fragmentation, breakage energy	Positive	Positive
	κ_{BM}	Higher rate of breakage — more porosity change		Negative
	N_{BM}	Higher rate of porosity change; higher plastic strain rate — more breakage, more volumetric deformation		Positive
	ϕ_u	ϕ_{max} increases		
	l	ϕ_{min} decreases		
	E_C	Higher threshold strain energy density for particle breakage	Negative	Negative
	M_{BM}	Lower plastic strain rate — less porosity change		
	γ_B	Lower rate of breakage — less breakage		
	γ_d	Lower porosity change rate — less volumetric deformation		
	u	ϕ_{max} decreases		

lar flow (N_{BM}) is important for the depth of penetration. This study provides us insights that could guide material processing modifications. It is difficult if not impossible to control some of these parameters, particularly the granular mechanics parameters other than M_{BM} and E_C. Fortunately, those parameters are not the most significant ones. As mentioned earlier, researchers have explored different techniques to improve K_{IC}, G_0 [157–159]. Although these parameters have been assumed to be independent, some of them might be related to one another through available processing routes, and they may be challenging to independently control. For example, it might not be possible to vary the

Table 4.15. Summary of sensitivity analysis: top 10 model parameters in decreasing order. The colour code represents the mechanisms corresponding to the parameters. Olive, purple and teal correspond to wave speed, crack growth and granular mechanics, respectively. GMP is more strongly influenced by fracture related parameters, while MDR is more strongly influenced by granular mechanics parameters.

Granular material %		**Depth of penetration**	
Original Parameters	**Derived Parameters**	**Original Parameters**	**Derived Parameters**
K_{IC}	K_{IC}	M_{BM}	M_{BM}
s_{min}	s_{mean}	ϑ_{BM}	ϑ_{BM}
M_{BM}	Ω_i	G_0	G_0
G_0	M_{BM}	K_{IC}	K_{IC}
ϑ_{BM}	G_0	N_{BM}	N_{BM}
θ_{flaw}	ϑ_{BM}	E_C	E_C
s_{max}	θ_{flaw}	s_{min}	V_L
E_C	V_L	γ_d	s_{mean}
μ_{flaw}	E_C	ρ_0	Ω_i
ρ_0	μ_{flaw}	ϕ_u	γ_d

defect population without affecting the polycrystalline fracture toughness or the modulus.

The initial damage (Ω_i) is physically related to the volume fraction of defects. While processing a ceramic, Ω_i might be optimized to meet a certain performance goal. Further optimization to improve performance would likely involve controlling the defect size and the defect spacing. Our study suggests that the flaw density (η) or flaw spacing ($s_{spacing}$) are not as significant as the minimum flaw size (s_{min}) or the mean flaw size (s_{mean}). This might mean that ensuring smaller closely spaced defects might be more desirable than larger ag-

glomerates. Flaw distribution parameters are related to the secondary phases in boron carbide matrix. The most abundant of these secondary phases is free carbon. Location of free carbon along boundaries of fragments suggest crack growth from these sites [182, 183]. Therefore, controlling the size and volume fraction of these graphitic inclusions [184] can help address fracture mechanisms. Smaller defect spacing might also lead to smaller initial fragments. In addition to this, smaller fragments might also increase E_C, due to size effect, which might improve impact performance. Higher granular friction (M_{BM}) is one of the most desirable traits and more angular particles can achieve that. However it is not clear how to control angularity. [105] suggests that larger fragments have lower circularity. However, it might not be fair to compare a bulk-averaged estimate of granular friction with individual particle shape. [185] investigated the influence of particle morphology on frictional behaviour of sand. Further research towards microstructural features that control angularity of subsequent fragments and therefore granular friction will be useful.

4.4.3 Implications towards modelling and calibration

The results from the sensitivity analysis suggest that certain parameters, some of which control the evolution of state variables in CBM model (Eqn. (3.16, 3.17, 3.18)), are not significant for the output quantities of interest studied in this work. If the same can be replicated for simulation of other impact experiments (summarized in [186]), it might be assumed that either the model can be simplified to ignore those parameters or that those parameters do not need recalibration with slight changes in the material. For example, many of the granular mechanics parameters are calibrated through multiple drained and undrained triaxial compression tests, oedometric compression tests on granular solids [88]. Often the classical geomechanics experimental setups cannot be employed at the high pressure conditions of impact experiments. So, for a new material, while it will be ideal to recalibrate granular friction (M_{BM}) using pressure shear impact experiments [160], one can rely on past data for γ_B, γ_d, κ_{BM}. Similarly, accurate estimation of polycrystalline fracture toughness (K_{IC}) is essential [187], and should be prioritized over flaw friction (μ_{flaw}) or relative density tests to calibrate l, u and dry density test to calibrate ϕ_u. This can save both computational and experimental effort and expenditure.

4.5 Summary

Two simulation outputs from sphere indentation experiments have been identified as quantities of interest for a sensitivity analysis study: % granular material and indentation depth, $15\mu s$ after impact. 20 micro-mechanical and granular flow model parameters have been varied to generate 500 space-filled samples. Linear regression analysis for the two quantities of interest has been conducted to identify the most significant model parameters. Connections to physical mechanisms for these model parameters have been argued and the implications towards material design from the sensitivity analysis have been explored. The results from the sensitivity study assists in prioritizing calibration experiments for new materials.

Chapter 5

Microstructure & fragment morphology

5.1 Introduction

Impact performance of armor ceramics, such as their penetration resistance or overall energy dissipation, is strongly influenced by the local behaviour in the region immediately under the impactor. This region is subjected to very high pressure and extensive fragmentation and is commonly referred to as the Mescall zone [17]. Depending on the ceramic material and the impact velocity, this region witnesses some or all of the following: fracture, local plasticity [41], amorphization [24], granular plasticity [8]. Performance enhancement can be attained by targeting the material properties to address each of the aforemen-

tioned mechanisms dominant in the Mescall zone.

Previous modelling efforts exploring model sensitivity on material parameters either employ simplistic phenomenological models of some of the less-understood mechanisms [176,177] or complicated micromechanical models (Chapter 4) that ignore correlations between model parameters [188]. The latter is mostly acceptable because generally the intercorrelation between model parameters is such that the overall trends in material performance are unaffected by the assumption of parameter independence. For example, increase in flaw size might lead to a reduction in fracture toughness and modulus. Assuming independence in each of these parameters would not change the processing implications because flaw size is negatively correlated with performance while the latter two are positively correlated. One can therefore argue that reduction in flaw size could be beneficial. However, the same argument cannot be made for some of the less-studied parameters associated with micromechanical models of granular mechanics [90] or quasi-plasticity [134].

Chapter 4 conducted a sensitivity analysis study on sphere indentation simulations of boron carbide using a ceramics model that integrated submodels accounting for various mechanisms. They found that granular friction, polycrystalline fracture toughness, flaw size and modulus are among the significant material parameters. The observations echo the conclusions of [188]. While some of these parameters can be controlled directly via available processing

routes, it is unclear how to modify granular friction through material processing, even though it is a critical parameter dictating penetration resistance of armor ceramics.

It is well established that mechanical properties of granular media, including granular friction, are related to particle morphology. Generally, the more angular or non-spherical a particle, the higher the granular friction. [189, 190] have reviewed various literature on the morphological dependence of mechanical properties of granular media.

In geomechanics, a plethora of morphological descriptors have been developed over time [128, 191–194] that facilitate an evaluation of morphology-property relationships. Such descriptors mostly try to capture the following properties:

1. Form & Sphericity: The form or the aspect ratio of a particle refers to the overall flatness/platiness of a particle. Although not exactly the same, form bears close resemblance to another property which measures the closeness of a particle to a true sphere - sphericity.

2. Roundedness: The roundedness of a particle captures its smoothness on the scale of its own dimensions. In other words, roundedness is a measure of the local features on a particle which are not too small compared to the particle itself. The earliest measurement of roundedness was defined

by [191] as

$$R = \frac{\sum_{i=1}^{N} r_i/N}{r_{in}}, \tag{5.1}$$

where r_i is the radius of curvature of the i^{th} corner, N is the total number of corners, and r_{in} is the radius of the largest inscribed sphere.

[192] developed charts to calculate roundedness. Using charts to estimate surface peaks is cumbersome, hence other measures of closely correlated indices [195–197] have been developed.

3. Surface texture: The surface texture quantifies the asperities and the overall roughness of a particle. Like roundedness, it is also a measure of local features on the surface, but at a much smaller scale.

For comminuted armor ceramics, in order to control granular flow, one must understand the influence of initial material microstructure on morphology of the initially fragmented media at the onset of granular flow. This chapter attempts to address that connection using a modified version of the 3D fragmentation model developed in chapter 2 to predict fragment morphology from initial microstructure. The chapter then uses existing relations between shape descriptors and granular friction to predict the relative granular friction between different initial microstructures. Finally, suggestions about material modifications to improve impact performance are made.

5.2 Microstructural Fragmentation - Fragment statistics

Chapter 2 developed a 3D fragmentation model to predict the transition of a cracked ceramic to a granular medium. This necessiated the ability to model crack growth and coalescence at a high degree of fragmentation. Unlike chapter 2, the focus of the current model is not to predict a granular transition criterion, rather, more accurate fragment morphology that relates to granular friction of the fragmented material. Hence a few modifications are made in the present work, as summarized in Tab. 5.1. The following sections will briefly outline these modifications and summarize the fragmentation model.

Table 5.1. Summary of the changes made to the fragmentation model.

	Chapter 2	**Modified fragmentation model**
Damage model	Modified [55]	Anisotropic crack growth [118]
Modelling of cracks	Effective crack (Fig. 5.2a)	Explicitly modelled defect and wing crack (Fig. 5.2b)
Crack coalescence	Fixed duration of coalescence before fragmentation	Coalescence initiation at peak strength

5.2.1 Input Crack Statistics

[118] discusses development of a 3D micro-mechanics based anisotropic damage model. The model is able to handle multi-axial stress states and corresponding cracking mechanisms. Under low confining stress, the model can

estimate evolution of wing crack populations corresponding to different flaw orientations. Crack statistics predicted by this model have been used as inputs to the modified version of the three-dimensional fragmentation model developed in chapter 2 to estimate changing fragment statistics.

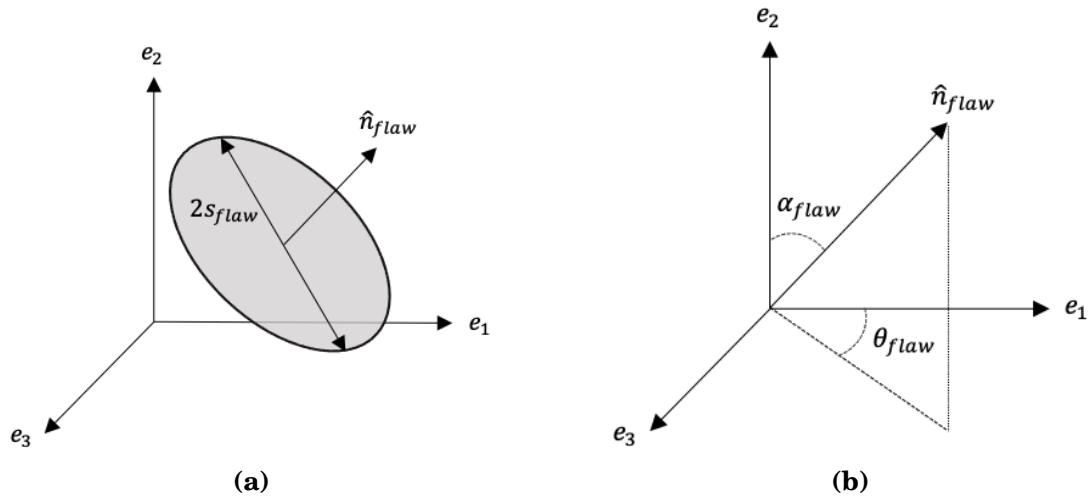

Fig. 5.1. Illustration of flaw orientation, fully defined in three dimensions by angles α_{flaw} and θ_{flaw}.

In [118], flaws are described as penny shaped cracks with their normal $\hat{n}_{flaw}$ defined by angles α_{flaw} and θ_{flaw} as shown in Fig. 5.1. Wing crack growth from these flaws at every time increment is calculated for each flaw population. This model provides the basis for voxelized three dimensional cracks represented here in what we refer to as the simulation box. Using this model, the voxelized crack population is updated at every load step until the desired fragmentation level is obtained. The size of each voxel is referred to as the resolution size.

In chapter 2 initial defects with adjoining wing cracks were modelled as el-

liptical cracks with effective size and orientation (see Fig. 5.2a). While this model helps evaluate the degree of fragmentation reasonably well, the fragment morphology is not well preserved. Hence in this chapter, wing cracks and the initial defects are modelled separately (see Fig. 5.2b). Here, we assume that as the wing cracks grow vertically, they grow in the horizontal direction as well, keeping the aspect ratio of the equivalent crack equal to that of the defect. Since the initial flaw orientation is known (Fig. 5.1b), it is used to generate the crack assemblies.

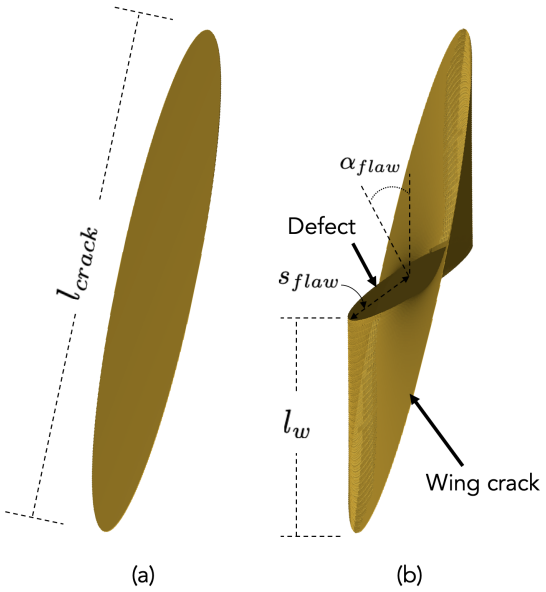

Fig. 5.2. Generation of 3D crack assembly: (a) Effective crack in chapter 2, (b) Defect with wing crack model.

5.2.2 Crack Coalescence

Cracks compete with each other to coalesce in different modes [99] both with and without secondary cracks [101]. Crack coalescence neither initiates at the same instant for all cracks, nor does it terminate at once. Throughout the loading phase cracks connect with one another forming larger crack assemblies and thereby modifying the underlying density of individual crack populations. This has been addressed by a micromechanics model in [120]. However, in the post peak unloading phase of ceramics under high strain rate, cracks grow quickly and connect to rapidly fragment the material. Chapter 2 addressed the rapid fragmentation through a coalescence zone approach and established a new microstructure-dependent granular transition criterion. The predicted fragment size distribution was comparable to experimentally observed dynamic fragmentation of boron carbide, and the granular transition criterion implemented in an integrated ceramics model was able to precisely replicate fracture patterns in impact experiments (Chapter 3). This chapter adopts a similar crack coalescence approach. Figure 5.3 shows a representative image of a crack (in red) with the coalescence zone (in cyan). In chapter 2 the duration of crack coalescence was kept constant. In the current model, instead, crack coalescence is assumed to initiate at peak strength and it does not terminate after a fixed duration; rather, the coalescence zone, the extent of fragmentation and the morphology evolves with time until granular flow initiates. One chal-

lenge is that limitations on resolution mean that as fragmentation increases, the associated larger coalescence zone obscures fragment morphology. In this chapter, crack coalescence is terminated relatively early to preserve the morphology present at the onset of granular flow. Because we are only interested in the relative morphology changes associated with changes in the initial defect populations, comparable degrees of fragmentation between different microstructures is ensured by using a criterion similar to the granular transition criterion developed in chapter 2. Crack coalescence is terminated when the overall effective crack length (l_{crack}) reaches a certain threshold fraction of the radial active flaw spacing ($s_{spacing}$),

$$l_{crack} = C s_{spacing}, \tag{5.2}$$

where C is a constant chosen as 0.2. Assuming Poisson distributed flaws, this corresponds to around 18% of active flaw centers being connected (Eq. 2.21 in chapter 2).

The effective crack length is calculated as,

$$l_{crack} = E\left[\left(2\left(\sqrt{\left(s_{flaw}\sin\left(\alpha_{flaw}\right)+l_w\right)^2+\left(s_{flaw}\cos\left(\alpha_{flaw}\right)\right)^2}\right)\right)^3\right]^{1/3}, \tag{5.3}$$

where l_w is the wing crack length.

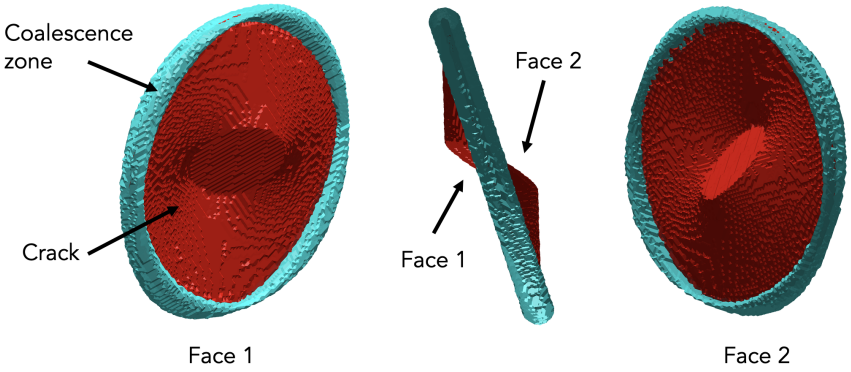

Fig. 5.3. Representative image showing different views of a crack (in red) with a coalescence zone (in cyan).

The radial flaw spacing of active cracks is calculated as,

$$s_{spacing} = \left(\frac{4}{3}\pi\eta_{flaw}r_{actv}\right)^{-1/3}, \tag{5.4}$$

where r_{actv} is the fraction of cracks that are active and η_{flaw} is the flaw density.

5.2.3 Extracting Fragment Statistics

Similar to chapter 2, a connected region algorithm is adopted for fragment morphology analysis that uses the bwconncomp function in MATLAB for periodic boundary conditions, followed by dilation to compensate for resolution size. The regionprops3 function in MATLAB is used to extract the principle axes dimensions of equivalent ellipsoids for each fragment (a_{el}, b_{el}, c_{el}) using principal component analysis (PCA), volume ($\mathcal{V}$), and surface area ($\mathcal{S}$). Analysis is restricted to particles not contacting the boundary of the simulation box.

$\mathcal{S}$ is calulated using the Crofton formula [198, 199] which becomes less accurate when the resolution is close to the fragment size. Fragment size (d_{frag}) is estimated as the cube root of $\mathcal{V}$.

Different initial microstructures are studied. For most of the simulations, unless mentioned otherwise, a resolution size (∇_{res}) of 2μ and a simulation box size of $1mm$ is used. We have presented here some commonly used morphological indices computed for a particular case of $\eta_{flaw} = 22e12\ cracks/m^3$, $s_{flaw} = 10\mu$ and $C = 0.2$ in Eqn. 5.2:

1. Form and Aspect Ratio of fragments:

   Form and aspect ratio provide estimates of particle platiness. The effective dimensions of a particle can either be estimated from the principal axes dimensions of an equivalent ellipsoid fit to each fragment using PCA (a_{el}, b_{el}, c_{el}), or the the bounding box dimensions ($a_{box}, b_{box}, c_{box}$) of the fragment. The form factor is calculated based on the former, when $a_{el} \geq b_{el} \geq c_{el}$:

   $$Form = \frac{c_{el}}{a_{el}}. \tag{5.5}$$

   Particle analyzers that use 2D image analysis typically report only the intermediate and longest bounding box dimension. During such imaging, the smallest dimension is often perpendicular to the plane and not captured in the bounding box. Hence, the aspect ratio is estimated from the

largest and intermediate dimensions of a particle, for $a_{box} \geq b_{box} \geq c_{box}$:

$$AR = \frac{b_{box}}{a_{box}}. \tag{5.6}$$

Figs. 5.4a,5.4b show the mean values (red dotted line) and variation in $Form$ and AR, respectively, with increasing fragment size based on fragmentation model. There appears to be a higher variation in the indices for smaller fragment sizes. From the aspect ratio it seems that the average platiness of particles also seems to slightly decrease with increase in fragment size, whereas the form factor relationship is more complicated. AR, calculated from the bounding box, can only take specific values due to the limited bounding box dimensions that can accommodate a fragment.

2. Roundedness Index:

   The index developed by [128] is used to compute roundedness as,

$$R_H = \frac{\mathcal{V}}{\mathcal{S}\sqrt[3]{a_{el}b_{el}c_{el}}}. \tag{5.7}$$

   A perfectly round fragment will have $R_H = 0.33$, whereas for all other fragments, $R_H < 0.33$ implies higher angularity (and potentially higher value of granular friction). Figure 5.4c shows the mean values (red dotted line) and variation in R_H with increasing fragment size at different

fragmentation levels. Roundedness decreases with increases in fragment size with smaller fragments exhibiting greater variation. $R_H > 0.33$ near the resolution size is due to numerical inaccuracies in using the Crofton formula to approximate surface area.

3. Sphericity :

   The True Sphericity Index (TSI) [200] is a measure of how similar a fragment is to a perfect sphere. Similar to the the other metrics, TSI describes a fragment's angularity. TSI is the three dimensional analogue to the two dimensional measure circularity and is calculated by

$$TSI = \frac{\left(36\pi\mathcal{V}^2\right)^{1/3}}{\mathcal{S}}. \tag{5.8}$$

   Figure 5.4d shows the mean values (red dotted line) and variation of TSI with increasing fragment size at different fragmentation levels. $TSI = 1$ indicates a spherical shape. Any other shape will have $TSI < 1$ due to isoperimetric inequality. In our results, $TSI > 1$ close to the resolution size is a consequence of Crofton formula limitations near the resolution limit [201, 202]. Smaller particles are more spherical than larger ones. This is comparable to observations of circularity measured in [42] for microstructure dependent fragmentation.

Surface roughness is a subscale property below the resolution in our model.

Depending on the ceramic and the loading condition, the fracture surfaces can be smooth - transgranular or rough - intergranular [41]. For intergranular fracture, crack path tortuosity and the resultant surface roughness is related to grain size [203]. Controlling grain size can therefore further influence granular friction through control of roughness. However, given that the fracture type is a property intrinsic to materials, and altering grain size can affect other material properties, studying the influence of grain size on surface roughness and granular friction is beyond the scope of this study.

5.2.4 Morphology and Granular Friction

While there are several studies providing qualitative relationships between shape parameters and granular material properties, few empirical quantitative relationships exist. Although quantification of granular friction is not the aim of the study, empirical equations that relate morphology to granular friction can provide useful insight into the differences between the mechanical properties of fragments corresponding to different initial microstructures. The following sections will focus on two prior studies that discuss such relationships.

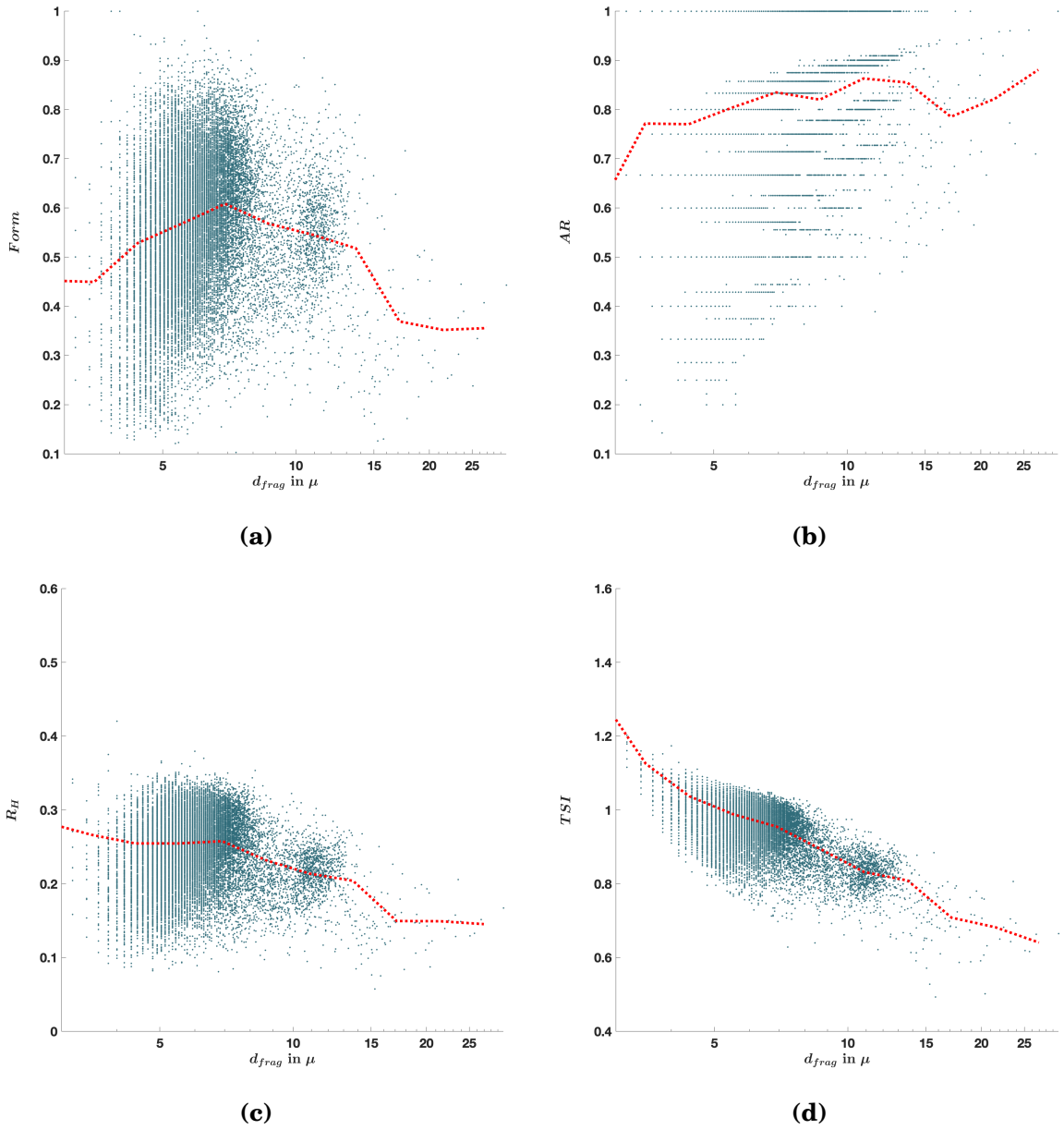

Fig. 5.4. Fragment Statistics for $\eta_{flaw} = 22e12 cracks/m^3$, $s_{flaw} = 10\mu$ and $C = 0.2$: (a)Form Factor ($Form$); (b) Aspect Ratio (AR); (c) Roundedness Index (R_H); (d) True Sphericity Index (TSI). Red dotted lines represent the mean values of indices.

5.2.4.1 Critical state friction angle - Alshibli & Cil

[194] developed new morphological indices to compute sphericity (I_{sph}) and roundedness (I_r). [185] investigated the influence of the relative density (D_r), inital mean stress (p'_o), and morphological indices characterizing form (F_{AC}), roundedness (I_r), sphericity (I_{sph}), and surface texture (R_q), on granular friction and dilatancy angles. The morphological indices used in the chapter are defined as follows:

$$I_{sph} = \frac{\mathcal{V}}{\mathcal{V}_S}, \tag{5.9a}$$

$$I_r = \frac{\mathcal{S}}{\frac{4}{\pi}\left(\frac{d_L+d_I+d_S}{6}\right)^2}, \tag{5.9b}$$

$$F_{AC} = \frac{d_S}{d_L}, \tag{5.9c}$$

where d_S, d_I, d_L are the diameters of the smallest, intermediate and largest spheres passing through the centroid and calculated using PCA. They are equal to twice the values of the equivalent ellipsoid dimension defined earlier. $\mathcal{V}_S$ is the volume of a sphere with diameter equal to d_S. F_{AC} is identical to the $Form$.

Empirical critical state friction angle (ϕ_{CS}) was found by [185] to vary as

$$\phi_{CS} = 23 - 134.06F_{AC} + 142.04I_r - 21.02R_q - 0.861\left(\frac{p'_o}{p_{atm}}\right) + 0.043D_r, \quad (5.10)$$

where p_{atm} is the atmospheric pressure.

In this chapter, we are only interested in the morphological contributions to friction. R_q, the surface texture, depends on the specific material, as mentioned earlier. p'_o, the initial mean stress, depends on the impact velocity, wave velocity, and ceramic density (which does not change between microstructures). D_r, the relative density, is close to 1 and is unlikely change between microstructures as the material transitions from a cracked to a granular stage. Because of these details, our focus is only on the contribution to friction from the form and roundedness of particles. Hence, Eqn. 5.10 can be rewritten as

$$\phi_{CS} = \phi_{CS_o} + \Delta\phi_{CS}, \quad (5.11)$$

where ϕ_{CS_o} does not change between different microstructures, whereas $\Delta\phi_{CS}$ varies as the morphology of fragments change with microstructure.

$$\phi_{CS_o} = 23 - 21.02R_q - 0.861\left(\frac{p'_o}{p_{atm}}\right) + 0.043D_r, \quad (5.12a)$$

$$\Delta\phi_{CS} = -134.06F_{AC} + 142.04I_r. \tag{5.12b}$$

5.2.4.2 Critical state friction angle - Extreme Vertices Model Roundedness

[204] found that the roundedness index (R in Eqn. 5.1) is negatively correlated with the critical state friction angle as

$$\phi_{CS} = 42 - 17R. \tag{5.13}$$

Negative correlation between R and granular friction has been reported in literature by other authors as well [205].

Since computing R is difficult, we have used a closely correlated index - the Extreme Vertices Model (EVM) roundedness index (R_{EV}) developed by [197]. EVM is a surrogate to voxel discretization for storing 3D-binary information. In the voxel analogue, an extreme vertex can be defined as a node where only three edges meet. Figure 5.5 shows a simplistic demonstration of extreme vertices (red dots) for fragments denoted by different colours.

Following [197], EVM roundedness is computed via the followings steps:

1. Determination of extreme vertices in a fragment from the voxel model.

2. Determination of principal directions and transformation to align with

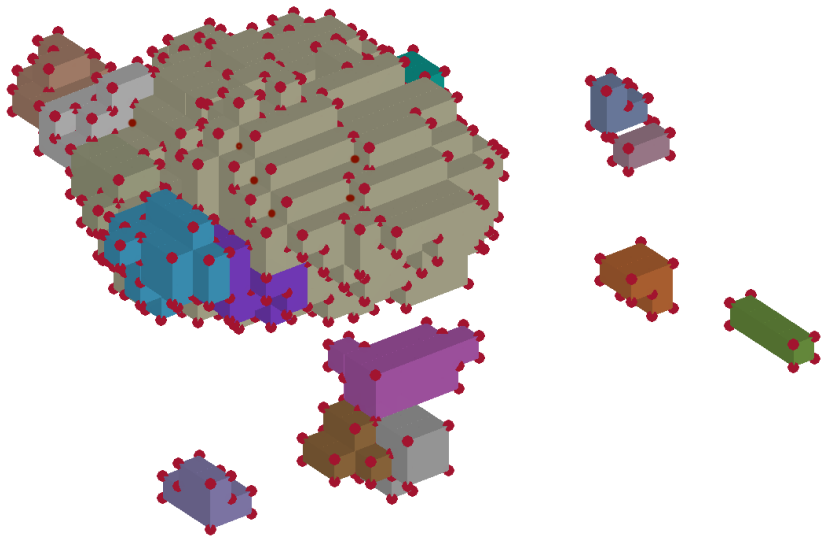

Fig. 5.5. Representative image of voxellized fragments with extreme vertices indicated as red dots.

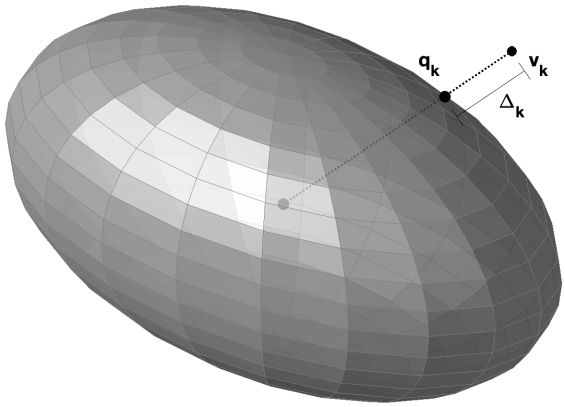

Fig. 5.6. Representative image of the largest ellipsoid inscribed in the orthogonal bounding box containing the fragment aligned along the principal directions.

principal directions

3. Finding the projection of the line joining an extreme vertex (v_k) with the centroid of the equivalent ellipsoid contained within the orthogonal bounding box on the surface of an ellipsoid (q_k); Computation of the distance (Δ_k) between v_k and q_k as shown in Fig. 5.6.

4. Computing the roundedness index as

$$R_{EV} = 1 - \frac{10}{N_{EV}\left(a_{bel}b_{bel}c_{bel}\right)^{1/3}\sum_{k=1}^{N_{EV}}\Delta_k}, \tag{5.14}$$

where $a_{bel}, b_{bel}, c_{bel}$ are the axes lengths of the bounding ellipsoid, N_{EV} is the total number of extreme vertices.

R_{EV} computed from the voxel model is strongly correlated with the Krumbien roundedness (correlation of 0.902) and can therefore be used to determine the

qualitative variation of granular friction between microstructures (Eqn. 5.13).

5.3 Results & Discussion

5.3.1 Resolution dependence of morphological indices

Voxel models are incapable of resolving the shape of objects with size close to the voxel size. For a perfect sphere, the theoretical values of $Form$, I_r, R_{EV} are equal to 1. However as the sphere diameter (d_{sphere}) approaches the voxel size (∇_{res}), the discretized shape differs from that of a true sphere, as does the morphological indices. As an example, in Fig. 5.7a, $d_{sphere} = 2\nabla_{res}$. The random placement of the sphere centroid leads to specific geometries with the morphological index values and the corresponding friction coefficient (Eqn. 5.12b) differing significantly. As the resolution is improved to $d_{sphere} = 4\nabla_{res}$ (Fig. 5.7b) and $d_{sphere} = 10\nabla_{res}$ (Fig. 5.7c), the discretized sphere approaches an actual sphere in appearance and the variation in index values reduces. Figure 5.8 shows box plots of index values: $Form$ (Fig :5.8a), I_r (Fig :5.8b), R_{EV} (Fig :5.8c) with varying resolution for 100 random simulations at each resolution. The range of values is shown by the vertical line, outliers are marked as circles, the median value is denoted by a black dot, and the 25^{th} and 75^{th} percentile values

are denoted by thick lines. With improved resolution, not only does the variation in index values reduce, but the values also approach unity. It is worth noting that while $Form$ is bounded between 0 and 1, R_{EV} only has a theoretical upper bound of 1 and I_r is not bounded [194]. All three indices approach 1 for a perfect sphere.

5.3.2 Constant volume fraction of defects

The motivation of this work is to explore the implications of material processing on impact performance with the goal of suggesting processing modifications that will improve performance by modifying granular friction. One way to control the microstructure is by controlling the kind, shape, size, and spacing of defects in the material. These defects can be either pores or secondary phases [42] in the material. For pressure assisted densified boron carbide, the free carbon added during material processing are graphitic inclusions which become defects in the final ceramic and serve as microcrack initiation sites [133, 183]. The amount of carbon added affects the material porosity, the underlying defect density and the corresponding defect size. Each of these individually affect the impact performance via crack growth as discussed in chapter 4 In addition, it is also of interest to understand the influence on granular friction at a constant carbon percentage but varying defect size. For the same carbon content, larger graphitic inclusions lead to larger and more sparsely

$\frac{d_{sphere}}{\nabla_{res}} = 2$

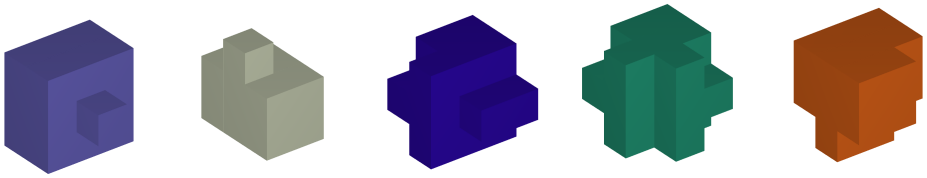

I_r	0.8354	0.7979	0.8267	0.8400	0.8299
$Form$	0.7777	0.6705	0.8705	0.9239	0.7886
$\Delta\phi_{CS}$	14.4067	23.4494	0.7219	-4.5548	12.1587
R_{EV}	0.4646	0.5410	0.6134	0.6963	0.8246

(a)

$\frac{d_{sphere}}{\nabla_{res}} = 4$

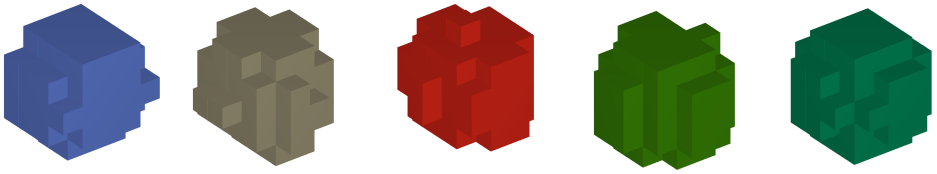

I_r	0.9265	0.9228	0.9249	0.9174	0.9216
$Form$	0.8820	0.8860	0.8561	0.8963	0.9113
$\Delta\phi_{CS}$	13.3550	12.3058	16.6009	10.1383	8.7288
R_{EV}	0.7595	0.8092	0.8242	0.8412	0.8616

(b)

$\frac{d_{sphere}}{\nabla_{res}} = 10$

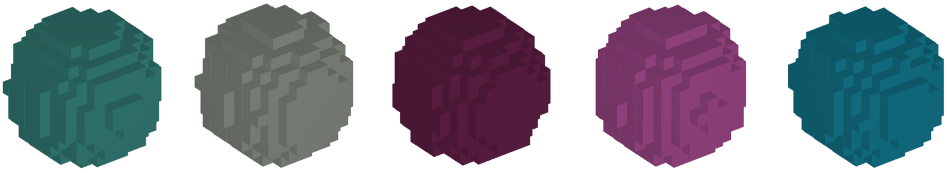

I_r	0.9797	0.9807	0.9846	0.9790	0.9758
$Form$	0.9766	0.9629	0.9850	0.9581	0.9791
$\Delta\phi_{CS}$	8.2314	10.2077	7.8148	10.6198	7.3460
R_{EV}	0.8927	0.9011	0.9015	0.9016	0.9032

(c)

Fig. 5.7. Resolution dependence of morphological indices: (a) $d_{sphere} = 2\nabla_{res}$, (b) $d_{sphere} = 4\nabla_{res}$, (c) $d_{sphere} = 10\nabla_{res}$.

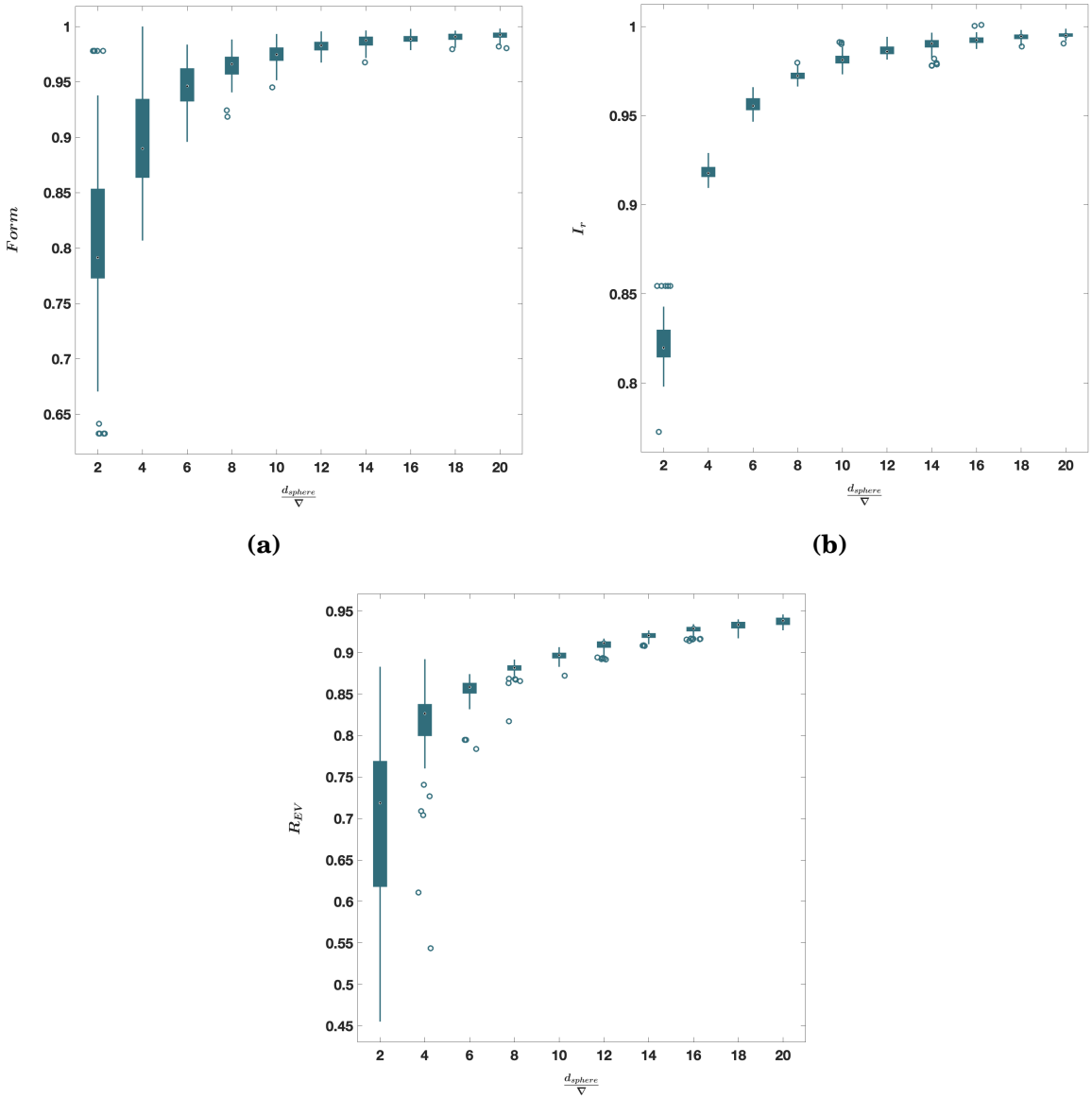

Fig. 5.8. Box plots showing the spread of morphological indices for a sphere with varying resolution: (a) $Form$, (b) I_r, (c) R_{EV}.

populated defects. However it is not clear whether the defect thickness scales proportionally with the defect size. Hence we have studied two different cases: one case in which we assume the defect thickness remains constant as defect size increases and the other case in which the thickness scales proportionally with the defect size. Since the model material is boron carbide, we shall hereafter refer to the two cases as constant carbon and constant initial damage, respectively. From a modelling perspective, since all flaws are assumed to be of the same size, the former means a constant value of $\eta_{flaw}{s_{flaw}}^2$, while the latter means a constant value of $\eta_{flaw}{s_{flaw}}^3$ or Ω_i. We have studied the fragmentation and fragment morphology for four different cases summarized in Tab. 5.2 for varying initial defect sizes between $2 - 20\mu$.

Table 5.2. Cases of constant values of initial carbon and initial damage content studied.

Constant carbon Ω_i/s_{flaw} in m^{-1}		**Constant damage** Ω_i	
2200	4400	0.022	0.044

5.3.2.1 General morphological trends

Figures 5.9a,5.9b, 5.9c show the variation in the average values of $Form$, I_r, and R_{EV} at a given d_{frag} for $\Omega_i = 0.022$ and varying initial defect sizes (s_{flaw}). $\mathcal{F}_{sphere}$, $\mathcal{I}_{sphere}$, $\mathcal{R}_{sphere}$ correspond to the average values of $Form$, I_r, and R_{EV},

respectively, for a true spherical shape. The lines serve as references for resolution dependence of morphological indices. The inset images show the relative variation in standard error at three d_{frag} values for $s_{flaw} = 2\mu$ and 14μ. The standard error insets provide information about the variability of index values across fragment sizes. The scale for standard error bars in the three plots are varied to facilitate visualization.

Figure 5.9d shows the variation in the total number of fragments (N_{frag}) at a given d_{frag} and s_{flaw}. N_{frag} decreases with increase in d_{frag}. This implies that statistical significance of morphological estimates increases with decrease in d_{frag}.

Initially, with increase in d_{frag}, fragments become less platy and more rounded, as conveyed by the initial rise in $Form$ and R_{EV}. However, we suspect this could largely be an artifact of resolution dependence (Fig. 5.8) of morphological indices: the initial rise in $Form$ mimics $\mathcal{F}_{sphere}$. Thereafter, $Form$ seems to decrease with increase in d_{frag} as the resolution effect dies off. The trend becomes more noisy and less reliable as d_{frag} increases beyond 10μ. This is largely a consequence of more statistical error due to a reduction in N_{frag} at larger d_{frag}, as seen in Fig. 5.9d. For larger d_{frag}, the trends observed for larger s_{flaw} are slightly more reliable as indicated by the standard error plot. The error increases more with increase in d_{frag} for $s_{flaw} = 2\mu$ than for $s_{flaw} = 14\mu$. $Form$ increases with d_{frag}, until it reaches a peak value and then starts decreasing

with increasing fluctuations as the corresponding sample size (N_{frag}) decreases. An intermediate plateau region is observed only for $s_{flaw} = 2, 8\mu$. This suggests that after accounting for resolution dependence, platiness of fragments increases with increase in d_{frag}. For the region of statistically significant N_{frag}, there appears to be a decrease in $Form$ with increase in s_{flaw} at a given d_{frag}.

On the other hand, I_r does not depend significantly on s_{flaw} (Fig. 5.9b). I_r does, however, increase with increase in d_{frag}. This effect is much stronger than any resolution dependence observed in Fig. 5.8b, or the $\mathcal{I}_{sphere}$ values conveying resolution effects in Fig. 5.9b. Furthermore, I_r does not seem to plateau as the resolution effect decreases with increase in d_{frag}. Maximum roundedness ($I_r = 1$) is observed around $d_{frag} \sim 11-15\mu$. Unlike R_H and R_{EV}, I_r is not bounded by unity although $I_r = 1$ signifies maximum roundedness [194]. Similar to Fig. 5.9a, standard error for larger d_{frag} is higher for $s_{flaw} = 2\mu$ than $s_{flaw} = 14\mu$.

R_{EV} initially increases sharply with increase in d_{frag} and then plateaus until it reaches a value between $0.7 - 0.8$ as the resolution dependence dies off (Fig. 5.9c). R_{EV} decreases with increase in s_{flaw}, until around $d_{frag} = 7\mu$ after which the trend either ceases or slightly reverses. It is not clear whether this is an actual trend due to insufficient N_{frag}. For $d_{frag} > 7\mu$, R_{EV} at a given d_{frag} seem to be less sensitive to s_{flaw}. The standard error increases with increase in d_{frag} and decreases with increase in s_{flaw}.This result coupled with the previous

observations, indicate that fragments become less rounded or more angular with increase in initial flaw size, at least for small flaw sizes, before becoming independent of flaw size for larger flaw sizes.

5.3.2.2 Average particle friction

While Fig. 5.9 gives an estimate of the nature of morphology variation with initial defect size for fragments of comparable sizes, it does not provide information about the overall variation in bulk friction. Although the trends suggest an increase in granular friction with s_{flaw} at a given d_{frag} because of an increase in particle angularity, the effect of changes in particle gradation manifested by the variation in size distribution (Fig. 5.9d) is not well understood.

While [185] studied different kinds of granular media with varying gradation, [204] studied particles at a constant size. [206] showed that average granular friction of reconstituted sand sample with varying particle gradation is closely correlated with average granular friction of individual samples weighted by their contribution in the mix. In order to obtain global average measures of granular friction, we have weighted the morphological indices with respect to size, surface area, and volume (or weight) of individual fragments. We observed that the overall trends do not significantly differ with either technique, although the absolute values change.

Given the low level of fragmentation chosen to preserve fragment morphol-

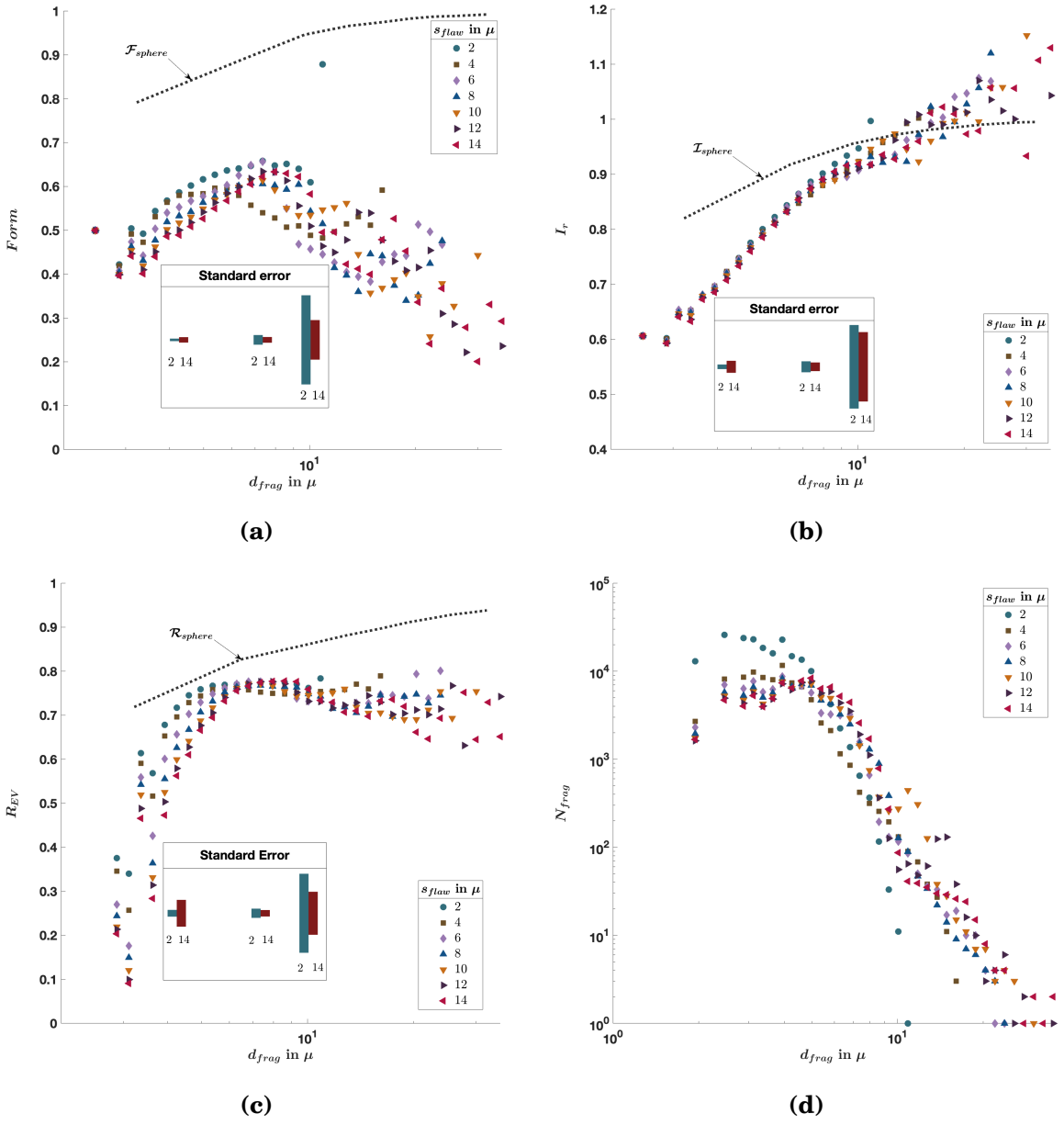

Fig. 5.9. Average values of morphological indices and total number of fragments at a given d_{frag} for varying s_{flaw} and constant initial damage, $\Omega_i = 0.022$: (a) $Form$, (b) I_r, (c) R_{EV}, (c) N_{frag}.

ogy, we do not obtain large fragments. This leads to a significant portion of fragments with resolution dependence. One way to overcome this resolution dependence is by excluding smaller fragments while averaging index values over the entire range of fragment sizes.

Figure 5.10 shows the average values of $Form$, I_r, R_{EV}, $\Delta\phi_{CS}$ weighted by the surface area of an equivalent ellipsoid for each particle size ignoring fragments smaller than or equal to 6 times the resolution size. The platiness of particles indicated by $Form$ increases with increase in s_{flaw} for both the constant damage and constant carbon cases (Fig. 5.10a). When Ω_i is held constant, I_r increases with increase in flaw size initially, and becomes less sensitive to flaw size thereafter. Whereas, for the constant carbon case (Ω_i/s_{flaw}), after an initial increase, I_r decreases with increase in s_{flaw}(Fig. 5.10b). This implies an initial increase in roundedness with increase in initial flaw size followed by either a decrease in roundedness for the constant carbon case or saturation for the constant damage case. In Fig. 5.10d, Eqn. 5.12b is used to calculate the relative change of the contribution to critical state friction from morphology for varying initial flaw size. Friction angle increases initially with s_{flaw} until it becomes less sensitive to flaw size beyond $s_{flaw} = 10 - 12\mu$. The other measure of roundedness, R_{EV}, is less sensitive to s_{flaw} for the constant damage case, and decreases with increase in s_{flaw} for the constant carbon case (Fig. 5.10c). Since R_{EV} is highly correlated with the Krumbien roundedness (R), this implies the

existence of an optimal flaw size that minimizes roundedness and maximizes the critical state friction angle (Eqn. 5.13).

It is worth noting that similar initial damage or a constant ratio of initial flaw size and flaw spacing does not lead to an exactly similar fragmented microstructure scaled by initial flaw size. The is revealed by the micro-mechanics of wing crack growth (Eqn. 26 in [118]). The rate of crack growth does not scale with initial flaw size, even if the wing crack length did. Hence the fragment sizes and the morphological trends are not a function of microstructure scaling alone. The current work assumes flat wing crack faces, any tortuosity in wing crack path prior to crack coalescence is not captured by this model.

5.3.3 Design implications

Although intuition might suggest smaller, closely placed flaws are more desirable for furnishing strength, this might not hold for penetration resistance. The deformation response in the region under the impactor is most sensitive to the friction parameter (Chapter 4). Irrespective of whether defect thickness is assumed to scale proportionally with defect size (constant damage) or remains constant (constant carbon), for a fixed volume fraction of defects, our results suggest that an optimal flaw size and flaw density would maximize granular friction.

In addition, at constant damage/carbon, flaw density decreases with in-

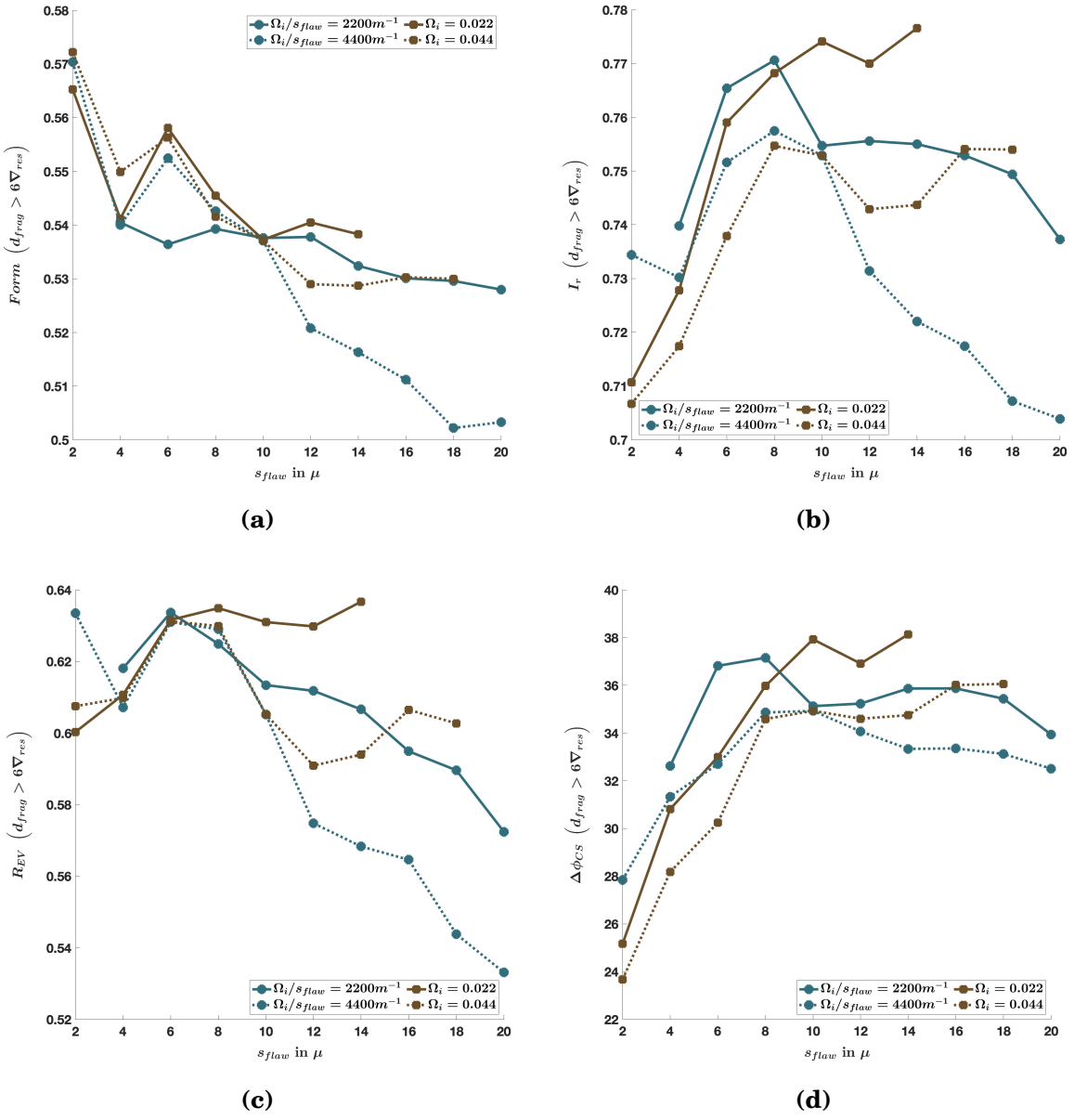

Fig. 5.10. Global average values of morphological indices and corresponding contribution to critical state friction angle for fragments larger than 6 times the resolution size: (a) $Form$, (b) I_r, (c) R_{EV}, (c) $\Delta\phi_{CS}$.

crease in flaw size leading to larger fragments. [188] observed that coarser fragments were correlated with increase abrasion resistance of ceramics. This is consistent with our observation of larger sparsely spaced defects, typically associated with coarser fragments leading to higher granular friction. One might expect smaller particles to play an important lubricating role in friction. At constant void ratio and morphology, ultimate granular friction increases with increase in particle size even though peak friction angle remains unchanged [207]. Although the exact nature of such dependence has not been quantified, it can be argued that this will lead to higher critical state friction for higher flaw size.

Based on the arguments above, there might exist an optimal flaw size and flaw density that improves granular friction and energy dissipation while reducing the extent of cracking. It is therefore necessary to carefully explore this link, both numerically and experimentally, between material microstructures and granular friction for different ceramics, and use it to suggest an optimal microstructure.

5.4 Conclusion

A previously developed anisotropic crack growth model is used to predict input crack statistics for a modified three dimensional crack coalescence and

fragmentation model. The resulting fragments are then used to estimate commonly used morphological indices for varying initial microstructures at a consistent level of fragmentation. Existing literature is then used to establish the connection between fragment morphology and the resulting bulk granular friction. The results suggest that, contrary to intuition, for the same overall defect content, fine distributed defects might not maximize bulk granular friction. Rather, for a constant defect content, an optimal defect size will enhance impact performance. The study thereby provides a crucial and previously unexplored link between ceramic microstructure and properties of the granular material in the Mescall zone under the indenter. It also highlights the importance of numerical and experimental evaluation of optimal microstructure for different ceramics.

Chapter 6

Summary & Future Directions

6.1 Summary

In chapter 2 a three dimensional fragmentation and crack coalescence model has been developed to predict initial fragments before the onset of granular mechanics in impacted ceramics. The fragmentation model employs a continuum damage model to predict instantaneous crack populations based on information from the initial microstructural defect characterization. Rapid and competitive crack coalescence is addressed via an approximate approach referred to as the coalescence zone approach. Discrete 3D cracks with coalescence zones are simulated in a voxellized space and fragment statistics are inferred. The fragmentation model can thus predict an evolving fragment distribution with crack growth in the material. A novel metric, described as the Effective Fragmenta-

tion Ratio, is used to estimate the extent of fragmentation in a material. Based on a critical threshold of this ratio, a new granular transition criterion has been established after conducting a parametric study on ceramic fragmentation. A simple phenomenological model also predicts a general granular transition criterion with a similar form that can be implemented for different damage models and crack orientations. The advantages of this model are:

1. The model predicts fragment statistics from initial defect statistics and can be used to calibrate granular flow models of comminuted ceramics.

2. The fragmentation tool is general and not tied to a particular damage model used to predict crack growth.

3. The general form of the granular transition criterion is applicable for any initial defect size and orientation distribution, and can be implemented for in any continuum crack growth model as a switch to activate granular physics.

It should be noted that since the fragmentation model only explored compression crack growth, the granular transition criterion and the resulting fragment statistics are not applicable for situations where tensile cracking leads to material failure.

In chapter 3 the granular transition criterion and new experimental data was used to recalibrate an integrated ceramics model and implemented for

ABAQUS simulations of impact experiments on boron carbide. The predictions for two different granular flow models were compared. The key takeaways from this work are as follows:

1. Recalibration leads to more accurate reproduction of failure patterns, observed via damage and density localization in impact experiments.

2. Breakage mechanics model of granular flow demonstrates better localization of cone crack like features than classical Drucker Prager plasticity model.

3. Damage front velocity in Edge On impact experiments is not well matched. This indicates lack of physical understanding of the wave velocity, the propagation of damage after the onset of phase transition due to amorphization.

In chapter 4 a sensitivity analysis study was performed on model outputs of sphere indentation simulations, and the connections of trends and predictions to physical mechanisms were intuitively argued. The results have important implications as summarized below:

1. Identifying the most significant model parameters and their corresponding trends provides valuable feedback to guide material processing. In other words it helps optimize material modification efforts by gearing them towards improving a sensitive material property.

2. It assists the materials-by-design loop in the MEDE program in prioritizing calibration experiments for new material iterations.

In chapter 5, the microstructure dependence of initial fragment morphology has been explored via a modified version of the fragmentation and crack coalescence model (Chapter 2). An anisotropic continuum damage model is used to provide input crack statistics to the fragmentation model. The results of this model indicate the following:

1. Material microstructure influences initial fragment morphology and thereby granular friction. Hence, initial microstructure and initial properties of granular flow are correlated.

2. An optimal defect size and spacing for a fixed free carbon content in boron carbide will lead to more angular fragments, help improve granular friction and thereby the penetration resistance of materials.

6.2 Future Directions

6.2.1 Carbon varying fragmentation of boron carbide

Although reducing the total amount of free carbon content in boron carbide improves material properties, lowering it for commerical production is often challenging and has its own drawbacks. Chapter 5 of the thesis sheds light on the importance of optimizing free carbon size distribution at a constant carbon content. The work needs to be validated by investigating the fragmentation of boron carbide with varying degrees of carbon content. One way to do so is by adding the same percentage of carbon during the sintering process, but varying the sizes of the graphitic inclusions. This will help judge whether larger sparsely spaced carbonaceous defects are more favorable than smaller dense defects. It is possible that the implications on impact performance are more complicated than a direct dependence through granular friction. This is because crack growth independently affects the impact performance of a ceramic irrespective of its correlation on fragment morphology and granular friction. It is also possible that at certain defect sizes and spacings, crack growth might initiate from pores as well. While the answer is not straightforward, experimentally exploring the morphological trends on microstructure is necessary.

In addition, it is of interest to evaluate the granular friction of fragments resulting from various microstructures. Despite abundance of literature on the dependence of granular friction on morphology, the dependence on size and grading is still not well understood, especially for very low initial porosity systems. It should also be noted that although important for penetration resistance of a ceramic, granular friction might not be the most important variable for all quantities of interest as indicated in chapter 4.

6.2.2 Sensitivity Analysis

Chapter 4 ignored the effect of amorphization parameters on outputs of sphere impact and edge on impact experiments. Amorphization, however, might play a significant role at higher impact velocities or for other kinds of impact experiments such as dynamic Vicker's indentation experiment. One possible future direction could be exploring the sensitivity of model outputs on amorphization parameters in these experiments and/or at high impact velocities. Another direction is using the existing simulation data to investigate other output metrics, such as energy dissipation due to granular flow. While the sensitivity study ranks the parameters based on their importance, it does not take into account the processing cost associated with changing each parameter. For commercial production, performance and cost optimization is necessary. One way to do so is by quantifying the cost associated with modifying each of the im-

portant model parameters and then investigating performance maximization at a given cost using the regression fit from chapter 4.

6.2.3 Structural Fragmentation

Fragmentation models developed in chapters 2 and 5 focus on microstructure driven fragmentation and granular transition, as observed in the Mescall zone. In addition to this, fragmentation might also be dominated by the geometry and loading conditions. This large scale fragmentation phenomenon is driven by the structure and wave interactions in a material. Understanding the sizes and kinetic energy of these large fragments is necessary in shielding applications [208] and planetary sciences [209]. One way to estimate the sizes of such fragmentation is via macroscale simulations using finite element methods or particle based methods. Another way of estimating structure-driven fragmentation is via phenomenological models, calibrated and validated against experimental data.

In appendices A and B, approaches to estimate compressive brittle structural fragmentation were discussed. Each of these approaches have their own limitations. FEA modelling of structural fragmentation, often underestimates the fraction of the region under structural fragmentation. Fragment statistics determined from finite element modelling are limited by resolution dependence associated with element size selection, approximation of cracks as high dam-

age/high porosity or low density regions. The phenomenological model has its own limitations stemming from the assumptions of parallel crack planes and weak zones driving failure. Failed area fraction based fragmentation criterion, shown in figure B.4, is not validated against experimental data. However, despite the many limitations, these approaches provide starting points for evaluating the extent of structural fragmentation and the fragment statistics. In future, experimental study on fragmentation of carbon varying boron carbide, such as Kolsky bar experiments for different microstructures and specimen shapes (eg: dumbbell, cuboid, and cylindrical), will provide valuable data for calibrating/validating structural fragmentation models with specific emphasis on microstructure dependence of fragmentation.

Appendix A

Structural Fragmentation - ABAQUS simulations

The following sections will discuss structural fragmentation estimated from split-Hopkinson pressure bar (Kolsky bar) experiments and discuss ways of estimating a comprehensive fragment size distribution after accounting for both microstructure-driven and structure-driven fragmentation.

A.1 ABAQUS simulations of Kolsky bar experiments

At high strain rates, given the small specimen dimension in Kolsky bar experiments compared to wave velocity, a steady stress state is reached soon after

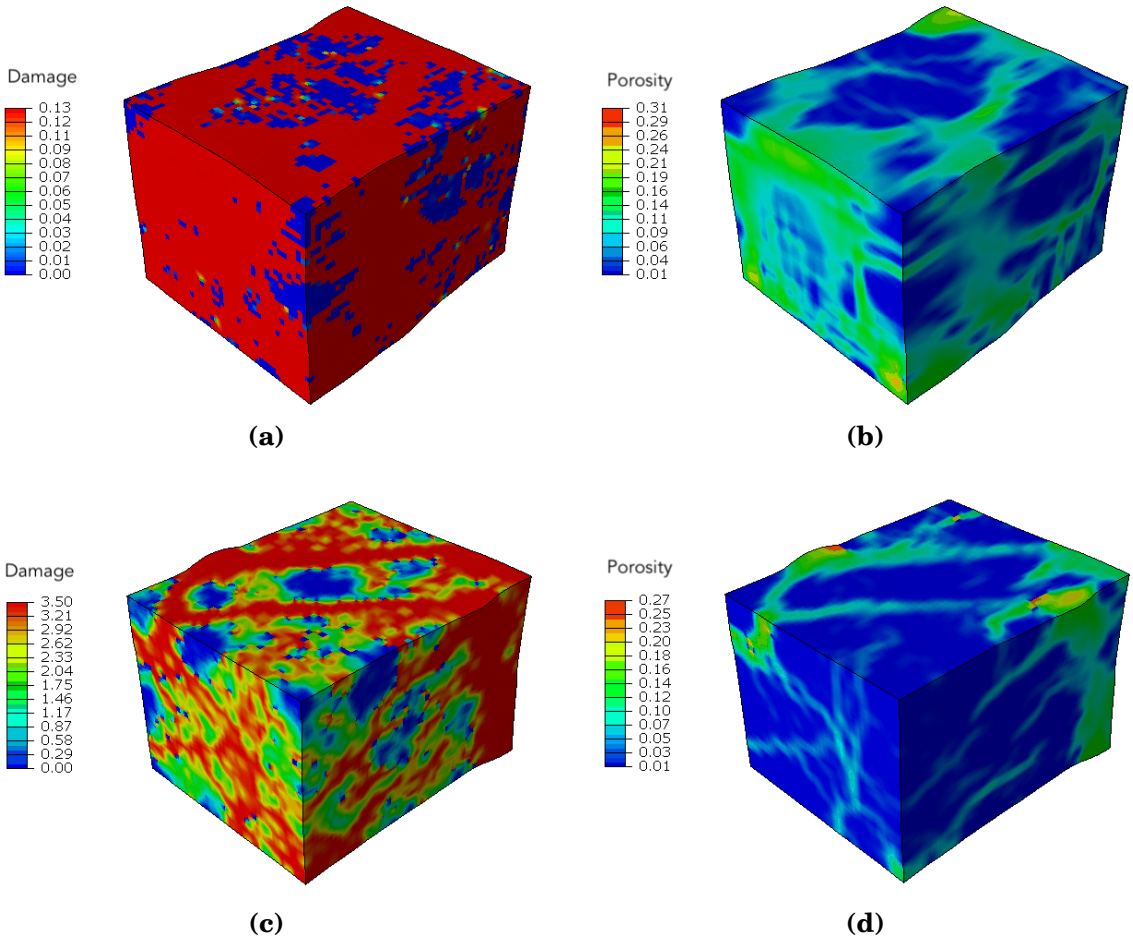

Fig. A.1. Damage and Porosity contours for ABAQUS simulations of unconfined Kolsky bar experiments at strain rate of 465 s^{-1}: (a) Damage contour for $\Omega_f = 0.125$, 20 μs after impact; (b) Porosity contour for $\Omega_f = 0.125$, 20 μs after impact; (c) Damage contour for $\Omega_f = 3.5$, 33.6 μs after impact; (b) Porosity contour for $\Omega_f = 3.5$, 33.6 μs after impact.

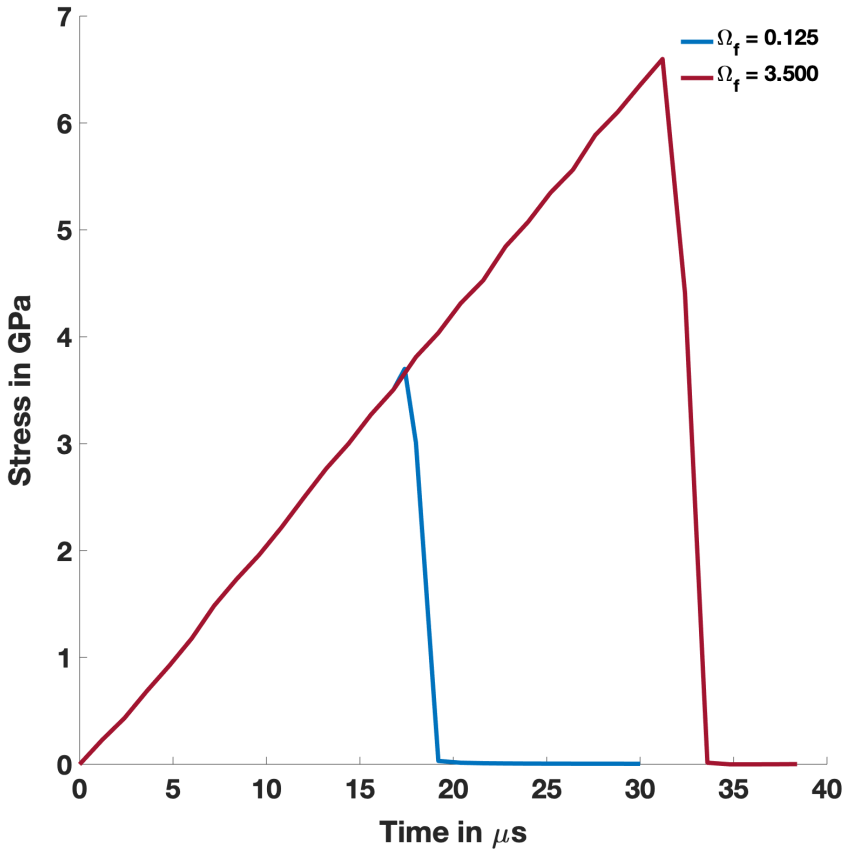

Fig. A.2. Stress time curve of ABAQUS simulation of unconfined dynamic Kolsky Bar experiment at strain rate of 465 s^{-1}.

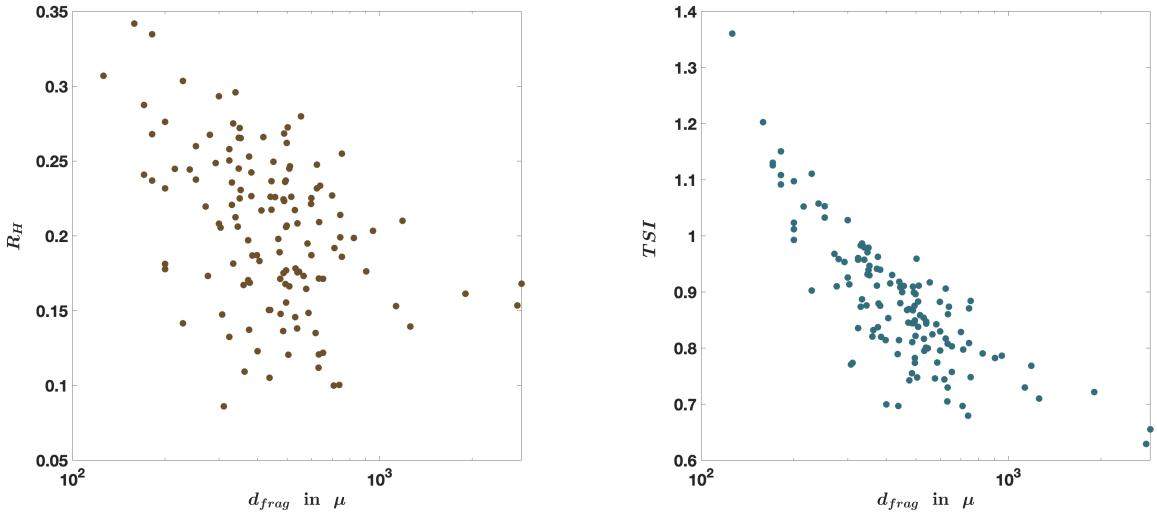

Fig. A.3. Fragment Statistics obtained from ABAQUS simulations of unconfined Kolsky bar experiments at strain rate of 465 s^{-1} and $\Omega_f = 0.125$: (a) Roundedness Index (R_H); (b) True Sphericity Index (TSI).

impact. Structural fragmentation of PAD B4C in unconfined dynamic Kolsky bar experiment conducted in [105] is simulated in ABAQUS using the integrated ceramics model described in chapter 3 with the CBM model for granular flow. The model setup is similar to [90]. C3D8R elements, 100 μ in size, are used to model the sample. 100 μ is the approximate limit of structural fragmentation observed in [105]. Further refinement of resolution will make the homogenization schemes adopted in the integrated model questionable. The list of material parameters are summarised in Tab. 3.1. Two different transition damage criteria are studied: (a) $\Omega_f = 0.125$ [82], (b) $\Omega_f = 3.5$ (Sec. 3.3.1.1). Figure A.1 shows the damage and porosity contours for the two different transition criteria. A higher damage threshold leads to a lower volume of granular

region, and more localized damage. Porosity shows much better localization into crack like features in either case than damage. The % damaged region represents the % of the volume under microstructural fragmentation. This is higher than what is typically observed in experiments, in either case. It is so cause cracks are represented as bands of damaged region rather than a network of micro-cracks. Figure A.2 shows a comparison of the change in stress for the two different transitional damage criteria. At a peak strength value of 3.7 GPa, $\Omega_f = 0.125$ shows a much better agreement with experimentally observed peak strength values (3.9 GPa in [105]). Hence it is possible that for unconfined Kolsky bar experiments, structure driven fragmentation dominates the response, unlike microstructure driven granular transition observed in Mescall region. Structure driven fragmentation is dependent on specimen geometry and is expected to occur at lower levels of fragmentation. In either case the average stress rate of around 210 $MPa/\mu s$ is close to what is observed in the experiments. Fragments representative of the structure dependent regime are then extracted from the porosity map. A porosity threshold of 0.1 is chosen to delineate unfragmented region from macrocracks. MATLAB function bwconncomp is used to extract the connected regions, followed by a dilation procedure. MATLAB function regionprops3 is then used to estimate the fragment statistics. It is worth noting that the thickness of macrocrack-like features observed in simulation is dependent on resolution. This is the reason why di-

lation is adopted even though it might mean assuming negligible macrocrack thinckness, which might not as well be accurate. Figure A.3 shows the aspect ratio roundedness index (R_H) and true sphericity (TSI) indices for structural fragments. These measures, are resolution dependent and can at best represent a qualitative relationship with fragment size. For fragment sizes close to the resolution size, surface area calculation using Crofton formula is inaccurate [201, 202], and this can lead to illogical R_H and TSI values.

A.2 Resolution dependence of fragment statistics

Surface area (or perimeter in 1-dimension) measurements are dependent on resolution size (∇). This effect was explored by [210] while calculating the perimeter of Great Britain. In general, a simplistic measure of surface area relative to resolution size can be expressed as

$$\mathcal{S}(\nabla) = C_{\mathcal{S}} \nabla^{2-D_{frac}}, \tag{A.1}$$

where $C_{\mathcal{S}}$ is a constant and D_{frac} is the fractal dimension. D_{frac} is related to surface roughness. It is equal to 2 for very smooth surfaces and equal to 3 for rough surfaces. So the surface area at two different resolution sizes ∇_1, ∇_2 are

related to each other as,

$$\mathcal{S}(\nabla_2) = \mathcal{S}(\nabla_1)\left(\frac{\nabla_2}{\nabla_1}\right)^{2-D_{frac}}. \tag{A.2}$$

Since, R_H, TSI are all dependent on $\mathcal{S}$, they must be dependent on ∇ as well. From Eqns. 5.7, 5.8, A.2, indices R_H, TSI at resolutions ∇_1, ∇_2 are dependent as given by Eqn. A.3 and Eqn. A.4 respectively.

$$R_H(\nabla_2) = R_H(\nabla_1)\left(\frac{\nabla_1}{\nabla_2}\right)^{2-D_{frac}}. \tag{A.3}$$

$$TSI(\nabla_2) = TSI(\nabla_1)\left(\frac{\nabla_1}{\nabla_2}\right)^{2-D_{frac}}. \tag{A.4}$$

Assuming $D_{frac} = 2.3$, for $\nabla_1 = 100$ and $\nabla_2 = 5$, $R_{H2} = 0.4071 R_{H1}$ & $TSI_2 = 0.4071 TSI_1$. Subscript 1 and 2 indicate resolution ∇_1 and ∇_2 respectively. Figure A.4 shows the roundedness index and true sphericity index for microstructural fragments and structural fragments obtained from ABAQUS simulations of unconfined Kolsky bar experiments at strain rate of 465 s^{-1} and $\Omega_f = 0.125$. The R_H and TSI values for structural fragments have been corrected for resolution size of microstructural fragments. For fragments around twice the resolution size, accuracy is low due to limitations of the Crofton formula as discussed before. This low accuracy region is demonstrated in Fig.

A.4 using yellow bands. The transition region is represented by a gray band between 70 μ and 150 μ.

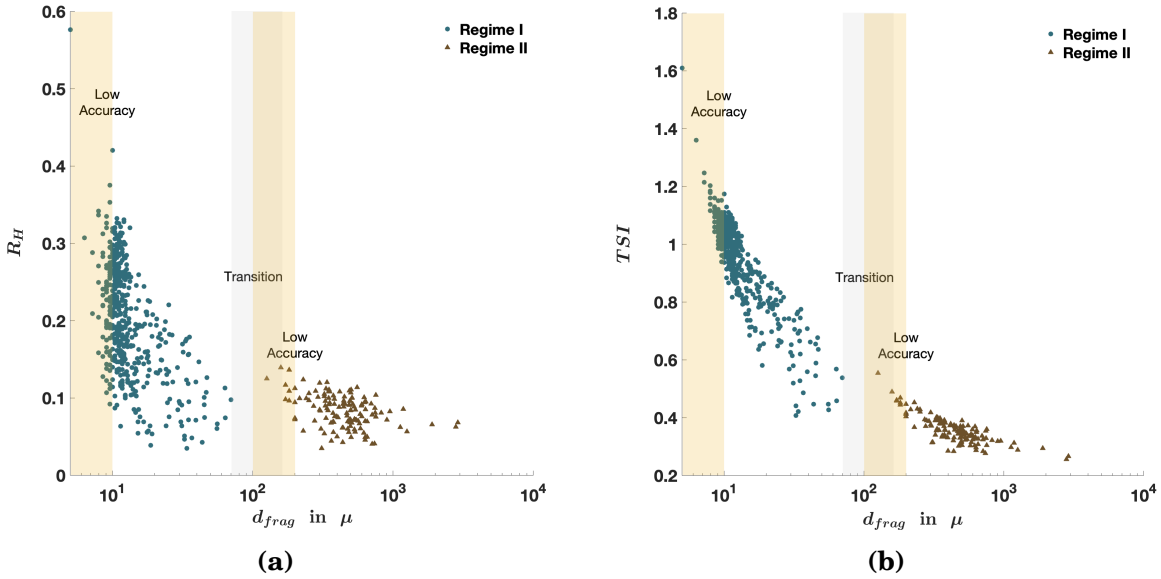

Fig. A.4. Fragment statistics using fragmentation model (Chapter 5) for $trace(\Omega) = 2$ and resolution corrected statistics from ABAQUS simulations of unconfined Kolsky bar experiments at strain rate of 465 s^{-1} and $\Omega_f = 0.125$: (a) Roundedness Index (R_H); b) True Sphericity Index (TSI).

Appendix B

Structural Fragmentation - Phenomenological Model

This appendix section discusses the development of a phenomenological model that can be used to predict a structural fragmentation criterion and macroscale fragment size distribution.

[105] concluded that fragmentation occurs in two different regimes. A microstructure controlled regime and a structure dependent fragmentation regime. The latter is a consequence of the coalescence of axial and transverse cracks, in addition to being particularly influenced by the specimen geometry and boundary conditions. We have assumed that large scale weak zones in addition to interactions with the specimen boundary leads to such fragments. The initiation of such weak zones in quasistatic loading conditions is clearly from the

largest microcracks lying along favorable crack growth directions leading to the formation of macro-crack features. However, in dynamic loading conditions, macrostructural fragmentation is dominated by very few large cracks. It can be hypothesized that some micro-cracks together lead to weaker zones that subsequently become responsible for macro-crack driven structural fragmentation. This kind of fragmentation is not completely independent of the microstructure but is also significantly influenced by the stress state and the strain rate. In our problem, these weak zones comprise structurally failed micro-slabs of material contained between wing crack planes (Fig. B.1). These microcracks under uniaxial compression are assumed to fail due to linear elastic buckling. Figure B.1a shows a microstructure under compression with wing cracks growing from defects. These defect-wing crack assemblies are simplified as cracks growing along the direction of compression in Fig. B.1b. Figure B.1c shows shaded weak zones in between cracks that are close to each other. These weak zones comprise microslabs of material contained between wing crack planes, that fail under uniaxial compression due to linear elastic buckling (Fig. B.1d). Such a micro-column of width, h_{col} and length, ℓ_{col} (length of overlap of cracks) buckles when $\sigma_c \geq \sigma_{cr}$, where σ_c is the maximum principal compressive stress and σ_{cr} is the critical buckling stress of the column.

Assuming pinned connections, $\sigma_{cr} = \frac{\pi^2 E {h_{col}}^2}{12 {\ell_{col}}^2}$.

APPENDIX B. STRUCTURAL FRAGMENTATION - PHENOMENOLOGICAL MODEL

The buckling criterion can be rewritten as

$$h_{col} \leq \mathcal{H}, \tag{B.1}$$

where, $\mathcal{H} = l_{col}\sqrt{\frac{12\sigma_c}{\pi^2 E}}$.

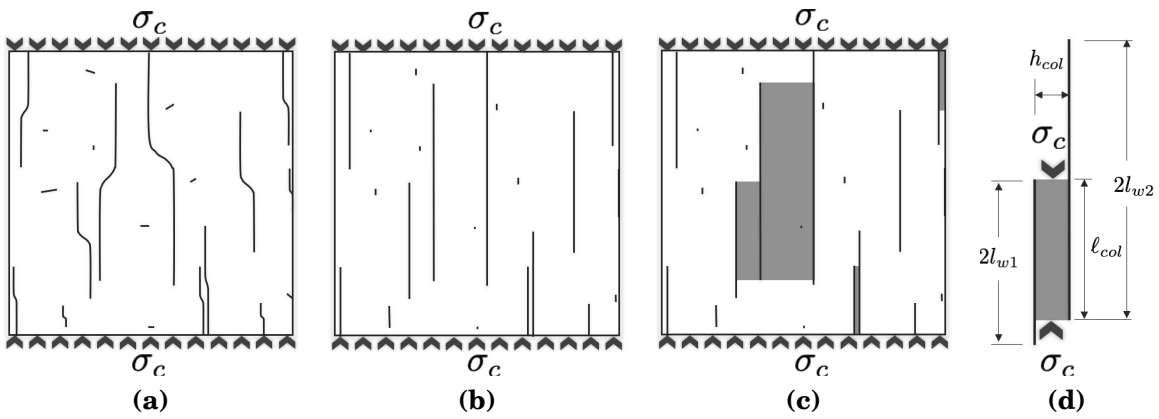

Fig. B.1. Representative image of weak zones in a cracked microstructure. (a) Crack wing crack assemblies, (b) Simplified cracks, (c) Cracked microstructure with weak zones represnted by buckled or failed columns, (d) Enlarged view of a buckled or failed micro-column.

For two successive cracks of wing crack lengths l_{w1} and l_{w2}, two dimensional crack density (η_{2D}), the average distance between two successive cracks ($E\Big[h_{col}(l_{w1}, l_{w2})\Big]$) is given by Eqn. B.2.

$$E\Big[h_{col}(l_{w1}, l_{w2})\Big] = \frac{1}{2\eta_{2D}\Big(l_{w1} + l_{w2}\Big)}. \tag{B.2}$$

This has been calculated by assuming that there is on an average one crack in a box of height ($2l_{w1} + 2l_{w2}$) and width equal to the mean spacing of such

cracks. The height of the box represents the maximum possible distance between the farthest tips of the two cracks of lengths $2l_{w1}$ and $2l_{w2}$, such that overlap can still occur between these cracks. Assuming random crack location, the spacing between two such cracks ($h_{col}(l_{w1}, l_{w2})$) is exponentially distributed (inter-arrival distance of a poisson distribution) as $f_{h(l_{w1},l_{w2})}(h_{col})$ with parameter $\lambda_{1,2} = 2\eta_{2D}\Big(l_{w1} + l_{w2}\Big)$ as shown in Eqn. B.3.

$$f_{h(l_{w1},l_{w2})}(h_{col}) = \begin{cases} \lambda_{1,2}e^{-\lambda_{1,2}h_{col}} & \text{if } h_{col} \geq 0, \\ 0 & \text{if } h_{col} < 0. \end{cases} \tag{B.3}$$

For all cracks having the same wing crack length, l_w, the exponential distribution has a parameter, $\lambda = 2\eta_{2D}l_w$.

For two cracks of lengths $2l_{w1}$ and $2l_{w2}$, the corresponding length of the micro-column ($l_{col}(l_{w1}, l_{w2})$) representing the length of overlap between the two

cracks is distributed as Eqn. B.4.

$$f_{l(l_{w1},l_{w2})}(l_{col}) = \begin{cases} \dfrac{1}{l_{w1}+l_{w2}} & \text{if } l_{col} \in (0, 2min(l_{w1}, l_{w2})), \\ \dfrac{max(l_{w1}, l_{w2}) - min(l_{w1}, l_{w2})}{l_{w1}+l_{w2}} & \text{if } l_{col} = 2min(l_{w1}, l_{w2}), \\ 0 & \text{if } l_{col} \notin (0, 2min(l_{w1}, l_{w2})). \end{cases} \tag{B.4}$$

For all wing cracks having the same length l_w, the length of the micro-column (l_{col}) is uniformly distributed as $f_l(l_{col})$ between $[0, l_w]$. Equation B.5 expresses the distribution of the micro-column length.

$$f_l(l_{col}) = \begin{cases} \dfrac{1}{2l_w} & \text{if } l_{col} \in (0, l_w), \\ 0 & \text{if } l_{col} \notin (0, l_w). \end{cases} \tag{B.5}$$

Using the failure criterion from Eqn. B.1, the probability of a crack being succeeded by a failed-microcolumn can be expressed as,

$$p = \int_0^{2l_w} \left\{ \int_0^{\mathcal{H}} f_h(h_{col})dh \right\} f_l(l_{col})dl_{col} = 1 - \frac{1-e^{-\theta}}{\theta}, \tag{B.6}$$

where, $\theta = 8\Omega_{2D}\sqrt{\frac{12\sigma_c}{\pi^2 E}}$ and $\Omega_{2D} = \eta_{2D}{l_w}^2$ is the two dimensional damage

metric [55].

Similarly, probability of a crack being succeeded by a micro-column that does not fail is $s = 1 - p$.

Since the width of a micro-column is exponentially distributed with parameter λ, the summation of widths of n such micro-columns (h_{col_n}) is erlang distributed as $j_{h_{col_n}}\left(h_{col_n}\right)$ (Eqn. B.7) with shape parameter, n and scale parameter, $\frac{1}{\lambda}$.

$$j_{h_{col_n}}\left(h_{col_n}\right) = \lambda^n \frac{{h_{col_n}}^{(n-1)}}{(n-1)!} e^{-\lambda h_{col_n}}. \tag{B.7}$$

Looking at all possible cases, a crack can either be succeeded by a failed micro-column or n unfailed micro-columns till a failed micro-column is reached. So, our object of interest is the distance h_{col_n}, between a crack and the beginning of the next failed micro-column. Considering one such case with n unfailed micro-columns in between, probability of occurrence is given by $j_{h_{col_n}}\left(h_{col_n}\right)s^n p$. Considering all such possible cases, probability of the distance between a crack and the beginning of the next failed micro-column being $\hbar$ is given by Eqn. B.8.

$$g_{\hbar}\left(\hbar\right) = \begin{cases} \sum_{n=1}^{\infty} j_{h_{col_n}}\left(\hbar\right)s^n p & \text{if } \hbar > 0 \\ p & \text{if } \hbar = 0 \\ 0 & \text{if } \hbar < 0 \end{cases} \tag{B.8}$$

APPENDIX B. STRUCTURAL FRAGMENTATION - PHENOMENOLOGICAL MODEL

One measure of fragment size in the direction transverse to maximum principal compressive stress or the direction of wing crack growth is the width of such contiguous chunks of unfailed columns (Fig. B.2a). Considering that logic, we are only interested in the cases where $\hbar > 0$. So, after simplification, the fragment size (transverse to the direction of maximum principal compressive stress) distribution is given by Eqn. B.9.

$$f_{\hbar}\Big(\hbar\Big) = \begin{cases} \dfrac{g_{\hbar}\Big(\hbar\Big)}{1-p} = p\sum_{n=1}^{\infty}(1-p)^{(n-1)}\lambda^{n}\dfrac{\hbar^{(n-1)}}{(n-1)!}e^{-\lambda\hbar} = \lambda p e^{-\lambda p\hbar} & \text{if } \hbar > 0, \\ 0 & \text{if } \hbar \leq 0. \end{cases} \tag{B.9}$$

So, the structure driven (Regime II) fragment size in the direction perpendicular to maximum principal compression is exponentially distributed with parameter λp. The mean fragment size along this direction (ℓ^{I}_{R2}) is given as,

$$\ell^{I}_{R2} = \frac{1}{\lambda p}. \tag{B.10}$$

Assuming statistical independence of sizes along orthogonal directions, fragment area is a product of two independent exponentially distributed random variables.

The probability distribution of the product, $Z = X_1 X_2$ of two independent random variables, X_1 and X_2, with probability density functions, $f_{X_1}(x1)$ and

$f_{X_2}(x2)$ respectively, can be given as: [211]

$$f_Z(z) = \int_{-\infty}^{\infty} f_{X_1}(x) f_{X_2}(z/x) \frac{1}{|x|} dx. \tag{B.11}$$

For two independent and exponentially distributed random variables, X_1 and X_2, with parameters λ_1 and λ_2 respectively, their product, $Z = X_1 X_2$ is always positive. The probability distribution of Z can be given as (for $Z > 0$):

$$f_Z(z) = \int_0^{\infty} \frac{\lambda_1 \lambda_2}{x} e^{-\lambda_1 x - \lambda_2 z/x} dx. \tag{B.12}$$

Using Eqn. 8.432.6 from [212], Eqn. B.12 can be simplified as,

$$f_Z(z) = 2\lambda_1 \lambda_2 K_0^b\Big(2\sqrt{\lambda_1 \lambda_2 z}\Big), \tag{B.13}$$

where, K_0^b is the modified bessel function of the second kind.

So, if ℓ_{R2}^I is the representative fragment size, the fragment area, a_{frag}^I is distributed as (for $a_{frag}^I > 0$)

$$f_{A^I}(a_{frag}^I) = 2(\lambda p)^2 K_0^b\Big(2\lambda p\sqrt{a_{frag}^I}\Big), \tag{B.14}$$

with mean fragment size of $\left(\ell_{R2}^I\right)^2$. In reality, however, the fragment area will be associated with a shape factor which will depend on the circularity of

fragments.

Another measure of fragment size is the distance between the centers of weak zones (failed micro-columns) as shown in Fig. B.2b. Assuming that the centers of failed micro-columns are randomly distributed, their spacing is exponentially distributed (inter-arrival distance of a poisson distribution). For radially spaced defects in a 2D plane, mean distance between the centers of such failed micro-columns ($\mathfrak{h}$) is related to the number density of failed micro-columns (η_f) as Eqn. B.15. This is calculated by assuming that there is on an average one such failed micro-column in a circle of radius equal to the mean spacing ($\mathfrak{h}$).

$$\mathfrak{h} = \pi^{-1/2} {\eta_f}^{-1/2}, \tag{B.15}$$

where $\eta_f = p\eta_{2D}$.

A fragment size measure along the direction of maximum principal compression (Fig. B.2b) is related to expected value of the projection of $\mathfrak{h}$ along the said direction. For a line joining two failed micro-columns centers (weak zones), inclined at an angle θ_{def} with the direction of maximum principal compressive stress, the mean projection of the line along the principal stress direction is given by Eqn. B.16. This assumes that the spacing between the micro-column centers and the direction of weak zone connection is independent.

$$\ell_{R2}^{II} = \mathfrak{h}\frac{2}{\pi}\int_0^{\pi/2} \cos\theta_{def} d\theta_{def} = \mathfrak{h}\frac{2}{\pi}. \tag{B.16}$$

This measure gives us another estimate of fragment area, a_{frag}^{II}, distributed as (for $a_{frag}^{II} > 0$),

$$f_{A^{II}}(a_{frag}^{II}) = 2(\lambda p)^2 K_0^b\left(2\lambda p\sqrt{a_{frag}^{II}}\right), \tag{B.17}$$

with mean fragment size of $\left(\ell_{R2}^{II}\right)^2$. The average fragment size, and the corresponding area can also be estimated by assuming that Eqn. B.10 and Eqn. B.16 are representative of sizes in two orthogonal directions. Assuming statistical independence between the fragment sizes, the area averaged mean fragment size (ℓ_{R2}^{Area}) can be expressed as,

$$\ell_{R2}^{Area} = \sqrt{\ell_{R2}^{I}\ell_{R2}^{II}}. \tag{B.18}$$

The corresponding measure of fragment area, a_{frag}, is distributed as (for $a_{frag} > 0$)

$$f_A(a_{frag}) = 2\left(\frac{1}{\ell_{R2}^{Area}}\right)^2 K_0^b\left(2\frac{\sqrt{a_{frag}}}{\ell_{R2}^{Area}}\right), \tag{B.19}$$

with mean fragment area of $\left(\ell_{R2}^{Area}\right)^2$.

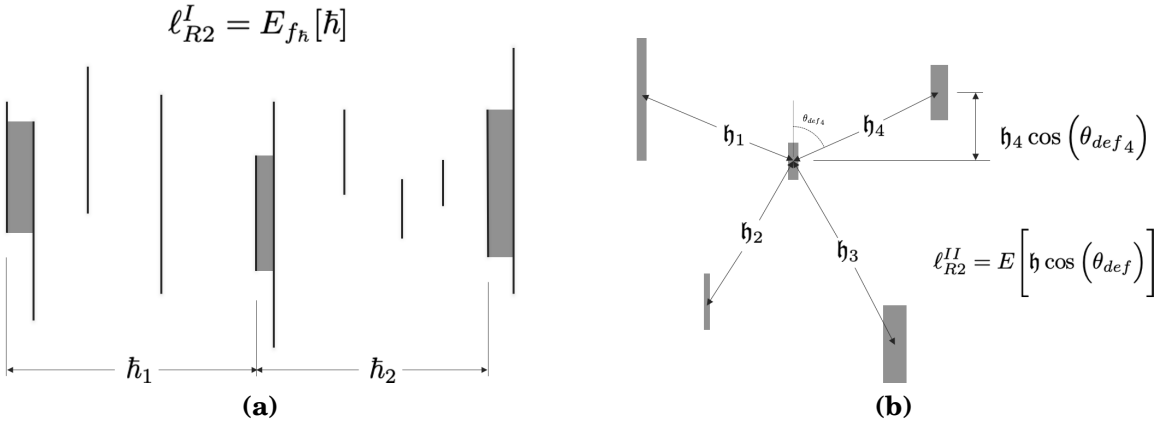

Fig. B.2. Representative image of fragment sizes contained between weak zones. (a) Mean fragment size measure transverse to the direction of maximum principal compressive stress, (b) Mean fragment size measure along the direction of maximum principal compressive stress.

B.1 Fragmentation Criterion - micostructure driven transition

Transition to granular mechanics driven by microstructural fragmentation (Regime I), as discussed in chapter 2, occurs when the wing crack length reaches a certain threshold determined by the initial defect density and defect size. This can be reformulated in terms of a damage based transition criterion as Eqn. B.20. The transition occurs when the current damage exceeds a threshold damage, Ω_f which is a function of the initial damage, Ω_i and two constants C_1, C_2 which are functions of the defect orientation distribution.

$$\Omega_f = \left(C_1 - C_2\Omega_i^{1/3}\right)^3. \tag{B.20}$$

B.2 Fragmentation Criterion - failed area fraction driven transition

Failure in a sample can occur structurally before significant microstructural fragmentation occurs. This is possible in unconfined Kolsky bar experiments, where structural fragmentation can limit the strength of the sample and the extent of microstructural fragmentation.

As the material progressively damages due to wing crack growth from microstructural defects, more and more failed micro-columns or weak zones appear. This leads to an increase in the fraction of material that becomes a weak zone. In this work, the area of failed micro-columns is referred to as failed area, and the percentage of material that is a part of this area is referred to as the failed area fraction.

Using the failure criterion of Eqn. B.1, and the distributions on the lengths (Eqn. B.4) and widths (Eqn. B.3) of micro-columns, the expected value of the area of failed (buckled) micro-column associated with a crack of length $2l_{w1}$

which is succeeded by a crack of length $2l_{w2}$ can be expressed as

$$\begin{aligned} a_f(l_{w1}, l_{w2}) &= \int_0^{2x} \left\{ \int_0^{\mathcal{H}} h_{col} f_{h(l_{w1},l_{w2})}(h_{col}) dh_{col} \right\} l_{col} f_{l(l_{w1},l_{w2})}(l_{col}) dl_{col} \\ &\quad + \left[\left\{ \int_0^{\mathcal{H}} h_{col} f_{h(l_{w1},l_{w2})}(h_{col}) dh_{col} \right\} l_{col} f_{l(l_{w1},l_{w2})}(l_{col}) \right]_{l_{col}=2x} \\ &= \frac{x}{\eta_{2D}(l_{w1}+l_{w2})^2} \left[(3+\theta)e^{-\theta}x + (1-e^{-\theta}-\theta e^{-\theta})\Big(y - \frac{6x}{\theta^2}\Big) \right], \end{aligned} \tag{B.21}$$

where $x = min(l_{w1}, l_{w2}), y = min(l_{w1}, l_{w2})$

and $\theta = \eta_{2D} x(x+y)\sqrt{\frac{12\sigma}{\pi^2 E}}$.

In general, the failed area associated with a crack is an integration of $a_f(l_{w1}, l_{w2})$ over the distribution of crack lengths.

The total fraction of material comprising such failed area is a product of the failed area associated with a crack and the total number of cracks per unit area. Thus, given a certain distribution of wing crack lengths ($f_{wing}(l_w)$), the failed area fraction is given as

$$FAF = \eta_{2D} \int_{l_{lower}}^{l_{upper}} f_{wing}(l_{w1}) \Big[\int_{l_{lower}}^{l_{upper}} a_f(l_{w1}, l_{w2}) f_{wing}(l_{w2}) dl_{w2} \Big] dl_{w1}. \tag{B.22}$$

For all defects being of the same size, FAF can be expressed as,

$$FAF = \frac{1}{4} \left[(3+\theta)e^{-\theta} + (1-e^{-\theta}-\theta e^{-\theta})\Big(1 - \frac{6}{\theta^2}\Big) \right], \tag{B.23}$$

where $\theta = 2\Omega_{2D}\sqrt{\frac{12\sigma}{\pi^2 E}}$.

The average fragment size of PAD B4C, subjected to uniaxial compressive loading at a strain rate of $360s^{-1}$, in the structural fragmentation regime [105] is $290.6\mu m$. A single integration point simulation of this experiment using the [82] model has been performed. Stress and damage, obtained from the simulation is used to compute the FAF using Eqn. B.23. The experimentally measured average fragment size is used to calibrate the EFR threshold necessary for fragmentation to occur. Figure B.3a shows a comparison of the time evolution of the two different average structural fragment measures with the evolution of stress. It is observed that the experimentally measured average structural fragment size corresponds to the post peak strength part of the stress-time curve for ℓ^{I}_{R2}, and before the peak strength is reached for ℓ^{II}_{R2}. The latter is highly unlikely. So for all further estimates the ℓ^{II}_{R2} measure of fragment size has been ignored. Figure B.3b shows a similar comparison the time evolution of the two different average structural fragment measures with FAF. The FAF threshold has been measured to be approximately equal to $3x10^{-3}$.

B.3 Comparison of prediction with fragmentation models

In this subsection, the stress state and material parameters are used to obtain the ℓ^{I}_{R2} and ℓ^{II}_{R2} measures of Regime II fragmentation and compared

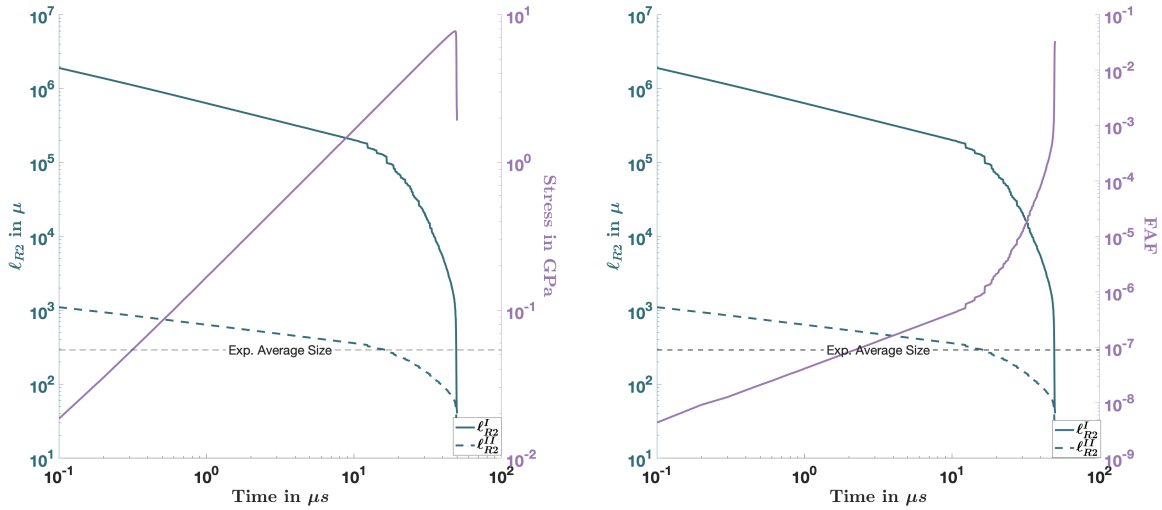

(a) **(b)**

Fig. B.3. Evolution of ℓ_{R2} with time for PAD B4C at a strain rate of $360ms^{-1}$, calculated using TR code. (a) Comparison with Stress, (b) Comparison with FAF.

against existing brittle fragmentation models in literature.

[105] defined characteristic measures of length scale (Eqn. B.24) and strain rate (Eqn. B.25), that were used to normalize the fragment size predicted by different brittle fragmentation models in literature as a function of normalized strain rate.

The characteristic length scale (L_0) was defined as

$$L_0 = \frac{{K_{IC}}^2}{2{\sigma_t}^2}, \tag{B.24}$$

where, K_{IC} is the fracture toughness, σ_t is the tensile strength of the material. It has been assumed that $\sigma_t = \sigma_c/10$, where σ_c is the peak compressive strength

of the material.

The characteristic strain rate ($\dot{\epsilon}_0$) was defined as

$$\dot{\epsilon}_0 = \frac{2{\sigma_t}^3 c}{E{K_{IC}}^2}, \tag{B.25}$$

where, c is the wave speed of the material.

Since most fragmentation models are in tension, they also established an equivalent tensile strain rate for a given compressive strain rate via the peak compressive strength (σ_c) of the material (Eqn. B.26).

The equivalent tensile strain rate was defined as

$$\dot{\epsilon}_{equiv} = \sqrt{\frac{{\sigma_c}^2}{\rho E R^2}}, \tag{B.26}$$

where ρ is the density of the material, E is the elastic modulus and $R = 3.2L_{sp}$, L_{sp} is specimen size. For Kolsky bar experiments $L_{sp} \approx 3 - 5mm$.

The normalized fragment size developed by [113] ($\bar{\ell}_{Grady}$), [114] ($\bar{\ell}_{GC}$), [115, 116] ($\bar{\ell}_{ZMR}$), [117] ($\bar{\ell}_{LM}$) considering tensile fragmentation was expressed as a function of the normalized strain rate by Eqns. B.27,B.28,B.29,B.30 respectively. [105] also modified the equations predicted by [113] for compressive fragmentation. Equation B.31 describes fragment size predicted by the Modified

APPENDIX B. STRUCTURAL FRAGMENTATION - PHENOMENOLOGICAL MODEL

Grady model ($\bar{\ell}_{Grady\_M}$) for compressive fragmentation.

$$\bar{\ell}_{Grady} = \left(\frac{24}{\bar{\dot{\epsilon}}^2}\right)^{\frac{1}{3}}, \tag{B.27}$$

$$\bar{\ell}_{GC} = \frac{4}{\bar{\dot{\epsilon}}} \sinh\left(\frac{1}{3} sinh^{-1}\left(\frac{3}{2}\bar{\dot{\epsilon}}\right)\right), \tag{B.28}$$

$$\bar{\ell}_{ZMR} = \frac{4.5}{1 + 4.5\bar{\dot{\epsilon}}^{2/3}}, \tag{B.29}$$

$$\bar{\ell}_{LM} = \frac{3}{1 + 4.5\bar{\dot{\epsilon}}^{2/3}}, \tag{B.30}$$

$$\bar{\ell}_{Grady\_M} = 2\left(\frac{2C{v_c}^2}{M^2 c^2 \bar{\dot{\epsilon}}^2}\right)^{\frac{1}{3}}, \tag{B.31}$$

where, C and M are constants dependent on the problem dimensions, the loading and failure conditions. v_c is the crack speed.

The mean measures of structural fragment size (ℓ^I_{R2} and ℓ^{II}_{R2}), obtained in the current work, are normalized by L_0 (Eqn. B.24) and expressed as $\bar{\ell}$. Equivalent tensile strain rate ($\dot{\epsilon}_{equiv}$) calculated using Eqn. B.26 is normalized by $\dot{\epsilon}_0$ (Eqn. B.25) and expressed as $\bar{\dot{\epsilon}}$. Figure B.4 shows a comparison of normalized values of ℓ^I_{R2} for the microstructure driven and FAF threshold based transition criteria with the predicted mean from [113], [114], [115,116], [117], and Modified Grady

([105]). For Eqn. B.31, $C, M, c,$ and v_c are chosen as 2, 2, 14 km/s, and 3200 m/s respectively. This corresponds to an expanding ring problem and results from PAD B4C observed in [105]. The fits corresponding to microstructure driven fragmentation and FAF threshold criterion are given by Eqn. B.32 and Eqn. B.33 respectively.

$$\bar{\ell}_{MS} = 0.1766\bar{\epsilon}^{-0.8384}. \tag{B.32}$$

$$\bar{\ell}_{FAF} = 0.0674\bar{\epsilon}^{-1.1499}. \tag{B.33}$$

B.4 Extension to three dimensions

The concept of a critical threshold of failed area fraction driving structural fragmentation can be extrapolated to three dimensions. The cracks and rectangular weak zones in two dimensions (Fig. B.1d) are analogous to crack plane and cuboidal weak zones in three dimensions. The normal to a wing crack plane is orthogonal to the direction of maximum principal compression. But two successive wing crack planes are not necessarily parallel to each other. To simplify the problem we have assumed that these planes are parallel to each other. A micro-column contained between two parallel crack planes of dimension, $2l_{w1}, 2w_{w1}$ and $2l_{w2}, 2w_{w2}$ respectively is defined by length, $l_{col_{3D}}(l_{w1}, l_{w2})$,

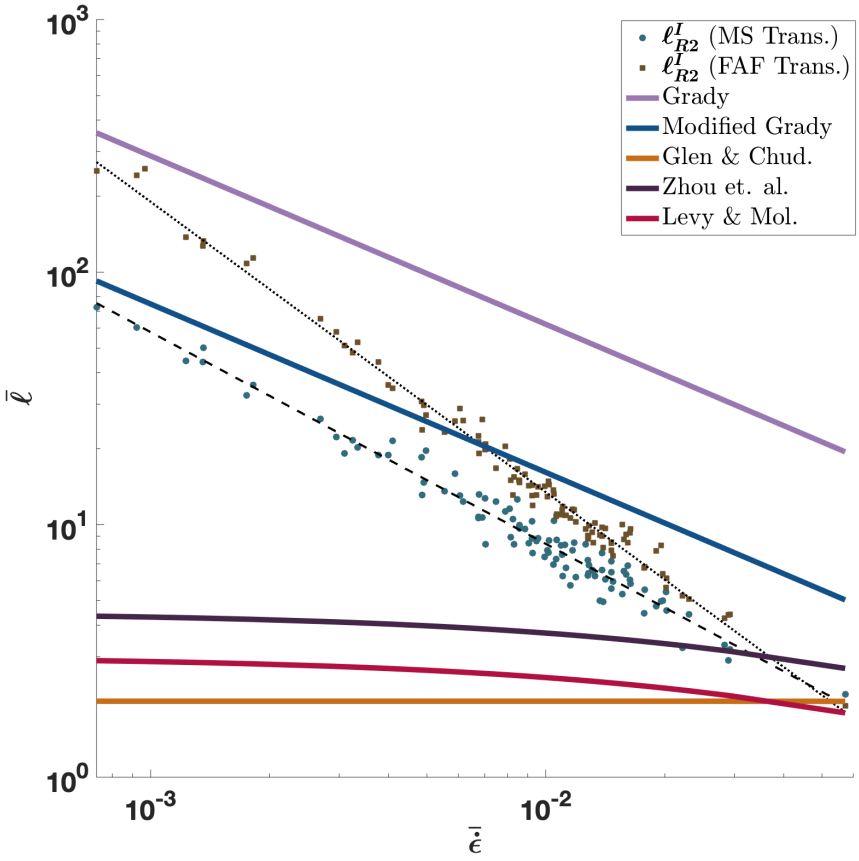

Fig. B.4. Comparison of average normalized structural fragment size ($\bar{\ell}$) computed using a microstructure fragmentation criterion and a FAF criterion with normalized strain rate ($\dot{\bar{\epsilon}}$) for structure driven fragmentation with the models of Grady, Glen & Chudnovsky, Zhou et al., Levy & Molinari, Modified Grady as well as the model developed in this work.

width along the in-plane dimension, $h_{col_{3D}}(l_{w1}, l_{w2})$ and width along the out-of-plane dimension, $w_{col_{3D}}(w_{w1}, w_{w2})$. The distribution of micro-column width along the latter dimension is defined as Eqn. B.34.

$$f_{w(w_{w1},w_{w2})_{3D}}(w_{col_{3D}}) = \begin{cases} \dfrac{1}{w_{w1}+w_{w2}} & \text{if } l_{col} \in (0, 2min(w_{w1}, w_{w2})), \\ \dfrac{max(w_{w1}, w_{w2}) - min(w_{w1}, w_{w2})}{w_{w1}+w_{w2}} & \text{if } w_{col} = 2min(w_{w1}, w_{w2}), \\ 0 & \text{if } w_{col} \notin (0, 2min(w_{w1}, w_{w2})). \end{cases} \tag{B.34}$$

The three dimensional damage metric is defined as $\Omega_{3D} = \eta_{3D} {l_w}^3$ [82], where η_{3D} is the three dimensional crack density. We have assumed that all cracks have the same aspect ratio of α_c. In that case, for a crack of length, $2l_{w0}$, the width, $2w_{w0} = \alpha_c 2l_{w0}$. The average distance between two successive cracks ($E\Big[h_{col_{3D}}(l_{w1}, l_{w2})\Big]$) is given by Eqn. B.35.

$$E\Big[h_{col_{3D}}(l_{w1}, l_{w2})\Big] = \frac{1}{4\eta_{3D}\alpha_c\Big(l_{w1}+l_{w2}\Big)^2}. \tag{B.35}$$

Similar to the 2D case, this has been calculated by assuming that there is on an average one crack in a box of height, $2l_{w1} + 2l_{w2}$, in-plane width equal to the

mean spacing of such cracks, and out of plane width, $(2l_{w1}+2w_{l2})\alpha_c$. Assuming, random crack location, the spacing between two such cracks, ($h_{col_{3D}}(l_{w1},l_{w2})$) is exponentially distributed as $f_{h(l_{w1},l_{w2})_{3D}}(h_{col_{3D}})$ with parameter, $\lambda_{1,2_{3D}}=4\eta_{3D}\alpha_c\Big(l_{w1}+l_{w2}\Big)^2$ as shown in Eqn. B.36.

$$f_{h(l_{w1},l_{w2})_{3D}}(h_{col_{3D}})=\begin{cases}\lambda_{1,2_{3D}}e^{-\lambda_{1,2_{3D}}h_{col_{3D}}} & \text{if } h_{col_{3D}}\geq 0,\\ 0 & \text{if } h_{col_{3D}}<0.\end{cases} \tag{B.36}$$

Using the same concept as in two dimensions, the expected value of the volume of failed (buckled) micro-column associated with a crack of length, $2l_{w1}$ which is succeeded by a crack of length, $2l_{w2}$, and crack aspect ratio, α_c, can be expressed as,

$$v_f(l_{w1},l_{w2})=a_{f_{3D}}(l_{w1},l_{w2})\int_0^{2min(w_{w1},w_{w2})}w_{col_{3D}}f_{w(w_{w1},w_{w2})_{3D}}(w_{col_{3D}})dw_{col_{3D}}, \tag{B.37}$$

where $a_{f_{3D}}$ is defined the same way as a_f in Eqn. B.21, but $\lambda_{1,2}$ is replaced by $\lambda_{1,2_{3D}}$.

The Failed Volume Fraction (FVF) can be similarly estimated as

$$FAF=\eta_{3D}\int_{l_{lower}}^{l_{upper}}f_{wing}(l_{w1})\Big[\int_{l_{lower}}^{l_{upper}}v_f(l_{w1},l_{w2})f_{wing}(l_{w2})dl_{w2}\Big]dl_{w1}. \tag{B.38}$$

APPENDIX B. STRUCTURAL FRAGMENTATION - PHENOMENOLOGICAL MODEL

For all defects being of the same size, FVF can be expressed as,

$$FVF = \frac{1}{16}\left[(3+\theta_{3D})e^{-\theta_{3D}} + (1-e^{-\theta_{3D}} - \theta_{3D}e^{-\theta_{3D}})\left(1-\frac{6}{{\theta_{3D}}^2}\right)\right], \tag{B.39}$$

where $\theta_{3D} = 8\alpha_c\Omega_{3D}\sqrt{\frac{12\sigma}{\pi^2 E}}$.

A threshold criterion for fragmentation in terms of FVF would require estimation of fragment sizes using three dimensional arguments. The mean fragment size analogous to ℓ^I_{R2} in three dimensions ($\ell^I_{R2_{3D}}$) is given as

$$\ell^I_{R2_{3D}} = \frac{1}{\lambda_{3D}p_{3D}}, \tag{B.40}$$

where $\lambda_{3D} = 16\alpha_c\eta_{3D}{l_w}^2$, $p_{3D} = 1 - \frac{1-e^{-\theta_{3D}}}{\theta_{3D}}$ and l_w is the equivalent wing crack length.

Bibliography

[1] P. Hazell, *Armour: Materials, Theory, and Design*, 1st ed. CRC Press, 2015.

[2] R. L. Cook, "Hard faced ceramic and plastic armour," *US 350983 Goodyear Aerospace*, 1970.

[3] M. Wilkins, C. Honodel, and D. Sawle, "Approach to the study of light armor," 1 1967.

[4] M. Wilkins, "Second progress report of light armor program," 11 1967.

[5] M. L. Wilkins, "Third progress report of light armor program," 7 1968.

[6] M. Wilkins, C. Cline, and C. A. Honodel, "Fourth progress report of light armor program," 6 1969.

[7] T. J. Holmquist, C. E. Anderson, T. Behner, and D. L. Orphal, "Mechanics of dwell and post-dwell penetration," *Advances in Applied Ceramics*, vol. 109, no. 8, pp. 467–479, 2010.

BIBLIOGRAPHY

[8] D. A. Shockey, A. Marchand, S. Skaggs, G. Cort, M. Burkett, and R. Parker, "Failure phenomenology of confined ceramic targets and impacting rods," *International Journal of Impact Engineering*, vol. 9, no. 3, pp. 263 – 275, 1990.

[9] A. G. Evans, M. E. Gulden, and M. Rosenblatt, "Impact Damage in Brittle Materials in the Elastic-Plastic Response Régime," *Proceedings of the Royal Society of London. Series A, Mathematical and Physical Sciences*, vol. 361, no. 1706, pp. 343–365, 1978.

[10] H. Hertz, "Uber die beruhrung fester elastischer korper (on the contact of elastic solids)," *J Reine Angew Math*, vol. 92, pp. 156–171, 1882.

[11] L.-B. Tremblay and L. A. Mysak, "Modeling Sea Ice as a Granular Material, Including the Dilatancy Effect", journal = "Journal of Physical Oceanography," vol. 27, no. 11, pp. 2342 – 2360, 1997.

[12] D. L. Feltham, "Granular flow in the marginal ice zone," *Philosophical Transactions of the Royal Society A: Mathematical, Physical and Engineering Sciences*, vol. 363, no. 1832, pp. 1677–1700, 2005.

[13] S. Dartevelle, "Numerical modeling of geophysical granular flows: 1. A comprehensive approach to granular rheologies and geophysical multiphase flows," *Geochemistry, Geophysics, Geosystems*, vol. 5, no. 8, 2004.

BIBLIOGRAPHY

[14] D. Scheeres, C. Hartzell, P. Sánchez, and M. Swift, "Scaling forces to asteroid surfaces: The role of cohesion," *Icarus*, vol. 210, no. 2, pp. 968–984, 2010.

[15] N. Murdoch, B. Rozitis, S. F. Green, T. L. de Lophem, P. Michel, and W. Losert, "Granular shear flow in varying gravitational environments," *Granular Matter*, vol. 15, pp. 129–137, 2013.

[16] J. Gray, "Granular flow in partially filled slowly rotating drums," *Journal of Fluid Mechanics*, vol. 441, pp. 1–29, 2001.

[17] J. Mescall and V. Weiss, *Material behavior under high stress and ultra-high loading rates*. Springer, 1983, vol. 29.

[18] R. Woodward, W. Gooch, R. O'Donnell, W. Perciballi, B. Baxter, and S. Pattie, "A study of fragmentation in the ballistic impact of ceramics," *International Journal of Impact Engineering*, vol. 15, no. 5, pp. 605–618, 1994.

[19] J. C. LaSalvia, M. J. Normandia, H. T. Miller, and D. E. MacKenzie, *Sphere Impact Induced Damage in Ceramics: II. Armor-Grade B4C and WC*. John Wiley & Sons, Ltd, 2005, ch. 21, pp. 183–192.

[20] R. B. Leavy, R. M. Brannon, and O. E. Strack, "The Use of Sphere Indentation Experiments to Characterize Ceramic Damage Models," *Interna-*

tional Journal of Applied Ceramic Technology, vol. 7, no. 5, pp. 606–615, 2010.

[21] J. Clayton, "A continuum description of nonlinear elasticity, slip and twinning, with application to sapphire," *Proceedings of the Royal Society A: Mathematical, Physical and Engineering Sciences*, vol. 465, no. 2101, pp. 307–334, 2009.

[22] G. Hu, C. Chen, K. Ramesh, and J. McCauley, "Mechanisms of dynamic deformation and dynamic failure in aluminum nitride," *Acta Materialia*, vol. 60, no. 8, pp. 3480–3490, 2012.

[23] N. Bourne, "The relation of failure under 1D shock to the ballistic performance of brittle materials," *International Journal of Impact Engineering*, vol. 35, no. 8, pp. 674–683, 2008.

[24] M. Chen, J. W. McCauley, and K. J. Hemker, "Shock-Induced Localized Amorphization in Boron Carbide," *Science*, vol. 299, no. 5612, pp. 1563–1566, 2003.

[25] "High pressure phase transition in aluminium nitride," *Solid State Communications*, vol. 79, no. 12, pp. 1033–1034, 1991.

[26] K. Kondo, A. Sawaoka, K. Sato, and M. Ando, "Shock compression

and phase transformation of AlN and BP," *AIP Conference Proceedings*, vol. 78, no. 1, pp. 325–329, 1982.

[27] M. Kipp and D. Grady, "Shock phase transformation and release properties of aluminum nitride," *Journal de Physique IV Proceedings*, vol. 04, no. C8, pp. C8–249–C8–256, 1994.

[28] J. Clayton, "Penetration resistance of armor ceramics: Dimensional analysis and property correlations," *International Journal of Impact Engineering*, vol. 85, pp. 124–131, 2015.

[29] E. Medvedovski, "Ballistic performance of armour ceramics: Influence of design and structure. Part 1," *Ceramics International*, vol. 36, no. 7, pp. 2103–2115, 2010.

[30] I. Crouch, G. Franks, C. Tallon, S. Thomas, and M. Naebe, "7 - Glasses and ceramics," in *The Science of Armour Materials*, ser. Woodhead Publishing in Materials, I. G. Crouch, Ed. Woodhead Publishing, 2017, pp. 331 – 393.

[31] F. Ernst, O. Kienzle, and M. Rühle, "Structure and Composition of Grain Boundaries in Ceramics," *Journal of the European Ceramic Society*, vol. 19, no. 6, pp. 665–673, 1999.

BIBLIOGRAPHY

[32] Y.-M. Chiang, D. P. Birnie, and W. D. Kingery, *Physical ceramics : principles for ceramic science and engineering*. John Wiley & Sons, Ltd, 1996.

[33] M. Ashby and S. Hallam, "The failure of brittle solids containing small cracks under compressive stress states," *Acta Metallurgica*, vol. 34, no. 3, pp. 497 – 510, 1986.

[34] K. Ravi-Chandar and W. G. Knauss, "An experimental investigation into dynamic fracture: I. Crack initiation and arrest," *International Journal of Fracture*, vol. 25, pp. 247–262, 1984.

[35] ——, "An experimental investigation into dynamic fracture: II. Microstructural aspects," *International Journal of Fracture*, vol. 26, pp. 65–80, 1984.

[36] ——, "An experimental investigation into dynamic fracture: III. On steady-state crack propagation and crack branching," *International Journal of Fracture*, vol. 26, pp. 141–154, 1984.

[37] ——, "An experimental investigation into dynamic fracture: IV. On the interaction of stress waves with propagating cracks," *International Journal of Fracture*, vol. 26, pp. 189–200, 1984.

[38] C. Jiang, G.-F. Zhao, J. Zhu, Y.-X. Zhao, and L. Shen, "Investigation of Dy-

namic Crack Coalescence Using a Gypsum-Like 3D Printing Material," *Rock Mechanics and Rock Engineering*, vol. 49, pp. 3983–3998, 2016.

[39] Z. Yue, L. Peng, X. Yue, J. Wang, and C. Lu, "Experimental study on the dynamic coalescence of two-crack granite specimens under high loading rate," *Engineering Fracture Mechanics*, vol. 237, p. 107254, 2020.

[40] P. G. Karandikar, G. Evans, S. Wong, M. K. Aghajanian, and M. Sennett, *A Review of Ceramics for Armor Applications*. John Wiley & Sons, Ltd, 2008, ch. 16, pp. 163–175.

[41] C. Shih, M. Meyers, V. Nesterenko, and S. Chen, "Damage evolution in dynamic deformation of silicon carbide," *Acta Materialia*, vol. 48, no. 9, pp. 2399–2420, 2000.

[42] J. D. Hogan, L. Farbaniec, M. Shaeffer, and K. T. Ramesh, "The Effects of Microstructure and Confinement on the Compressive Fragmentation of an Advanced Ceramic," *Journal of the American Ceramic Society*, vol. 98, no. 3, pp. 902–912, 2015.

[43] Falk, M. L., Needleman, A., and Rice, J. R., "A critical evaluation of cohesive zone models of dynamic fracture," *J. Phys. IV France*, vol. 11, pp. Pr5–43–Pr5–50, 2001.

[44] Z. P. Bažant and B. Oh, "Crack band theory for fracture of concrete," *JMatériaux et Construction*, vol. 16, pp. 155–177, 1983.

[45] J.-L. Le and J. Eliáš, "A Probabilistic Crack Band Model for Quasibrittle Fracture," *Journal of Applied Mechanics*, vol. 83, no. 5, 02 2016.

[46] C. Daux, N. Moës, J. Dolbow, N. Sukumar, and T. Belytschko, "Arbitrary branched and intersecting cracks with the extended finite element method," *International Journal for Numerical Methods in Engineering*, vol. 48, no. 12, pp. 1741–1760, 2000.

[47] E. Budyn, G. Zi, N. Moës, and T. Belytschko, "A method for multiple crack growth in brittle materials without remeshing," *International Journal for Numerical Methods in Engineering*, vol. 61, no. 10, pp. 1741–1770, 2004.

[48] J. Réthoré, A. Gravouil, and A. Combescure, "An energy-conserving scheme for dynamic crack growth using the eXtended finite element method," *International Journal for Numerical Methods in Engineering*, vol. 63, no. 5, pp. 631–659, 2005.

[49] D. Grégoire, H. Maigre, J. Réthoré, and A. Combescure, "Dynamic crack propagation under mixed-mode loading – Comparison between experiments and X-FEM simulations," *International Journal of Solids and Structures*, vol. 44, no. 20, pp. 6517–6534, 2007.

BIBLIOGRAPHY

[50] R. Abedi, R. B. Haber, and P. L. Clarke, "Effect of random defects on dynamic fracture in quasi-brittle materials," *International Journal of Fracture*, vol. 208, pp. 241 – 268, 2017.

[51] R. Spatschek, E. Brener, and A. Karma, "Phase field modeling of crack propagation," *Philosophical Magazine*, vol. 91, no. 1, pp. 75–95, 2011.

[52] M. Hofacker and C. Miehe, "Continuum phase field modeling of dynamic fracture: variational principles and staggered FE implementation," *International Journal of Fracture*, vol. 178, pp. 113–129, 2012.

[53] M. J. Borden, C. V. Verhoosel, M. A. Scott, T. J. Hughes, and C. M. Landis, "A phase-field description of dynamic brittle fracture," *Computer Methods in Applied Mechanics and Engineering*, vol. 217-220, pp. 77 – 95, 2012.

[54] A. Schlüter, A. Willenbücher, C. Kuhn, and R. Müller, "Phase field approximation of dynamic brittle fracture," *Computational Mechanics*, vol. 54, pp. 1141 – 1161, 2014.

[55] B. Paliwal and K. Ramesh, "An interacting micro-crack damage model for failure of brittle materials under compression," *Journal of the Mechanics and Physics of Solids*, vol. 56, no. 3, pp. 896 – 923, 2008.

[56] C. Katcoff and L. Graham-Brady, "Modeling dynamic brittle behavior of

materials with circular flaws or pores," *International Journal of Solids and Structures*, vol. 51, no. 3, pp. 754 – 766, 2014.

[57] T. Nguyen, J. Yvonnet, M. Bornert, and C. Chateau, "Initiation and propagation of complex 3D networks of cracks in heterogeneous quasi-brittle materials: Direct comparison between in situ testing-microCT experiments and phase field simulations," *Journal of the Mechanics and Physics of Solids*, vol. 95, pp. 320 – 350, 2016.

[58] H. K. Clark and J. L. Hoard, "The Crystal Structure of Boron Carbide," *Journal of the American Chemical Society*, vol. 65, no. 11, pp. 2115–2119, 1943.

[59] V. Domnich, S. Reynaud, R. A. Haber, and M. Chhowalla, "Boron Carbide: Structure, Properties, and Stability under Stress," *Journal of the American Ceramic Society*, vol. 94, no. 11, pp. 3605–3628, 2011.

[60] T. J. Vogler, W. D. Reinhart, and L. C. Chhabildas, "Dynamic behavior of boron carbide," *Journal of Applied Physics*, vol. 95, no. 8, pp. 4173–4183, 2004.

[61] K. M. Reddy, P. Liu, A. Hirata, T. Fujita, and M. Chen, "Atomic structure of amorphous shear bands in boron carbide," *Nature Communications*, vol. 4, p. 2483, 2013.

[62] K. Y. Xie, Q. An, T. Sato, A. J. Breen, S. P. Ringer, W. A. Goddard, J. M. Cairney, and K. J. Hemker, "Breaking the icosahedra in boron carbide," *Proceedings of the National Academy of Sciences*, vol. 113, no. 43, pp. 12 012–12 016, 2016.

[63] K. M. Reddy, D. Guo, S. Song, C. Cheng, J. Han, X. Wang, Q. An, and M. Chen, "Dislocation-mediated shear amorphization in boron carbide," *Science Advances*, vol. 7, no. 8, 2021.

[64] J. E. Proctor, V. Bhakhri, R. Hao, T. J. Prior, T. S. E. Gregoryanz, M. Chhowalla, and F. Giulani, "Stabilization of boron carbide via silicon doping," *Journal of Physics: Condensed Matter*, vol. 27, no. 1, p. 015401, 2015.

[65] A. U. Khan, A. M. Etzold, X. Yang, V. Domnich, K. Y. Xie, C. Hwang, K. D. Behler, M. Chen, Q. An, J. C. LaSalvia, K. J. Hemker, W. A. Goddard, and R. A. Haber, "Locating Si atoms in Si-doped boron carbide: A route to understand amorphization mitigation mechanism," *Acta Materialia*, vol. 157, pp. 106 – 113, 2018.

[66] A. Chauhan, M. C. Schaefer, R. A. Haber, and K. J. Hemker, "Experimental observations of amorphization in stoichiometric and boron-rich boron carbide," *Acta Materialia*, vol. 181, pp. 207 – 215, 2019.

[67] M. C. Schaefer and R. A. Haber, "Amorphization Mitigation in Boron-

Rich Boron Carbides Quantified by Raman Spectroscopy," *Ceramics*, vol. 3, pp. 297–305, 2020.

[68] G. R. Johnson, T. J. Holmquist, and S. R. Beissel, "Response of aluminum nitride (including a phase change) to large strains, high strain rates, and high pressures," *Journal of Applied Physics*, vol. 94, no. 3, pp. 1639–1646, 2003.

[69] T. J. Holmquist and G. R. Johnson, "Characterization and evaluation of boron carbide for plate-impact conditions," *Journal of Applied Physics*, vol. 100, no. 9, p. 093525, 2006.

[70] J. Clayton, "Towards a nonlinear elastic representation of finite compression and instability of boron carbide ceramic," *Philosophical Magazine*, vol. 92, no. 23, pp. 2860–2893, 2012.

[71] ——, "Mesoscale modeling of dynamic compression of boron carbide polycrystals," *Mechanics Research Communications*, vol. 49, pp. 57–64, 2013.

[72] J. Clayton and A. Tonge, "A nonlinear anisotropic elastic–inelastic constitutive model for polycrystalline ceramics and minerals with application to boron carbide," *International Journal of Solids and Structures*, vol. 64-65, pp. 191–207, 2015.

[73] Q. Zeng, A. L. Tonge, and K. Ramesh, "A multi-mechanism constitutive

model for the dynamic failure of quasi-brittle materials. Part I: Amorphization as a failure mode," *Journal of the Mechanics and Physics of Solids*, vol. 130, pp. 370 – 392, 2019.

[74] A. Di Renzo and F. P. Di Maio, "Comparison of contact-force models for the simulation of collisions in DEM-based granular flow codes," *Chemical Engineering Science*, vol. 59, no. 3, pp. 525–541, 2004.

[75] J. T. Clemmer, "An improved computational constitutive model for brittle materials," Ph.D. dissertation, Johns Hopkins University, 2019.

[76] S. Bardenhagen, J. Brackbill, and D. Sulsky, "The material-point method for granular materials," *Computer Methods in Applied Mechanics and Engineering*, vol. 187, no. 3, pp. 529–541, 2000.

[77] G. R. Johnson and T. J. Holmquist, "A computational constitutive model for brittle materials subjected to large strains, high strain rates and high pressures," in *Shock-wave and High Strain-rate Phenomena in Materials*, M. A. Meyers, L. E. Murr, and K. P. Staudhammer, Eds. Marcel Dekker Inc., 1992, pp. 1075–1081.

[78] ——, "An improved computational constitutive model for brittle materials," *AIP Conference Proceedings*, vol. 309, no. 1, pp. 981–984, 1994.

[79] H. Espinosa and B. Gailly, "Modeling of shear instabilities observed in

cylinder collapse experiments performed on ceramic powders," *Acta Materialia*, vol. 49, no. 19, pp. 4135–4147, 2001.

[80] S. Satapathy, "Dynamic spherical cavity expansion in brittle ceramics," *International Journal of Solids and Structures*, vol. 38, no. 32, pp. 5833–5845, 2001.

[81] J. D. Walker and C. E. Anderson, "A time-dependent model for long-rod penetration," *International Journal of Impact Engineering*, vol. 16, no. 1, pp. 19–48, 1995.

[82] A. L. Tonge and K. Ramesh, "Multi-scale defect interactions in high-rate brittle material failure. Part I: Model formulation and application to ALON," *Journal of the Mechanics and Physics of Solids*, vol. 86, pp. 117 – 149, 2016.

[83] V. S. Deshpande, E. A. N. Gamble, B. G. Compton, R. M. McMeeking, A. G. Evans, and F. W. Zok, "A Constitutive Description of the Inelastic Response of Ceramics," *Journal of the American Ceramic Society*, vol. 94, no. s1, pp. s204–s214, 2011.

[84] C. Foster, R. Regueiro, A. Fossum, and R. Borja, "Implicit numerical integration of a three-invariant, isotropic/kinematic hardening cap plasticity model for geomaterials," *Computer Methods in Applied Mechanics and Engineering*, vol. 194, no. 50, pp. 5109–5138, 2005.

BIBLIOGRAPHY

[85] D. Curran, L. Seaman, and D. Shockey, "Dynamic failure of solids," *Physics Reports*, vol. 147, no. 5, pp. 253–388, 1987.

[86] D. Curran, L. Seaman, T. Cooper, and D. Shockey, "Micromechanical model for comminution and granular flow of brittle material under high strain rate application to penetration of ceramic targets," *International Journal of Impact Engineering*, vol. 13, no. 1, pp. 53 – 83, 1993.

[87] D. Curran and T. Cooper, "Modeling the comminution and flow of granular brittle material," *J. Phys. IV France*, vol. 110, pp. 45 – 50, 2003.

[88] M. B. Cil, R. C. Hurley, and L. Graham-Brady, "Constitutive Model for Brittle Granular Materials Considering Competition between Breakage and Dilation," *Journal of Engineering Mechanics*, vol. 146, no. 1, 2020.

[89] ——, "A rate-dependent constitutive model for brittle granular materials based on breakage mechanics," *Journal of the American Ceramic Society*, vol. 102, no. 9, pp. 5524–5534, 2019.

[90] M. B. Cil, Q. Zeng, R. C. Hurley, and L. Graham-Brady, "An Integrative Model for the Dynamic Behavior of Brittle Materials Based on Microcracking and Breakage Mechanics," *Journal of Dynamic Behavior of Materials*, 2020.

BIBLIOGRAPHY

[91] I. Einav, "Breakage mechanics—Part I: Theory," *Journal of the Mechanics and Physics of Solids*, vol. 55, no. 6, pp. 1274 – 1297, 2007.

[92] ——, "Breakage mechanics—Part II: Modelling granular materials," *Journal of the Mechanics and Physics of Solids*, vol. 55, no. 6, pp. 1298 – 1320, 2007.

[93] ——, "Fracture propagation in brittle granular matter," *Proceedings of the Royal Society A: Mathematical, Physical and Engineering Sciences*, vol. 463, no. 2087, pp. 3021–3035, 2007.

[94] P. Tapponnier and W. Brace, "Development of stress-induced microcracks in Westerly Granite," *International Journal of Rock Mechanics and Mining Sciences & Geomechanics Abstracts*, vol. 13, no. 4, pp. 103–112, 1976.

[95] G. Vekinis, M. Ashby, and P. Beaumont, "The compressive failure of alumina containing controlled distributions of flaws," *Acta Metallurgica et Materialia*, vol. 39, no. 11, pp. 2583–2588, 1991.

[96] S. Nemat-Nasser and H. Deng, "Strain-rate effect on brittle failure in compression," *Acta Metallurgica et Materialia*, vol. 42, no. 3, pp. 1013 – 1024, 1994.

[97] J.-L. Le, J. Eliáš, and Z. P. Bažant, "Computation of Probability Distribution of Strength of Quasibrittle Structures Failing at Macrocrack Ini-

tiation," *Journal of Engineering Mechanics*, vol. 138, no. 7, pp. 888–899, 2012.

[98] V. Grechka and M. Kachanov, "Effective elasticity of rocks with closely spaced and intersecting cracks," *Geophysics*, vol. 71, no. 3, pp. D85–D91, 2006.

[99] R. H. Wong and K. Chau, "Crack coalescence in a rock-like material containing two cracks," *International Journal of Rock Mechanics and Mining Sciences*, vol. 35, no. 2, pp. 147 – 164, 1998.

[100] P. Cao, T. Liu, C. Pu, and H. Lin, "Crack propagation and coalescence of brittle rock-like specimens with pre-existing cracks in compression," *Engineering Geology*, vol. 187, pp. 113–121, 2015.

[101] A. Bobet, "The initiation of secondary cracks in compression," *Engineering Fracture Mechanics*, vol. 66, no. 2, pp. 187 – 219, 2000.

[102] J. Åström and J. Timonen, "Fragmentation by Crack Branching," *Phys. Rev. Lett.*, vol. 78, pp. 3677–3680, May 1997.

[103] P. Kekäläinen, J. A. Åström, and J. Timonen, "Solution for the fragment-size distribution in a crack-branching model of fragmentation," *Phys. Rev. E*, vol. 76, p. 026112, Aug 2007.

[104] E. Katzav, M. Adda-Bedia, and R. Arias, "Theory of dynamic crack

branching in brittle materials," *International Journal of Fracture*, vol. 143, no. 3, pp. 245–271, 2007.

[105] J. D. Hogan, L. Farbaniec, N. Daphalapurkar, and K. Ramesh, "On Compressive Brittle Fragmentation," *Journal of the American Ceramic Society*, vol. 99, no. 6, pp. 2159–2169, 2016.

[106] J. D. Hogan, L. Farbaniec, D. Mallick, V. Domnich, K. Kuwelkar, T. Sano, J. W. McCauley, and K. T. Ramesh, "Fragmentation of an advanced ceramic under ballistic impact: Mechanisms and microstructure," *International Journal of Impact Engineering*, vol. 102, pp. 47 – 54, 2017.

[107] Y. Ben-Zion, "Collective behavior of earthquakes and faults: Continuum-discrete transitions, progressive evolutionary changes, and different dynamic regimes," *Reviews of Geophysics*, vol. 46, no. 4, 2008.

[108] S. Chocron, C. E. Anderson Jr., K. A. Dannemann, A. E. Nicholls, and N. L. King, "Intact and Predamaged Boron Carbide Strength under Moderate Confinement Pressures," *Journal of the American Ceramic Society*, vol. 95, no. 1, pp. 350–357, 2012.

[109] E. Krimsky, K. Ramesh, M. Bratcher, M. Foster, and J. D. Hogan, "Quantification of damage and its effects on the compressive strength of an advanced ceramic," *Engineering Fracture Mechanics*, vol. 208, pp. 107 – 118, 2019.

[110] V. Lyakhovsky, Y. Hamiel, and Y. Ben-Zion, "A non-local visco-elastic damage model and dynamic fracturing," *Journal of the Mechanics and Physics of Solids*, vol. 59, no. 9, pp. 1752 – 1776, 2011.

[111] V. Lyakhovsky and Y. Ben-Zion, "Damage–breakage rheology model and solid-granular transition near brittle instability," *Journal of the Mechanics and Physics of Solids*, vol. 64, pp. 184 – 197, 2014.

[112] F. Kun and H. J. Herrmann, "Transition from damage to fragmentation in collision of solids," *Phys. Rev. E*, vol. 59, pp. 2623–2632, Mar 1999.

[113] D. E. Grady, *Fragmentation of rings and shells : the legacy of N.F. Mott*, 2006.

[114] L. A. Glenn and A. Chudnovsky, "Strain-energy effects on dynamic fragmentation," *Journal of applied physics*, vol. 59, pp. 1379 – 1380, 1986.

[115] F. Zhou, J.-F. Molinari, and K. Ramesh, "Analysis of the brittle fragmentation of an expanding ring," *Computational Materials Science*, vol. 37, no. 1, pp. 74 – 85, 2006.

[116] F. Zhou, J.-F. Molinari, and K. T. Ramesh, "Effects of material properties on the fragmentation of brittle materials," *International Journal of Fracture*, vol. 139, pp. 169 – 196, 2006.

[117] S. Levy and J. Molinari, "Dynamic fragmentation of ceramics, signature

of defects and scaling of fragment sizes," *Journal of the Mechanics and Physics of Solids*, vol. 58, no. 1, pp. 12 – 26, 2010.

[118] G. Hu, J. Liu, L. Graham-Brady, and K. Ramesh, "A 3D mechanistic model for brittle materials containing evolving flaw distributions under dynamic multiaxial loading," *Journal of the Mechanics and Physics of Solids*, vol. 78, pp. 269 – 297, 2015.

[119] K. Kolari, "A complete three-dimensional continuum model of wing-crack growth in granular brittle solids," *International Journal of Solids and Structures*, vol. 115-116, pp. 27 – 42, 2017.

[120] F. Huq, J. Liu, A. Tonge, and L. Graham-Brady, "A micromechanics based model to predict micro-crack coalescence in brittle materials under dynamic compression," *Engineering Fracture Mechanics*, vol. 217, p. 106515, 2019.

[121] R. Wong, K. Chau, C. Tang, and P. Lin, "Analysis of crack coalescence in rock-like materials containing three flaws - Part I: Experimental approach," *International Journal of Rock Mechanics and Mining Sciences*, vol. 38, no. 7, pp. 909–924, 10 2001.

[122] K. Vijayakumar and S. N. Atluri, "An Embedded Elliptical Crack, in an Infinite Solid, Subject to Arbitrary Crack-Face Tractions," *Journal of Applied Mechanics*, vol. 48, no. 1, pp. 88–96, 1981.

[123] X. Zhu, G. Liu, and Y. Chao, "Three-dimensional stress and displacement fields near an elliptical crack front," *International Journal of Fracture*, vol. 109, pp. 383–401, 2001.

[124] D. Hills, P. Kelly, D. Dai, and A. Korsunsky, *Solution of Crack Problems*, 1st ed. Springer, 1996.

[125] M. Kachanov, "Elastic Solids with Many Cracks and Related Problems," ser. Advances in Applied Mechanics, J. W. Hutchinson and T. Y. Wu, Eds. Elsevier, 1993, vol. 30, pp. 259–445.

[126] S. Li and G. Wang, *Introduction to Micromechanics and Nanomechanics*, 2nd ed. World Scientific, 2008.

[127] G. Hello, M. Ben Tahar, and J. M. Roelandt, "Analytical determination of coefficients in crack-tip stress expansions for a finite crack in an infinite plane medium," *International Journal of Solids and Structures*, vol. 49, no. 3, pp. 556 – 566, 2012.

[128] Y. Hayakawa and T. Oguchi, "Evaluation of gravel sphericity and roundness based on surface-area measurement with a laser scanner," *Computers and Geosciences*, vol. 31, no. 6, pp. 735 – 741, 2005.

[129] F. J. Richards, "A Flexible Growth Function for Empirical Use," *Journal of Experimental Botany*, vol. 10, no. 2, pp. 290–301, 06 1959.

[130] G. Ravichandran and G. Subhash, "A micromechanical model for high strain rate behavior of ceramics," *International Journal of Solids and Structures*, vol. 32, no. 17, pp. 2627 – 2646, 1995.

[131] V. Deshpande and A. Evans, "Inelastic deformation and energy dissipation in ceramics: A mechanism-based constitutive model," *Journal of the Mechanics and Physics of Solids*, vol. 56, no. 10, pp. 3077 – 3100, 2008.

[132] D. Fernández-Fdz, R. Zaera, and J. Fernández-Sáez, "A constitutive equation for ceramic materials used in lightweight armors," *Computers & Structures*, vol. 89, no. 23, pp. 2316 – 2324, 2011.

[133] L. Farbaniec, J. Hogan, K. Xie, M. Shaeffer, K. Hemker, and K. Ramesh, "Damage evolution of hot-pressed boron carbide under confined dynamic compression," *International Journal of Impact Engineering*, vol. 99, pp. 75 – 84, 2017.

[134] Q. Zeng, A. L. Tonge, and K. Ramesh, "A multi-mechanism constitutive model for the dynamic failure of quasi-brittle materials. Part II: Integrative model," *Journal of the Mechanics and Physics of Solids*, vol. 131, pp. 20 – 42, 2019.

[135] E. Strassburger, "Investigation of fracture propagation during impact in boron carbide," United States Army, European Research Office of the U.S. Army, Tech. Rep., 01 2002.

[136] ——, "Visualization of Impact Damage in Ceramics Using the Edge-On Impact Technique," *International Journal of Applied Ceramic Technology*, vol. 1, no. 3, pp. 235–242, 2004.

[137] ——, *Edge-On Impact Investigation of Fracture Propagation in Boron Carbide*. John Wiley & Sons, Ltd, 2013, ch. 2, pp. 15–24.

[138] J. Simo and M. Ortiz, "A unified approach to finite deformation elastoplastic analysis based on the use of hyperelastic constitutive equations," *Computer Methods in Applied Mechanics and Engineering*, vol. 49, no. 2, pp. 221 – 245, 1985.

[139] S. Nemat-Nasser and H. Horii, "Compression-induced nonplanar crack extension with application to splitting, exfoliation, and rockburst," *Journal of Geophysical Research: Solid Earth*, vol. 87, no. B8, pp. 6805–6821, 1982.

[140] L. B. Freund, *Dynamic Fracture Mechanics*, ser. Cambridge Monographs on Mechanics. Cambridge University Press, 1990.

[141] F. Thévenot, "Boron carbide—A comprehensive review," *Journal of the European Ceramic Society*, vol. 6, no. 4, pp. 205 – 225, 1990.

[142] D. P. Dandekar, "Shock Response of Boron Carbide," Army Research Lab, Aberdeen Proving Ground, MD, USA, Tech. Rep., 04 2001.

[143] P. Nicewicz, P. Peciar, O. Macho, T. Sano, and J. D. Hogan, "Quasi-static confined uniaxial compaction of granular alumina and boron carbide observing the particle size effects," *Journal of the American Ceramic Society*, vol. 103, no. 3, pp. 2193–2209, 2020.

[144] C. Sammis, G. King, and R. Biegel, "The kinematics of gouge deformation," *Pure and Applied Geophysics*, vol. 125, pp. 777 – 812, 1987.

[145] J. Åström and H. Herrmann, "Fragmentation of grains in a two-dimensional packing," *The European Physical Journal B - Condensed Matter and Complex Systems*, vol. 5, pp. 551 – 554, 1998.

[146] G. McDowell and A. Amon, "The Application of Weibull Statistics to the Fracture of Soil Particles," *Soils and Foundations*, vol. 40, no. 5, pp. 133 – 141, 2000.

[147] A. L. Tonge and K. Ramesh, "Multi-scale defect interactions in high-rate failure of brittle materials, Part II: Application to design of protection materials," *Journal of the Mechanics and Physics of Solids*, vol. 86, pp. 237 – 258, 2016.

[148] T. Holmquist and G. Johnson, "Modeling the 14.5 mm BS41 projectile for ballistic impact computations," *Computational Ballistics II, WIT Trans. on Modelling and Simulation*, vol. 4, no. 2087, pp. 61–75, 2005.

[149] T. Niezgoda and A. Morka, "On the numerical methods and physics of perforation in the high-velocity impact mechanics," *World J Eng*, 01 2009.

[150] B. Aydelotte and B. Schuster, "Observation and Modeling of Cone Cracks in Ceramics," in *Dynamic Behavior of Materials, Volume 1*, B. Song, L. Lamberson, D. Casem, and J. Kimberley, Eds. Cham: Springer International Publishing, 2016, pp. 19–23.

[151] M. F. Toksoy, W. Rafaniello, K. Y. Xie, L. Ma, K. J. Hemker, and R. A. Haber, "Densification and characterization of rapid carbothermal synthesized boron carbide," *International Journal of Applied Ceramic Technology*, vol. 14, no. 3, pp. 443–453, 2017.

[152] H.-W. Kim, Y.-H. Koh, and H.-E. Kim, "Densification and Mechanical Properties of B4C with Al2O3 as a Sintering Aid," *Journal of the American Ceramic Society*, vol. 83, no. 11, pp. 2863–2865, 2000.

[153] S. Yamada, K. Hirao, Y. Yamauchi, and S. Kanzaki, "High strength B4C–TiB2 composites fabricated by reaction hot-pressing," *Journal of the European Ceramic Society*, vol. 23, no. 7, pp. 1123 – 1130, 2003.

[154] N. Frage, S. Hayun, S. Kalabukhov, and M. P. Dariel, "The effect of Fe addition on the densification of B4C powder by spark plasma sintering," *Powder Metallurgy and Metal Ceramics*, vol. 46, pp. 533–538, 2007.

BIBLIOGRAPHY

[155] C. Subramanian, T. Roy, T. Murthy, P. Sengupta, G. Kale, M. Krishnaiah, and A. Suri, "Effect of zirconia addition on pressureless sintering of boron carbide," *Ceramics International*, vol. 34, no. 6, pp. 1543 – 1549, 2008.

[156] J. Sun, C. Liu, and C. Duan, "Effect of Al and TiO2 on sinterability and mechanical properties of boron carbide," *Materials Science and Engineering: A*, vol. 509, no. 1, pp. 89 – 93, 2009.

[157] K. Madhav Reddy, J. Guo, Y. Shinoda, T. Fujita, A. Hirata, J. Singh, J. McCauley, and M. Chen, "Enhanced mechanical properties of nanocrystalline boron carbide by nanoporosity and interface phases," *Nature Communications*, vol. 3, p. 1052, 2012.

[158] Y. Shen, G. Li, and Q. An, "Enhanced fracture toughness of boron carbide from microalloying and nanotwinning," *Scripta Materialia*, vol. 162, pp. 306 – 310, 2019.

[159] Y. He, Y. Shen, B. Tang, and Q. An, "Strengthening boron carbide through lithium dopant," *Journal of the American Ceramic Society*, vol. 103, no. 3, pp. 2012–2023, 2020.

[160] X. Sun, A. Chauhan, D. D. Mallick, A. L. Tonge, J. W. McCauley, K. J. Hemker, J. C. LaSalvia, and K. Ramesh, "Granular flow of an advanced ceramic under ultra-high strain rates and high pressures," *Journal of the Mechanics and Physics of Solids*, vol. 143, p. 104031, 2020.

BIBLIOGRAPHY

[161] E. Borgonovo and E. Plischke, "Sensitivity analysis: a review of recent advances," *European Journal of Operational Research*, vol. 248, no. 3, pp. 869–887, 2016.

[162] A. Saltelli, M. Ratto, T. Andres, F. Campolongo, J. Cariboni, D. Gatelli, M. Saisana, and S. Tarantola, *Global sensitivity analysis: the primer*. John Wiley & Sons, 2008.

[163] A. Saltelli, P. Annoni, I. Azzini, F. Campolongo, M. Ratto, and S. Tarantola, "Variance based sensitivity analysis of model output. Design and estimator for the total sensitivity index," *Computer physics communications*, vol. 181, no. 2, pp. 259–270, 2010.

[164] J. E. Campbell, G. R. Carmichael, T. Chai, M. Mena-Carrasco, Y. Tang, D. Blake, N. Blake, S. A. Vay, G. J. Collatz, I. Baker *et al.*, "Photosynthetic control of atmospheric carbonyl sulfide during the growing season," *Science*, vol. 322, no. 5904, pp. 1085–1088, 2008.

[165] J. C. Helton, "Uncertainty and sensitivity analysis techniques for use in performance assessment for radioactive waste disposal," *Reliability Engineering & System Safety*, vol. 42, no. 2-3, pp. 327–367, 1993.

[166] J. P. Kleijnen, "Sensitivity analysis of simulation models," *Wiley Encyclopedia of Operations Research and Management Science*, 2010.

BIBLIOGRAPHY

[167] R. M. Errico, "What is an adjoint model?" *Bulletin of the American Meteorological Society*, vol. 78, no. 11, pp. 2577–2592, 1997.

[168] S. IM, "Sensitivity estimates for nonlinear mathematical models," *Math. Model. Comput. Exp*, vol. 1, no. 4, pp. 407–414, 1993.

[169] T. Homma and A. Saltelli, "Importance measures in global sensitivity analysis of nonlinear models," *Reliability Engineering & System Safety*, vol. 52, no. 1, pp. 1–17, 1996.

[170] S. Chatterjee and A. S. Hadi, *Sensitivity analysis in linear regression*, ser. Wiley Series in Probability and Statistics. Hoboken, NJ: Wiley, 1988.

[171] X. Yan and X. G. Su, *Linear Regression Analysis*. World Scientific, 2009.

[172] M. D. Buhmann, *Radial basis functions: theory and implementations*. Cambridge university press, 2003, vol. 12.

[173] A. Bhaduri and L. Graham-Brady, "An efficient adaptive sparse grid collocation method through derivative estimation," *Probabilistic Engineering Mechanics*, vol. 51, pp. 11–22, 2018.

[174] A. Bhaduri, Y. He, M. D. Shields, L. Graham-Brady, and R. M. Kirby, "Stochastic collocation approach with adaptive mesh refinement for parametric uncertainty analysis," *Journal of Computational Physics*, vol. 371, pp. 732–750, 2018.

BIBLIOGRAPHY

[175] A. Bhaduri, D. Brandyberry, M. D. Shields, P. Geubelle, and L. Graham-Brady, "On the usefulness of gradient information in surrogate modeling: Application to uncertainty propagation in composite material models," *Probabilistic Engineering Mechanics*, vol. 60, p. 103024, 2020.

[176] R. Batra and A. Pydah, "Impact analysis of PEEK/ceramic/gelatin composite for finding behind the armor trauma," *Composite Structures*, vol. 237, p. 111863, 2020.

[177] Z. Shen, D. Hu, G. Yang, and X. Han, "Ballistic reliability study on SiC/UHMWPE composite armor against armor-piercing bullet," *Composite Structures*, vol. 213, pp. 209 – 219, 2019.

[178] J. Matoušek, "On the L_2-discrepancy for anchored boxes," *Journal of Complexity*, vol. 14, no. 4, pp. 527–556, 1998.

[179] S. Joe and F. Y. Kuo, "Remark on algorithm 659: Implementing Sobol's quasirandom sequence generator," *ACM Transactions on Mathematical Software (TOMS)*, vol. 29, no. 1, pp. 49–57, 2003.

[180] G. James, D. Witten, T. Hastie, and R. Tibshirani, *An introduction to statistical learning*. Springer, 2013, vol. 112.

[181] S. Sheather, *A modern approach to regression with R*. Springer Science & Business Media, 2009.

[182] L. Farbaniec, J. Hogan, and K. Ramesh, "Micromechanisms associated with the dynamic compressive failure of hot-pressed boron carbide," *Scripta Materialia*, vol. 106, pp. 52 – 56, 2015.

[183] K. Y. Xie, K. Kuwelkar, R. A. Haber, J. C. LaSalvia, and K. J. Hemker, "Microstructural Characterization of a Commercial Hot-Pressed Boron Carbide Armor Plate," *Journal of the American Ceramic Society*, vol. 99, no. 8, pp. 2834–2841, 2016.

[184] M. Bakhshi, A. Souri, and M. K. Amin, "Carbothermic synthesis of boron carbide with low free carbon using catalytic amount of magnesium chloride," *Journal of the Iranian Chemical Society*, vol. 16, pp. 1265–1272, 2019.

[185] K. A. Alshibli and M. B. Cil, "Influence of Particle Morphology on the Friction and Dilatancy of Sand," *Journal of Geotechnical and Geoenvironmental Engineering*, vol. 144, no. 3, p. 04017118, 2018.

[186] H. Li, C. Lo, G. Toussaint, T. Sano, and J. D. Hogan, *Dynamic Fracture and Fragmentation of Boron Carbide*. Nova Science Publishers, 2020, ch. 4, pp. 105–218.

[187] J. Salem, G. Quinn, and M. Jenkins, "Measuring the Real Fracture Toughness of Ceramics: ASTM C 1421," in *Fracture Mechanics of Ce-*

ramics, R. C. Bradt, D. Munz, M. Sakai, and K. W. White, Eds. Boston, MA: Springer US, 2005, pp. 531–553.

[188] A. Krell and E. Strassburger, "Order of influences on the ballistic resistance of armor ceramics and single crystals," *Materials Science and Engineering: A*, vol. 597, pp. 422–430, 2014.

[189] J. M. R. Zavala, "Particle shape quantities and influence on geotechnical properties—A review." Ph.D. dissertation, Luleå Univ. of Technology, 2012.

[190] K. S. Shah, M. H. b. M. Hashim, M. Z. Emad, K. S. b. Ariffin, M. Junaid, and N. M. Khan, "Effect of particle morphology on mechanical behavior of rock mass," *Arabian Journal of Geosciences*, vol. 13, 2020.

[191] H. Wadell, "Volume, Shape, and Roundness of Rock Particles," *The Journal of Geology*, vol. 40, no. 5, pp. 443–451, 1932.

[192] W. C. Krumbein, "Measurement and geological significance of shape and roundness of sedimentary particles," *Journal of Sedimentary Research*, vol. 11, no. 2, pp. 64–72, 08 1941.

[193] E. D. Sneed and R. L. Folk, "Pebbles in the Lower Colorado River, Texas a Study in Particle Morphogenesis," *The Journal of Geology*, vol. 66, no. 2, pp. 114–150, 1958.

BIBLIOGRAPHY

[194] K. A. Alshibli, A. M. Druckrey, R. I. Al-Raoush, T. Weiskittel, and N. V. Lavrik, "Quantifying Morphology of Sands Using 3D Imaging," *Journal of Materials in Civil Engineering*, vol. 27, no. 10, p. 04014275, 2015.

[195] M. Diepenbroek, A. Bartholomä, and H. Ibbeken, "How round is round? A new approach to the topic 'roundness'by Fourier grain shape analysis," *Sedimentology*, vol. 39, no. 3, pp. 411–422, 1992.

[196] G. R. Drevin and L. Vincent, "Granulometric determination of sedimentary rock particle roundness," in *In Proc. International Symposium on Mathematical Morphology (ISMM*, 2002, pp. 315–325.

[197] I. Cruz-Matías, D. Ayala, D. Hiller, S. Gutsch, M. Zacharias, S. Estradé, and F. Peiró, "Sphericity and roundness computation for particles using the extreme vertices model," *Journal of Computational Science*, vol. 30, pp. 28–40, 2019.

[198] M. W. Crofton and J. J. Sylvester, "VII. On the theory of local probability, applied to straight lines drawn at random in a plane; the methods used being also extended to the proof of certain new theorems in the integral calculus," *Philosophical Transactions of the Royal Society of London*, vol. 158, pp. 181–199, 1868.

[199] L. A. Santaló, *Introduction to integral geometry*, ser. Actualités scientifiques et industrielles, 1198. Hermann, 1953.

[200] H. Wadell, "Volume, Shape, and Roundness of Quartz Particles," *The Journal of Geology*, vol. 43, no. 3, pp. 250–280, 1935.

[201] Y.-S. Liu, J. Yi, H. Zhang, G.-Q. Zheng, and J.-C. Paul, "Surface area estimation of digitized 3D objects using quasi-Monte Carlo methods," *Pattern Recognition*, vol. 43, no. 11, pp. 3900–3909, 2010.

[202] G. G. Lehmann and D. Legland, "Efficient N-Dimensional surface estimation using Crofton formula and run-length encoding," 2012.

[203] K.-H. Zum Gahr, W. Bundschuh, and B. Zimmerlin, "Effect of grain size on friction and sliding wear of oxide ceramics," *Wear*, vol. 162-164, pp. 269–279, 1993, wear of Materials: Proceedings of the 9th International Conference.

[204] G.-C. Cho, J. Dodds, and J. C. Santamarina, "Particle Shape Effects on Packing Density, Stiffness, and Strength: Natural and Crushed Sands," *Journal of Geotechnical and Geoenvironmental Engineering*, vol. 132, no. 5, pp. 591–602, 2006.

[205] P. C. Rousé, R. J. Fannin, and D. A. Shuttle, "Influence of roundness on the void ratio and strength of uniform sand," *Géotechnique*, vol. 58, no. 3, pp. 227–231, 2008.

[206] E. Mostefa Kara, M. Meghachou, and N. Aboubekr, "Contribution of Par-

ticles Size Ranges to Sand Friction," *Engineering, Technology & Applied Science Research*, vol. 3, no. 4, pp. 497–501, Aug. 2013.

[207] P. Vangla and G. M. Latha, "Influence of Particle Size on the Friction and Interfacial Shear Strength of Sands of Similar Morphology," *International Journal of Geosynthetics and Ground Engineering*, vol. 1, 2015.

[208] J. A. Sanchidrián, P. Segarra, and L. M. López, "Energy components in rock blasting," *International Journal of Rock Mechanics and Mining Sciences*, vol. 44, no. 1, pp. 130–147, 2007.

[209] P. Michel, P. Tanga, W. Benz, and D. C. Richardson, "Formation of Asteroid Families by Catastrophic Disruption: Simulations with Fragmentation and Gravitational Reaccumulation," *Icarus*, vol. 160, no. 1, pp. 10–23, 2002.

[210] B. Mandelbrot, "How Long Is the Coast of Britain? Statistical Self-Similarity and Fractional Dimension," *Science*, vol. 156, no. 3775, pp. 636–638, 1967. [Online]. Available: https://science.sciencemag.org/content/156/3775/636

[211] V. K. Rohatghi, *An Introduction to Probability Theory and Mathematical Statistics*. John Wiley & Sons, 1976.

BIBLIOGRAPHY

[212] I. Gradshteyn and I. Ryzhik, *Table of Integrals, Series, and Products*. Academic Press, 1980.

Vita

Amartya Bhattacharjee was born in Calcutta, India. He completed his B.E. in Construction Engineering from Jadavpur University (2013) and thereafter pursued a Structural Engineering master's degree from the Civil Engineering Department at the Indian Institute of Technology, Kharagpur (2013-2015). In 2015 he moved to Baltimore to join the Civil & Systems Engineering Department at Johns Hopkins University as a graduate student. Amartya received the Hoomes Rich Fellowship for the academic year 2015-2016 and was thereafter supported by the Materials in Extreme Dynamics Environment program at the Hopkins Extreme Materials Institute for the remainder of his graduate studies. He joined Professor Lori Graham-Brady's group to understand the fracture and fragmentation of armor ceramics and its implications on ceramic material design. Amartya received a master's degree in Mechanical Engineering at Johns Hopkins in 2018, and completed the requirements for a doctoral degree in the Civil & Systems Engineering department in May 2021.